Development of a Data Acquisition System for the Custom Front-End Prototypes of the PANDA Micro Vertex Detector and Study of the Reaction $\overline{p}p \rightarrow \Xi^-\overline{\Xi}^+\pi^+\pi^-$

Dissertation

zur Erlangung des Grades einer
Doktorin der Naturwissenschaften

in der Fakultät für Physik und Astronomie
der Ruhr-Universität Bochum

von

Alessandra Lai

aus

Oristano

Bochum (2018)

Versicherung gemäß §7 Abs. 2 Nr. 6 PromO 2011

Hiermit versichere ich, dass ich meine Dissertation selbständig und ohne unerlaubte fremde Hilfen angefertigt und verfasst habe und keine anderen als die angegebenen Hilfsmittel und Hilfen benutzt habe. Meine Dissertation habe ich in dieser oder ähnlicher Form noch bei keiner anderen Fakultät der Ruhr-Universität Bochum oder bei einer anderen Hochschule eingereicht.

Erster Gutachter: Prof. James Ritman, Ph.D.
Zweiter Gutachter: Prof. Dr. Ulrich Wiedner

Datum der Abgabe: 10.10.2018
Datum der Disputation: 17.12.2018

iv

Contents

Abstract

The Antiproton Annihilation at Darmstadt (PANDA) experiment is a multipurpose modern detector which aims to study the transition between perturbative and non-perturbative Quantum Chromodynamics in the energy range of charmonium. This fixed target experiment will contribute to the understanding of fundamental questions of hadron and nuclear physics by exploiting a high quality $\overline{p}$ beam provided at the Facility for Antiproton and Ion Research. The PANDA detector is composed of several subparts, optimized for specific tasks. The subdetector closest to the interaction point, needed to precisely reconstruct primary and secondary vertices of the interaction, is the Micro Vertex Detector. It is equipped with silicon pixel and strip sensors and custom front-end electronics to readout their data. This thesis describes the contribution to the development of a data acquisition system for the verification of the custom front-end prototypes and its use to asses the performance of the first strip front-end chip prototype, called PASTA. In addition, it reports on the possibility to study the reaction $\overline{p}p \rightarrow \Xi^-\overline{\Xi}^+\pi^+\pi^-$ with PANDA's software framework.

Das PANDA Experiment basiert auf einem modernen Mehrzweck-Teilchendetektor, der den Übergang zwischen perturbativer und nicht-perturbativer Quantenchromodynamik untersuchen wird. Durch die Untersuchung der neu erzeugten Teilchen aus der Annihilation von Antiprotonen und Protonen am High Energy Storage Ring von FAIR wird dieses Fixed-Target Experiment zum Verständnis grundlegender Fragen im Bereich der Hadronen- und Kernphysik beitragen. Der PANDA Detektor besteht aus unterschiedlichen Komponenten, optimiert auf bestimmte Aufgaben. Die Detektoreinheit, die sich am nächsten zum Interaktionspunkt befindet, ist der Micro Vertex Detektor. Er basiert auf Silizium-Sensoren, die in Pixel und Mikrostreifen aufgeteilt sind, und für die Erkennung und Vermessung von primären und sekundären Wechselwirkungspunkten benutz werden. Experimentspezifische Elektronik, um die Sensoren auszulesen, ist zur Zeit in Entwicklung. Diese Doktorarbeit beschreibt den Beitrag zur Entwicklung und Implementierung eines Datenerfassungssystems zur Vermessung dieser Elektronik sowie erster Tests, die mit dem Datenerfassungssystem an dem Mikrostreifen Front-End Prototyp PASTA durchgeführt wurden. Des Weiteren berichtet sie über die Untersuchung der Reaktion $\overline{p}p \rightarrow \Xi^-\overline{\Xi}^+\pi^+\pi^-$ mit PANDA's Software Framework.

x

Preface

Quantum Chromodynamics (QCD) is considered the basic theory of the strong interaction. The fundamental building blocks of this theory are the quarks, which interact with each other by gluon exchange. QCD is extremely successful in describing phenomena at quark distance scales smaller than the size of a nucleon, where the strength of the quark-gluon interaction is weak and perturbation theory can be applied. The perturbative approach fails when the distance among the quarks becomes comparable with the nucleon size and the force among them so strong that they cannot be separated. Consequently, quarks have only been observed as confined within hadrons and never as free particles over a large length scale. This behavior is considered to be related to the interaction among gluons, in addition to their interaction with quarks. This leads to the prediction of the existence of hadronic systems containing only gluons (so-called *glueballs*) and bound systems of $q\bar{q}$ pair and gluons (so-called *hybrids*), which needs a clear experimental confirmation. The confinement of quarks in hadrons and the existence of glueballs and hybrids are only two examples of long-standing open questions in the field of QCD. A clear interpretation of the excitation spectra of hadrons is another missing piece of the puzzle. In the recent years, studies in the charmed meson and baryon sector indicate the existence of states, which await for either confirmation or a consistent theoretical description. On the other hand, several others states that are predicted by theory have not been observed so far. Including strangeness as an additional degree of freedom, the available experimental data becomes scarce. Very little is know about resonances with multi-strange content.

PANDA proposes to contribute to the understanding of fundamental questions of hadron and nuclear physics by exploiting $\bar{p}p$ collisions at the new Facility for Antiproton and Ion Research (FAIR). The key aspects of its physics program focus on the precision spectroscopy of multi strange and charmed baryons, the investigation of charmonium state and open charm production, and the search for exotic matter.

The broad and challenging physics case demands excellent performance from the detector, in terms of mass, momentum, and energy resolution, as well as particle identification and solid angle coverage. To achieve that, the PANDA detector is divided into subdetectors specialized in particular tasks.

The innermost subsystem, the Micro Vertex Detector, is composed of silicon pixel and strip detectors. Its main role is the precise reconstruction of primary and secondary vertices. Due to its position surrounding the interaction point, several constraints on the compactness of the electronics, maximum power consumption, and radiation tolerance exist. Moreover, the PANDA data readout scheme requires the electronics to be self-triggering. Consequently, custom front-end electronics needs to be developed to accommodate all the requirements.

The systematic evaluation of the readout solutions plays a key role in the development phase. Therefore, a suitable data acquisition system is a mandatory tool to perform systematic verification of the prototypes.

The work described in this thesis has its main focus on the development of the data acquisition for the custom front-end prototypes for the Micro Vertex Detector and its use to evaluate PASTA, the first available strip front-end chip. Additionally, the possibility to study the reaction $\bar{p}p \to \Xi^-\bar{\Xi}^+\pi^+\pi^-$ with PANDA is investigated.

The text is structured as follows:

Chapter 1 gives an overview of the FAIR facility, describes the key points of the PANDA physics program, and illustrates the technical design of each subdetector.

Chapter 2 is dedicated to the Micro Vertex Detector, given its importance for this thesis.

Chapter 3 follows with the description of the first prototype of the custom front-end for the strip part of the Micro Vertex Detector.

Chapter 4 provides a detailed description of the data acquisition system developed for the verification of the front-end chips, with particular emphasis on the features implemented during the course of this thesis.

The data acquisition system is then used to carry on the verification of PASTA, described in Chapter 5.

The feasibility study of the reaction $\bar{p}p \to \Xi^-\bar{\Xi}^+\pi^+\pi^-$ is illustrated in Chapter 6.

Finally, Chapter 7 summarizes the studies presented in the previous chapter and the achieved results.

Chapter 1

The PANDA Experiment

The Antiproton Annihilation at Darmstadt (PANDA) experiment is currently under construction at the Facility for Antiproton and Ion Research (FAIR) and will be a unique tool for precision measurements in the field of hadron physics. It aims to provide new knowledge for the quantitative understanding of strongly interacting complex systems, which is one of the major challenges of hadron physics. The physics program of PANDA will help the understanding of quark confinement by means of precision spectroscopy of charmonium states, including their electromagnetic and hadronic properties, as well as the internal structure of hadrons, by measuring open charm production. It will also contribute to the search and study of exotic hadronic matter, such as hybrid mesons and glueballs. PANDA, in fact, will have the capability to perform scans of resonance curves of narrow states, determining with high precision the width and lifetime of such particles. Studies of the nucleon structure and baryon spectroscopy are also part of a very promising physics program, which will address many of the open questions that have recently arose in the field of hadron physics.

This chapter begins with an overview of the FAIR complex. A detailed description of the main aspects of the PANDA physics program follows. Finally, the technical design of the detector is presented.

1.1   The FAIR Accelerator Facility

If not stated otherwise, the reader can refer to FAIR Baseline Technical Report [1] for further information about the FAIR facility.

1.1.1   General Layout of FAIR

FAIR is a laboratory complex that aims for a multifaceted science program that covers three major research areas: nuclear structure and astrophysics, QCD and hadron physics, plasma and applied physics. It will make use of beams of stable and unstable nuclei as well as antiprotons in a wide range of intensities and energies. It is currently under construction in an area adjacent to the already existing GSI Helmholtzzentrum für Schwerionenforschung GmbH (GSI) facility, which consists of a linear accelerator, Universal Linear Accelerator (UNILAC), a heavy ion synchrotron (SIS18), and an Experimental Storage Ring (ESR) (Fig. 1.1). The heart of FAIR is a superconducting synchrotron complex, consisting of two synchrotrons of 1100 m circumference each, called SIS100 and SIS300 (the numbers indicate the rigidity in $T \cdot m$), which will be installed in the same tunnel. The SIS100 will use the present UNILAC and SIS18 as injectors. This synchrotron is designed for the fast acceleration of high intensity proton and ion beams. It can operate in different modes and therefore provide beams with different characteristics, depending on the physics program.
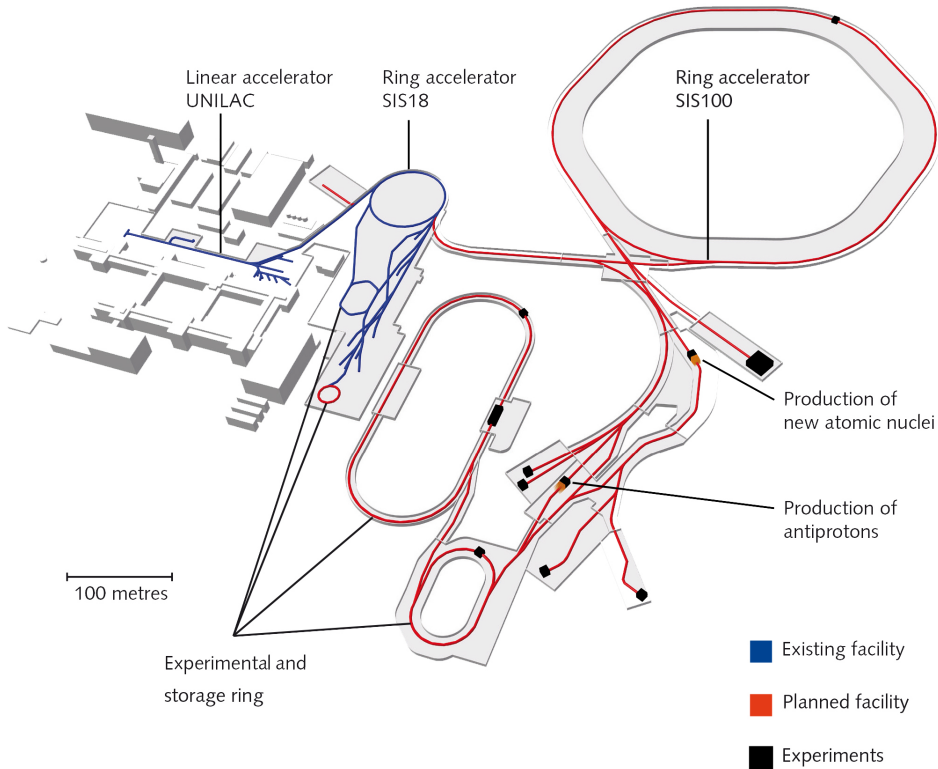

Figure 1.1: The accelerator facility FAIR and GSI. Image from [2].

More specifically, the SIS100 is meant to:

- produce U^{28+} ions up to 2700 MeV/u, compressed into bunches of 50 ns to 100 ns if needed, that can be directly extracted or injected in the SIS300 for further acceleration;
- accelerate protons up to 29 GeV for subsequent interaction with the antiproton production target. For the production of antiprotons, an intense proton beam is needed. Therefore, a separate Proton Linear Accelerator (p-LINAC) will be built and used as an injector for the SIS18.

It is foreseen for the SIS300 to operate in two modes:

- as a stretcher: providing continuous slowly extracted beam in the energy range from 1.5 GeV/u up to the maximum energy of SIS100;
- in high energy mode: acceleration of fully stripped heavy ion beam (e.g., U^{92+} up to 34 GeV/u) and slow extraction.

Some additional storage rings will complement the double-ring synchrotron:

- the High Energy Storage Ring (HESR) for antiprotons with momenta between 1.5 GeV/c and 15 GeV/c.
- the Collector Ring (CR) for stochastic cooling of radioactive nuclei up to 0.74 GeV/u for U^{92+} and antiproton beams up to 3 GeV, as well as measurements of short-lived nuclei
- the Recuperated Experimental Storage Ring (RESR) for accumulation of antiprotons previously cooled in the CR and fast deceleration of radioactive secondary beams
- the New Experimental Storage Ring (NESR) for cooling and deceleration of stable and radioactive ions and antiprotons for low energy and trap experiments. Stochastic and electron cooling up to 0.74 GeV/u for U^{92+} and 3 GeV for antiprotons.

In the starting phase of FAIR, the so-called Modularized Start Version (MSV) [3], the RESR and NESR, as well as the SIS300 synchrotron, are not included. They are considered a desirable upgrade, aiming to strengthen the long-term potential of the FAIR facility and therefore it is foreseen to proceed with their construction when funding will be secured.

Since PANDA is the internal target of the HESR, some more details on this storage ring are given.

1.1.2 The HESR

The HESR has the shape of a racetrack with 574 m circumference and two straight sections of 132 m in length each (Fig. 1.2). It counts 44 dipole magnets for a total bending power of 50 T · m.
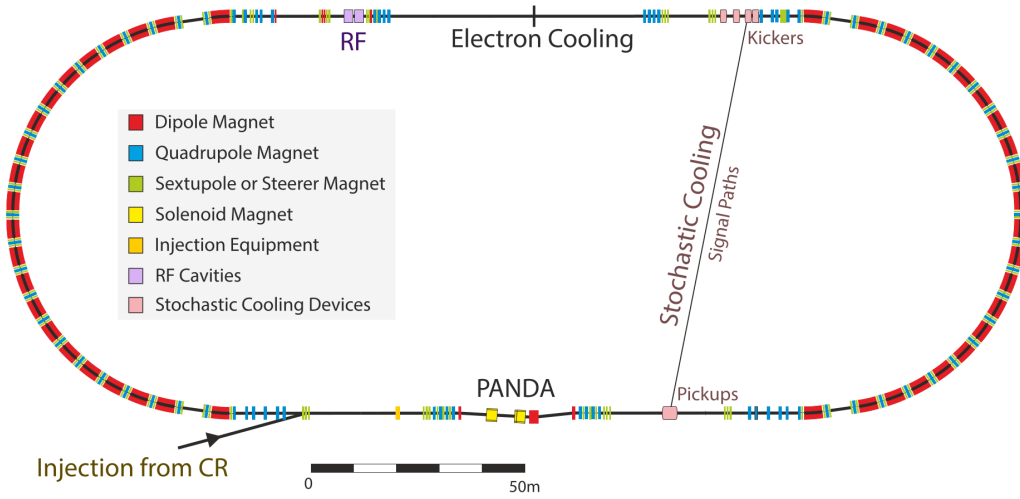
Figure 1.2: Layout of the HESR. Image from [4].

PANDA, the acceleration cavities, and the cooling equipment will be installed in the straight sections.

Two kinds of beam cooling techniques are necessary in order to meet the design specification: electron cooling and stochastic cooling. Electron cooling is based on the idea of shrinking the size and energy spread of a charged particle beam without removing particles from it. This method was invented by Gersh Budker at INP Novosibirsk, in 1966 [5]. The basic principle works as follows: a beam of quasi-monoenergetic electrons is merged with the ion beam that needs to be cooled. The average velocity of the electrons is made equal to the average velocity of the other particles in the beam. Momentum is exchanged among electrons and ions until thermodynamic equilibrium is reached. Due to these interactions, the energy spread of the ions is reduced and the occupied phase space shrinks. In other words, the temperature of the beam is reduced. The electrons are significantly lighter than the ions in the beam and, correspondingly, have a much lower rigidity than the ions that are moving at the same average velocity. Consequently, at the end of the electron-ion overlap region the electron beam is easily separated and removed from the storage ring. Stochastic cooling instead, invented by Simon van der Meer at CERN at the beginning of the 1970s, reduces the energy spread and angular divergence of a charged particle beam by using a measurement and feedback system [6]. As particles travel around a circular accelerator, a so-called pick-up measures the deviation of the beam orbit from the ideal orbit and sends a signal across the ring to the so-called kicker, which adjusts their trajectories by means of an electric field.

To meet the requirements for high intensity and high quality beams, the HESR has two possible operating modes: high luminosity and high resolution. The first mode will allow for luminosities up to $2 \times 10^{32}\,\mathrm{cm}^{-2}\,\mathrm{s}^{-1}$ and a momentum spread of $\Delta p/p = 10^{-4}$, in the whole energy range for the antiprotons. The second mode will reach a peak

luminosity one order of magnitude smaller than the previous mode with a better momentum resolution (i.e., $\Delta p/p = 4 \times 10^{-5}$) . The antiprotons will be delivered at a rate of $2 \times 10^7 \, \text{s}^{-1}$, in bunches of $200 \, \text{m}$ length. The RESR, meant for collection of the antiprotons, is needed to reach the high luminosity mode. Since the RESR is not part of the MSV, this operating mode will be available only in a second phase. For more detail on the technical aspects concerning the design of the HESR and the planned operating modes refer to [7].

1.1.3 FAIR Parallel Operation

In general, at accelerator facilities, it is possible to split the primary beam and direct it to different target areas. This does not necessarily allow parallel operation of different physics programs. The construction scheme of FAIR aims to such synergy. FAIR will thus operate as a dedicated facility for each of the programs. Fig. 1.3 shows how up to four different physics programs can be served simultaneously.
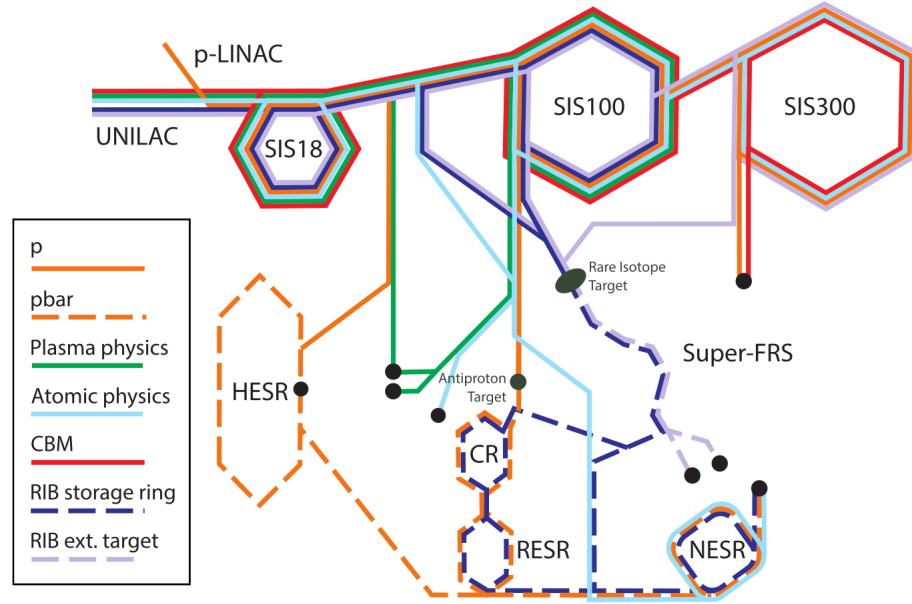
Figure 1.3: Different beam lines that can be operated in parallel at FAIR. The orange lines are the two relevant for PANDA. Image from [1].

1. Antiproton physics: a proton beam (orange), accelerated in SIS100, produces antiprotons (orange dashed) in the antiproton target-station, which are then collected, accumulated and cooled in the CR/RESR storage-ring combination (when available), and transferred either to the HESR or to the NESR for experiments.
2. Radioactive ion beams: during the fraction of time in which the SIS100 is not needed for the protons, a primary ion beam is accelerated in it and slowly extracted

to the Super-Fragment Separator (FRS) for radioactive secondary beam production. These beams are then used for fixed target experiments (violet-dashed) or for storage in the CR and NESR instead of antiprotons (blue-dashed).

3. High energy nuclear physics: every 10 s to 100 s a high-energy heavy-ion beam (red) is accelerated in SIS100/300 and slowly extracted for nuclear collision experiments.

4. Plasma or atomic physics: plasma physics experiments that require very low repetition rates, receive intense compressed beam pulses (green) at intervals of few minutes. Alternatively, atomic physics experiments (light blue) may be served in the pauses of the antiproton production.

1.2 The PANDA Physics Program

The PANDA experiment is the internal target of the HESR. It has been designed to address fundamental questions of QCD, mostly in the non-perturbative regime, exploiting interactions between an antiproton beam and the protons or nuclei of a fixed target. In contrast to e^+e^- annihilations which only allow $J^{PC} = 1^{--}$, in $\bar{p}p$ collisions all non-exotic quantum number combinations are allowed in formation and exotic quantum number can be observed in production reactions. The tiny spread of the energy of the antiproton beam, achievable with the high energy resolution mode of operation of the HESR, will allow for high precision measurements of the widths of narrow states, independently of the mass resolution of the detector. PANDA will cover a large mass-scale spectrum (energy from $\sqrt{s} = 2.26\,\text{GeV}$ to $\sqrt{s} = 5.48\,\text{GeV}$) and will benefit from high statistics thanks to high hadronic production rates. Fig. 1.4 shows the physics spectrum available at the HESR. The region between the blue dashed lines indicates the portion of such spectrum accessible with PANDA. Since the start version of FAIR will not allow to reach the highest designed luminosity, the physics cases that require it will be studied in a second phase of the experiment.

The following paragraph describes the main physics cases that PANDA proposes to study. For additional information the reader can consult [8].

1.2.1 Charmonium

Charmonium is a bound state of c and $\bar{c}$ quarks. The spectrum of charmonium states has features that resemble those of positronium, despite the different energy scales (0.1 GeV to 1 GeV and 1 eV, respectively), therefore an analogy between the strong interaction and the electromagnetic processes is suggested. The potential that describe the interaction in the case of positronium is Coulomb-like. In the case of charmonium, a linear correction term that accounts for the quark confinement has to be introduced. The charmonium spectrum is shown in Fig. 1.5. The states below the open charm
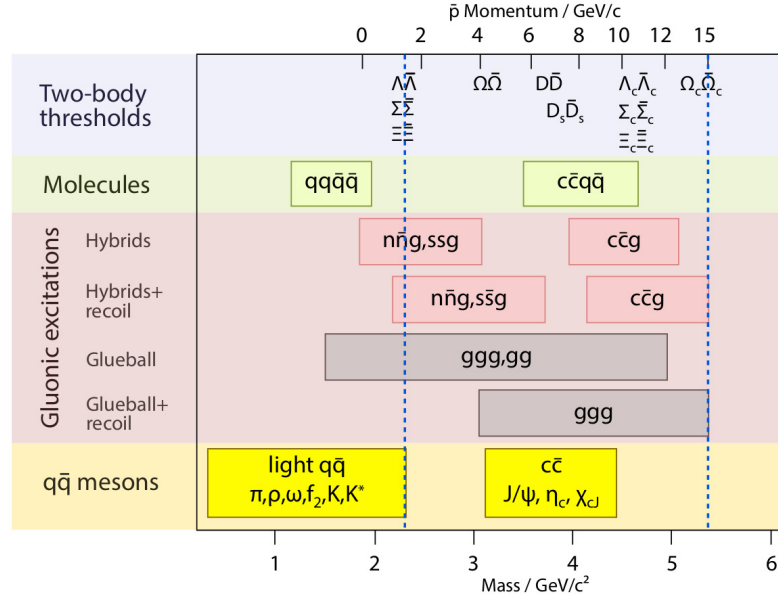
Figure 1.4: Physics spectrum available at the HESR. The region between the dashed lines indicates the range accessible with PANDA. The top axis shows the momentum of the antiproton beam and the bottom axis shows the respective center of mass energy. Image from [4], adapted from [9].

threshold of $3.7\,\mathrm{GeV}$, have all been observed. Good accuracy measurements are achieved for triplets states but not for singlet states. For example, η_c has been observed by various experiments, but the results show large discrepancies concerning the measured mass and width. The region above the open charm threshold is considered as a possible source of new physics. In the recent years many new states have been observed, which are associated with charmonium because of their predominant decay into charmonium states (e.g., the X(3872) state [10–13]). Theoretical model can describe some of these states. However, no consistent theoretical description of the complete spectrum is available. Such states are referred to as X, Y, Z states. The vector states (i.e., $J^{PC} = 1^{--}$) have been named Y and the charged states Z. Theoretical studies suggest a few possible interpretation that would explain the nature of the newly discovered XYZ states. The possible explored scenarios are summarized below and sketched in Fig. 1.6 [14].

- Molecular states: two charmed mesons loosely bound to each other by means of a quark/color exchange interaction at short distance or a π exchange at long distance.

- Tetraquarks: bound state of four quarks, possibly caused by spin-spin interactions.

- Hybrids: charmonium states with an additional gluonic degree of freedom.
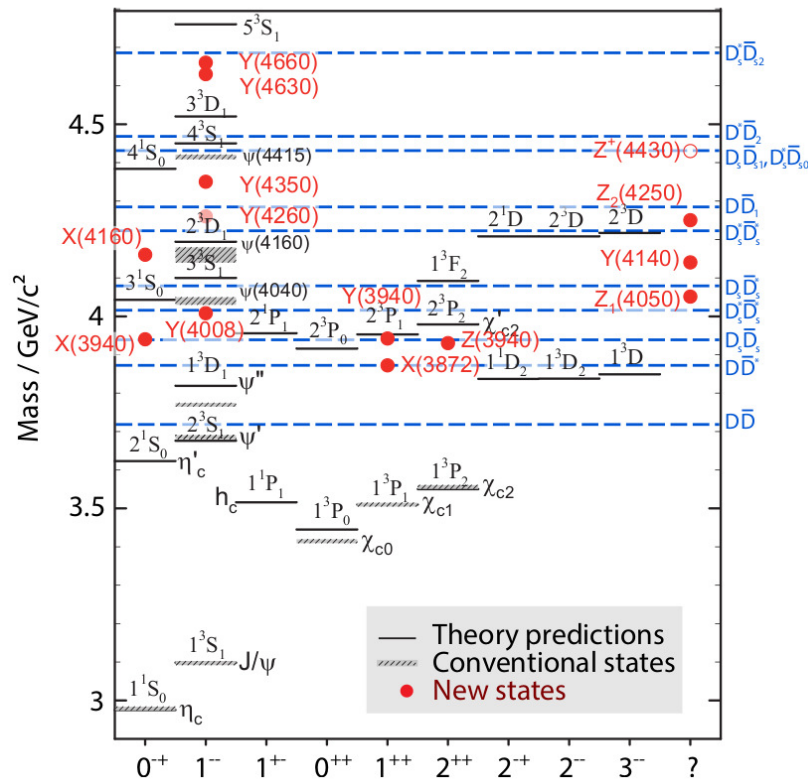
Figure 1.5: The charmonium spectrum with states predicted by theory (black solid lines) and measured states. Shaded black lines indicate conventional states, while red dots indicate newly observed XYZ states. The blue dashed lines indicate the thresholds for D meson pairs decays. Image from [4], adapted from [15].

(a) Molecular state.   (b) Diquark-diantiquark state.   (c) Gluon hybrid.
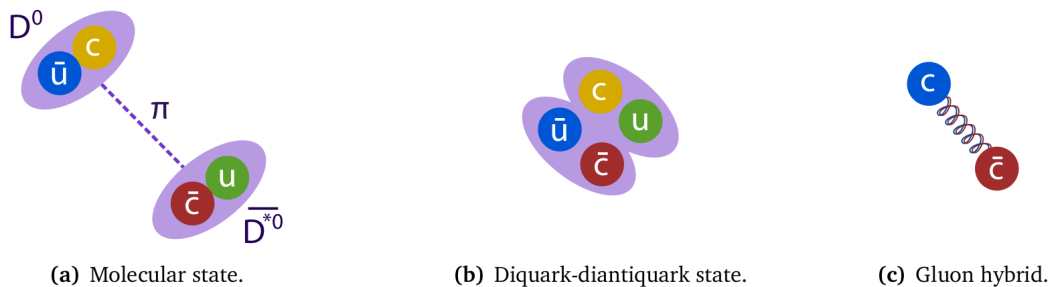
Figure 1.6: Possible explanation for the nature of the hadronic states not predicted by the conventional quark model. Image from [4].

So far, the highest luminosity and momentum resolution have been achieved by the Fermilab experiments E760 and E835 ($2 \times 10^{31}\,\mathrm{cm^{-2}\,s^{-1}}$ and 10^{-4} , respectively). Having modest charged particle tracking and identification capabilities, their studies were focused on neutral final states. PANDA will be able to explore the entire energy region below and above the open charm threshold with high statistics (it is expected to collect several thousand $c\bar{c}$ states per day), reaching ten times higher luminosity and momentum resolution than the Fermilab experiments. Moreover, PANDA will benefit from the design of a technologically advanced detector which will provide a high angular coverage and excellent capability in detecting hadronic decays. The accuracy will be of the order of $100\,\mathrm{keV}$ for the masses and for the widths.

1.2.2 Hybrids

By adding an excited gluon to a $q\bar{q}$ pair, a so-called *hybrid* is produced. A gluonic degree of freedom is therefore introduced in addition to the standard $q\bar{q}$ pair, leading to the formation of hybrids which exhibit quantum numbers that cannot be formed by the sole $q\bar{q}$ pair. These hybrids are therefore called exotics. Exotic charmonia are predicted to exist in the mass region between $3\,\mathrm{GeV}/c^2$ and $5\,\mathrm{GeV}/c^2$, well within the range of PANDA. Theory predictions are mainly based on the bag model, the flux tube model, and recently also from Lattice Quantum Chromodynamics (LQCD) [16, 17]. It is foreseen to study charmonium hybrids with production reactions at the maximum momentum achievable for the antiprotons (i.e., $15\,\mathrm{GeV}/c$). Production reactions are the only possibility to obtain charmonium hybrids with exotic quantum numbers. Hybrids could thus be identified by comparing the production and formation spectra and looking for missing excitation in the latter.

1.2.3 Glueballs

Glueballs are states with only gluons in their valence content. Theory predicts the existence of about 15 such states in the mass range of the HESR (Fig. 1.7) [19]. Glueballs can be generated in formation or production reactions, depending on their spin-parity quantum numbers. Glueballs with exotic quantum numbers (oddballs) do not mix with standard mesons. Therefore, their widths are predicted to be rather narrow and easily identifiable [20]. Many studies have been carried out to detect glueball states. For example, the Jetset and Obelix collaborations at LEAR found some hints on the existence of glueball states. In one case the acquired statistics was not sufficient for the identification and in the other case the results were not in agreement with the predictions of LQCD [21, 22]. The PANDA experiment will be able to carry out similar studies with two orders of magnitude more statistics and a vastly improved detector setup.
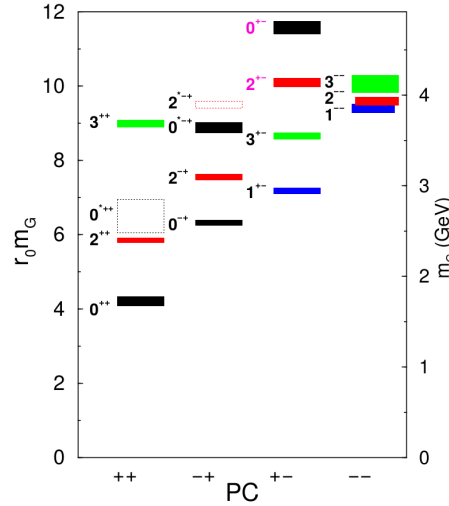
Figure 1.7: The glueball spectrum with predicted states accessible within the PANDA momentum range. The horizontal axis shows the charge and parity configuration, the vertical axis show the mass of the states in units of the hadronic scale parameter r_0 (left axis) and in GeV/c^2 (right axis). The color code refers to the total angular momentum J, while the numbers next to each state indicate its quantum number configuration J^{PC}. Pink numbers refer to oddballs. Image from [18].

1.2.4   Heavy-Light Systems

Mesons that are made of a heavy and a light constituent (e.g., the D meson) can be seen as the hydrogen atom of QCD, with a heavy element in the center and a lighter one surrounding it. Theory and experiment show a good agreement for non-strange states. The classification of newly found heavier states within the quark model proves to be difficult. Fig. 1.8 shows the predictions for the strange D meson spectrum, D_s, according to a relativistic quark model ([23], [24]) and the experimental observation. As one can see, many of the newly observed states do not fit the theoretical predictions. As an example, one can consider the case of the $D_s(2317)$, discovered by [25] and then confirmed by [26] and [27], which is found at least 150 MeV below the quark model expectation. At present, only an upper limit for the width of the $D_s(2317)$ state of 3.8 MeV/c^2 is available [28]. Thanks to the small momentum spread in the HESR, PANDA will be capable of measuring the width of this state with high energy resolution, down to $\mathcal{O}\left(100\,\mathrm{keV}/c^2\right)$, by means of a threshold scan [29]. Such measurements will allow to exclude or corroborate many of the theoretical models.
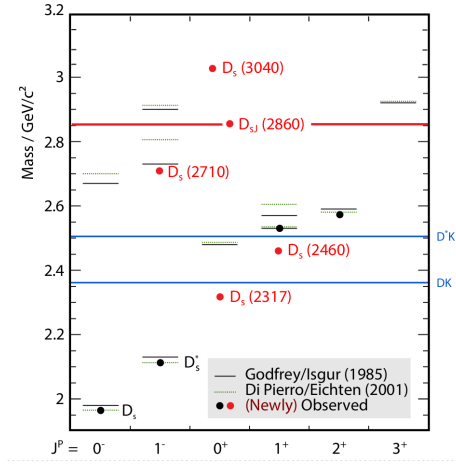
Figure 1.8: Comparison between the D_s predicted spectrum by Godfrey and Isgur [23] (solid lines) and Di Pierro and Eichten [24] (dotted lines) and the experimentally observed states (black and red dots, being the red the most recently observed). The horizontal axis shows the J^P of the states while the vertical axis shows the mass of the states expressed in GeV/c^2. The blue solid lines indicate the thresholds for the decays into D_s^*K pairs. Image from [4], adapted from [15].

1.2.5 Multi-Strange and Charmed Baryons

The understanding of the baryon excitation spectrum is one of the main goals of non-perturbative QCD. Most of the efforts are currently devoted to studies in the nucleon and Δ sector. So far, the agreement between the observations and the predictions of the quark model is rather poor. Several low-lying states have been observed at energies different from the predicted ones and, on the other hand, several predicted higher lying states have not yet been seen experimentally. This phenomenon is known as the *problem of the missing resonances* [30]. With the inclusion of strangeness as an extra degree of freedom (i.e., Λ, Σ, Ξ, Ω baryons), the experimental data quality becomes poorer. Some new states have been observed in the Λ and Σ spectra, but so far confirmation and unambiguous interpretation are missing [31], [32]. Considering double or triple strange baryons, namely Ξ and Ω, some excited states have been observed but spin-parity quantum numbers have not been determined.

In $\bar{p}p$ collisions at PANDA, a large fraction of the inelastic cross section is associated with channels resulting in a baryon-antibaryon pair in the final state. Moreover, the production of an extra particle (a K or D meson) is not necessary for strangeness conservation. This reduces the energy threshold and thus the background channels that would affect the reconstruction of such states. Ground state strange and charmed baryons decay via the weak interaction and thus have displaced decay vertices. This feature requires an excellent tracking capability that can be ensured by the main tracking

detectors in PANDA. Significant statistics will be collected to study excited states and decay channels with PANDA. For example, assuming the only existing theoretical prediction for $\bar{p}p \rightarrow \Omega\overline{\Omega}$ of $2\,\mathrm{nb}$ at $7\,\mathrm{GeV}/c$ $\bar{p}$ momentum, it is estimated to produce roughly 700 pairs per hour at the highest achievable luminosity [33].

1.2.6   Reaction Dynamics

In the field of hadron physics, the identification of the relevant degrees of freedom is of fundamental importance for the description of the reactions. In $p\bar{p}$ interactions, which result in two mesons in the final state, the scattering amplitude can be described in terms of quark content of the hadrons or can be purely hadronic, depending on the momentum transfer. It is likely that the transition between the two regimes happens within the PANDA energy range. In the quark picture, hyperon pair production either involves the creation of a $q\bar{q}$ pair or the knock out of such pairs out of the nucleon sea. PANDA will be able to study creation mechanisms of $q\bar{q}$ pairs and their arrangement in hadrons via reactions like $p\bar{p}$ going to a hyperon-antihyperon pair. Both strange and single charmed hyperons are energetically accessible in PANDA. Therefore, PANDA could contribute to the picture with a high statistics and a large amount of observables. This will allow to access the spin observables, which play a key role in understanding the interactions and the production mechanisms, and to perform partial wave analysis to study the quantum numbers. The data collected for momenta above $2\,\mathrm{GeV}/c$ will have a particular importance, since almost nothing is known about differential distributions and spin observables, except for low statistics bubble chamber experiment data. Although a significant data set exist from LEAR for single strange hyperons for momenta below $2\,\mathrm{GeV}/c$ [34], the measurements of hyperon pair production with PANDA will help the understanding of the production mechanism, by extending this type of studies to higher energies and to double and triple strangeness.

1.2.7   Hypernuclei

Hypernuclei are nuclei in which at least one up or down quark has been replaced by a strange quark. In this way a new quantum number, the strangeness, is introduced in the nucleus. Despite the experimental effort that followed the discovery of double-Λ hypernuclei [35], up to now, only six double-Λ hypernuclei are known. The use of an antiproton beam will allow to produce a high quantity of multi-strange hypernuclei, making PANDA competitive with dedicated facilities. Since an hyperon bound in a nucleus is not restricted by the Pauli principle when populating the possible nuclear states, it represents a selective probe of the nuclear many body problem. Moreover, it can not only probe the nuclear structure and the possible modifications due to its presence, but also change its properties. A comparison between standard nuclei and

hypernuclei can be also of interest to understand key questions of nuclear physics, e.g., the origin of the nuclear spin-orbit force [36]. Hyperon spectroscopy is therefore an interesting topic that can shed light on aspects related to different fields of science (i.e., astrophysics, nuclear physics, many body systems). Scattering experiments between two hyperons are impractical because hyperon targets are not available, due to their short lifetime. Therefore, it is foreseen to produce hyperons in PANDA via a two-step production mechanism (Fig. 1.9). A Ξ produced in the reactions $\bar{\mathrm{p}}\mathrm{p} \to \Xi + X$, will re-scatter within the primary target nucleus and be stopped in an external secondary target, where it will be captured by a nucleus. Cascade hypernuclei that have formed will then transform via the reaction $\Xi^- \mathrm{p} \to \Lambda\Lambda$. Since the experimental setup for hypernuclear physics is different from the standard one for PANDA, dedicated runs for this topic are foreseen.
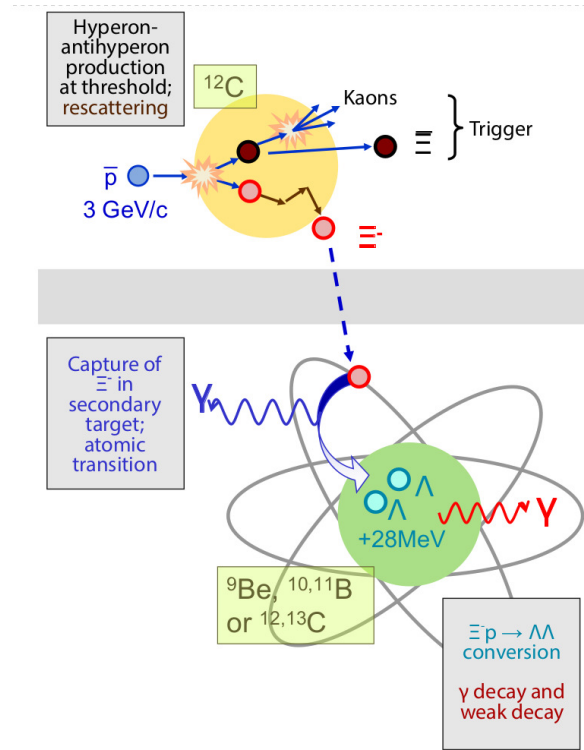

Figure 1.9: Production mechanism of a double-Λ hypernuclei using the antiproton beam. A Ξ produced in the initial reaction undergoes rescattering in the primary target. It is subsequently stopped in an external secondary target (e.g., ^{12}C) and captured by a nucleus, where it transforms into two Λ. Image from [4], adapted from [9].

1.2.8   Nucleon Structure

As already discussed, the physics program of PANDA covers various aspects of non-perturbative QCD. In addition to that, PANDA will be able to investigate the nucleon structure exploiting electromagnetic processes.

Proton Electromagnetic Form Factors in the Time-Like Region

Electromagnetic form factors are fundamental quantities that describe the intrinsic electric and magnetic distributions of hadrons. They therefore represent valuable probes to study the nucleon structure. An hadron with spin S is described by $2S+1$ independent form factors. Therefore, for protons and neutrons (spin $1/2$) two form factors exist: the electric G_E and the magnetic G_M. Form factors are experimentally accessible through measurements of differential and total cross section for elastic e^-p scattering in the space-like region (i.e., $q^2 > 0$) and the crossed annihilation process ($\bar{p}p \to e^+e^-$) in the time-like region (i.e., $q^2 < 0$). It is assumed that the interaction occurs through the exchange of a photon carrying a momentum transfer squared q^2. In the time-like region the precision of the proton form factors measurements has been limited by the achievable luminosity. Several attempts of studies have been recently made (e.g., by LEAR [37], BABAR [38], and BESIII [39]), but the results are not consistent with each other and/or have large total uncertainties.
PANDA, thanks to the high luminosity operating mode, the rich particle identification capabilities, and excellent coverage, will be able to perform precision measurements on the moduli of the form factors up to $q^2 = 14 \, (\text{GeV}/c)^2$, with an expected background suppression factor of approximately 10^8 [40]. The form factor program could run in parallel to many other measurements that require high energy beam (e.g., charmed hybrid studies).

Generalized Parton Distributions

Recently, a theoretical framework to study hard exclusive processes in lepton scattering experiments has been established. This framework is based on a factorization theorem, which in suitable conditions, allows to treat these processes using the QCD handbag diagram. The conditions are such that the process can be separated into a hard perturbative QCD process and a soft part which is parameterized by the so-called Generalized Parton Distributions (GPDs). The GPDs encode information on the distribution of partons both in the transverse plane and in the longitudinal directions. The experimental measurement of the exclusive processes involving GPDs is a challenge that requires high luminosity to compensate for the small cross sections. Moreover, high performance detectors capable of ensuring the exclusivity of the final state are needed as well [41]. PANDA intends to carry on these studies by measuring the reaction

$\overline{\mathrm{p}}\mathrm{p} \to \gamma\gamma$. The high luminosity and the excellent detector, especially the electromagnetic calorimeter close to 4π solid angle coverage, will enable PANDA to separate the signal from the hadronic background.

1.3 Detector System

The physics program of the PANDA experiment imposes several constraints on the design of the individual detector systems. In general, it is required that the detector is modular and flexible, able to detect both charged and neutral particles, covering the full solid angle, providing good particle identification and high resolution.

The PANDA detector is composed of two main parts: the Target Spectrometer and the Forward Spectrometer (Fig. 1.10 and Fig. 1.11). The transition between the two parts happens at 10° in the horizontal plane and 5° in the vertical plane. The total length of the detector is around 13 m.

Following is an overview of the main components of the PANDA detector. Since the description of the subdetectors will not be detailed, references will be given. Only the Micro Vertex Detector (MVD) will have a dedicated chapter, for the focus of this thesis is related to it (refer to Chapter 2).
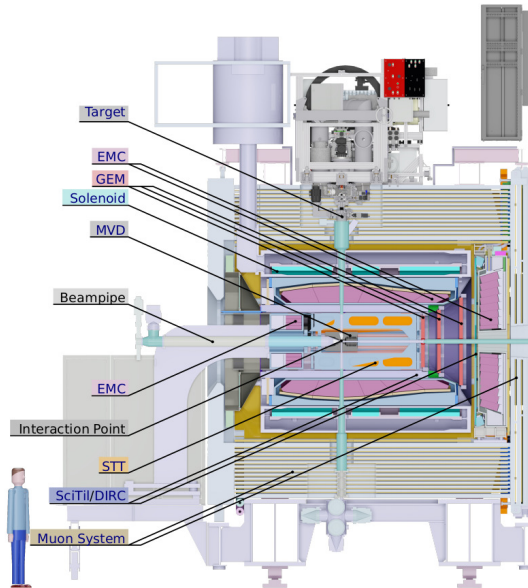

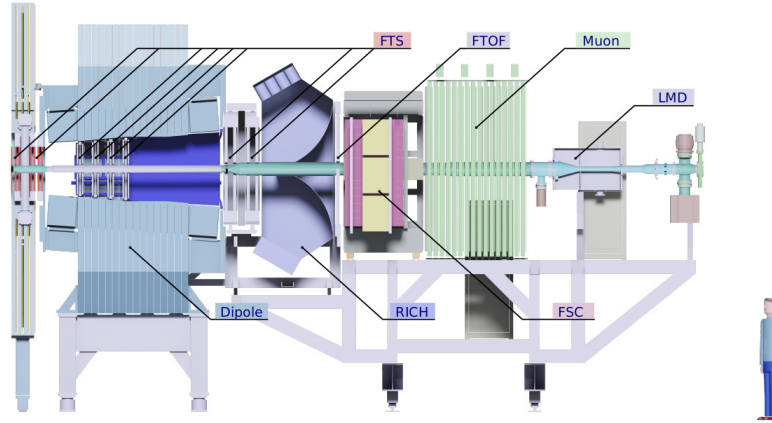Figure 1.10: The Target Spectrometer of PANDA. The labels indicate the sub-systems. Image from [4], [42].

Figure 1.11: The Forward Spectrometer of PANDA. The labels indicate the sub-systems. Image from [4], [42].

1.3.1   Target System

Two types of targets are foreseen for PANDA: a cluster jet target and a pellet target [43]. A cluster-jet beam can be produced by means of the expansion of a pre-cooled gas (hydrogen but also deuterium or heavier gases) in laval-type nozzles of size of the order of µm in vacuum. As the gas passes through such nozzles, a supersonic beam forms when the gas cools down, condensating in nano-particles. Fig. 1.12a shows a jet coming out of the nozzle. These nano-particles, consisting of 10^3 to 10^5 atoms, are called clusters. Before the jet stream is inserted into the vacuum pipe that interfaces with the HESR vacuum by means of a valve, a skimmer and a collimator act as shaping devices (Fig. 1.12b).

A target made of clusters has the advantage of a homogeneous volume density distribution and no time structure. The thickness of a cluster target can be adjusted during operation. The required target density for the operation of PANDA in the high luminosity mode is 4×10^{15} atoms/cm^2. Currently, the available prototype reaches 2×10^{15} atoms/cm^2. A second development involves the design of a pellet target. It consists of frozen hydrogen microspheres with size of 20 µm to 40 µm in a regular stream that traverse the antiproton beam vertically. The starting point for the production of the pellets is the cooling and liquefaction of pressurized hydrogen. The liquid hydrogen is then pressed through a nozzle which is forced to vibrate vertically by means of a piezo-electric transducer. The liquid jet is then broken into droplets which are subsequently injected into a vacuum chamber through a capillary. During this transit, the microspheres turn from liquid to solid, forming the pellets (Fig. 1.13a). Before reaching the interaction point, the pellet stream is shaped by means of a skimmer. Fig. 1.13b shows a schematic drawing of the production chain of a pellet stream.

The pellets can reach a speed of 60 m/s. Other materials like nitrogen, deuterium or all

noble gases can be used to produce a pellet target.

The major advantages of the pellet target are: the high density, of the $\mathcal{O}\left(10^{15}\,\text{atoms/cm}^2\right)$, and the possibility to know the position of the individual pellets accurately at the time of the interaction with the beam, allowing to achieve a high resolution. On the other hand, due to the discrete structure of the target, variations of the thickness of the pellets is possible on a short time scale.

Table 1.1 shows an overview of the properties of the two target systems.

Table 1.1: Main properties of the two target systems.

	cluster target	pellet target
effective target thickness	$4 \times 10^{15}\,\text{atoms/cm}^2$	$5 \times 10^{15}\,\text{atoms/cm}^2$
target thickness adjustable	yes	yes (by modification of pellet rate)
volume density distribution	homogeneous	granular
size transversal to beam	2 to 3 mm	≤ 3 mm
size longitudinal to beam	15 mm	≤ 3 mm
target particle size	nm scale	20 µm
mean vertical particle distance	≤ 10 µm	2 mm to 20 mm
target material	H_2 , D_2	H_2, D_2, N_2, Ar
	heavier gases optional	heavier gases optional
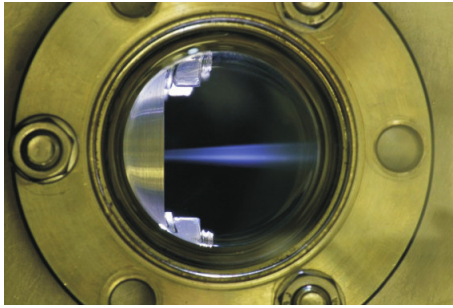
(a) Hydrogen cluster-jet beam after passing the nozzle. The cluster-jet is illuminated by Light Emitting Diodes (LEDs) placed inside the vacuum chamber. Image from [43].
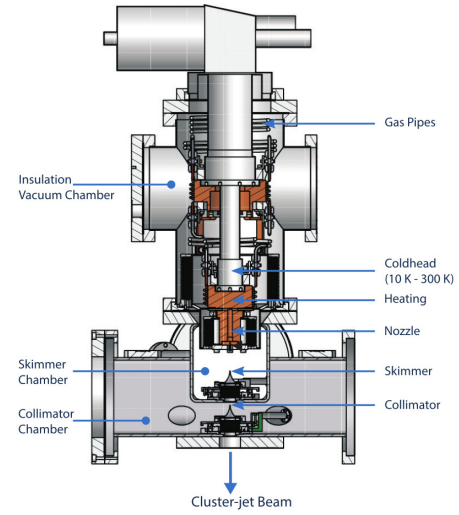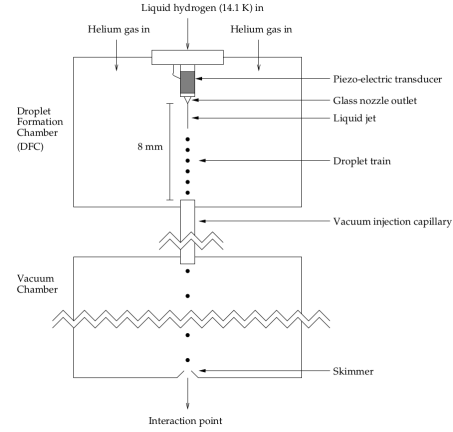
(b) A Computer Aided Design (CAD) drawing of the cluster-jet source. Image from [4], adapted from [43].

Figure 1.12: Illustration of the cluster target system.

(a) Pellets formation: the microspheres turn solid during the vacuum injection. The long traces are the pellets that bounce around. The stream is illuminated by a laser.

(b) Schematic drawing of the production technique of the pellet stream.

Figure 1.13: Illustration of the pellet target system. Images from [44].

1.3.2   Magnets

The momentum reconstruction of charged particles and the subsequent identification relies on appropriate magnetic fields which bend their trajectories. Two large magnets are designed for PANDA, in order to provide an ideal combination of fields: a superconducting solenoidal magnetic field in the Target Spectrometer and a resistive dipole field in the Forward Spectrometer [45].

Around the interaction region a superconducting solenoid of 2 T will be installed (Fig. 1.14a). It is made of a split coil with Rutherford type cables and indirect cooling. The dimensions are 4 m length and 1.9 m diameter. The solenoid will operate at the liquid helium temperature for superconductivity at 5 kA current. It will ensure a homogeneity of the field better than 2 %. The whole structure will weigh around 300 t and it will be retractable to a parking position outside the beam (e.g., for maintenance and commissioning).

Forward going particles will experience a field 2 T · m generated by the dipole (Fig. 1.14b). With its total weight of 220 t, it will have a total aperture of 1 m × 3 m and will be placed around 3.5 m downstream of the interaction point. In order to keep the production costs and the maintenance efforts low, a resistive dipole has been chosen, instead of a superconductive one. The dipole will operate at a current of 2.16 kA and its operation will be fully synchronous with the HESR.
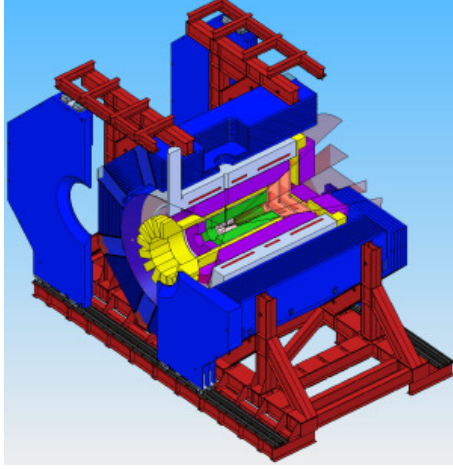
(a) CAD drawing of the solenoid magnet mounted on its support structure. Image from [45].
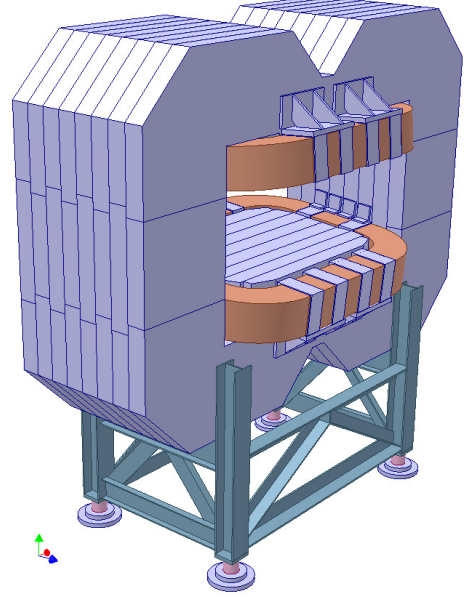
(b) Dipole magnet view from downstream side. Image from [45].

Figure 1.14: Illustration of the two PANDA magnets.

1.3.3 Tracking Detectors

The measurement of charged particle trajectories with high resolution over the complete solid angle is provided by four different tracking systems: the MVD, the Straw Tube Tracker (STT), the Gas Electron Multipliers (GEMs), and the Forward Tracker (FT).

Micro Vertex Detector

The MVD is the innermost subdetector of PANDA. Its fundamental task is the reconstruction of the primary vertex of the interaction, as well as of displaced vertices for short-lived particle decays. It does not only provide spatio-temporal information about the collision, but also gives a measure of the deposited energy, to help the particle identification.

As already mentioned, since this thesis is centered on the MVD, a separated chapter will be dedicated to its description in more depth.

Straw Tube Tracker

The STT, covering the polar angle region between 10° and 140°, is positioned around the beam-target interaction point and it is made of straw tubes, each one with a length of 1400 mm and a diameter of 10 mm [46]. Fig. 1.15 shows a CAD drawing of the STT. The straws are composed of a cylindrical tube filled with a gas mixture of Ar and CO_2 at 2 bar pressure. Each tube has a conductive inner layer, made of Al-Mylar film, as cathode and a gold-plated tungsten-rhenium wire of 20 μm diameter along the cylinder axis as the anode. An incoming particle produces electron-ion pairs in the gas, which are then separated by an electric field applied between the wire and the outer conductor. Avalanche multiplication, of $\mathcal{O}\left(10^4–10^5\right)$ depending on the applied voltage, takes place inside the volume of the detector, allowing to have a measurable signal. The STT will make use of 4232 straws arranged in 27 layers: 19 axial layers (i.e., parallel to the beam) and 8 skewed by 3° with respect to the beam (Fig. 1.16) [47]. A fully assembled double-layer is shown in Fig. 1.17. Due to the pressurized straws, the structure is self-supporting, thus reducing the material budget. The STT provides spatio-temporal information, by measuring the drift time of the electrons, and energy loss information, useful for particle identification, by measuring the deposited charge. The detection efficiency for this system is around 99.5 %, the position resolution is 150 μm, and the momentum resolution is about 3 % for operation as a stand-alone detector at a magnetic field of 2 T.

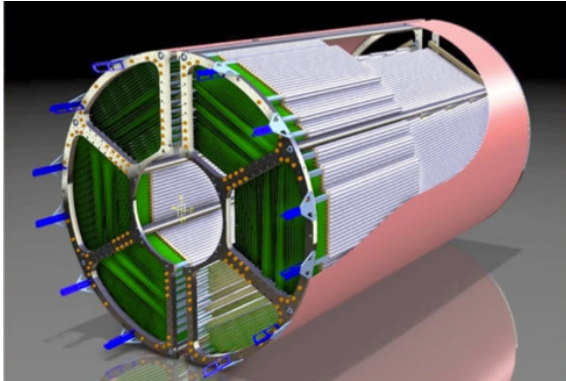

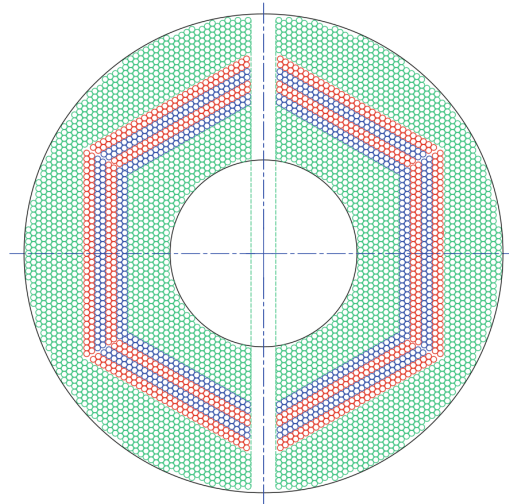Figure 1.15: CAD drawing of the PANDA STT together with its mechanical frame. Image from [46].

Figure 1.16: Layout of straw tubes in the STT. The green-colored straws are parallel to the beam line, while the blue- and red-colored are skewed by ±3° relative to the axially aligned ones. Image from [46].
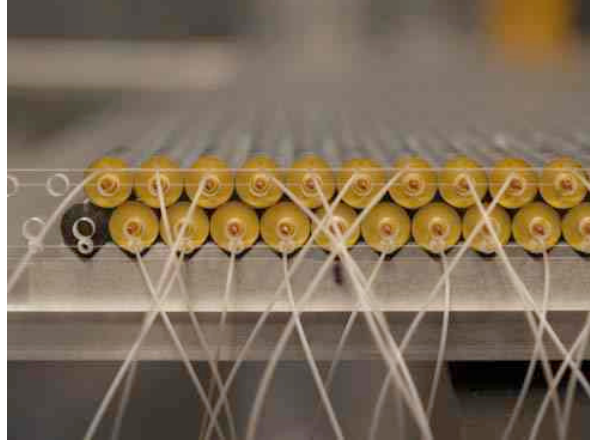
Figure 1.17: A straw tube double-layer mounted on a reference plate. Image from [46].

Gas Electron Multiplier

For the tracking of forward going particles, outside the acceptance of the STT, it is foreseen to install three disks of GEMs that will cover a region between 80 cm and 189 cm downstream of the target. The GEMs are gaseous micro-pattern detectors that use gas electron multiplier foils as amplification stages. They are made from 50 µm polymer foils of kapton, with a metal coating on both sides, pierced with a high number of holes, typically of $\mathcal{O}\left(10^4\,\mathrm{holes/cm^2}\right)$. An example of a typical GEM electrode is shown in Fig. 1.18. A potential of a few kV/cm applied between a drift and a charge collection electrode, creates field lines around the holes. The electrons produced by an incoming particle will be accelerated along these field lines developing an avalanche multiplication of the primary charge that can then be collected at the readout anode (Fig. 1.19) [48]. The expected spatial resolution for the GEM detector for PANDA is better than 100 µm.

1.3.3.1 Forward Tracker

The FT is intended for momentum analysis of particles deflected by the dipole at an angle between ±5° in the vertical direction and ±10° in the horizontal direction, with respect to the beam. It is foreseen to have three pairs of planar tracking stations: one in front, one behind, and one inside the magnetic gap, as illustrated in Fig. 1.20. The FT, as the STT, is based on straw tubes, but arranged in a different layout. Each tracking station consists of four double-layers: the first and the last have vertical straws, while the innermost ones have straws skewed by 5°. This arrangement allows to reconstruct tracks in each pair of tracking station independently, which is particularly useful in case of multi-track events. The FT has a resolution of 0.1 mm for the spatial information and better than 1 % for the momentum.
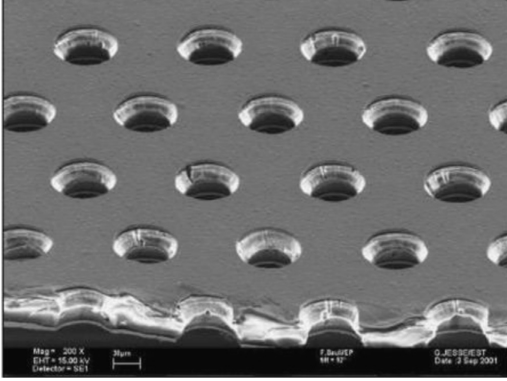
Figure 1.18: Electron microscope picture of a section of typical GEM electrode. The thickness is 50 μm, the holes pitch and diameter measure 140 μm and 70 μm, respectively. Image from [49].
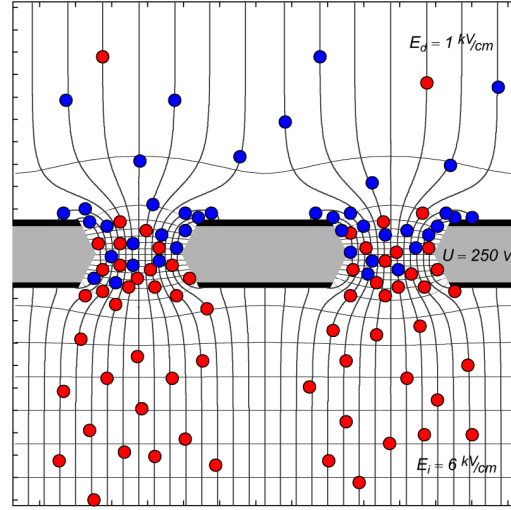

Figure 1.19: An illustration of the working principle of the GEM detector. The red and blue dots represent electrons and ions, respectively. Image from [50].
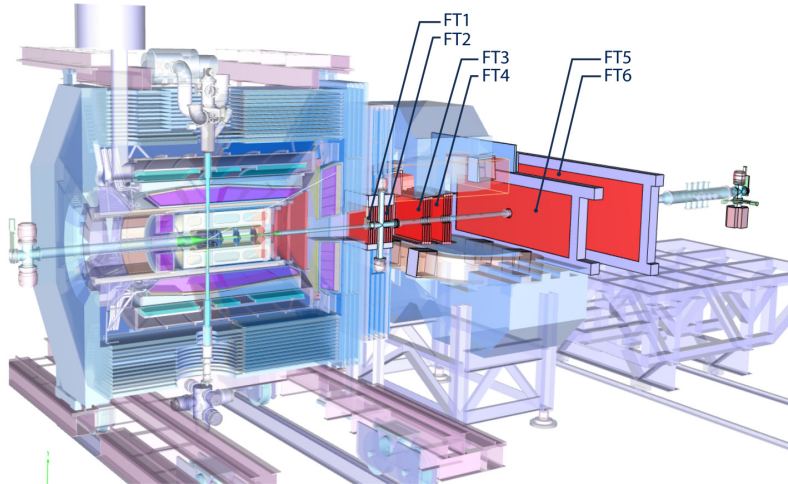

Figure 1.20: Position of the six stations of the FT in PANDA. Image from [4].

1.3.4 PID Detectors

Particle identification over the whole kinematic range of interest is a key aspect for the physics program of PANDA. A set of Particle Identification (PID) systems (namely two Cherenkov detectors: Detection of Internally Reflected Cherenkov Light (DIRC) and Ring Image Cherenkov (RICH), two time of flight systems: Scintillator Tile Hodoscope (SciTil) and Forward Time of Flight (FTOF), and a Muon Detector System (MDS)) has been designed to complement the information on the momentum and energy loss coming from the tracking detectors. Here follows an overview of the PID detectors.

Cherenkov Detectors: DIRC and RICH

Cherenkov detectors exploit the characteristic emission of a light cone from particles in particular kinematical conditions. Given a medium with refractive index n, a particle traversing it with velocity $\beta \cdot c$ bigger than the speed of light in that medium, emits radiation at an angle $\theta = \arccos(1/\beta \cdot n)$ that can be measured. Combining the information on the angle of emission of the radiation and the momentum of the particle provided by the tracking detectors, it is possible to determine with a certain resolution the mass of the particle, and therefore its species.

Two DIRC systems based on the same principles, but different geometry, are foreseen in the Target as well as in the Forward Spectrometer [51]. These systems are based on the detection of internally reflected Cherenkov radiation. The barrel DIRC, located in the Target Spectrometer, consists of 1.7 cm thick quartz slabs with refractive index $n = 1.544$ extending along the beam line at a radial distance of 48 cm for 2.4 m. At the end of each slab towards the forward direction, a mirror is placed to redirect the photons to the readout end, to avoid having to instrument both ends of the slab with photo detectors. The images are focused by lenses, conserving the original angle of emission of the photons, onto Micro-Channel Plate Photo Multiplier Tubes (MCP-PMTs) that convert the light into electrical signal, providing a spatial resolution of 22 mm and a temporal resolution of 100 ps. Fig. 1.21 illustrates the layout of the DIRC in the Target Spectrometer. The barrel DIRC has an acceptance between 22° and 140° and provides a π/K separation up to 4 GeV/c. The disk DIRC, located in the Target Spectrometer, as the name suggests, is composed of dodecagonal-shaped disk radiators with a radius of 110 cm and 2 cm thickness (Fig. 1.22). They are placed directly upstream of the forward endcap calorimeter, covering the polar angle region between 5° and 22°, which is outside of the barrel DIRC acceptance.

The second Cherenkov detector is the RICH. It is located in the Forward Spectrometer and covers the polar angle region between 0° and 5° vertically and between 0° and 10° horizontally. It is meant for the identification of hadrons with high momenta. The Cherenkov light is produced in a double-layer radiator made of aerogel and gas.
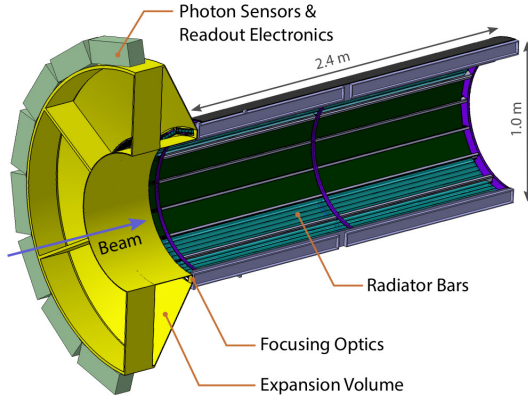
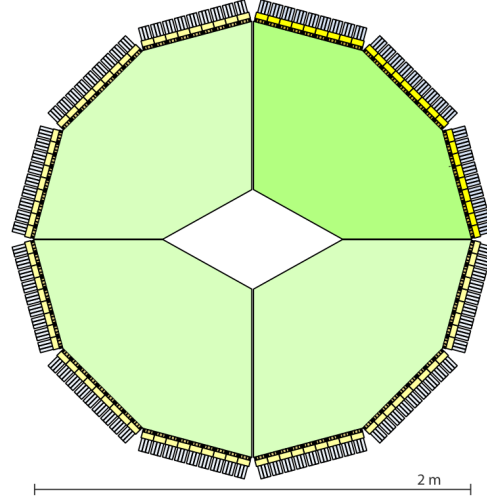Figure 1.21: Barrel DIRC. Image from [52], adapted from [53].

Figure 1.22: Disk DIRC. Image from [52], adapted from [54].

A mirror is used to focus the light onto an array of Photo Multiplier Tubes (PMTs) located outside the detector acceptance. The RICH system provides π/K separation up to $2.8\,\mathrm{GeV}/c$ and K/p separation up to $4.7\,\mathrm{GeV}/c$.

Time of Flight Systems: SciTil and FTOF

The SciTil is meant to identify low momentum particles emitted at large angles [55]. It is foreseen to position it in the small gap between the barrel DIRC and the calorimeter. Its basic unit is a squared scintillator tile of $28.5\,\mathrm{mm}$ length and $5\,\mathrm{mm}$ thickness. Four tiles are joined together to form a quad-tile module (Fig. 1.23). Ninety quad-modules are assembled to form super-modules, which are then positioned on top of the DIRC bars (Fig. 1.24). Each tile is equipped with two Silicon Photo Multipliers (SiPMs) to reduce the loss of photons from the scintillating material. Due to the fast response of the scintillation material, the timing information on the incoming particle is determinable with a resolution of $\mathcal{O}\,(100\,\mathrm{ps})$.

Since PANDA does not have a start detector, the information on the time of each event needs to be reconstructed otherwise. In this context, due to the fast response and the high precision, the SciTil could provide a valuable time reference for online tracking.

In the Forward Spectrometer a forward wall complements the Time of Flight (TOF) system [57]. The working principle is the same as for the SciTil, but the system is shaped as a wall with $140\,\mathrm{cm}$ height and $2.5\,\mathrm{cm}$ thickness. The time resolution is expected to reach $100\,\mathrm{ps}$. Fig. 1.25 illustrates the FTOF wall.
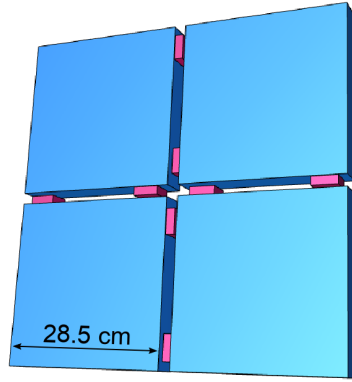
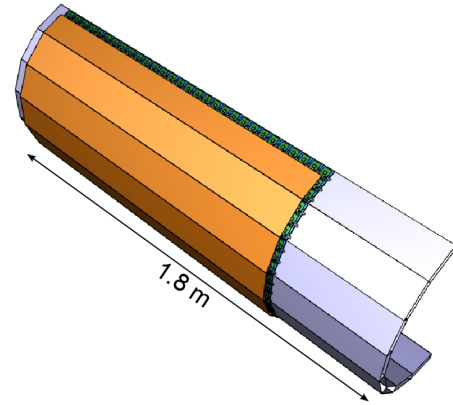Figure 1.23: SciTil quad-tile module. Each tile is equipped with two SiPMs, which are shown in purple. Image from [56].

Figure 1.24: SciTil half barrel composed of 8 super modules (orange), mounted on top of the DIRC bars (gray). Image from [56].
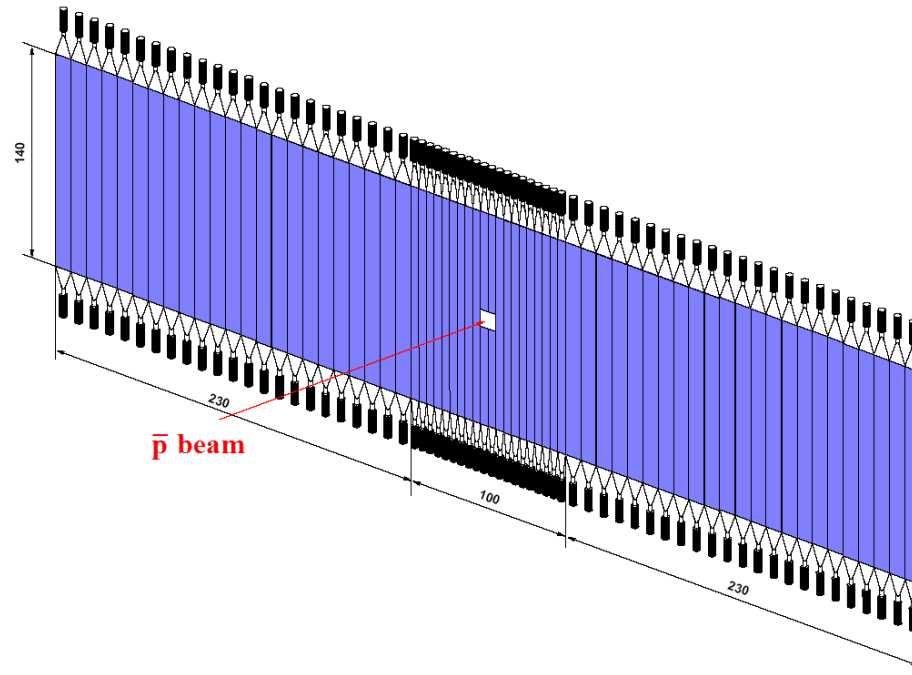

Figure 1.25: FTOF wall. The direction of the antiproton beam is indicated by the red arrow. The dimensions are given in cm. Image from [57].
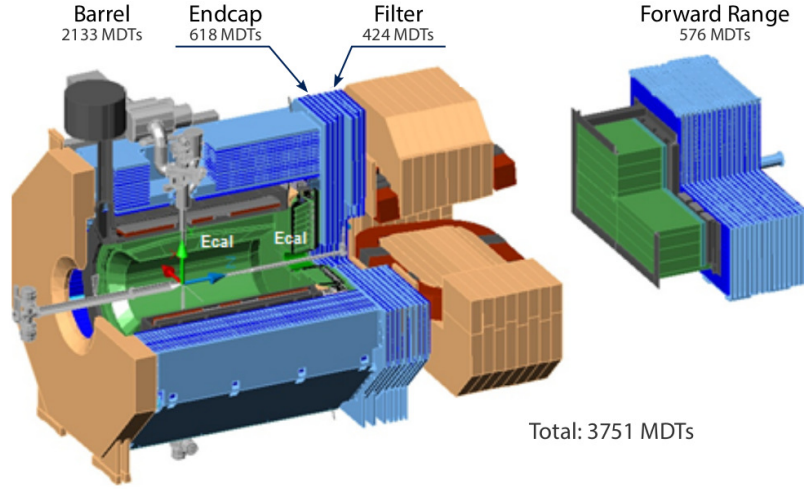
Figure 1.26: MDS components (blue). The number of MDTs is given for each component. Image from [4], adapted from [58].

Muon Detector System

The interesting processes for PANDA having muons in the final state are generally characterized by a small cross section. Therefore, an excellent capability of detecting muons is a crucial point for studying these processes. The aim is to detect muons in the energy range from sub-GeV up to 10 GeV with a polar angle acceptance between 0° and 150°. The MDS is comprised of a barrel part and an endcap part in the Target Spectrometer, and a forward range system in the Forward Spectrometer [58]. An additional muon filter is also foreseen between the solenoid and the dipole. The barrel part is composed of thirteen sensitive layers, each 3 cm thick, alternated with 3 cm thick iron absorber layers for sampling. The first and last iron layers are 3 cm thicker for mechanical reasons. These sensitive layers are MDT, operated in proportional mode, with additional capacitive coupled strips. Each tube is read out on both ends to obtain the longitudinal coordinate information. For a better identifications of high momentum muons, more material is needed in the endcap part. Therefore an optimized design with six sensitive layers interleaved with five iron layers, each 6 cm thick, is planned. In the forward region sixteen sampling layers are used and they also serve as a hadron calorimeter with modest resolution. The additional muon filter is mechanically very similar to the endcap part, but it uses a different number of layers. In fact, it is composed of four iron layers with 6 cm thickness each and five MDT layers. The filter is introduced not only to increase the efficiency in the detection on muons, but also to provide an additional magnetic screen between the solenoid and the dipole. Around 4000 MDTs will be used in total to equip the full MDS. Fig. 1.26 shows an illustration of the MDS.

1.3.5 Electromagnetic Calorimeter

The physics cases that PANDA proposes to study require detection of photons and dielectron pairs in the energy range between 10 MeV and 15 GeV, with high efficiency and low background. An electromagnetic calorimeter is foreseen for the reconstruction of these particles via the measurement of the deposited energy and point of impact over the full solid angle [59]. Fast scintillation material is needed in order to be able to separate events that happen close in time.

The Electromagnetic Calorimeter (EMC) consists of a cylindrical barrel part and two endcaps in the Target Spectrometer, having different dynamic range and angular coverage (Table 1.2). An additional shashlik-type sampling calorimeter module is included in the Forward Spectrometer [55]. The calorimeter in the Target Spectrometer is homogeneous and it is made of more than 15,000 $PbWO_4$ crystals of 20 cm length each and transverse size of 2.1 cm, wrapped in a high reflective foil, with different geometrical shapes. It will be operated at a temperature of $-25\,°C$ to gain in light yield, namely a factor 4 with respect to the operation at room temperature. It is foreseen to have tapered crystals in the barrel, straight crystals in the backward endcap, and slightly tapered crystals in the forward endcap. The readout will be carried out with Avalanche Photo Diodes (APDs). Radiation hardness is a key feature for the calorimeter: doses from 0.15 Gy for the backward part up to 125 Gy for the forward part should be tolerated by the detector. The energy resolution is $\frac{\sigma_E}{E} \leq 1\,\% + \frac{\leq 2\,\%}{\sqrt{E[\mathrm{GeV}]}}$ and the time resolution should be better than 2 ns. Fig. 1.27 shows a CAD drawing of the barrel and forward endcap part of the EMC.

The shashlik calorimeter covers the most forward part of the solid angle. It makes use of a lead absorber and plastic scintillator tiles, which are read out via wavelength shifting fibers with PMTs. Fig. 1.28 shows the front view of the shashlik calorimeter.

Table 1.2: Energy and polar angle range for each sub-component of the electromagnetic calorimeter.

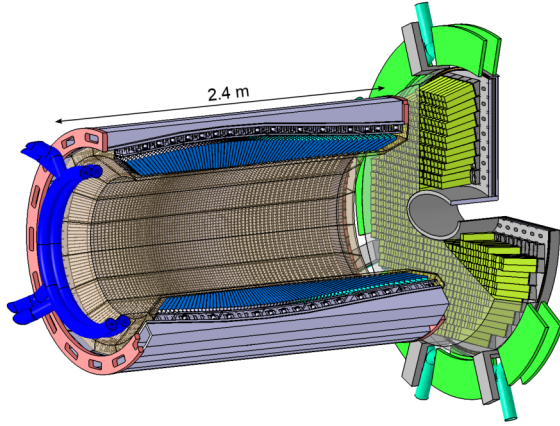|	energy range	polar angle
backward endcap	10 MeV to 0.7 GeV	140° to 170°
barrel	10 MeV to 7.3 GeV	22° to 140°
forward endcap	10 MeV to 14.6 GeV	5° to 22°
shashlik	10 MeV to 15 GeV	0° to 5°

Figure 1.27: CAD drawing of the barrel and forward endcap part of the EMC colored in blue and green, respectively. The backward endcap is not visible. Image from [59].
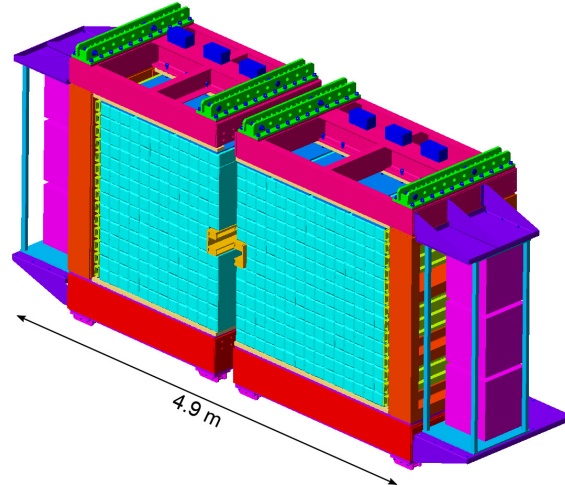

Figure 1.28: Front view of the shashlik calorimeter. Image from [55].
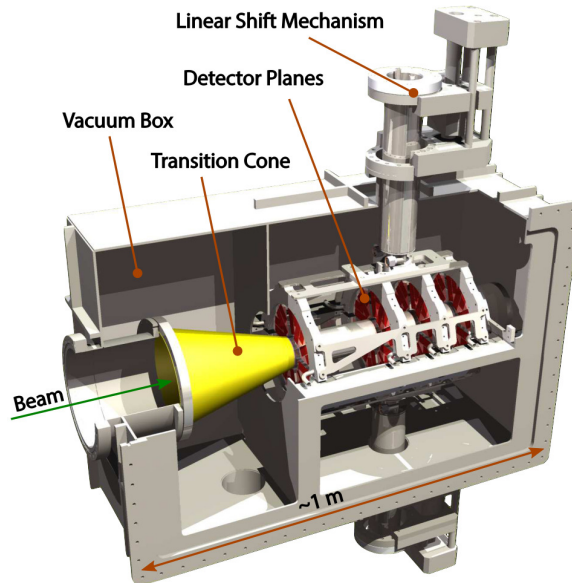
Figure 1.29: Luminosity Detector. Image from [4], adapted from [60].

1.3.6 Luminosity Detector

The measurement of the absolute and relative integrated luminosity is of fundamental importance for the determination of the absolute cross sections of interesting processes. The Luminosity Detector (LMD) (Fig. 1.29) will carry out this task by reconstructing the angle of elastically scattered antiprotons at angles between 3 mrad and 8 mrad with respect to the beam axis [60]. The reconstruction of the trajectories is performed using four tracking planes, placed between 11 m and 13 m downstream of the target, equipped with High Voltage Monolithic Active Pixel Sensor (HVMAPS). Every plane consists of roughly 100 HVMAPS glued on both sides to a Chemical Vapour Deposition (CVD) diamond substrate. This material has several advantages, among which the fact that it is a hard material that allows for a thin supply structure that will help minimizing the material budget. The HVMAPS are installed onto half disks, which can be moved by means of a linear shift mechanism. The vacuum chamber of the LMD is separated from the beam pipe vacuum by means of a transition cone, which allows scattered particles close to the beam to hit the sensors. The absolute precision is expected to be better than 5 % for the absolute and better than 1 % for the relative luminosity.

Chapter 2

The Micro Vertex Detector

One of the key points of the PANDA physics program is the study of hadrons with charm and strange quark content. These states exhibit decay length scales in the range of hundreds of micrometers, up to several centimeters. Therefore, dedicated measurements rely on the capability to resolve such displaced vertices. In this scenario, the MVD plays a fundamental role. The MVD delivers 3D hit information very close to the interaction point and provides additional information on deposited energy and particle momenta, contributing to particle identification.

The information presented in this chapter is taken from [61], unless otherwise specified.

2.1 Requirements

The goals mentioned above impose several basic requirements on the design of the MVD:

- optimal coverage over the full azimuthal angle and the polar angular range of $3° < \Theta < 150°$
- three-dimensional hit information with spatial resolution of the order of $100\,\mu m$ in the longitudinal coordinate and better than $100\,\mu m$ in the transverse direction
- time resolution better than $10\,ns$
- low material budget to minimize photon conversion and multiple scattering
- high rate capability (2×10^7 interactions/s are expected)
- free running readout since no first level hardware trigger will be implemented
- flexible readout to cope with anisotropic occupancy and different kinds of target
- radiation hard technologies to withstand an estimated dose of $10^{14}\,\mathrm{n_{1\,MeVeq}cm^{-2}}$ corresponding to approximately 10 years of operation in the high luminosity mode.

31

2.2   Design

The MVD will extend for ca. 40 cm along the beam axis (see Fig. 2.1 for a CAD drawing, including the support structures). It will be composed of four concentric barrels, placed at the nominal radius of 2.5 cm, 5 cm, 9.2 cm and 12.5 cm around the beam axis, and six disks in the forward direction, between 2.2 cm and 22 cm downstream from the interaction point. The length of the barrels increases with the radial distance from the interaction point from 5 to 31.2 cm. The disks have three different outer diameters: 75 mm for the first two, 150 mm for the two in the middle, and 260 mm for the last two. The inner diameter measures 22 mm for all the disks. For central tracks (i.e., with polar angle between 9° and 140°), at least four hits will be delivered. The barrel meets the disks at a polar angle of 40°. The angular coverage of the MVD is illustrated in Fig. 2.2. The two innermost barrels and the inner part of the disks will be equipped with pixel sensors, while the outer barrels and the outer rim of the last two disks will be covered with double-sided microstrip sensors. Fig. 2.3 shows the basic layout of the MVD and the position of the pixel and strip detectors. Due to the high granularity of pixel sensors, a precise two-dimensional spatial information can be obtained close to the interaction point, despite the high occupancy. On the other hand, the number of channels needed to cover large areas grows rapidly. Large surfaces can be covered with a significantly smaller amount of channels using double-sided microstrip sensors. However, their use in the close vicinity of the interaction point is not optimal, due to the high probability of double hits in a long strip and the increased number of ambiguities if the sensor is hit by more than one track. The MVD operating temperature will be kept constantly around 30 °C by means of a cooling system, which uses water at 16 °C as the cooling fluid. Simulations using a CAD model of the MVD show a very low overall material budget in the active area of the detector at polar angles below 145°. The major contribution comes from cabling and support structures (Fig. 2.4) [62].

2.2.1   Pixel Detectors

Sensors

The innermost surfaces of the MVD will be covered with hybrid pixel detectors. This technology foresees to separate the active part (i.e., a pixelated silicon p-n junction with reverse bias) and the front-end part by small conducting bumps, applied by using the bump bonding and the flip-chip technology. An ionizing particle that passes through the sensor, produces electron-hole pairs that can be separated applying a suitable electric field. The motion of the carriers induces a signal on the pixel electrodes. This signal is then amplified, discriminated, and digitized by the front-end electronics [65].
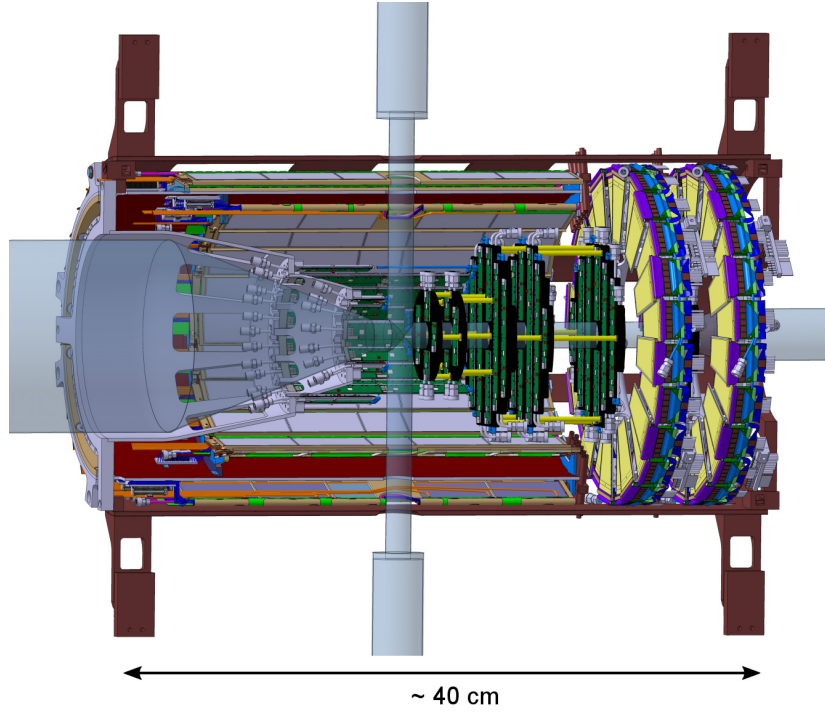
Figure 2.1: CAD drawing of the MVD including support structures. Image from [63].
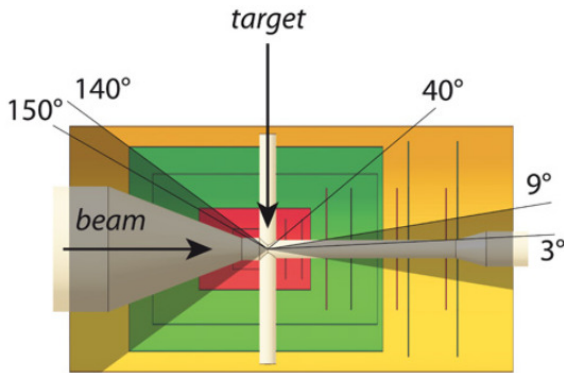
Figure 2.2: Polar angle range covered by the MVD. The MVD covers the polar angles between 3° and 150°. Except for the polar angles in the shadowed area, four hits points are delivered from the sensors. Image from [64].
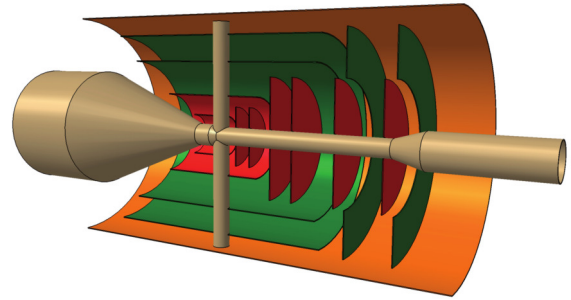
Figure 2.3: Basic layout of the MVD illustrating the position of the detectors: pixel detectors are colored in red, strip detectors in green. Image from [61].
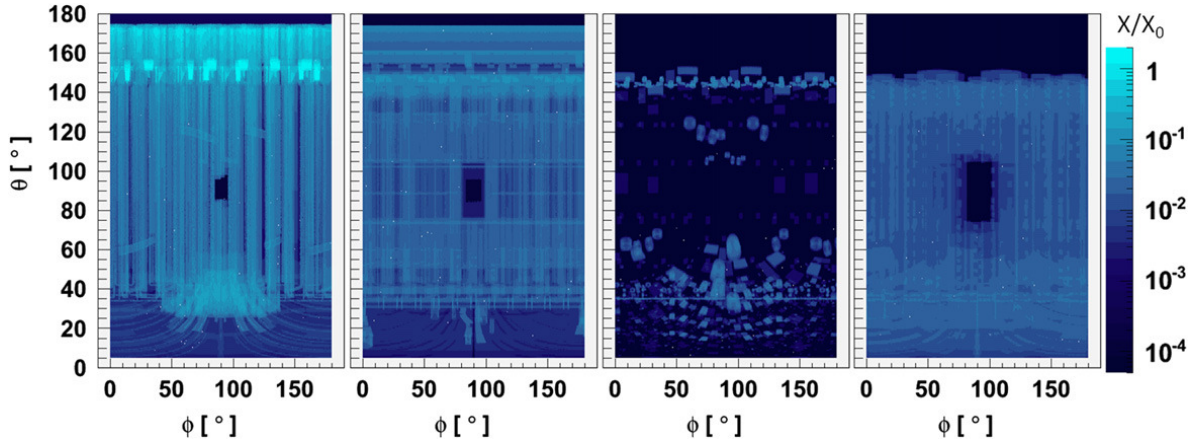
Figure 2.4: Contribution to the material budget of the four main parts of the MVD model in terms of radiation length X/X_0. From left to right: routing (i.e., service structures for sensors and front-end chips, including cables and cooling pipes), support (i.e., global and local support structures), component (i.e, electronics and cooling connectors), and silicon (i.e., sensors and associated readout chips). Image from [62].
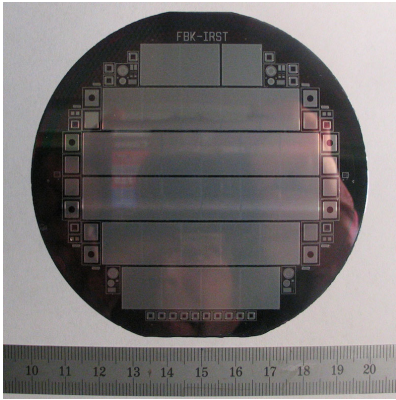
Figure 2.5: Wafer of pixel sensors for the MVD. Image from [61].
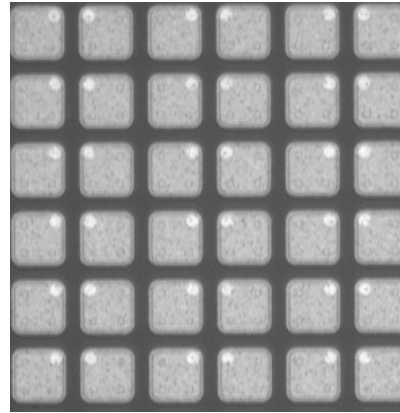
Figure 2.6: Partial view of a sensor. Each square is a pixel cell and the white circles at the corners are the pads for the bump bonding. The sensor pitch is 100 µm. The distance between the bump bonds is alternating 50 µm and 150 µm. Image from [61].
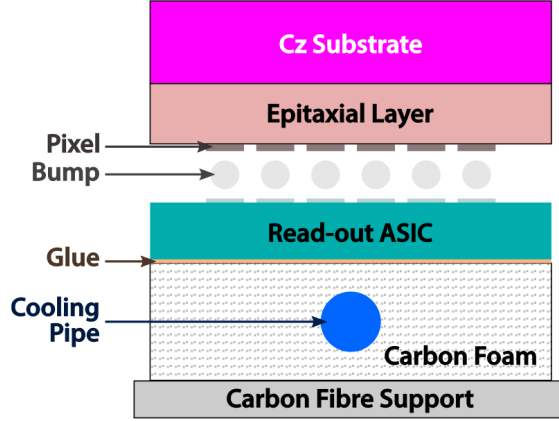
Figure 2.7: Cross section of the hybrid pixel assembly adopted in PANDA. Image from [52], adapted from [61].

The sensor wafers are made by growing an epitaxial layer of $100\,\mu$m thickness, which presents good properties in terms of radiation hardness, on a Czochralski (Cz) substrate thinned to about $20\,\mu$m to reduce the material budget (Fig. 2.5). The resistivity of the material is around $1500\,\Omega$ cm. To achieve the required spatial resolution, a size of $100\,$mm $\times\,100\,$mm is chosen for each pixel cell. The height of the active part of a sensor is 116 pixel cells, while the width is 2 to 6 times 110 pixel cells. A total of 176 sensors will be used to equip the full MVD [64]. Fig. 2.6 shows a portion of the pixel matrix for one sensor, with visible bump bonding pads. Fig. 2.7 shows a cross-section of the bonding scheme adopted for the hybrid pixel sensors.

The readout Application Specific Integrated Circuit (ASIC) for the pixel part is called Torino Pixel (ToPix) ASIC (Fig. 2.8) and it is designed using a $130\,$nm Complementary Metal Oxide Semiconductor (CMOS) technology [66].
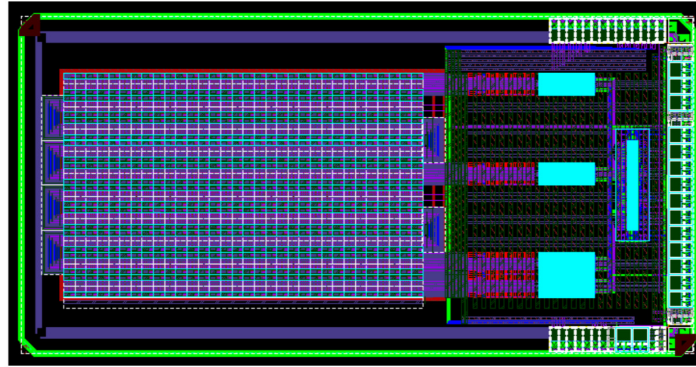
Figure 2.8: Layout of the 4$^{\text{th}}$ prototype of ToPix, the pixel front-end ASIC designed for the PANDA MVD. Image from [66].

It delivers a spatio-temporal information of the events, correlated with a deposited energy measurement via a Time over Threshold (ToT) measurement. According to this method, two measurements of time are performed: the first one corresponds to the signal going above a defined threshold (leading edge) and the second to the signal returning below the threshold (trailing edge). The difference between the two timestamps is used to reconstruct the energy deposited by the interacting particle.

The lack of a first level hardware trigger in PANDA poses challenging requirements on the readout chip, which will have to perform a triggerless data acquisition. The main specifications of ToPix are summarized in Table 2.1. ToPix will be connected via electrical differential lines to the Gigabit Transceiver ASIC developed at CERN [67]. This chip acts as a Serializer-Deserializer (SERDES), transmitting serial data at a maximum speed of 4.8 Gbit/s, and as an electrical-optical transceiver. The pixel part of the MVD will consist in total of 810 front-end chips [64].

Table 2.1: Main specifications of the readout chip designed for the pixel sensors of the MVD.

Self trigger capability	
Pixel size	$100\,\mu m \ \times \ 100\,\mu m$
Chip active area	$11.4\,mm \ \times \ 11.6\,mm$
dE/dx measurement	ToT - 12 bit dyn. range
Max input charge	50 fC
Input clock frequency	160 MHz
Time resolution	6.25 ns
Power consumption	$< 800\,mW/cm^2$
Max data rate/chip	450 Mbit/s
Total ionizing dose	$< 100\,kGy$

Assembly

The functional electronic unit, made of a sensor and from two to six readout chips, is called detector module. Four different pixel modules will share the same width, but different length, depending on the number of readout chips (Fig. 2.9 left). The modules are then combined in so-called super-modules, each composed by a detector module and a multilayer bus. The latter is used for power supply and signal transmission. The super-modules are arranged with different geometries for different detector layers (Fig. 2.9 right). They are then glued onto staves, which have different geometries for the barrel and for the disks, but the same components (Fig. 2.10).
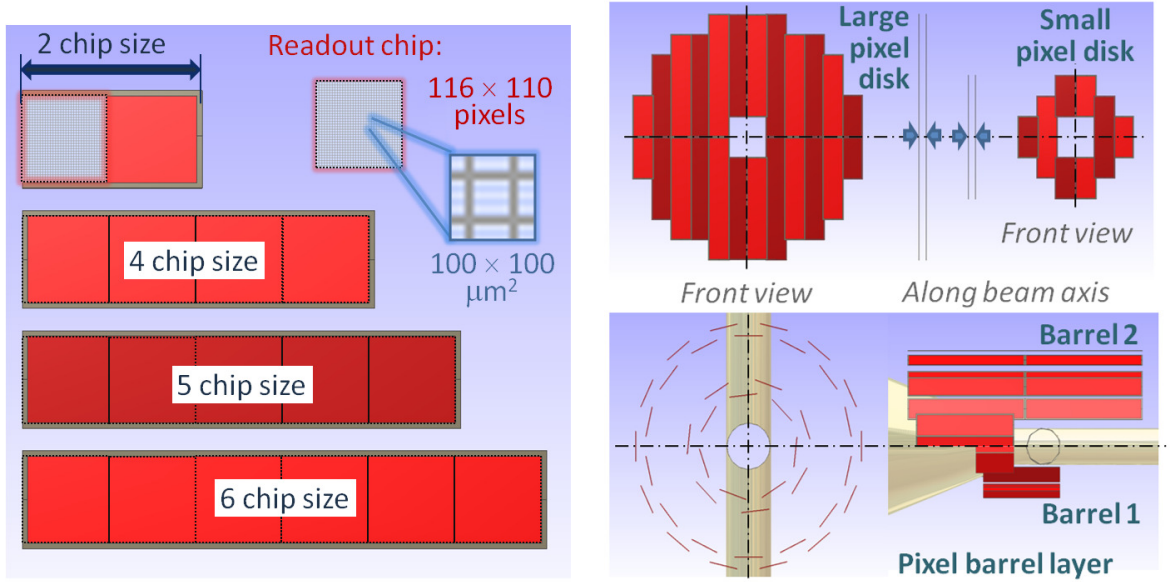
Figure 2.9: Pixel detector module (left): a single module can include from a minimum of two up to a maximum of six readout chips. Pixel sensor arrangement (right): assembly of the pixel disks and barrel layers. Image from [61].
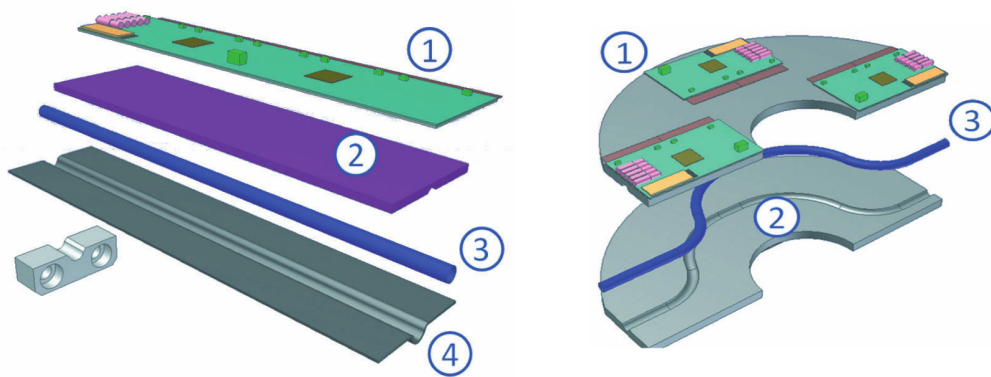
Figure 2.10: Pixel barrel stave (left): (1) detector super-module, (2) carbon foam, (3) cooling pipe, (4) carbon fiber Ω-support. Pixel disk stave (right): (1) detector super-module, (2) carbon foam, (3) cooling pipe. Image from [64].

2.2.2 Strip Detectors

Sensors

The sensors chosen for the outer layers of the MVD are Double-Sided Silicon Micro-Strip Detectors (DSSDs). These detectors have orthogonally oriented readout strips on the opposite faces of the detector wafer [68]. The detection principle is the same explained for the pixels, but in the case of DSSDs electrons and holes are collected on the two different sides, where a signal with approximately the same amplitude is generated. In this way, it is possible to reconstruct two-dimensional information on the hit with a good spatial resolution. The relatively small thickness of the sensor (generally between 300 to 500 µm) minimizes multiple scattering. Two particles hitting the sensor within a small time window will generate two pairs of coordinates that, when combined, can lead to a wrong creation of hits (i.e., two real, two fake). This is the biggest disadvantage for this kind of detectors, which are therefore not suitable to cover areas where the event rates are high.

The sensors for the MVD are produced from a monocrystalline Floating Zone silicon wafer. Three different sensor geometries, all with the same thickness of 285 µm, are needed for the MVD: squared (35 mm × 35 mm) and rectangular shapes (35 mm × 60 mm) for the barrel, trapezoidal (57 mm height, 22 mm and 37 mm length for the short and long side, respectively) for the disks. The barrel strips have 65 µm pitch, while the disks have 45 µm pitch (Fig. 2.12). It is foreseen to read out every second strip to reduce the number of channels. Due to the capacitive coupling of adjacent strips, the charge collected on the one that is not being read out is measured by its neighbors. This results in a better resolution compared to the case in which the intermediate strip is not present [69]. Monte Carlo simulations show that this readout scheme does not cause a significant deterioration of the spatial resolution, provided that the signal-to-noise ratio is of $\mathcal{O}(10)$ [70].

Readout

The readout ASIC for the strip part is called PANDA Strip ASIC (PASTA) and it is designed in a 110 nm CMOS technology (Fig. 2.13). Similar to ToPix, PASTA will operate without a trigger signal and it will deliver a spatio-temporal information about the events together with the deposited charge information obtained via the ToT technique. The strip part of the MVD will consist in total of 3112 front-end chips [64].

Since PASTA plays an important role for the work of this thesis, a whole chapter will be dedicated to its description (Chapter 3).
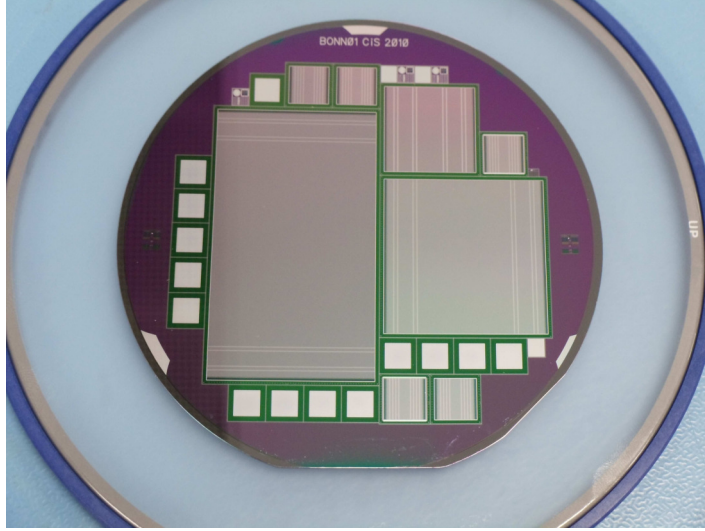
Figure 2.11: 4"-Wafer of strip sensors for the MVD. Image from [61].
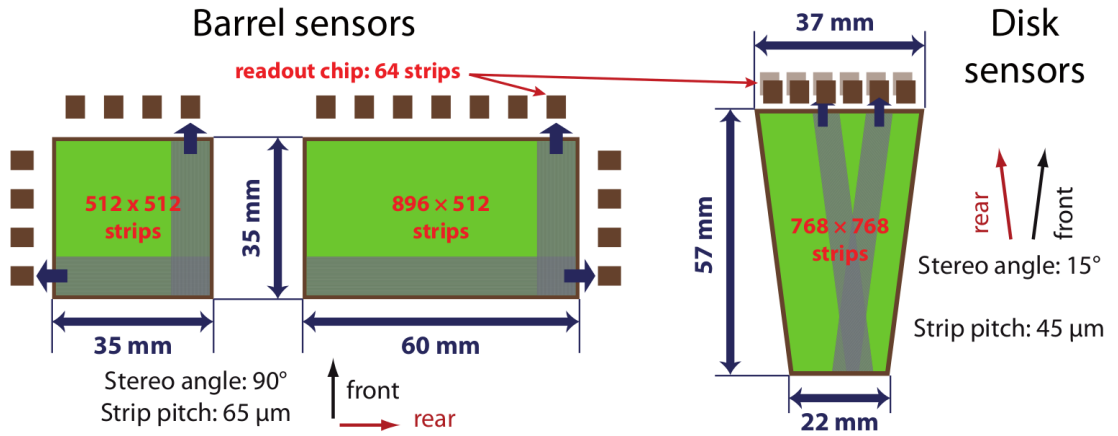
Figure 2.12: The three different strip sensor geometries for the MVD. Image from [64].
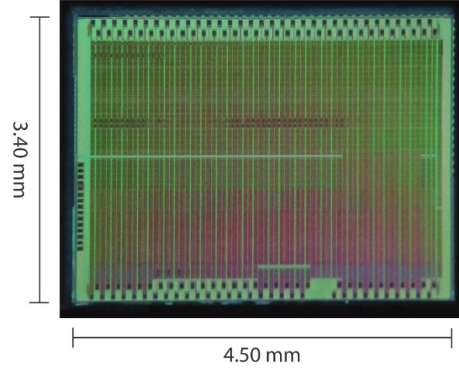
Figure 2.13: Layout of the 1st prototype of PASTA, the strip front-end ASIC designed for the PANDA MVD. Image from [71].

Assembly

For the strip detectors, the readout electronics is placed outside the acceptance of the sensors. The assembly is different for the barrel and the forward part, due to purely geometrical reasons. In the barrel a super-module comprises from four to six sensors aligned in a row and a flexible multilayer bus. The staves onto which the super-modules are glued, are arranged in a cylindrical shape around the beam pipe (Fig. 2.14 left). Each stave is also provided with a cooling system (Fig. 2.15 left). Concerning the two disks, each module has one of the trapezoidal sensors glued onto a carbon fiber frame, and twelve PASTA chips, six on each side. Six modules share the same cooling system and form a quarter of a disk (Fig. 2.14 right). The chips are placed on a carbon foam block, which is thermally connected to the cooling pipe, and their connections to the sensors is achieved via flexible multilayer buses (Fig. 2.15 right).
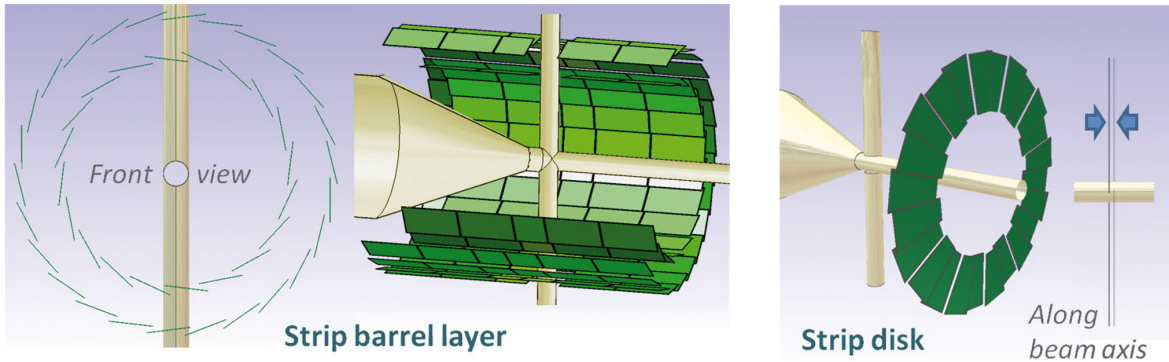
Figure 2.14: Strip detector super-module for the barrel (left) and for the disks (right). Image from [61].
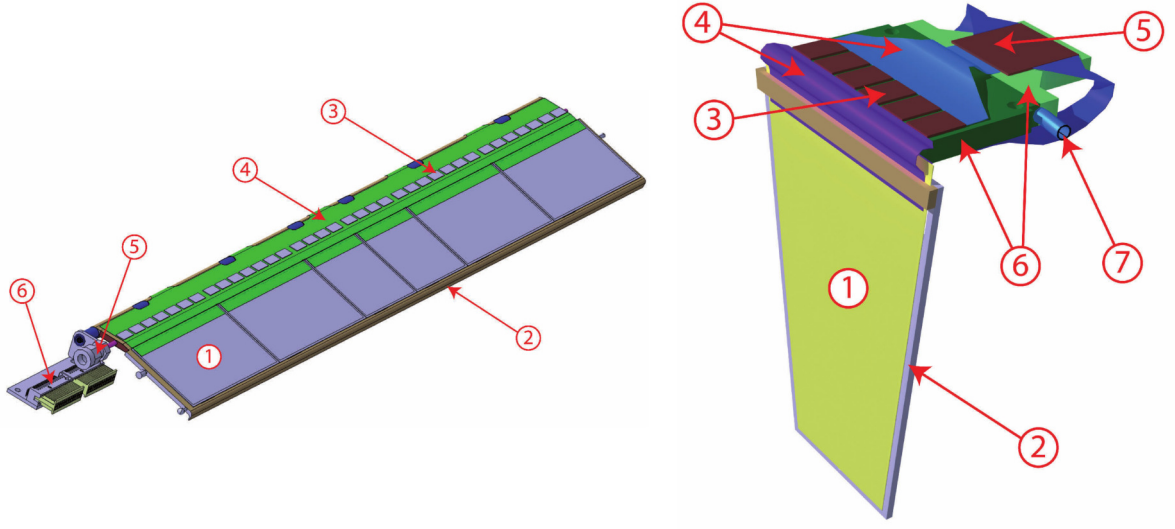
Figure 2.15: Strip barrel stave (left): (1) sensor, (2) carbon fiber stave, (3) readout chips, (4) flexible bus, (5) cooling pipe, and (6) power connector. Strip disk stave (right): (1) sensor, (2) carbon fiber stave, (3) readout chips, (4) flexible bus, (5) MDC (see Section 2.2.2). Image from [64].

Module Data Concentrator

The MDC is an additional component introduced for the strip part, to link the front-end ASICs to the off-detector data acquisition system, through the Gigabit Transceiver (GBTX) links [72]. This addition is needed, in contrast to the pixel part, to avoid having too many data lines. The main tasks of this element are:

- read out, decode, time-order, and multiplex of the data of the front-ends belonging to one sensor, for up to 12 inputs;
- basic data analysis in order to reduce the load on the transmission (e.g., clustering and mapping algorithms, hit finding, pedestal subtraction);
- slow control and monitor.

A block scheme of the MDC is shown in Fig. 2.16. The final implementation of the MDC is foreseen to be a $6\,\text{mm} \times 6\,\text{mm}$ ASIC, with similar radiation tolerance as the PASTA ASIC.
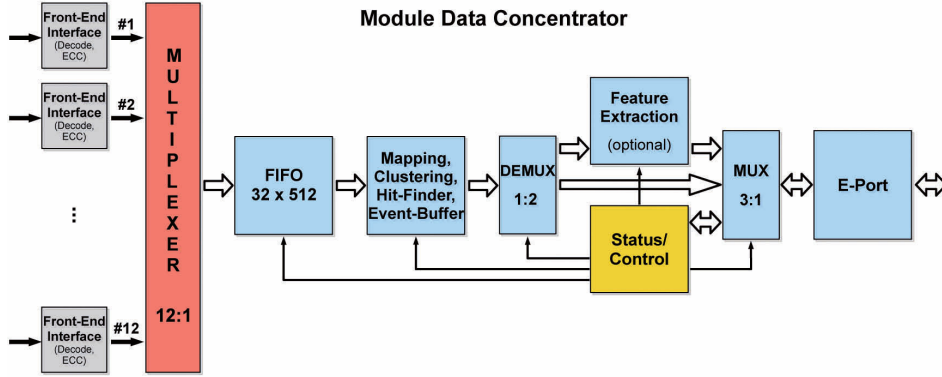
Figure 2.16: Block scheme of the MDC for the strip part of the MVD. Image from [64].

2.3   Off-detector components

The data coming from several MVD front-ends, transported via the GBTX links, are multiplexed into a single outgoing link and sent to the computing node. The task will be performed by the MVD Multiplexer Boards (MMBs) implemented as MicroTCA boards, hosting a commercial Field Programmable Gate Array (FPGA) [73]. The MMB communicates with the global Data Acquisition (DAQ) of PANDA, called Synchronization Of Data Acquisition (SODANET), to receive information on the beam structure and global timing, in order to provide proper timestamps of the detector data [74]. Fig. 2.17 illustrates the data path from the MVD sensors up to the computing nodes located outside the detector area.
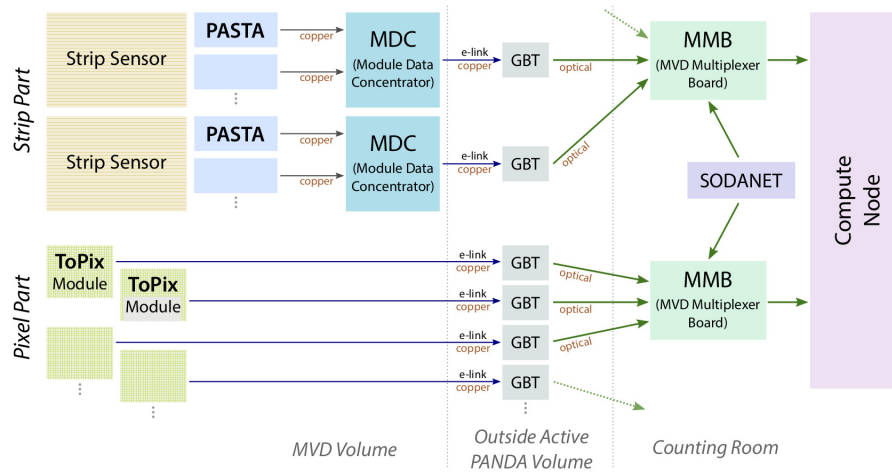
Figure 2.17: Data path from the MVD sensors (both pixel and strip) to the off-detector computing nodes. Image from [52].

Chapter 3

The PANDA Strip ASIC

This chapter describes the newly developed readout ASIC for the strip sensors of the MVD, called PASTA. Particular emphasis is placed on the aspects which are more relevant for this thesis. In addition, references are given for further reading. The information discussed here has been partially published during the course of this thesis [75].

3.1 Requirements and Motivation

In PANDA no external signal will be used to distinguish relevant events from background events. As a consequence, the DAQ has to be triggerless and continuous. Moreover, the distinction between event signals and detector noise has to be done inside the front-end, by means of an internal signal amplitude threshold. Due to the restricted space foreseen for the placement of the MVD, but most importantly in order to limit the material budget, the amount of cables and cooling systems has to be reduced to the minimum. This has an impact on the total maximum power consumption of the whole front-end, which has to be kept below 1 W. To efficiently transmit the collected signal to the following stages, digitization needs to be performed on the front-end. The digitization resolution is required to be 8 bit or better, to achieve a sufficiently precise charge measurement and a high spacial resolution for each event. Additionally, the front-ends have to be able to cope with the expected rate of one event every 50 ns on average. The time resolution is required to be better than 10 ns. Given the position of the MVD in a radiation intense environment, the capability to withstand rather high ionization doses is a key feature for the electronics. Simulations predict a total dose of 100 kGy for 10 years of operation in the high luminosity mode [61].

When a decision on which front-end to adopt for the strip part of the MVD was made, no option that could comply with all the mentioned requirement was available. Therefore, it was decided to start a custom development: the PANDA Strip ASIC (PASTA).

3.2   Specifications and Working Principle

PASTA is designed using a 110 nm commercial CMOS technology. The first release of PASTA is a full size prototype, with 64 identical channels. PASTA shares the measurement principle with the Time of Flight for Positron Electron Tomography (TOFPET) ASIC, although a general restructuring of the architecture during the design phase was necessary, in order to meet the specific requirements. TOFPET was designed in the context of the EndoTOFPET-US project [76], to read out SiPMs for medical applications [77]. Similar to the pixel readout, the timestamp of each event and the deposited charge information are provided by means of the ToT technique. In the present case, two leading edge discriminators are used (Fig. 3.1).
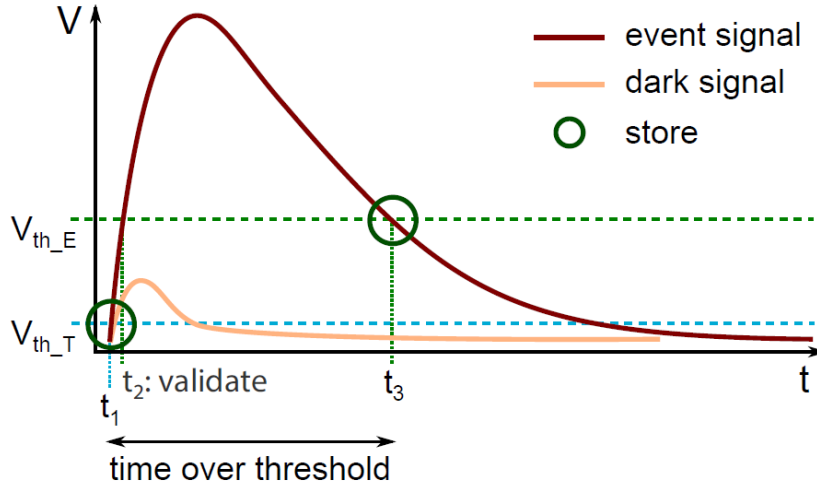
Figure 3.1: Measurement concept in PASTA. A low threshold provides good time resolution on the rising edge of the incoming signal, while a higher threshold is used to measure the deposited energy with the ToT method. Image from [52].

The first discriminator defines the so-called *time branch*. Its aim is to resolve precisely the time of the leading edge of the incoming signal. The second discriminator is used to validate the event, resolve the falling edge of the signal, and measure the energy deposition. The name *energy branch* is associated with it. The two thresholds can be adjusted individually and optimized to reduce the impact of the signal jitter due to noise fluctuations. Specifically, since the falling edge of the expected input signals is slower than the rising one, as standard configuration the threshold for the energy branch is higher than the one for the time branch. For each measurement, two timing information are provided: a coarse and a fine time. The resolution of the coarse time is intrinsically limited by the clock, i.e., 6.25 ns for the nominal operation frequency of 160 MHz. The fine time is provided by means of a time interpolation and has the nominal value of 50 ps. More details on the time interpolation technique will be given in Section 3.3.2. The main design specifications of PASTA are summarized in Table 3.1.

Table 3.1: Main specifications of the readout chip designed for the MVD strip sensors.

Self trigger capability	
Channel pitch	$63\,\mu m$
dE/dx measurement	ToT - 8 bit dyn. range
Max input charge	$38\,fC$
Input clock frequency	$160\,MHz$
Time resolution (coarse)	$6.25\,ns$
Time resolution (fine)	$50\,ps$
Power consumption	$< 4\,mW/ch$
Total ionizing dose	$< 100\,kGy$

3.3 Architecture

The architecture of the PASTA chip can be divided in four interconnected main building blocks: two in the analog and two in the digital domain (Fig. 3.2). The first block is the analog front-end. The main purpose of this stage is a preamplification of the signal generated in the sensor. An analog Time to Digital Converter (TDC) follows this stage, completing the analog part of the ASIC. Here the time interpolation technique is implemented, in order to achieve the enhanced time resolution. On the digital domain, a TDC controller handles the event validation. These three blocks handle local operations. That is to say that each one of the 64 channels is provided with its own analog front-end, analog TDC, and TDC controller. All the operations that affect the chip as a whole are handled by a single module: the global controller. PASTA features also a few auxiliary modules such as a calibration circuit, to generate configurable signals for testing purposes, and bias cells to provide the correct voltage level to the analog components. The data collected in the ASIC is transmitted to the outside world through Scalable Low Voltage Signaling (SLVS) links.

3.3.1 Analog Front-end

The analog front-end has four stages. The one directly connected to the sensor is a Charge Sensitive Amplifier (CSA). The CSA amplifies a small current signal, coming from either a p-type or an n-type strip sensor. Follows a current buffer, used as second amplification stage with a high gain and an impedance adjustment. Its output signal is then handed over to the ToT stage. There, the rising and falling edge of the signal are sampled to retrieve the amplitude information. The final block consists of a hysteresis comparator, which compares the signal with a given threshold voltage. The output of the hysteresis comparator is then forwarded to the analog TDC.
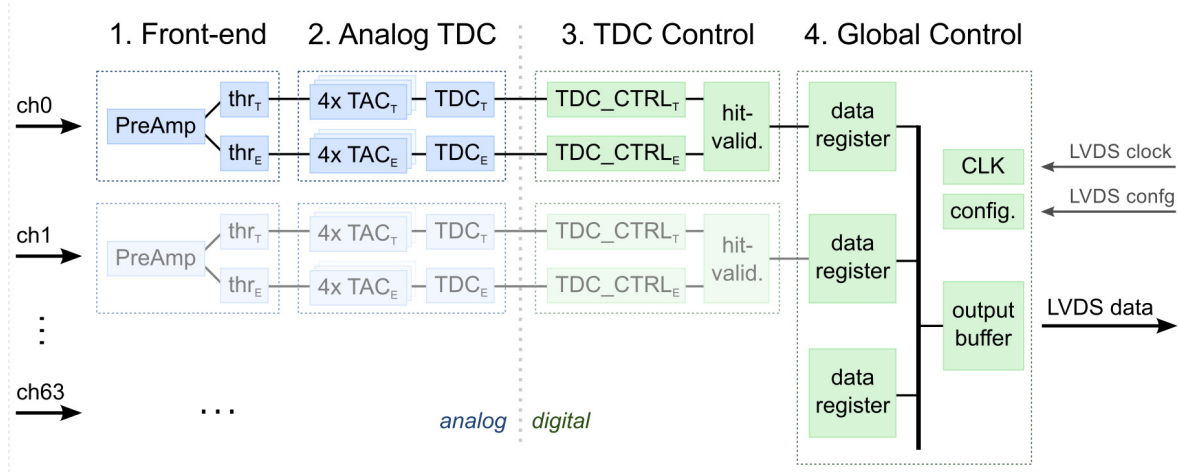
Figure 3.2: A schematic representation of the architecture of PASTA. Image from [52].
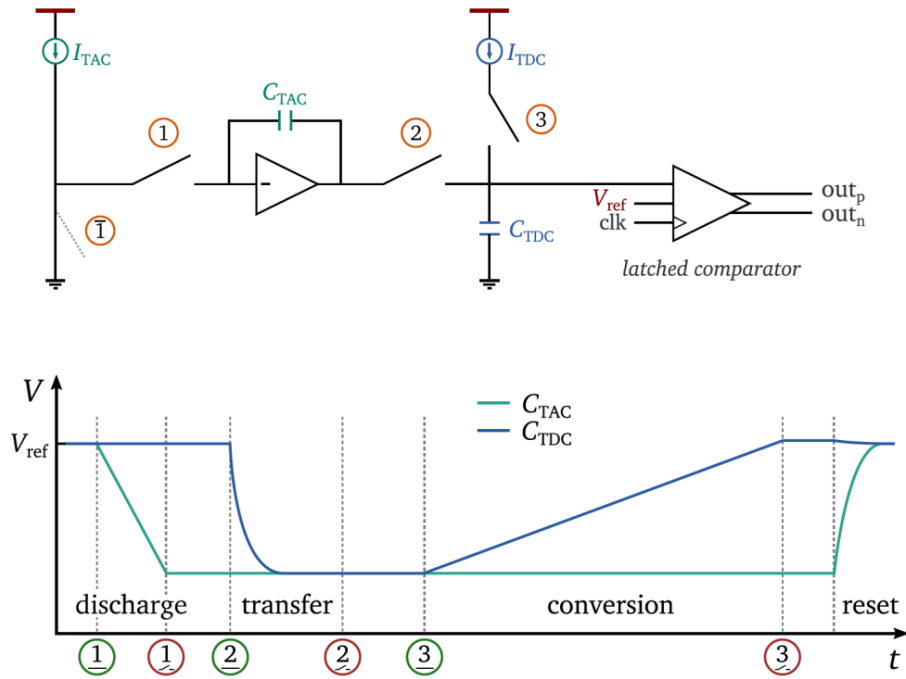
Figure 3.3: Top: a schematic representation of the analog TDC of PASTA. The outputs of the comparator are connected to the digital part. The numbers indicate switches (1 and $\bar{1}$ are always in opposite states). Bottom: voltage levels during event processing in the analog TDC. The numbers refer to the top part of the picture. Open and closed switches are indicated by green and red circles, respectively. Image from [52].

3.3.2 Analog TDC

The analog TDC is the stage where the time interpolation takes place, allowing to determine a time information with a resolution that is finer than the intrinsic clock resolution. The analog TDC includes four Time to Analog Converter (TAC) per channel and a latched comparator. The advantage of the presence of multiple TACs per channel, activated according to a round-robin scheme, lies in the possibility to reduce the dead time in the processing of incoming data. Fig. 3.3 shows the scheme of the circuit and helps understanding the working principle. When a signal edge is detected by the sensor, a trigger to start a time measurement is generated. From this starting point on, the capacitor C_{TAC} is connected to a constant current source I_{TAC}. Due to the presence of an inverting amplifier, this capacitor is discharged. When the next clock edge arrives, the time measurement is terminated. The aim of this procedure is to convert the time difference between the trigger signal and the clock edge into a proportional voltage drop in the capacitor C_{TAC}. Subsequently, by connecting the two capacitors C_{TDC} and C_{TAC} for a sufficient amount of time, it is ensured that they share the same voltage level. Once the balance is achieved, C_{TDC} is recharged via a second current source I_{TDC}. When a voltage level equal to the original reference is measured by the latched comparator, a signal is forwarded to the TDC controller in order to store the event time information. The following simple calculation shows how the choice of the capacitors and of the currents determines the smallest achievable fine time. The charge in a capacitor Q is related to the current I according to

$$Q = C \cdot U = I \cdot t$$

where U is the voltage level and t is the charging time. Given t_{TAC} and t_{TDC} the discharge time and the conversion time, respectively, it follows that

$$U_{\mathrm{TAC}} = \frac{I_{\mathrm{TAC}} \cdot t_{\mathrm{TAC}}}{C_{\mathrm{TAC}}}$$

$$U_{\mathrm{TDC}} = \frac{I_{\mathrm{TDC}} \cdot t_{\mathrm{TDC}}}{C_{\mathrm{TDC}}}.$$

When the voltage level is balanced in the two capacitors: $U_{\mathrm{TAC}} = U_{\mathrm{TDC}}$

$$t_{\mathrm{TDC}} = t_{\mathrm{TAC}} \cdot \frac{I_{\mathrm{TAC}}}{I_{\mathrm{TDC}}} \cdot \frac{C_{\mathrm{TDC}}}{C_{\mathrm{TAC}}}.$$

Choosing the following values for the capacitors and the constant currents

$$C_{\mathrm{TDC}} = 4 \cdot C_{\mathrm{TAC}}$$

$$I_{\mathrm{TDC}} = 1/32 \cdot I_{\mathrm{TAC}}$$

one obtains the amplification factor

$$t_{\mathrm{TDC}} = t_{\mathrm{TAC}} \cdot 32 \cdot 4 = t_{\mathrm{TAC}} \cdot 128.$$

This value leads to 50 ps fine time resolution at the nominal clock frequency of 160 MHz.

3.3.3   TDC Controller

The first digital block is the TDC controller. It represents the interface between the analog circuitry and the digital handling of the data. Its role is to detect valid events and store a measurement for them. Comparing PASTA with its predecessor TOFPET, one can observe a size reduction for this block of 80 % (Fig. 3.4). In addition, the power consumption is reduced by half. For integrated circuits that operate in an intense radiation environment, there is a non-zero probability that a single particle hit might induce a charge that can cause a bit flip in a register of the ASIC. This effect is called Single Event Upset (SEU) and can be counteracted by employing radiation-hard logic in the design [78]. Since TOFPET was never meant to be used in presence of ionizing particles, no radiation-hard logic was introduced. In the TDC controller of PASTA, the implemented SEU protection techniques are: Triple Modular Redundancy (TMR) for upsets affecting single-bit registers and Hamming encoding for upsets affecting multiple-bit registers [79, 80].
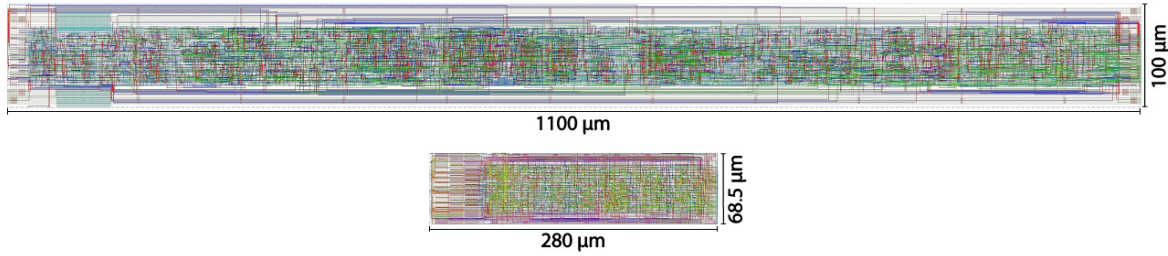
Figure 3.4: Comparison between the TDC controller of PASTA (bottom) and its predecessor TOFPET (top). Image from [52].

3.3.4   Global Controller

The global controller represents the common back-end for the multiplexing of the 64 channels of PASTA. Since this is the part that interacts directly with the DAQ system, which is one of the main focuses of this thesis, some more details about it are provided. Among its tasks are the configuration handling, the data collection and transfer, and the generation of a signal for testing purposes.

Configuration Handling

The configuration is the collection of operation settings of the chip. In PASTA the configuration is separated into a global part (46 parameters), shared among all the channels, and a local part, distributed on a channel basis (22 parameters per channel).

In both cases the configuration data are divided in four fields. Since not all of them are mandatory, the data stream does not have a fixed length. The fields are the following:

- 4 bit: configuration command (e.g., read/write configuration)
- 7 bit: channel address (in case of individual channel configuration)
- N bit: actual configuration data (if necessary; e.g., not needed for a read command)
- 8 bit: Cyclic Redundancy Check (CRC-8): an error detection code used to detect accidental changes after data transmission.

The communication interface for the configuration involves four data lines: Slow Clock (SCLK), Slow Data In (SDI), Slow Data Out (SDO), and Chip Select (CS).

- SCLK is the clock used only for configuration operations, therefore it can be significantly slower than the main one
- SDI carries the configuration data
- SDO carries acknowledgment information
- CS enables/inhibits the ASIC

The available configuration options are summarized in Table 3.2. Fig. 3.5 shows the configuration interface lines with timing information when a command for writing and reading a global configuration is issued. The respective timing schemes in case of local configuration operations are shown in Fig. 3.6.

Table 3.2: Single channel and global configuration options. Commands starting with 0 refer to local configuration, while commands starting with 1 refer to global configuration. N_{wr} indicates the number of bits to be written into a register for a successful transfer. N_{rd} represents the number of bits to be read in case of a read command, and the number of clock cycles necessary to fully process the request in case of a write command.

| Command	Description	N_{wr}	N_{rd}
0000	Write channel config.	41	41
0001	Read channel config.		41
0010	Enable calibration circuit	1	1
0011	Read channel test config.		1
0100	Read channel counter	10	10
1000	Write global config.	172	1
1001	Read global config.		172
1010	Configure test pulse	26	26
1011	Read global counter value	10	10
1100	Write test pulse config.	14	1
1101	Read global test config.		14
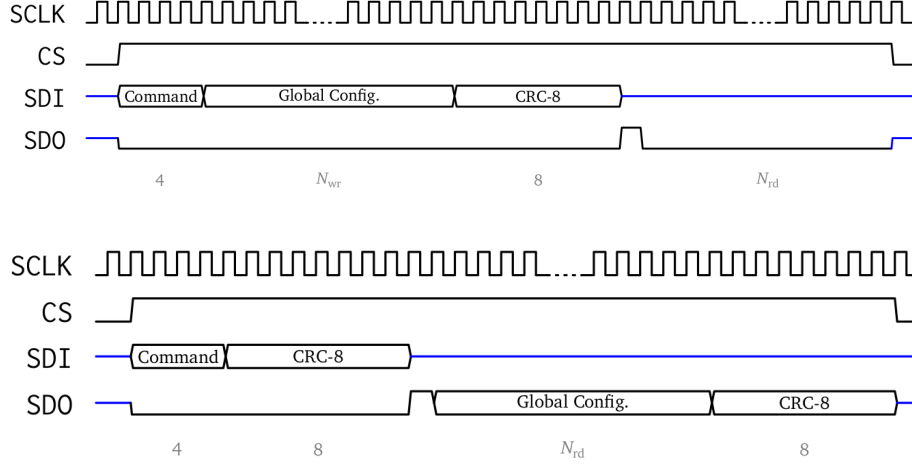
Figure 3.5: Configuration interface data lines with timing information in case of a write (top) and read (bottom) global command. Image from [52].
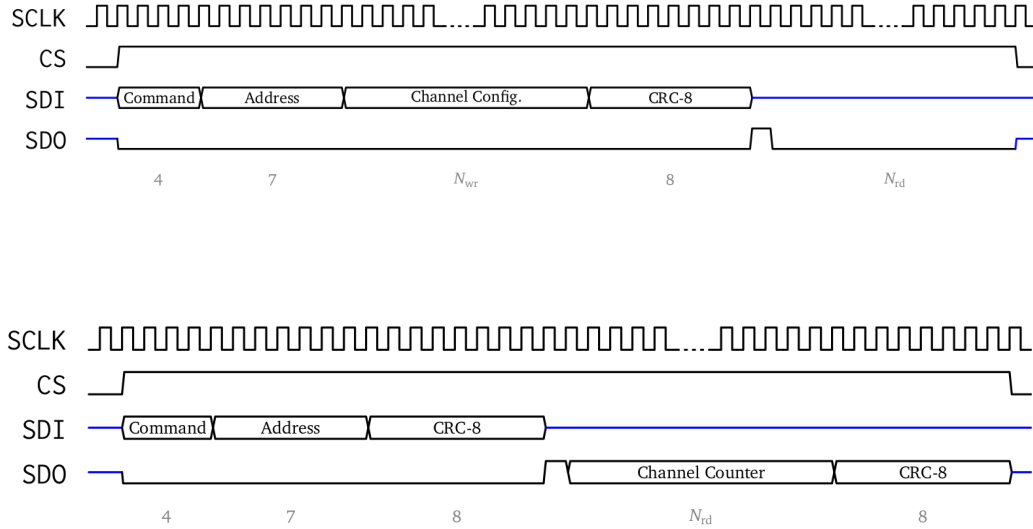

Figure 3.6: Configuration interface data lines with timing information in case of a write (top) and read (bottom) local command. Image from [52].

Data Collection and Transfer

The data corresponding to events that occurred in a time window of 1024 clock cycles are stored in a frame. Each frame is composed of 40 bit word blocks. Namely, it includes:

- the header: one 40 bit word which contains the total number of events in that frame and the global counter information;
- the data relative to the events: $N \times 40$ bit words containing the timestamps, channel number, and TAC number of the events in that frame;
- the trailer: which contains the CRC-8 to verify correct transmission.

The timestamps are determined by using a 42 bit wide clock counter. The timestamps are divided into a global frame counter (frame ID) and 5 timestamps stored by the TDC: coarse time counter $t_{\text{coarse,T}}$, coarse energy counter $t_{\text{coarse,E}}$, start of conversion t_{soc}, end of conversion time $t_{\text{eoc,T}}$, and end of conversion energy $t_{\text{eoc,E}}$.

Since the ASIC operation is not based on a trigger signal, data are continuously sent over the transmission line. If no events occur, a frame with only header and trailer will be transmitted. The data are 8b/10b encoded to ensure a balanced line. Between two consecutive frames, control sequences called comma words are sent. Two formats are available for the encoding of the event data: full and compact mode. The first one is intended for debug operations. It transmits two 40 bit words per event which contain the timestamps as they are stored internally, i.e., Gray encoded to reduce the registers switching and power consumption [81]. The second one transmits only one 40 bit word per event and uses standard binary representation. It reduces redundancy by avoiding the repeated transmission of certain bits (i.e., the channel and TAC number). Moreover, it performs some calculations on the internally stored timestamps before sending them out: the start and end of conversion are not transmitted individually, but as their difference (i.e. t_{fine}), as well as the coarse times (i.e., the individual time and energy coarse timestamps are replaced by the difference $t_{\Delta\text{coarse,E}} = t_{\text{coarse,E}} - t_{\text{coarse,T}}$). Fig. 3.7 and Fig. 3.8 sketch the data formats, including the length of each field expressed in bits.

Test Pulse Generation

PASTA offers the possibility to generate a configurable pulse using internal logic, to mimic the output of a connected sensor. The module that takes care of the generation of this pulse accepts as input the number of pulses, the length of each pulse, and the spacing between two consecutive pulses. It produces as output a digital signal that can have two mutually exclusive uses: it can substitute the discriminator output, or it can be used to produce an analog signal fed as input to selected channels through the calibration circuit. The generated pulse corresponds to a deposited charge that ranges between 1 fC and 63 fC. The step width corresponds to 1 fC deposited charge. The test pulse is a useful tool for the calibration of the ASIC and the optimization of

the configuration parameters. Moreover, it can be used to study the performance of the ASIC in a controlled environment.

More details on the architecture of the PASTA ASIC can be found in: [82] regarding the analog TDC, [83] concerning the analog front-end, and [52] about the digital domain.

The information regarding the configuration parameters and various modes of operation are collected in [84].
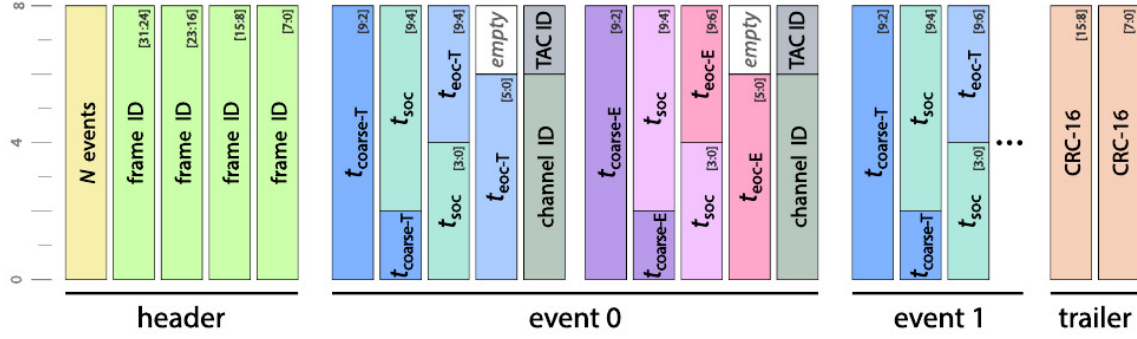

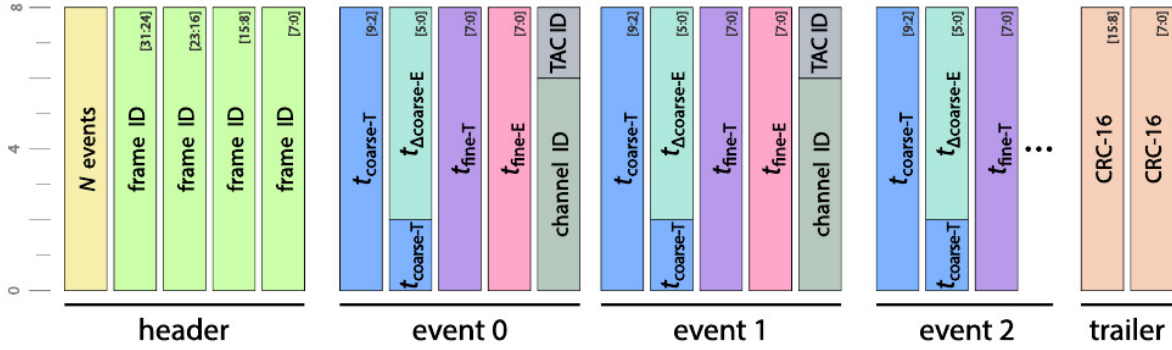Figure 3.7: Data structure in full mode. Image from [52].

Figure 3.8: Data structure in compact mode. Image from [52].

Chapter 4

The Data Acquisition System

4.1 Motivation and General Remarks

As described in Chapter 2, the MVD will make use of silicon pixel and strip detectors and for each of them, custom front-end chips are under development, respectively ToPix and PASTA. Typically, before obtaining a suitable working device, several design iterations are necessary. Considering the design time, the production phase, and the testing procedures to assess performance, it is reasonable to expect one prototype per year. A readout system that can be easily adapted to new prototypes is therefore a mandatory tool. Given the need to modify the functionalities or add new features to the readout system, according to the specifications of the prototype under test, a modular approach, intended as the aim to realize a complex structure composed by smaller semi-independent subsystems, is a suitable choice. Additionally, modularity allows reusability of resources. In fact, many subsystems that do not need to be modified when transitioning to a new prototype can be simply recycled without additional complications. Flexibility, intended as ability of the system to handle external changes, is also beneficial.
At present, each front-end prototype, for the pixels and for the strips, is tested individually. In a next step, the two chips, or more then one of the same kind, will be coupled to the same readout system, in order to combine their information in a way that is similar to the final operation scheme.

A data acquisition system that fulfills these requirements has been developed and is constantly improved. The development of the so-called Jülich Digital Readout System (JDRS) started with [85]. Several contributions from various people, based on this work, improved and extended the functionalities ([86] and [52]).

Currently, the fourth revision of the pixel ASIC is available [66]. ToPix has been integrated in the JDRS and its performance was thoroughly tested [87]. Concerning PASTA, the front-end ASIC for the strip part, a first full size prototype is available.

In the following chapter the modifications related to the integration of this new prototype in the existing data acquisition system will be illustrated in detail, since this implementation is one of the main focuses of this thesis. A general description of the JDRS, partially published in [88], will be given as well for the sake of completeness.

4.2   The Jülich Digital Readout System

The main components of the JDRS are an evaluation board from Xilinx (ML605), hosting a Virtex-6 FPGA, a custom-made readout board that hosts the Device Under Test (DUT), i.e., the ASIC, and a Personal Computer (PC). The logic scheme for the FPGA, commonly known as firmware, is written in Very High Speed Integrated Circuit Hardware Description Language (VHDL). The connection from the evaluation board to the PC is done via a network link. By means of this type of connection, the JDRS can be set-up on any machine with minimal effort, since no requirements from the software side, such as special driver installation on the operating system, nor from the hardware side exist. A C++ based software provides access to the elements of the readout chain. To facilitate this process, a Qt-based Graphical User Interface (GUI) is also part of the system. A schematic view of the system is shown in Fig. 4.1.
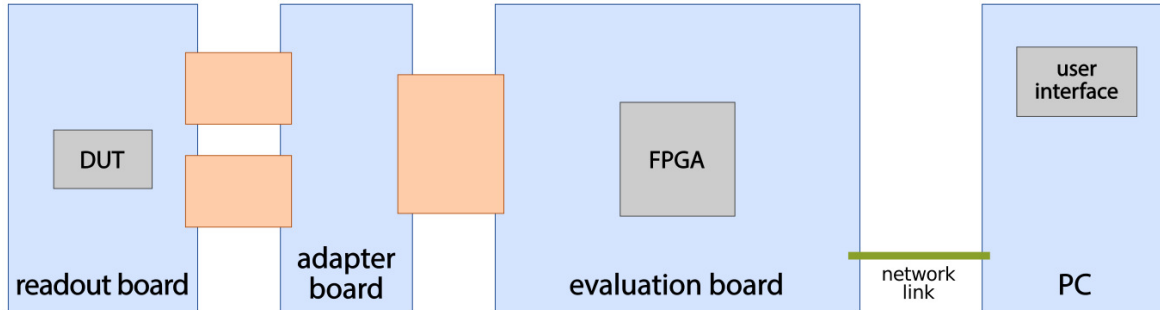
Figure 4.1: A sketch of the main building blocks of the Jülich Digital Readout System. Image from [52].

4.2.1   ML605 Evaluation Board

The ML605 evaluation board is an off-the-shelf product that allows to create or evaluate logic designs targeting a Virtex-6 FPGA (Fig. 4.2). It requires a 12 V power supply. The FPGA can be configured via a Joint Test Action Group (JTAG) interface or by storing a bitstream file encoding the logic on an Secure Digital (SD) card. A connection to the board can be achieved via Ethernet or Peripheral Component Interconnect Express (PCIe). The board provides an internally generated clock by means

of a 200 MHz oscillator. A Double Data Rate Type 3 (DDR3) memory of 512 MB is included on-board. Several General Purpose Input/Output (GPIO) SubMiniature version A (SMA) connectors, pushbuttons, and switches are available. The Input/Output (I/O) capabilities can be extended by means of FPGA mezzanine cards connected to low and high pin count connectors. An Liquid Crystal Display (LCD) screen to display verbose information and several status LEDs are also available.
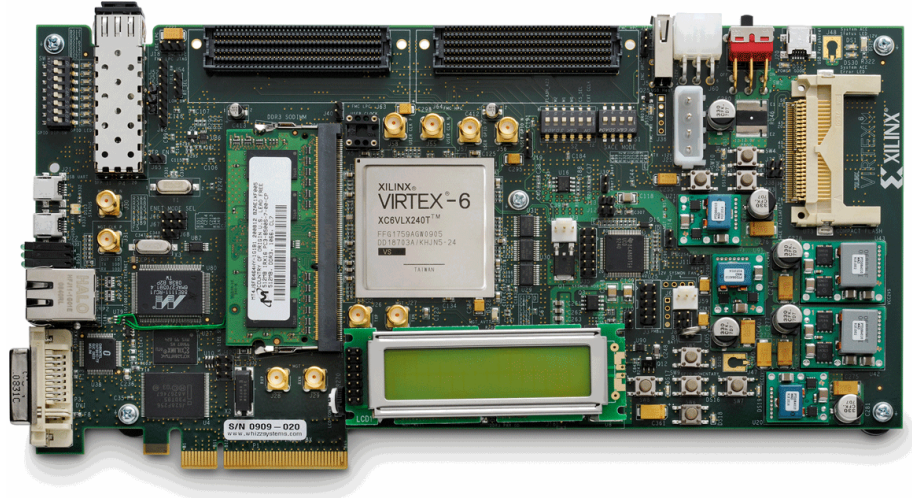
Figure 4.2: ML605 board hosting a Virtex-6 FPGA. Image from [89].

4.2.2   FPGA Firmware

Generalities

An FPGA is an integrated circuit designed to be configured after manufacturing, hence the name *field programmable*. FPGAs are intrinsically highly flexible off-the-shelf devices, which exploit parallel execution of instructions, and can in principle be used to implement any logical algorithm. The most common FPGA architecture can be thought of as an array of programmable logic blocks (look-up-tables and flip-flops), providing general purpose basic logic and storage functionality. These basic units communicate among themselves via reconfigurable interconnections or routing channels (i.e., wires and programmable switches) and to the outside world via I/O connections [90]. The circuitry built inside an FPGA requires a reference signal, the clock signal. FPGAs contain dedicated global and regional routing networks for clock and reset so they can be delivered with minimal skew, defined as the time difference between two or more destination pins in a path. Common features of most FPGAs are also memory blocks (like Random Access Memory (RAM), Digital Signal Processor (DSP) slices,

and serializers) and Phase-Locked Loops (PLLs)/Delay-Locked Loops (DLLs) to handle different clock domains. The process of designing and converting a circuit description into a format that can be understood by an FPGA can be schematized into several steps, which will be briefly described.

Circuit design and simulation: description of the desired circuit using a hardware description language (e.g., VHDL) and subsequent verification of its functionality through simulations. The design includes also the definition of the connection of used signals to the hardware pins, operating voltages, and clock frequencies. In the case of VHDL (which is the language used for this work), every design consists of at least one entity/architecture pair. The entity represents the interface of the circuit or component. Inside the entity the I/O elements (so-called ports) are defined and the direction of the corresponding signals specified (input or output). The architecture describes the functionality and timing of the corresponding entity. It is usually specified in terms of processes: within each process instructions are executed serially, while the processes are executed in parallel. Several mutually exclusive architectures can be implemented for the same entity, but not vice versa. An example of entity declaration will be presented in Section 4.3.

Logic synthesis: conversion of the Hardware Description Language (HDL) design into a set of boolean gates and flip-flops connected through wires.

Technology mapping: mapping algorithms optimize the boolean network (e.g., timing, resources, power optimization), resulting from the synthesis phase, and convert it into a functionally equivalent one that can be implemented in the FPGA.

Placement and routing: determination of specific logic blocks to be used to implement the desired design and their interconnection. Place and route algorithms aim to minimize the length of connecting wires and to assign net resources in the most efficient way (e.g., in order to maximize the speed of the circuit) .

Timing analysis: verification of the time performance of the circuit after place and route.

Bitstream generation: generation of a bitstream that encodes the designed circuit. This bitstream is then transferred to the FPGA to program it.

Firmware Structure

As previously mentioned, a key point in the development of the data acquisition system for the ASIC prototype is modularity. The structure of the firmware for the JDRS is schematized in Fig. 4.3 and the main modules are described in the following text.
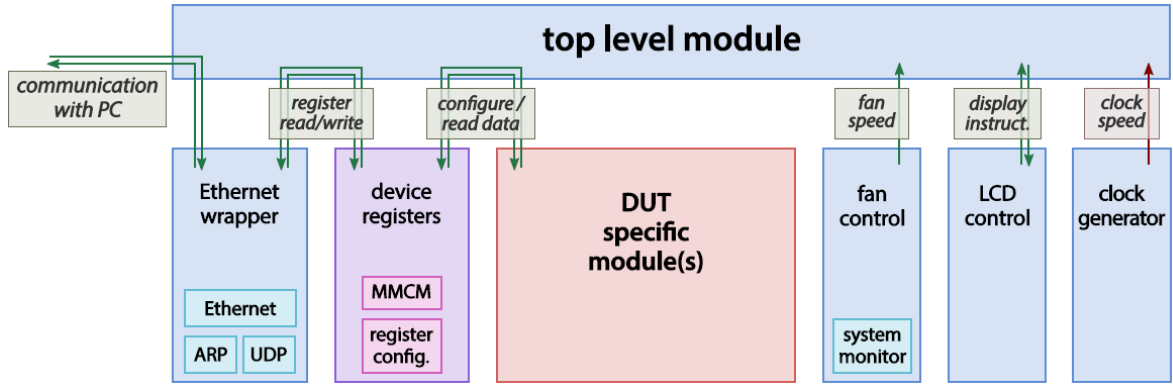
Figure 4.3: Scheme of the structure of the FPGA firmware. The top level module interfaces all the submodules and allows the communication among them. The arrows indicate the direction of the communication. The single modules are described in the text. Image from [52].

Top Level Module The top level module is the interface of the whole firmware. Here all the entities corresponding to the other modules (e.g., Ethernet module, register handling module, clock generation) are instantiated. Moreover, the connections among them and with the I/O blocks are specified.

Clock Generator Module The central clock, generated by the 200 MHz oscillator of the ML605 board, is received by the top level module and used to generate other clock signals with different frequencies. In particular, a clock signal with 125 MHz rate is produced and used as a central clock for the whole firmware. This value is determined by the desired transmission speed of the data over the Gigabit Ethernet, which transfers 8 bits per clock cycle.

Ethernet Wrapper This module is used as the interface to the Ethernet packages. It allows the bidirectional communication between the ML605 board and the PC. Its role is, thus, mainly to receive and process the incoming data according to the request forwarded from the other end of the communication. The data are transported using the User Datagram Protocol (UDP), which is based on a connection-less communication model. This means that each message, referred to as datagram, is individually addressed and routed on the basis of the sole information carried in the datagram itself, without relying on any prior communication. The UDP protocol provides checksums to ensure data integrity, but no handshaking dialogs. That is to say that the protocol does not intrinsically guarantee delivery, ordering, and duplicate protection. On the other hand, the feasibility of its implementation in VHDL on an FPGA and the low lag performance in case of unidirectional communication, outweighs the mentioned downsides. Moreover, it is considered preferable to lose some datagrams than to have to account for potentially long delays due to data retransmission, which might occur in case of a Transmission Control Protocol (TCP) connection.

Register Control Module Registers are basic elements used to store information and every one of them is identifiable through its unique address. More specifically, they are used to hold information sent from the outside to the FPGA and vice versa. The register control module implements the functions needed for reading and writing of the registers, as well as for their synchronization. The registers in the JDRS can be divided in two categories: *single* registers and *bulk data* registers. Among the single registers, a distinction is made depending on their purpose. Single registers related to board functionalities (i.e., common for different DUTs) are assigned fixed addresses stored in a central configuration file, as opposed to single registers related to device specific applications, which are potentially subjected to changes. An array of *status* and *configuration* registers suitable for device specific purposes is available in the logic. The synthesis tool takes care that only the amount of resources actually used will be implemented in the hardware. Status registers belong to the DUT module domain, while configuration registers are mostly handled by the Ethernet module. Bulk data registers come into play when the information to handle flows as a continuous stream, as it is the case for PASTA. This data stream is stored into a First In First Out (FIFO) buffer until a read request is received by the FPGA.

Auxiliary Modules Two auxiliary modules for the control of the ML605 built-in cooling fan for the FPGA and of the LCD display are also included in the firmware. The first one allows to adjust the rotational speed of the fan, according to the temperature measured close to the FPGA by means of a dedicated Intellectual Property (IP) core. With the second auxiliary module it is possible to control the output of the LCD display. For example, some basic information such as the Internet Protocol (IP) and Media Access Control (MAC) addresses, or the temperature and the fan speed can be retrieved and displayed.

4.2.3 Custom Readout Board

In order to be connected to the readout system, the DUT (i.e., ToPix or PASTA) has to be placed on a readout board. Since the characteristics of this element are highly dependent on the ASIC prototype, a description of the board designed for PASTA will be presented in Section 4.3.2.

4.2.4 MVD Readout Framework

The counterpart of the FPGA firmware on the software side is another fundamental part of the JDRS. A modular framework called MVD Readout Framework (MRF) collects functions that allow the communication between the PC and the DUT [85]. The MRF was originally developed as a tool to test the MVD ASIC prototypes. Nevertheless, due to its modular and general design it could be used also for other purposes. It is based

on C++ and depends only on the Standard Template Library. The structure of the code is based on an adaptation of the Open System Interconnection (OSI). This model has been developed by the International Organization for Standardization (ISO) in order to standardize the communication functions of a computing system regardless of the underlying internal structure of the system itself [91]. To achieve this goal, the model foresees different abstraction layers that separate low level functions from high level ones. Each layer serves the layer above and it is served by the one below. The original version of the model counts seven layers. In the case of the MRF four layers have been defined:

1. **Physical layer**: it is responsible for the connection between the readout board and the PC. It formerly used an optical link, but at present uses Ethernet communication.
2. **Generic Access Layer**: its main tasks are the management of the connection, the memory access, the data formatting and transfer in form of generic data packages.
3. **Transport Access Layer**: it provides board specific functions (e.g., clock generation, flush of data buffers).
4. **Chip Access Layer**: it implements configuration and readout functions that are specific to the DUT.

Since the chip access layer is the only layer strictly dependent on the structure of the DUT, its functions are the only ones that require adaptation when switching to a new ASIC prototype.

4.2.5 Graphical User Interface

A GUI based on Qt has been implemented in order to facilitate the access to the MRF functions. Qt is a widely used open source cross-platform application framework for developing software with GUIs as well as command-line tools [92]. It provides a large set of graphical control elements that can be included in the design. The layout of the interface can be carried out by writing Qt code or by operating the provided graphical design editor. In the second case, Qt itself takes care of generating a class for each layout, by using a code generator called User Interface Compiler (UIC). Qt supports standard C++, including multi-threading for parallel programming, and it is compatible with several compilers (e.g., GNU Compiler Collection (GCC), Visual Studio, etc.). Qt has a program that handles C++ extensions: the Meta Object Compiler (MOC). This tool is run on a Qt project to generate additional C++ code that contains meta information about the included classes. Such meta information is subsequently used by Qt itself to provide programming features not natively available in C++, e.g., the signals and slots mechanism which will be discussed in Section 4.3.3. Typically the MOC is not called manually, but automatically by the build system, therefore no additional effort

is required from the programmer. Qt provides a cross-platform build script generator tool, called `qmake`, to automate the generation of makefiles that are then used by the program `make` to build executables from the source code.

4.3   Integration of PASTA in the JDRS

4.3.1   FPGA Firmware

As previously mentioned, due to the modular structure of the FPGA firmware, almost all the modules included in the JDRS can be reused without modification when changing from one prototype to the other. However, there is one part that always needs to be adapted to the DUT, namely the interface to the ASIC itself. In the case of PASTA, this module is called `PASTA_CTRL`. Listing 1 shows the entity declaration. There, one can identify the clock and reset ports, the registers, the data lines, and the configuration ports. The architecture is composed of three submodules: the configuration module, the data receiver module and the reset module.

Configuration For the configuration of PASTA four lines are needed: `SCLK`, `SDI`, `SDO`, and `CS`. The `SCLK` is a clock signal only used for configuration and therefore it has a lower frequency compared to the other clock lines. The used value is 10 MHz. The `SDI` carries the actual configuration information and can be shared among different ASICs connected to the same control and data acquisition system. In this case, the `CS` is used to enable a specific one. The `SDO` is unique for each ASIC and it serves as an acknowledgment signal to verify correct communication. The configuration module uses data stored into dedicated registers as input. It processes them using a Finite State Machine (FSM) and produces the proper format to be sent to the ASIC.

Data Receiving The output data coming from the ASIC travel on one or two transmission lines. This module parses the content of these lines to extract the original 40 bit words (see Section 3.3.4) which are then sent to the PC. The data from PASTA are 8b/10b encoded and therefore they need to be decoded after transmission [93]. Performing this decoding by means of logic gates is more efficient than using a C++ software implementation, therefore this process has been included in the FPGA firmware. The logic is not only able to identify single 40 bit words, but also whole frames (refer to Section 3.3.4 for the definition of a frame). A special 40 bit word which is not present in the original PASTA data stream, called *frame indicator* (`0xff_ff_ff_ff_ff` in hexadecimal representation), is inserted before each frame in the stream of data transmitted to the PC to simplify the detection of frames in the software. As already mentioned, even eventless frames (i.e., frames with only header and trailer, but no event data) are constantly transmitted to the acquisition system, together with control sequences that fill the gaps between regular frames. To reduce the load on the network

```vhdl
entity pasta_ctrl is
 port (
   -- clock and reset
   GLBL_RST       : in  std_logic; --! global reset
   CLK_GTX        : in  std_logic; --! register clock
   CLK_ASIC       : in  std_logic; --! main ASIC clock
   CLK_SLOW       : in  std_logic; --! slow control clock

   -- registers
   REG_CONFIG     : in  reg_devX_config_type; --! generic config registers
   REG_CFG_WR     : in  reg_devX_cfg_wr_type; --! config register updated
   REG_STATUS     : out reg_devX_status_type; --! generic status registers
   REG_ST_RD      : in  reg_devX_st_rd_type;  --! status register was read
   REG_CTRL       : in  std_logic_vector(REG_LEN-1 downto 0); --! control register
   REG_CTRL_RST   : out std_logic_vector(REG_LEN-1 downto 0); --! reset register

   PASTA_CS       : out std_logic; --! chip select
   PASTA_SDI      : out std_logic; --! slow data input to the ASIC
   PASTA_SDO      : in  std_logic; --! slow data output from the ASIC
   PASTA_SYNC_RST : out std_logic; --! synchronous reset
   RST_TO_TELE    : out std_logic; --! reset signal to the strip telescope
   PASTA_TX_0     : in std_logic;  --! first transmission line
   PASTA_TX_1     : in std_logic;  --! second transmission line

   -- data transport
   BLK_DATA       : out std_logic_vector(REG_BULK_LEN-1 downto 0); --! data stream
   BLK_WREN       : out std_logic   --! write enable for the bulk register
 );
end pasta_ctrl;
```

Listing 1: Entity declaration of the `PASTA_CTRL` module.

link, the possibility to suppress empty frames has been included in the logic. Since the information on the amount of events in a given frame is stored in its header, it is easy to discard frames whose number of events is equal to zero. The core of the architecture of this receiver module is implemented using a FSM, similar to the configuration module.

Synchronous Reset PASTA responds to two reset signals, which are synchronous with its main operational clock: a partial reset and a full reset. The first one is a single clock cycle long signal that resets everything except for the configuration registers, while the second one is a two or more clock cycles long signal that also resets the configuration registers. The partial reset is particularly useful when the internal counter of PASTA needs to be reset, e.g., when synchronization with an external counter or with other chips is needed. After a full reset command, the ASIC operates with a default configuration stored inside it, which is the one loaded after power on.

A FSM generates the proper reset signal according to the input value stored in a dedicated register and sends it to the dedicated output pin. The input value is the actual length of the signal that needs to be generated, expressed in clock cycles. Specifically, the value 1 initiates a partial reset and either the value 2 or any other number between 4 and

31 induces a full reset. The input value 3 has a special meaning. When operating PASTA together with an external system (e.g., a tracking station during measurements under a particle beam, described in Section 5.2), it is not only useful to synchronize the systems with a reset signal, but also to compare their respective timestamps at specific points in time, to make sure that the independently measured times are in agreement. In order to request the timestamp of the connected system, a dedicated state in the mentioned FSM produces a timestamp readout signal when the input register holds a value equal to 3. This signal is then transmitted to a specific output pin and used as input for the other system, to record its timestamp. The length and type of the control signal depends on the specifications of the system that is connected to the PASTA DAQ. In the case of the beam test measurements, the tracking station requires a 3 clock cycles long control Low-Voltage Differential Signaling (LVDS) signal. An adaptation in this part, to accommodate other specifications is straightforward. The timestamp information from the ASIC side is included in every frame header. Therefore, whenever the control signal is issued, the next frame in the data stream sent to the PC is tagged with a special frame indicator (`0xfa_fa_fa_fa_fa` in hexadecimal representation), which can subsequently be used to retrieve the timestamp information.

4.3.2 PASTA Readout Board

The board that hosts PASTA, shown in Fig. 4.4, has a dimension of $18\,\text{cm} \times 10\,\text{cm}$ and the ASIC is wire-bonded to it [94]. It consists of four layers: three layers for the signal routing and a power layer, arranged on different planes to provide the needed voltages to the ASIC ($1.2\,\text{V}$ for the analog and digital part, $2.5\,\text{V}$ for the drivers, $5\,\text{V}$ for the board external biasing, and $3.3\,\text{V}$ for the services). Several access points are available in order to measure the provided current values. A separate region is also used to provide proper biasing to the sensor connected to PASTA. A selection of digital values is accessible through a 15 pin header. A few test points for analog signals are available as well. The I/O signals are connected to a 16 pin header. Among these input lines, three of them, namely the external test pulse, the reset, and the clock, can be disabled through a switch and the respective signals can be provided via SMA connectors.

4.3.3 Software

As previously stated, the JDRS has been used so far to read out data from the pixel front-end ASIC. Several adaptations, mainly due to the different internal architecture of PASTA (e.g., configuration, data structure) are needed in order to use the DAQ with the strip ASIC prototype. Although the development of the MRF was carried out following a modular paradigm, the code used to generate the whole GUI was held in a single Qt project. It was therefore not straightforward to reuse the parts of the
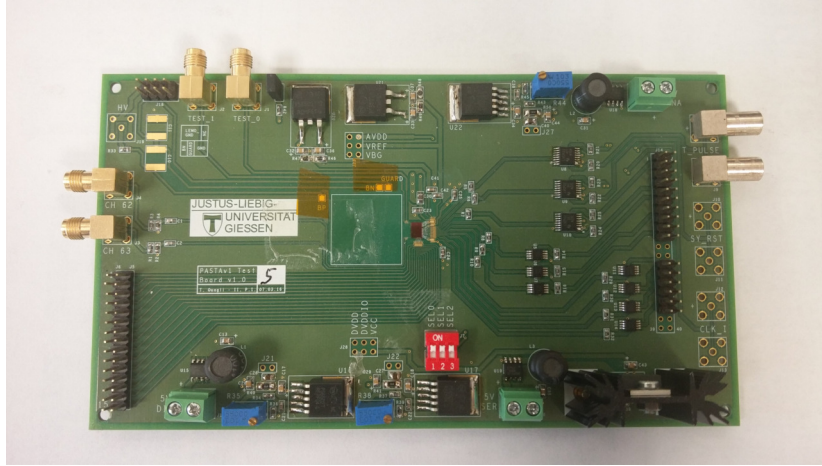
Figure 4.4: Custom developed board to host the PASTA chip. The square in the middle indicates the space reserved for the sensor. Next to it, to the right, one can see the wire-bonded PASTA chip. Proceeding to the right, there is the I/O pin header. The switch that multiplexes the input lines that can have alternative sources is the red box positioned under the ASIC. The pin header for probing selected digital outputs is placed on the bottom left.

code common to the two prototypes. Moreover, the whole software was customized for a specific machine, which lead to the time-consuming task of having to perform adjustments whenever the installation on a different machine was needed.

The integration of PASTA in the JDRS has been thus taken as a chance to restructure the code that was originally written for the pixel ASIC, exploiting the resources provided by the Qt environment. In the following paragraphs, a description of the renewed structure of the code and an overview of the main functionalities is provided. The emphasis is placed on the modules that have been introduced or extended during the work of this thesis. For the sake of completeness, the other modules are described as well and references to follow-up reading are given.

Code Restructuring: Multi-Widget Approach

The main goal of the restructuring is to improve modularity and reusability of the software components. This was achieved by separating functionalities in independent projects (so-called *widgets*), which are all sub-parts of a main container (so-called *main window*). Each Qt project consists of at least three basic components, which are described below.

Project file It is a file with the `.pro` extension that contains all the information required by `qmake` to build the project, which can be an application, a library or a plugin. The format used by `qmake` supports from easy to fairly complex build systems. In the simplest scenario, a project file is composed of a list of declarations that define standard variables. These variables hold lists of strings that specify configuration options as well as source and header files used in the project. Variables can also be used internally to store temporary lists of values and existing lists of values can be overwritten or extended with new values [95]. An example of a project file is shown in Listing 2. The highlighted words are variable names that `qmake` recognizes. A complete list of these variables with the description of their content is provided in [96].

```
# project location
PROJECTPATH = $$system(readlink -f $PWD/../../../)

# load Qt modules
QT += gui network widgets

# allow use of C++11
CONFIG += c++11

# set application parameters/directories
TEMPLATE = app
TARGET = UDP_connection

# provide a constant for the source code
DEFINES += STANDALONE = 1

DESTDIR = build
OBJECTS_DIR = $${DESTDIR}/obj
MOC_DIR = $${DESTDIR}/moc
RCC_DIR = $${DESTDIR}/rcc
UI_DIR = $${DESTDIR}/ui

# dependencies from other libraries
DEPENDPATH += .
INCLUDEPATH += $${PROJECTPATH}/MRF/include/ $${PROJECTPATH}/MRF/include/tools/
INCLUDEPATH += $${PROJECTPATH}/MRF/include/ltc/
INCLUDEPATH += $(SIMPATH)/include/
LIBS += -L$${PROJECTPATH}/MRF/lib -lMRF
LIBS += -L$(SIMPATH)/lib -lboost_thread -lboost_serialization -lboost_timer \
    -lboost_system -lboost_chrono

# files in the project
FORMS += UDP_connection.ui
HEADERS += udp_connection.h
SOURCES += main.cpp \
    udp_connection.cpp
RESOURCES += $${PROJECTPATH}/software/GUI_resources/resources.qrc
OTHER_FILES += Makefile
```

Listing 2: Example of a project file for a Qt widget

Designer UI file It is a file with extension `.ui` that represents the graphical layout of the widget (so-called *form*) in Extensible Markup Language (XML) format. This file is processed at compile time and converted into C++ code. The objects that build up the form are placed with the desired layout by using the provided Qt graphical designer editor.

Standard C++ class It implements the functionality of the graphical objects.

The communication among widgets is handled by the main window, as well as the initialization and distribution of global information, by means of the signals and slots mechanism. A single widget can also be executed standalone i.e., without interactions with other widgets. The signals and slots mechanism is a key feature of Qt and represents the aspect that differs the most from other frameworks. Therefore, follows a paragraph dedicated to its explanation.

The Signals and Slots Mechanism

In GUI programming, an event that occurs in one widget might need to trigger an action in another widget. More generally, it has to be possible to notify objects about a change that happened in another object. Some toolkits use a mechanism called *callback*. A callback is essentially a pointer to a function. When a function wants to be notified by a second function, it can do so by passing it a callback to a third function. The function that receives the callback then takes care to execute it when appropriate. Such a mechanism has two main downsides: it is not type-safe and the callback is strongly coupled to the receiving function, that has to know which callback to execute. The signals and slots mechanism is the Qt alternative to the callback technique [97]. All the classes that inherit from `QObject`, which is the base class of all Qt objects, or one of its sub-classes, e.g., `QWidget`, can contain signals and slots. Signals are automatically generated by the MOC and must not be implemented in the source code. Slots are special member functions that have the possibility to receive signals, but they can also be called as standard functions. They follow the standard C++ rules, except for the fact that they can be invoked in an instance of a different class than the one they are defined in and they cannot have a return value. When an event worth being notified of has occurred in a widget, a signal is emitted by that widget. If there is a slot connected to this signal, then it is executed. Qt widgets have a set of predefined signals and slots, but the user can also subclass widgets and add custom ones. There is no limit on the number of signals that a slot can receive, nor on the number of slots that can be connected to the same signal. If a slot is connected to multiple signals that trigger different responses, a signal mapper can be used to provide information about the sender to the slot. A signal can also be connected to another signal: in that case the second signal would be emitted immediately after the first one. This technique for communication among objects is completely type safe: the signature of a signal has to be compatible with the

one of the receiving slots. A shorter signature in the slot than in the signal is allowed and it would lead to ignoring the extra arguments. In any other case, a mismatch in the signatures would result in a runtime error. There is no limit on the number, nor on the type of arguments that signals and slots can take. Moreover, signals and slots are loosely coupled: in the standard usage the sender object does not know which widget, if any, would receive its signal. The same principle applies to the receiving slot, which is not aware of the origin of the signal. A signal is sent by using the keyword `emit` and the connection between a signal and a slot has to be specified with the syntax in Listing 3. An optional parameter can be specified after the receiving slot: the type of connection. By default, if no type is specified, the so-called direct connection is used. In this case, the slot is executed right after the signal is emitted, just like a standard function call. At this point, the signals and slots mechanism is independent of any event loop in the GUI and the execution of the instructions that follow the `emit` statement will happen only after the slot has returned. This behavior can be modified by specifying different kind of connections. For example, when using queued connections the code following the signal emission is executed immediately and the receiving slot will be called afterwards. This type of connection is of particular usefulness when dealing with multi-threaded applications. In general, if several slots are connected to the same signal, they are executed according to the order in which the `connect` statements are declared.

```
QObject::connect(&sender, SIGNAL(button_pressed(int)),
                 &receiver, SLOT(exec_instruction(int)));
```

Listing 3: Qt syntax to declare a connection between a signal and a slot.

MRF as Library

As described previously, the MRF is a collection of functions that allow communication between the PC and the DUT. In the former version of the software, the source and header of the needed MRF files where included individually in the project file. With the new approach, that foresees more than one project, it would be cumbersome to proceed with the same strategy. Therefore, it was decided to include all the source and header files of the framework in a dedicated Qt library. Such a library, differently than in the case of a Qt application, does not have a GUI. Following this approach, whenever a new project that requires access to the MRF functions is introduced, it is sufficient to add a single line of code to its project file to include the library (Listing 4).

```
LIBS += -L$${PROJECTPATH}/MRF/lib -lMRF
```

Listing 4: Qt syntax to include a library to a project.

Widgets Description

In order to improve reusability of the code, the functionalities implemented in the user interface are separated in *core* and *ASIC specific* modules. The first ones include every process that does not depend on the DUT, namely the communication layer between the hardware components and the register access and configuration of the ML605 board. These modules do not require any modifications when switching among different test devices, as long as the communication protocol and the involved hardware stay unchanged. The second ones are related to the data transmission to and from the ASIC, namely the device configuration procedures and the data receiving, thus requiring adaptations when changes in the ASIC design occur.

Core Modules

UDP connection It provides the fields to configure the parameters needed to establish the Ethernet connection between the ML605 board and the PC. The addresses of the devices have to be specified together with the dedicated ports. To establish the communication, a *Connect* button is used. The connection status (i.e., active or inactive) can be queried by issuing a ping signal. If the devices are successfully connected, a pong response will be received on the PC. For more details on the implementation of the UDP protocol refer to [52].

Registers access It is intended mainly for debugging purposes. Single FPGA registers can be accessed by specifying their address and the amount of data to be read.

Clock generator It allows the configuration of the clock generator internal to the FPGA. The only parameter requested from the user is the desired frequency value within a range 4.69 MHz to 600 MHz. The calculated frequency, according to the input, is then displayed.

ASIC Specific Modules

Global configuration It comprises both digital and analog configuration. Two possible modes are foreseen to edit the 46 parameters that build the configuration: a high level verbose mode intended for less experienced users and an "expert" mode, which provides access to the complete list of configuration parameters, showing the position in the bitstream and the ranges. In the latter, the values can be set manually or loaded from a file. Similarly, the user is given the possibility to store a configuration bitstream to file. The configuration data are stored using JavaScript Object Notation (JSON) format, to take advantage of its human-readability [98]. Moreover, Qt provides support to handle JSON-format data, with classes such as `QJsonObject` and `QJsonDocument` [99].

Local configuration For the configuration of the 22 local parameters for each of the channels, only the "expert" mode is implemented. The working principle is the same as for the global configuration. Additionally, this widget allows the user to forward the configuration of selected channels only, instead of all 63 of them.

Configuration Controller It handles the actual sending of the global and local configurations and allows readback operations. In order to verify a correct transmission, the configuration stored in memory can be retrieved. A bitwise comparison between the sent data and the read values is then performed. In case of a negative result of such a comparison for a certain bit, the relative cell in the respective configuration widget is colored in red, otherwise in green.

Synchronous reset It is a simple widget which initiates a reset of the ASIC, either partial or full, or requests the current timestamp.

Test pulse configuration As described in Section 3.3.4, a signal can be generated inside the chip for testing purposes. This signal is configurable in terms of number of consecutive pulses, amplitude, width, and frequency. The widget is used to supply the needed parameters and to enable the receiving channel.

Channel scanner It implements an automatic scanning procedure to study the response of multiple channels. The user can select the kind of pulse that will be generated, namely a digital or an analog signal, according to the description in Section 3.3.4. Furthermore, the range of channels to be tested has to be provided. Finally, up to two configuration parameters, together with a range of variation for each one of them, can be selected. Once the measurement is initiated, the first channel of the given range is enabled and will receive a train of pulses configured according to the selected parameters. When the injection for this channel is completed, the procedure starts again for the second channel. The scanning routine is over when the last channel in the list is reached. Fig. 4.5 shows the widget as it appears in the user interface.

Data receiver It collects the data produced by the ASIC, decodes it and finally stores it to disk. The user is required to specify a format for the data to be stored together with a file name and a location on the filesystem. The available formats at the moment are ASCII and BOOST serialization [100], but the code can be easily extended to accept other formats as well. Current data and timestamp are automatically appended to the filename. Additionally, this module foresees the possibility to reduce the amount of incoming data by suppressing frames that do not contain any event data and/or suppressing the comma words that are used as control sequences. The frame indicator, used to label the beginning of a frame, can be suppressed if desired. By default, a single request for stored data retrieves the maximum number of words that are transmittable within a UDP package. Multiple requests can be issued consecutively, by specifying an integer number in the dedicated field.

Figure 4.5: Channel scanner widget as it is displayed in the GUI. The configuration options are described in the text.

Figure 4.6: Data receiver widget as it is displayed in the GUI. The configuration options are described in the text.

The data that have been read out are handed over to a decoding routine, which identifies the data frames by searching for the frame indicators. Once a data frame is found, it is split in multiple words: one header, one trailer and the event data words, if present. The structure of the event data words depends on the data format selected in the global configuration of the ASIC. This information is forwarded from the configuration widget to the data receiver, in order to properly interpret the incoming data. The information contained within each word (e.g., timestamps, channel number) is then extracted and written to disk according to the user specified preferences. Additionally, the chip configuration used for the data taking is stored together with it. A maximum file size can be defined: when the size limit is reached a new file is created. The filename is formatted by taking the original filename and appending an increasing integer number. Fig. 4.6 shows the widget as it is displayed in the user interface.

Online monitoring In order to be able to control the data taking and visualize the readout information in real time, a monitoring widget is used. This tool is very useful during debugging measurements as well as during data taking runs. Having direct visual access to the readout data allows the user to identify problems, such as wrong configuration parameters, data corruption, or interrupted communication between the devices, and act to overcome them or ultimately stop the data taking, if necessary. Carrying out data taking without a monitoring system leads to saving potentially corrupted, and therefore useless, data to storage. This module accepts the data frames, after they have been processed by the data receiver module, and displays the information contained in each frame in the form of ROOT objects, such as histograms and graphs. A set of objects to display basic quantities is defined and it can be extended according to the needs of the user. The visualization is carried out by means of an Hypertext Transfer Protocol (HTTP) server and it is displayed in an interactive web browser session [101]. The displayed histograms are automatically stored into a *.root* file, which, for sake of consistency, is named according to the user preferences, specified in the data receiving widget.

Chapter 5

Evaluation of the Performance of PASTA

This chapter collects the measurements that have been carried out in order to assess the performance of the first revision of the PASTA chip. First, the ASIC has been evaluated by exploiting its internal signal generation and then by exposing it to an ionizing beam. The DAQ system used in both cases is the previously described JDRS. Some preliminary operations, such as establishing a reliable communication with the ASIC and configuring it, are necessary in order to have a solid ground to base the measurements on and they will be illustrated as well. The work presented in this thesis, does not cover the evaluation of the TDC and thus the determination of the fine time resolution. The TDC implemented in PASTA is inherited from its predecessor TOFPET. However, for the strip part of the MVD, a time resolution better than 10 ns is required and this goal can be achieved by only considering the coarse time information. The characterization of the TDC is described in another work of thesis [82].

Part of the measurements presented in this chapter have been published during the course of this work of thesis [75].

5.1   Measurements with Internal Injection

As will be discussed extensively in the text, PASTA presents some problems operating at readout frequencies close to the nominal value (160 MHz). The measurements presented in this paragraph, if not otherwise specified, are thus relative to a lower frequency, namely 80 MHz.

5.1.1 Power Consumption

The current provided by adjustable voltage regulators to the various parts of the ASIC can be measured through the test points provided on the readout board. The voltage drop is measured on a $100\,\mathrm{m}\Omega$ resistor placed in series at the output of the regulators. At the nominal operational frequency of $160\,\mathrm{MHz}$, the measured currents are: $30\,\mathrm{mA}$ for the digital part and $80\,\mathrm{mA}$ for the analog one. The total power consumption of PASTA corresponds to $143\,\mathrm{mW}$, well below the requirement ($256\,\mathrm{mW}$).

5.1.2 Configuration Operations

The first aspect that needs to be tested is the bilateral communication between the PC and the ASIC. In order to do so, the Ethernet connection is established and some configuration is forwarded to the ASIC via the GUI. The configuration stored in the ASIC registers is then read back and compared to the sent one, expecting no differences between the two. In case of mismatch, or as a cross-check, an integrated FPGA logic analyzer called ChipScope is used [102]. This tool allows to capture and display any FPGA signal at the speed of operation of the implemented logic. In this way, one can observe the complete configuration patterns, transmitted through the `SDI` line. The `SDO` line provides useful information as well, for it is meant to carry acknowledgment signals when a configuration request is received by the ASIC. An example of a ChipScope session is shown in Fig. 5.1. All the configuration commands listed in Table 3.2 have been successfully verified, leading to the conclusion that every possible configuration of the ASIC can be transmitted as expected.
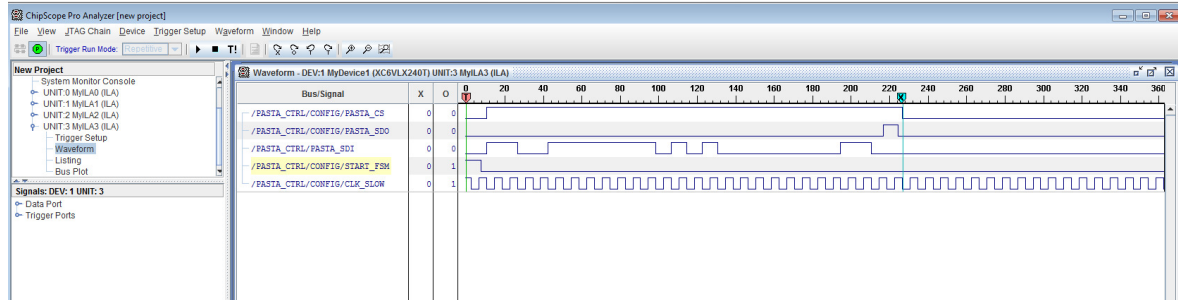

Figure 5.1: Example of a ChipScope session during a configuration operation.

5.1.3 Response of the Channels to Internal Stimuli

After having established that all the configuration commands are correctly received by PASTA, one can look at how the chip responds to stimuli. At this point, the possibility to generate a pulse internally to the ASIC comes in handy. The channel scanner module

of the GUI is used to inject the same kind of input pulse into all 64 channels sequentially. That is to say, the injection is performed on one channel at a time, starting from channel 0 up to 63. The global configuration is optimized in order to observe the maximum number of responsive channels. The selected pulse amplitude corresponds to 20 fC of deposited charge. This value is quite large compared to what is expected during the standard operation of the chip, but the aim at this point is simply to verify if there is any activity in the channels. Fig. 5.2 shows the result of both an analog and a digital injection. In the first case, about 10 % of the channels shows either a partially reduced efficiency or a non-responsive behavior. The channel 63 shows an excess of counts with respect to the number of injected pulses. This behavior is most likely due to noise pick up along the line that connects this channel to a test point on the ASIC Printed Circuit Board (PCB). Observing the chip response in case of digital injection, no efficiency loss is visibile and all the 64 channels correctly respond to the internal stimuli. This hints at a problem either in the analog part of the chip or in the routing of the channels. The same measurement performed on different PASTA chips gave comparable results, albeit with different patterns of unresponsive channels. To exclude that particular settings of the generated signals lead to the observed reduced efficiency of the chip, measurements using different combinations of pulse parameters (e.g., length and width) are carried out as well. No correlation is found between the pulse configuration and the response of the channels in terms of detected events.
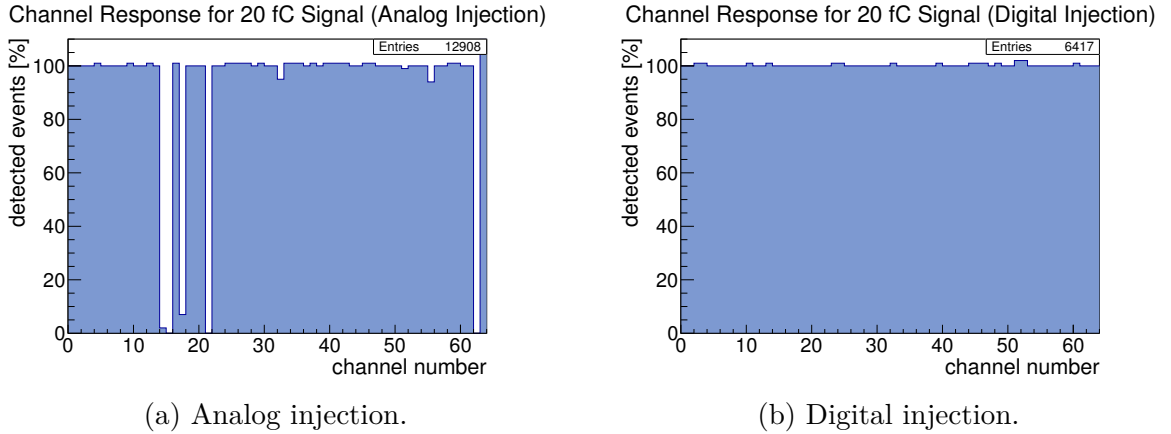

(a) Analog injection.

(b) Digital injection.

Figure 5.2: Channel response to a sequence of internally generated pulses corresponding to 20 fC deposited charge.

5.1.4 Threshold Studies

Generalities

The threshold of the ASIC is an important characteristic that has an impact on the performance of the detector. Its calibration consists in finding an operation point to optimize the signal-to-noise-ratio. The presence of hits that do not correspond to signal events, or in other words the noise, negatively influences the performance of the detector (e.g., reconstruction of particles trajectories is much harder in the presence of noise). Ideally, only incoming signals with an amplitude bigger than the set threshold value are detected. This leads to a response pattern, in terms of detected events as a function of the threshold, similar to a step function. In reality, due to the electronic noise and non-perfectly identical channels, the step function is smeared by a Gaussian curve, resulting in the so-called S-curve shape (Fig. 5.3). It follows, that the suitable threshold for a given pulse amplitude is defined as the value corresponding to the detection of 50% of the incoming signals, being this value a typical reference in the context of pixel and strip detector threshold tuning. An alternative determination of the threshold can be achieved by considering the S-curves that correspond to different pulse amplitudes for a given threshold. Typically, individual thresholds are calculated for each channel. Their distribution is expected to exhibit a Gaussian profile with a certain σ that can be reduced by tuning local threshold parameters. A convolution of a step function with a Gaussian error function is then fitted to the measured S-curve

$$F(x) = \frac{n}{2}(1 + erf\frac{(x-\mu)}{\sqrt{2}\cdot\sigma}) \quad \text{where} \quad erf\frac{(x-\mu)}{\sqrt{(2)}\cdot\sigma} = \frac{2}{\pi}\int_0^x e^- t^2 dt.$$

In the formula n is the number of events, μ is the mean of the function, and σ is the the electronic noise.

The described procedure has been successfully applied to the calibration of the chip for the pixel part of the MVD and the results are presented in [86].

Threshold Calibration for PASTA

Due to the architecture inherited from its predecessor TOFPET, PASTA has two parameters, instead of a single one, to define the global threshold: Hysteresis Comparator Global Digital to Analog Converter (Positive Input) (`HCGDAC+`) and Hysteresis Comparator Global Digital to Analog Converter (Negative Input) (`HCGDAC-`). The difference of these two defines the effective threshold as the mid-range of an interval with fixed amplitude. Moreover, there are two local threshold parameters per channel: one relative to the time branch and a second one relative to the energy branch. In order to reproduce the S-curve measurement, one of the two global threshold parameters, namely `HCGDAC-`, is kept at
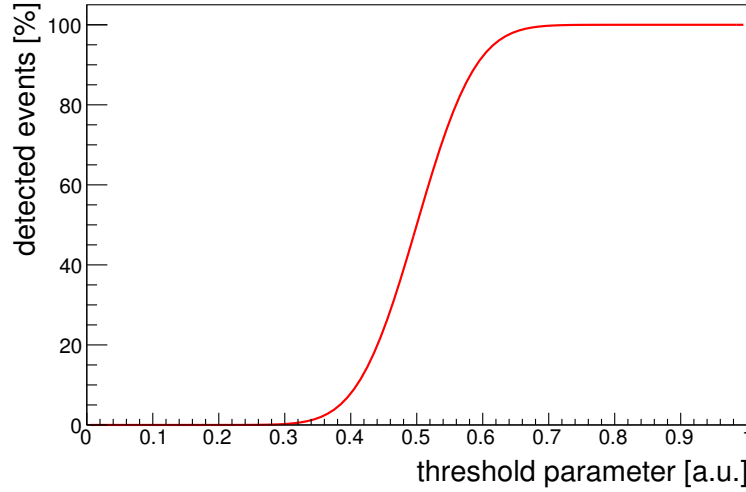
Figure 5.3: Typical S-curve shape: the number of detected events is given as a function of the threshold parameter, for a given pulse amplitude. In this example, the larger the threshold parameter value, the smaller the threshold level.

a fixed value, while `HCGDAC+` is varied in an interval between `HCGDAC+ = HCGDAC-` and `HCGDAC+ = HCGDAC+`$^{\text{max}}$. The measurement is repeated for several values of the pulse amplitude and the observed behaviors can be summarized in four cases:

1. S-curve. This is the expected behavior (Fig. 5.4a).
2. S-curve with efficiency drop for low thresholds. If the threshold is below the baseline the signal cannot be detected (Fig. 5.4b).
3. Box-like response. The signal is always above the threshold and therefore $100\,\%$ of the injected signals are detected (Fig. 5.4c).
4. Zero events detected. This behavior can be ascribed to two causes: either the effective threshold is always above the signal, or it is always below the baseline. In both cases, there is never a threshold crossing, so the signals are never detected.

The observed behavior for global threshold scans differs among the channels and the S-curve is visible for a few of them, only for low values of the injected amplitude. In case of a $2\,\text{fC}$ charge injection, for example, 25 channels show an S-curve transition, 12 present a loss in detection efficiency for low thresholds, 7 have a box-like response, and 20 detect either zero or few sparse events. Therefore, no threshold distribution can be studied. Moreover, the response appears to be dependent on the individual values of the two threshold parameters, which should not be the case, for only their difference should contribute to the effective threshold level, according to the design specification. As a consequence, the calibration of the threshold proves to be cumbersome. The alternative method, which foresees the calibration of the threshold by means of pulse amplitude scans at fixed global threshold, is also not suitable for PASTA. In this case, the bottleneck is the configuration of the pulse amplitude. In fact, from these

attempted measurements one learns that: several channels do not respond to pulses with amplitude smaller than 2 fC; for the ones that do respond, the number of detected events corresponding to the smallest generated amplitude is close to zero, even for the smallest selectable threshold, while for the nearest bigger generated amplitude, the number of detected events rises up to 100 %, without showing the smooth transition typical for these kinds of measurements. This indicates that the signals corresponding to a pulse amplitude bigger than 2 fC are always above threshold and that the separation between two consecutive amplitudes is too coarse.

Since the S-curve method is not applicable to PASTA, the electronic noise for this prototype cannot be determined.
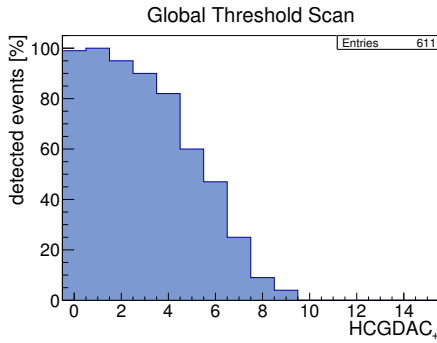
(a) S-curve shape.
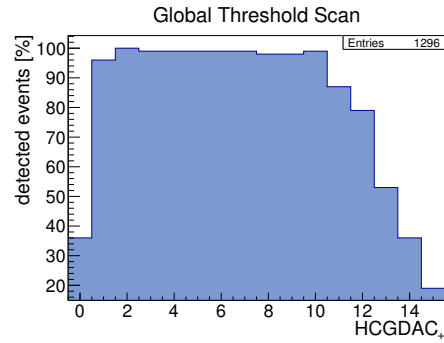
(b) S-curve with efficiency drop for low threshold.
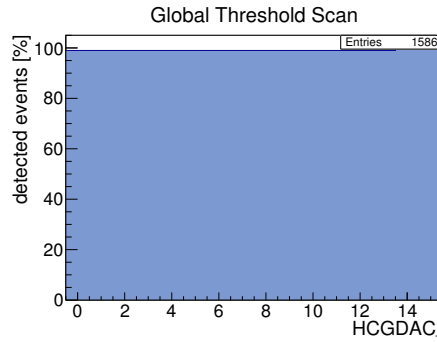
(c) Box-like response.

Figure 5.4: Global threshold parameter scan for various channels.

Another option needs to be found in order to optimize the operation of the ASIC. The strategy chosen to determine the threshold proceeds as follows: given a pulse amplitude, a defined amount of pulses is injected into each channel. The procedure is repeated for every possible combination of threshold parameters within their ranges. The combinations of `HCGDAC+` and `HCGDAC-` that correspond to a number of detected events between 50 % and 110 % of the generated ones are tagged as valid. The chosen global threshold is then the combination that is valid for the majority of the channels.

Fig. 5.5a shows the result of this measurement for signals corresponding to a pulse amplitude of 5 fC. The *z*-axis indicates the number of channels for which the pair of threshold parameters is valid. Only the combinations for which `HCGDAC+` $\geqslant$ `HCGDAC-` is considered, due to the design specification of the ASIC. One can observe that the most populated region lies above `HCGDAC+` = 6. The values corresponding to red colored cells are considered suitable settings for the specified pulse amplitude. The chip response is evaluated for one of these combination, i.e., `HCGDAC-` = 8 and `HCGDAC+` = 15 (Fig. 5.6a). The behavior is comparable to what was observed for the measurement with 20 fC signals (Fig. 5.2a): 5 channels are completely unresponsive and a few more have reduced detection efficiency. Moreover, as in the previous case, channel 63 has a high number of noise counts. In conclusion, one can state that the ASIC can be calibrated for 5 fC signals.

(a) 5 fC signal.

(b) 3 fC signal.

(c) 2 fC signal.
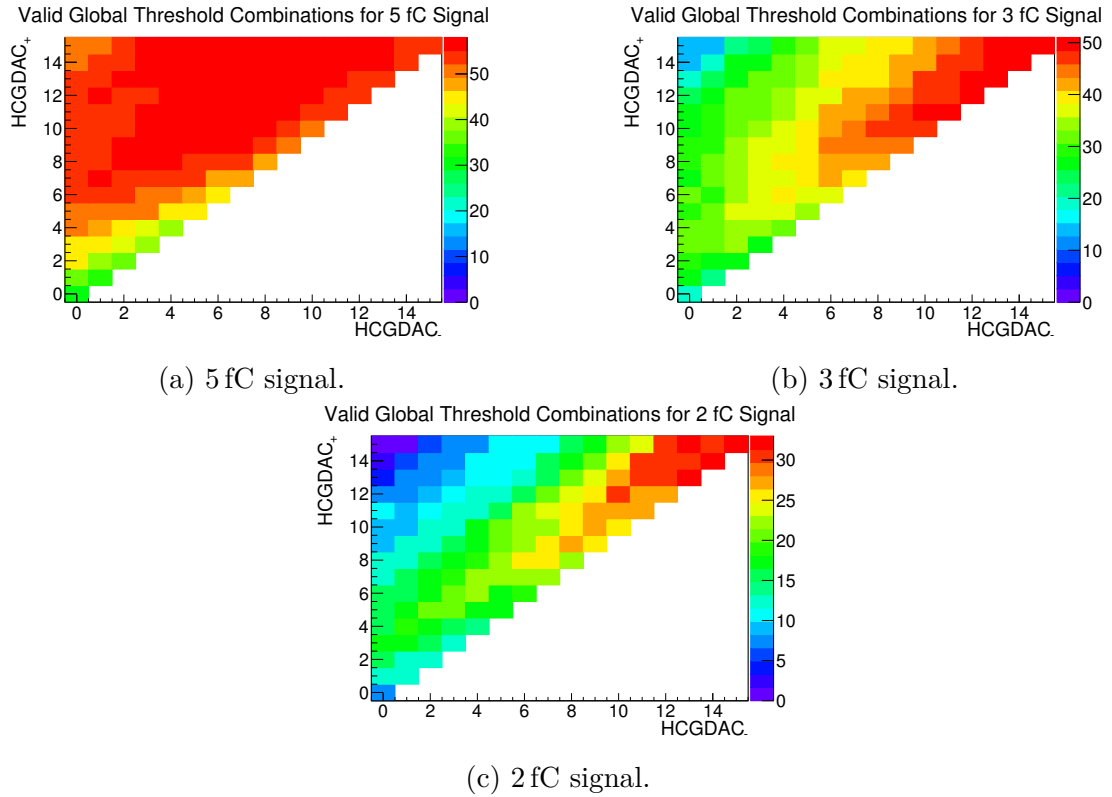
Figure 5.5: Valid combination of the global threshold parameters for signals with different amplitude.

The same procedure is repeated for smaller signals, namely 3 fC and 2 fC, and the outcome of the measurements is shown in Fig. 5.5b and Fig. 5.5c, respectively. By comparing these results with the ones obtained in the case of injection with 5 fC amplitude, one can observe how the smaller the pulse, the more the valid combinations for the majority of the channels are concentrated around high values of each of the two

parameters, i.e., smaller effective threshold. Moreover, for 2 fC signals, the maximum number of entries of the z-axis indicates that a valid pair of settings is shared among only half of the total number of channels, at best. This demonstrates that this input signal is detectable only for very low values of the effective threshold. The response of the chip for the two charges is evaluated for `HCGDAC-` $= 12$ and `HCGDAC+` $= 15$ (Fig. 5.6b and Fig. 5.6c). With the decreasing of the input charge, more and more channels are either completely non-responsive or show only some activity. The drop in efficiency becomes more significant for increasing channel numbers. This could be explained by a malfunction in the power distribution. An attempt to bring more channels into an operating mode is made, by tuning the local threshold parameters. However, the pattern of responsive channels does not change significantly. Considering the smallest signal that the internal circuit can generate, i.e., 1 fC, the situation becomes even more critical. In fact, only a few channels detect the injected charge and they exhibit a very low efficiency. The ASIC is not able to cope with such small signals and therefore no threshold calibration is carried out for this charge.

(a) 5 fC signal.

(b) 3 fC signal.

(c) 2 fC signal.
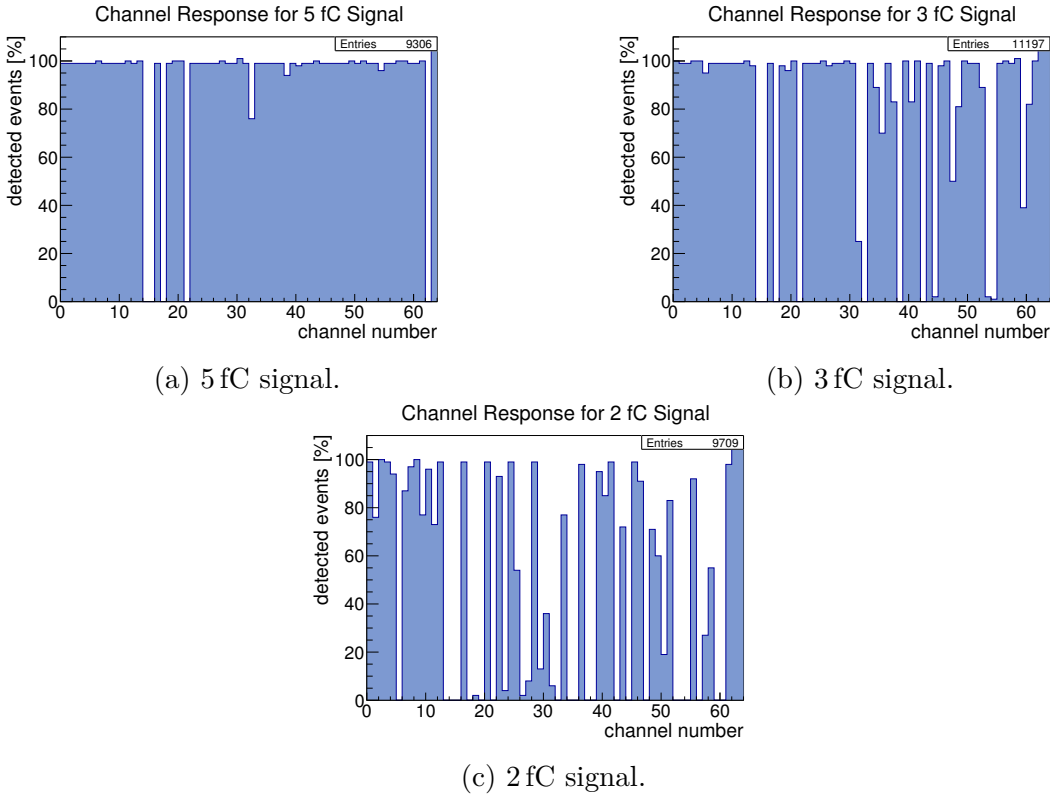
Figure 5.6: Channel response to sequence of internally generated pulses with different amplitudes and optimized global threshold.

5.1.5 Linearity of the Front-End

Within its dynamic input range, PASTA is expected, by design, to exhibit a linear response of the ToT as a function of the deposited charge. To verify this behavior, a pulse amplitude scan is performed in the range from 1 fC to 40 fC, repeating the signal injections for each amplitude and for each channel. Profile histograms are used to display the mean value of the ToT together with his standard deviation for each bin in the signal amplitude. While carrying out this linearity study, it is observed one more time that the channels present different behaviors. Approximately half of the total number of responsive channels exhibits a linear ToT response. The result for a representative working channel is shown in Fig. 5.7. The fit residuals are calculated as the difference between each bin content and the corresponding value of the fit function at the center of the bin, divided by the uncertainty. The ToT response of this channel is considered linear within the working range. An example of a non-linear response is presented as well (Fig. 5.8).
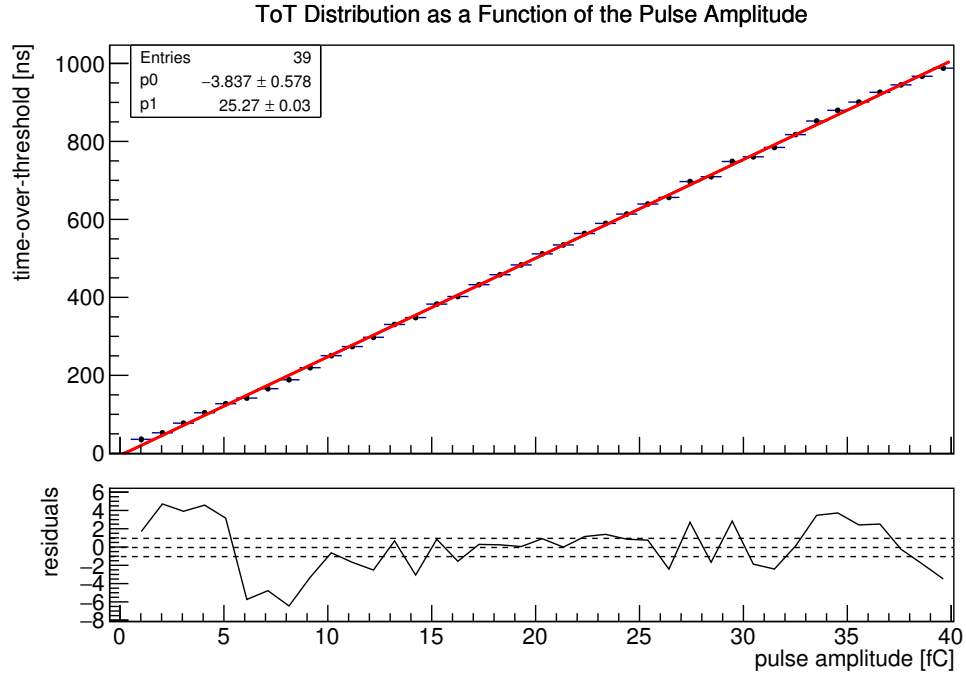
Figure 5.7: ToT distribution as a function of the pulse amplitude in the operating range of PASTA for a representative working channel. The response is linear as expected.
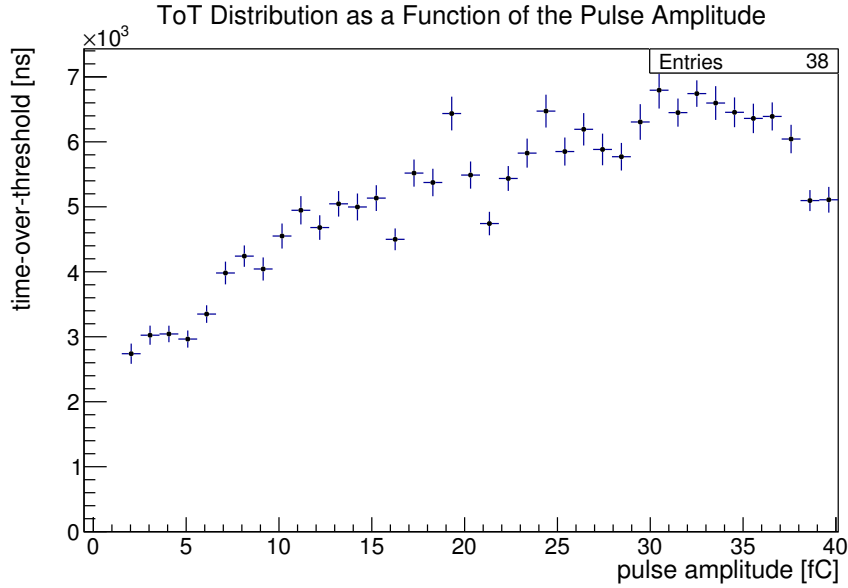
Figure 5.8: ToT distribution as a function of the pulse amplitude in the operating range of PASTA for a representative channel with a non-linear response.

5.2   Measurements Under Proton Beam

Tests using a beam of ionizing particles are important to study the response of the ASIC as well as the performance of the DAQ system. They represent a more realistic environment compared to the internal charge injection of the ASIC.

At the Research Center Jülich, as a part of the Institute for Nuclear Physics, a particle accelerator called Cooler Synchrotron (COSY) provides polarized and unpolarized proton beams in the energy range between 45 MeV and 2.7 GeV and deuteron beams in the range between 90 MeV and 2.1 GeV [103]. The protons are produced starting from a hydrogen ion source. The ions, extracted from plasma by a voltage of about 4000 V, are accelerated in a cyclotron up to 45 MeV and sent through a thin carbon foil to strip their electrons. The produced protons are then circulated in COSY. One lap around COSY has an average duration of 2 μs, while roughly 2 s are necessary to accelerate the particles to the required energy for the experiment. Experiments can be carried out internally, when the targets and detectors are placed inside the COSY ring, or externally, extracting the beam and directing it to the experimental halls located outside of the ring. The particles are delivered according to a spill structure (i.e., for a specified amount of time the particles are sent out and then a pause follows in order to refill the accelerator). The absolute number of protons per spill is not available. The intensity of the beam can be modified by varying the Micropulses (MP) settings. A number of MP equal to 1 corresponds to the maximum number of particles injected into COSY.

5.2.1 Setup

For the test of the strip readout, the setup was installed in the so-called Jessica hall, named after the previous experiment installed there. An existing tracking station was used in combination with the PASTA readout system [104]. It is composed of four planes of silicon strip sensors, read out by APV25 chips [105] and packed into one aluminum case per plane. The relative distance of the planes can be varied along roughly two meters length. At each of the two ends of the tracking planes two scintillators arranged in a cross are placed. The coincidence of these scintillators provides a useful trigger for the readout of the sensors of the four planes. A PASTA board, equipped with a double-sided sensor (but read out only on one side) was placed along the beam line by means of a rotatable holder positioned between the second and third plane of the tracking station. Fig. 5.9 provides a schematic view of the tracking station layout and Fig. 5.10 illustrates the complete setup.
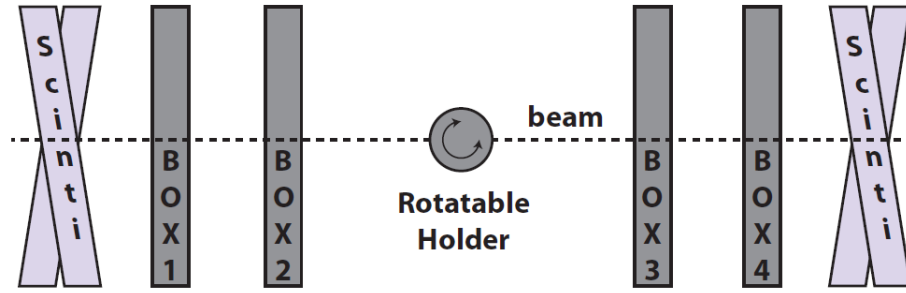
Figure 5.9: Schematic view of the tracking station layout. Image from [104].

The sensor was powered with a bias of 70 V. According to previous studies this value is sufficient to ensure that the sensor is fully depleted [64]. In order to combine the data from the tracking station with the PASTA data, for most measurements the two systems were operated synchronously with a clock frequency of 50 MHz. This value is at the upper limit for the operation of the tracking station and at the lower limit for PASTA. Measurements with PASTA standalone were performed at different frequencies and the value will be specified in the text. Despite the available data from the tracking station, no tracking studies were carried out after the beam test, due to the relatively high number of malfunctioning channels in PASTA. Nevertheless, the presence of the tracking station as a beam telescope was highly beneficial during the measurements for alignment and beam diagnostics.

Protons with two different momenta were used: 800 MeV/c and 2 GeV/c. Protons with a momentum of 800 MeV/c traveling through silicon, lose 3.5 MeV/cm on average (Fig. 5.11). The average deposited charge in the sensor volume, which has a thickness of 285 µm, corresponds to ~ 4 fC. In case of protons with 2 GeV/c momentum, the corresponding average deposited charge is approximately 2 fC.
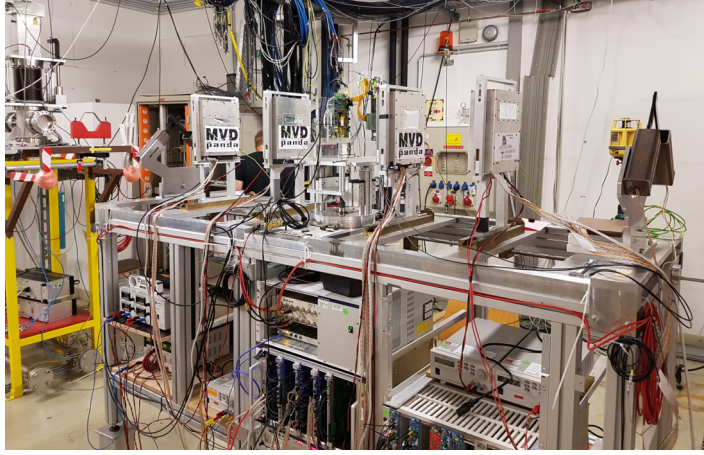
Figure 5.10: Setup prepared in the Jessica hall of COSY for the proton beam test. On the top left, the end of the beam line is visible. In the middle, the four planes of the strip telescope, held on the support structure. Before the first plane and after the last plane the scintillators crosses are placed. The board with PASTA bonded to the sensor and the FPGA are mounted on the movable platform and are positioned between the second and third telescope plane. Power supplies, clock generators and all the remaining electronic modules are stored below. The DAQ PC is located outside the hall.
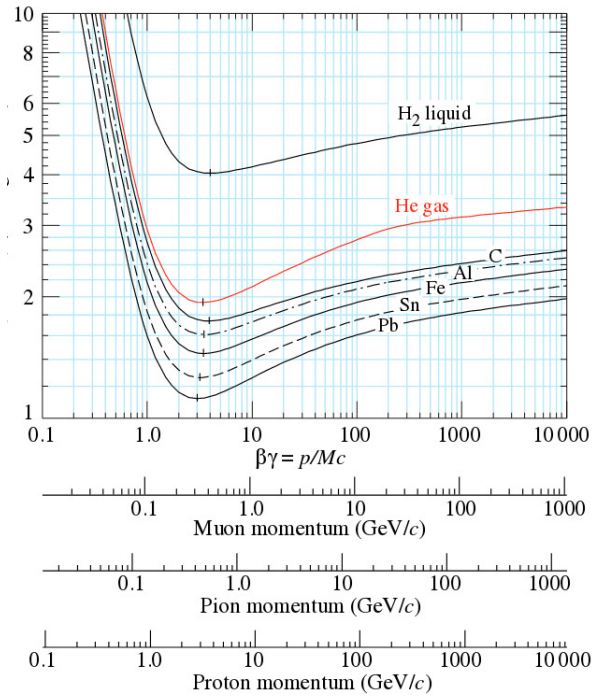
Figure 5.11: Mean energy loss for different particle species in various liquid and solid materials. Silicon, which is relevant for the present study, has a density of $2.3\,\mathrm{g/cm^3}$, which lies between Al $(2.7\,\mathrm{g/cm^3})$ and C $(2.26\,\mathrm{g/cm^3})$. Image from [106].

5.2.2 Threshold Scan

Once a reliable connection between the ASIC and the complete DAQ system was established, the first test that was performed was a threshold scan. As already discussed previously, the optimization of the threshold configuration parameters has proven to be not straightforward already in a controlled environment, where the event rates are rather low. During measurements involving a beam of ionizing particles and higher event rates, it is expected to experience similar problems. The response of PASTA to various threshold settings has been studied. Various combinations of the global threshold parameters have been chosen and for each one of them data was acquired. In order to be able to compare runs relative to different configurations, a normalization is introduced. Since it is reasonable to assume that the number of particles present in a spill is constant, the number of spills per run is used as a scaling factor. The same normalization criterion is applied for all the following studies. Fig. 5.12 collects the results relative to four runs, all sharing the highest possible value of `HCGDAC+`.
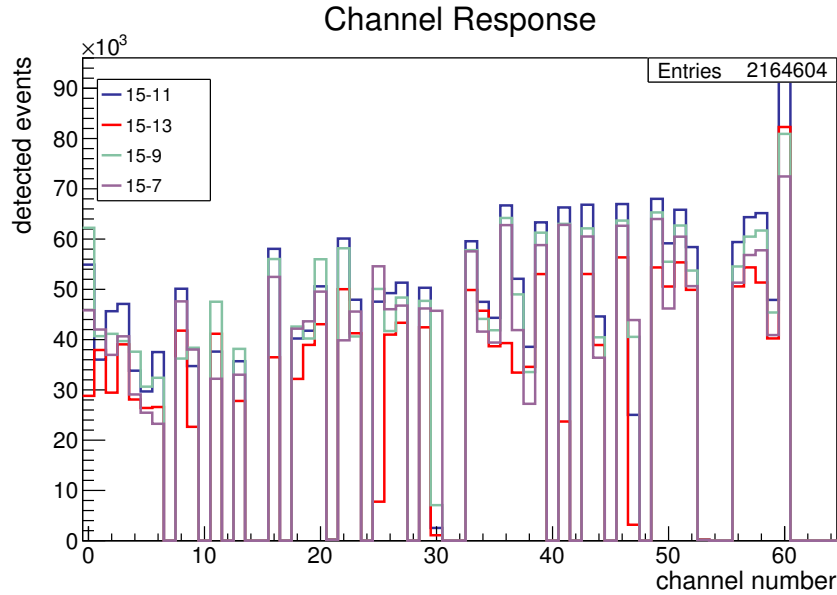
Figure 5.12: Detected events per channel for four different global threshold configurations. The effective threshold is given by the difference between the two individual threshold parameters `HCGDAC+` and `HCGDAC-`.

Out of 64 channels, 20 have been masked (i.e., disabled) due to an elevated noise level. For all four runs, the second half of the ASIC (i.e., from channel 30 onward) presents a higher activity than the first half. This behavior is not expected, assuming that the ASIC is uniformly irradiated by the beam, and it is currently lacking an explanation. A possible cause could lie in a power distribution asymmetry, or an internal readout priority in favor of high channel numbers. However, as of now, these interpretations are

purely speculative. Observing the detected number of events for each individual channel, one would expect to find increasing number of entries for lower threshold settings. Precisely, keeping in mind that the effective threshold value is given by the difference between the two threshold parameters `HCGDAC+` and `HCGDAC-`, the run with the lowest threshold (i.e., the one for which `HCGDAC-` = 13) is expected to exhibit the most detected events. The run with `HCGDAC-` = 11 first, and the one with `HCGDAC-` = 9 then, are expected to show a progressively lower number of entries. Finally, the highest threshold setting (`HCGDAC-` = 7) should detect the smallest number of events. The described trend is not visible in any of the 64 channels. A closer look, however, reveals that if one leaves out the run at the smallest threshold, the foreseen pattern occurs for 26 channels out of 44 active ones. This observation could be explained by considering that the lowest applied threshold might move the effective threshold below the baseline, causing event loss, as described in Section 5.1.4. According to these results, the combination `iHCGDAC+` = 15 - `HCGDAC-` = 13 should be avoided.

The cumulative ToT distribution (i.e., including the contributions of all the active channels) for `HCGDAC+` = 15 and `HCGDAC-` = 9 is shown in Fig. 5.13 with a Landau fit, since this distribution typically follows a Landau curve [106]. In the present case, the measured distribution follows the expected trend, despite the conditions in which the measurements were carried out. In fact, the ToT response requires a calibration, in order to ensure that a given charge corresponds to the same ToT value for all the channels, which was not yet performed at the time of the data taking. Moreover, due to the significant number of inactive or malfunctioning channels, the possible charge sharing among neighboring channels is not taken into account.
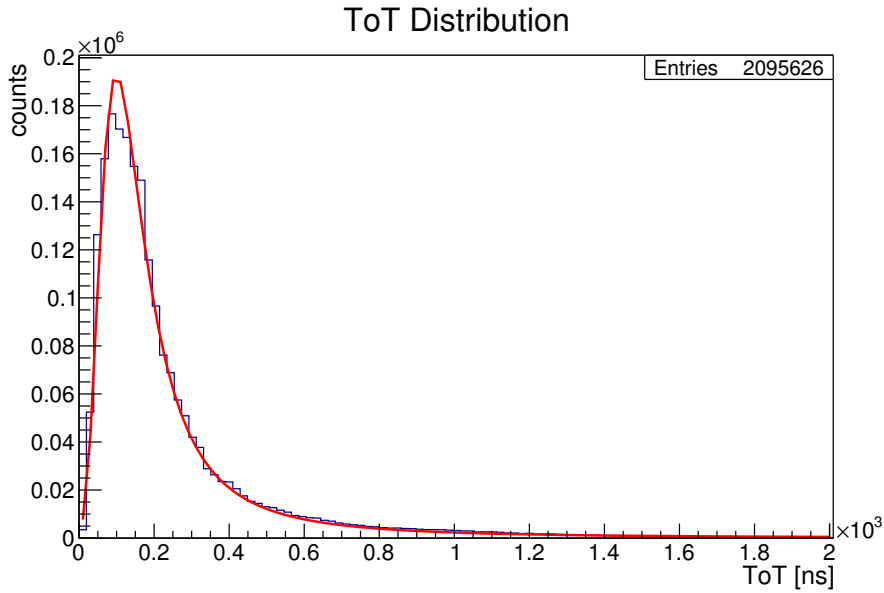

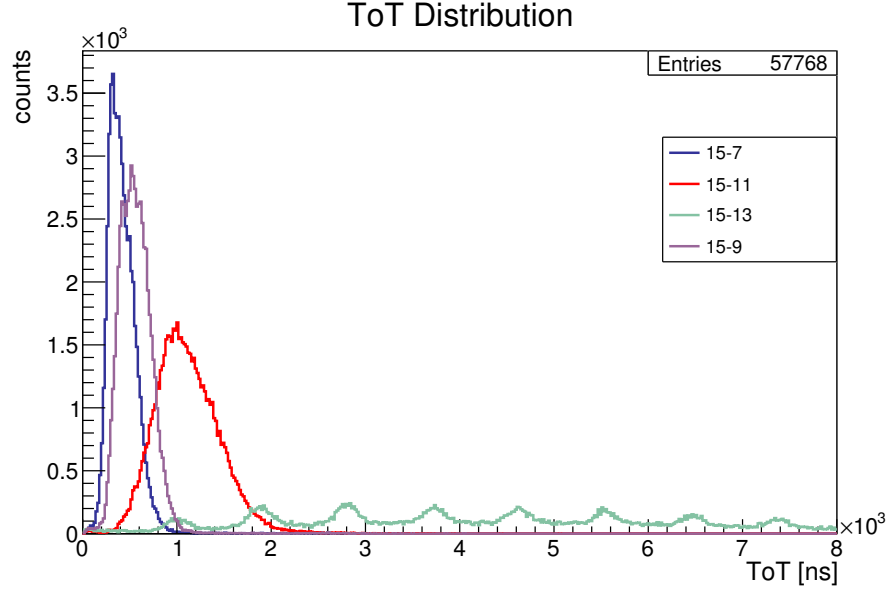Figure 5.13: Cumulative ToT distribution with a Landau fit for a selected threshold.

Figure 5.14: ToT distribution for a single channel for four different global thresholds.

Among the channels that respond to the threshold scan, a representative one is selected to discuss the ToT distribution (Fig. 5.14). The oscillating ToT response relative to the lowest effective threshold, confirms that this combination of parameters is not suitable for a stable operation. Considering the remaining three cases, the smaller the effective threshold, the more the ToT curve becomes wider and its mean shifts towards high values, as one would expect.

5.2.3   Frequency Scan

The response of the ASIC is studied as a function of the operating frequency. The results obtained from four runs with different frequencies, namely 50 MHz, 80 MHz, 100 MHz, and 120 MHz, are presented in a single histogram of the detected events as a function of the channel number in Fig. 5.15. Below channel 35 the runs at 80 MHz, 100 MHz, and 120 MHz show approximately the same number of counts for each channel. This indicates that the method to scale the different runs according to the number of spills per run is correct and that the chip is operational at these frequencies. At 50 MHz the distribution of the number of detected events per channel has a similar shape as for the other runs. However, the number of detected events is only 60 % of the values achieved for the other frequencies. This loss in efficiency was observed during other scans as well, leading to exclude as a possible cause a temporary reduction in the amount of protons per spills of the accelerator. One can observe that the ratio of recorded events in the two cases, namely the 50 MHz and the 80 MHz run, matches with the ratio of the frequency
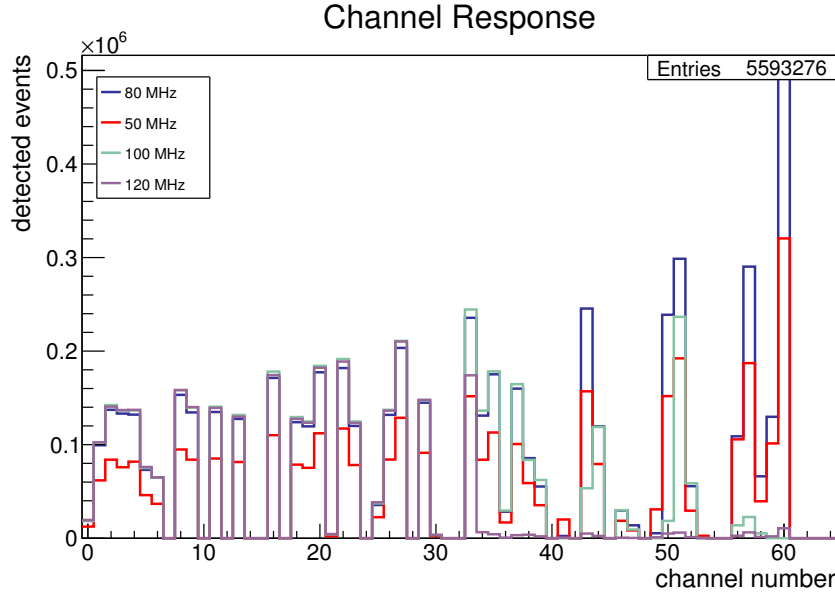
values.

Figure 5.15: Detected events per channel for four different operation frequencies.

Therefore, one plausible explanation could be that the 50 MHz clock frequency is not sufficient to write out all the data, while above 80 MHz all the measured events could be written out. A closer look at the data for 80 MHz, 100 MHz, and 120 MHz reveals that the 80 MHz run has systematically fewer counts than the other two. This could indicate that this frequency is actually slightly below the value needed for correct readout. Above channel 35 the scenario looks different. The number of counts per channel is highest for the 80 MHz run and drops significantly for the run at 100 MHz. At 120 MHz the drop is even more pronounced. Furthermore, the observed reduction is stronger the higher the channel number. This behavior could point towards a problem either in the clock distribution or in the power lines of PASTA. An operation at the nominal frequency of 160 MHz was not possible, due to instabilities in the operation of PASTA, e.g., data corruption. The impossibility to operate the ASIC at its nominal frequency limits the achievable time resolution.

As shown for the threshold scan, for the frequency scan an example of ToT distributions for a representative channel is given as well (Fig. 5.16). The distributions, which present a broad peak, do not match well the Landau shape, as one can see in Fig. 5.17 for a selected frequency. This shape might be caused by the charge loss to neighboring channels due to the missing clusterisation of the deposited energy. For all four runs the number of detected events is comparable, indicating that the detected amplitude does not vary significantly with the frequency as expected, except for the 50 MHz run, as previously observed.
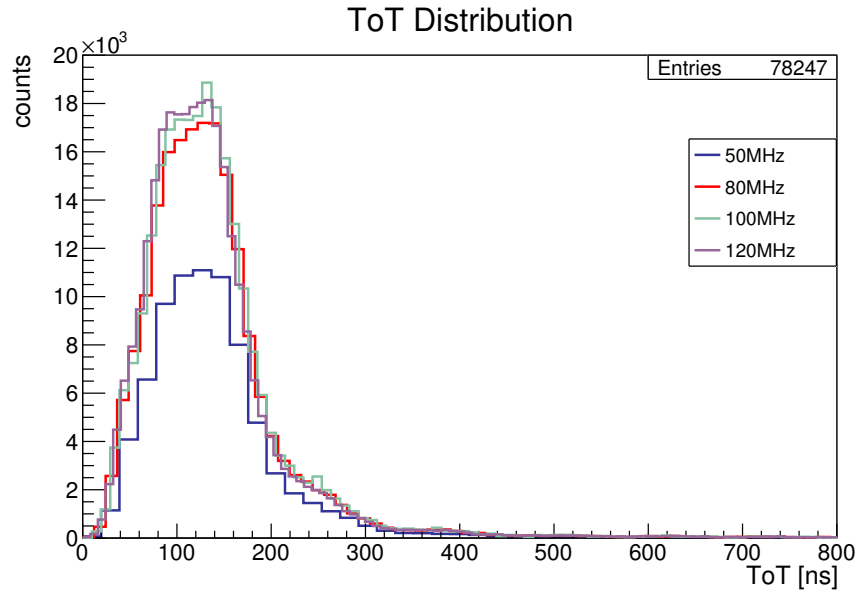
Figure 5.16: ToT distribution for a single channel for four different operation frequencies.
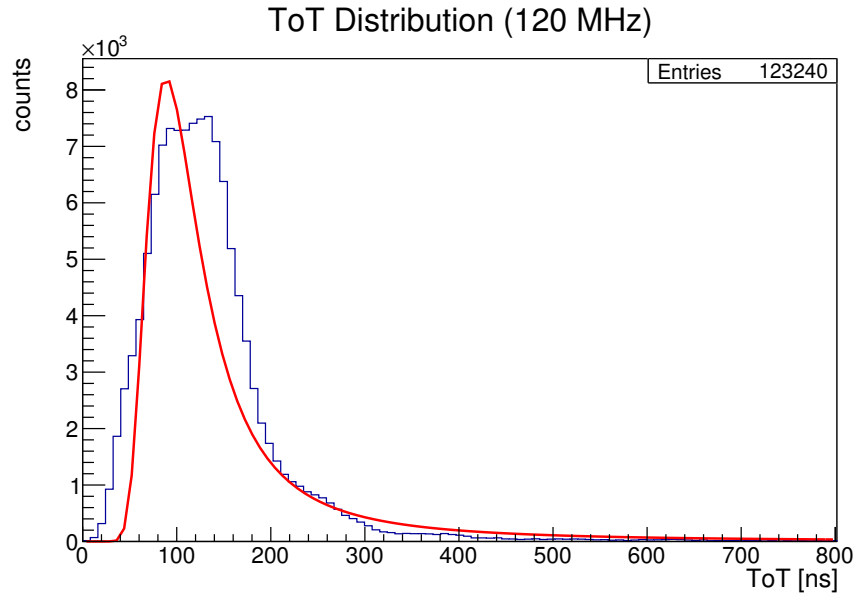

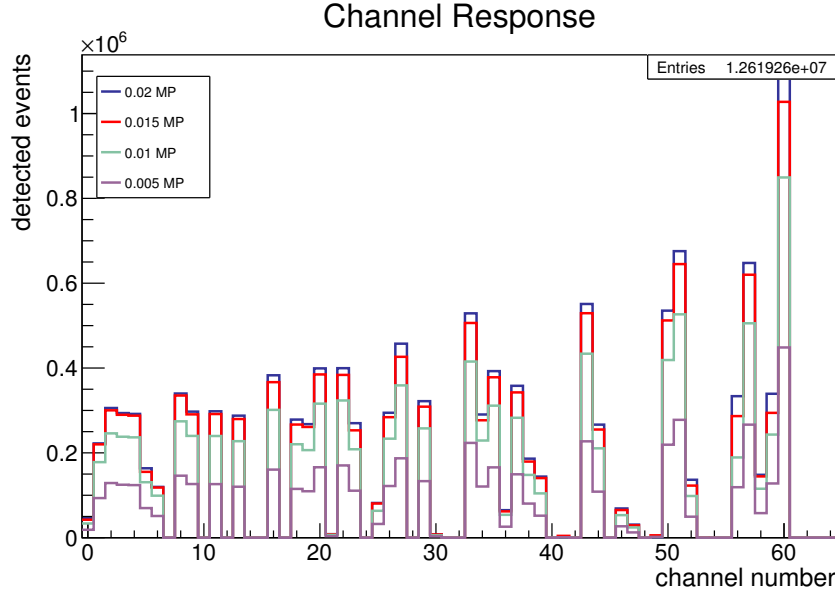Figure 5.17: ToT distribution for a single channel for 120 MHz run with Landau fit.

Figure 5.18: Detected events per channel for four different beam intensities of the proton beam. The intensity is expressed in MP: the bigger the number of MP the more intense the beam.

5.2.4 Beam Intensity Scan

As previously described, the intensity of the proton beam in COSY can be varied by setting the MP value, 1 being the maximum available number of particles per spill. The response of the ASIC is studied as a function of the intensity of the beam with $2\,\mathrm{GeV}/c$ momentum. Fig. 5.18 joins together the results for four runs at different intensities, corresponding to 0.005, 0.01, 0.015, and 0.02 MP. The number of detected events per channel increases with the intensity, as one would expect. The shapes of the four distributions are consistent with each other, indicating that the chip is operating in a stable configuration throughout the whole measurement. The rising profile towards high channel numbers occurs for these runs as well. Since it is not possible to deduce the number of protons per spill from the setting of the MP, one cannot identify event losses.

5.3 Summary and Outlook

The first prototype of the front-end ASIC designed for the strip part of the PANDA MVD is tested to evaluate its performance. The charge generation circuit included in the chip architecture is used, as well as a proton beam. The tests prove that a reliable connection to the ASIC can be established and that the necessary configuration operations and data collection can be performed successfully. The calibration of the

threshold parameters is critical, mostly due to the differential scheme. Significantly different behaviors are observed among the 64 channels. Due to the high number of configurable parameters and their wide variations, it is not possible to find a common operational point which would bring all the channels into proper working conditions. Moreover, it is observed that deposited charges corresponding to the low end of the foreseen working range cannot be detected reliably. At this stage it is not clear whether this aspect is related to the inability to optimize the configuration parameters for such charges, or whether the cause lies in a general malfunction of the chip. A detailed screening of the chip response in this region cannot be carried out due to the too coarse granularity of the internal test pulse signal. The evaluation of the ASIC response to different frequencies reveals some critical issues which might be an indication of problems concerning the clock and/or power distribution inside the ASIC. Moreover, it shows that the operation of PASTA at its nominal frequency of 160 MHz is not possible for the current prototype, and consequently the requirement for the time resolution are not met. Despite these difficulties and a not fully optimized set of configuration parameters, PASTA can be tested under an ionizing particle beam.

The JDRS proves to operate in stable conditions even for long measurement runs and to be able to successfully acquire data during measurements with low event rates, as well as during the measurements under the proton beam. Inexperienced users were able to operate the DAQ without difficulties, thanks to its user-friendly interface. The flexibility and modularity of the JDRS allowed to easily implement modification on the firmware as well as on the software to accommodate various requests that arose during data taking.

The outcome of the described measurements plays an important role in the currently ongoing design of the new version of the front-end strip ASIC prototype. The reported issues are being investigated and modifications to the architecture are under evaluation. In particular, the possibility to reduce the number of tunable parameters is being discussed. Moreover, the logic that implements the enhanced time resolution will be revised, even possibly removed, for its presence is not mandatory for the MVD. The calibration circuit will be also optimized, in order to provide more sensitivity in the low deposited charge region (i.e., 1 fC to 2 fC).

Concerning the JDRS software, some development has started, which aims to the implementation of parallel processing of the incoming data transmitted from PASTA, in order to reduce the risk of data losses at high event rates.

Chapter 6

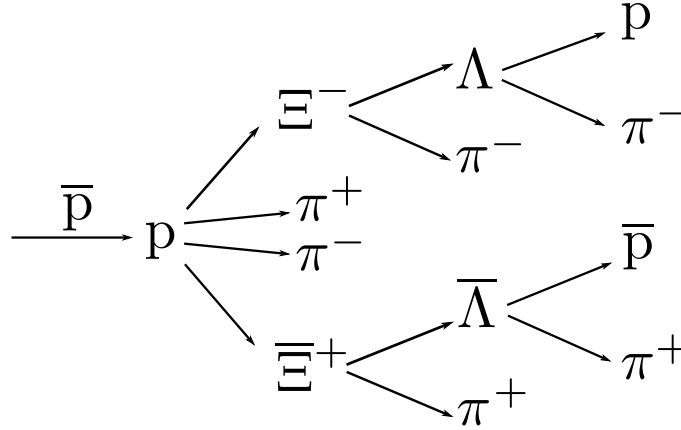# Study of the Reaction $\overline{\mathrm{p}}\mathrm{p} \rightarrow \Xi^{-}\overline{\Xi}^{+}\pi^{+}\pi^{-}$

Figure 6.1: Pictorial representation of the process under study.

This chapter describes a feasibility study of the reaction $\overline{\mathrm{p}}\mathrm{p} \rightarrow \Xi^{-}\overline{\Xi}^{+}\pi^{+}\pi^{-}$ for antiprotons with $4.6\,\mathrm{GeV}/c$ momentum, carried out with the PandaRoot framework [107]. The continuum case is studied, as well as all the known decay branches involving the production of Ξ resonances. This study foresees the development of an algorithm which should be able to reconstruct the events according to the decay tree in Fig. 6.1, including the reconstruction of Ξ resonances. The quality of the analysis procedure is measured in terms of reconstruction efficiencies for the single particles involved in the decay tree as well as for the complete decay tree. Furthermore, spatial, momentum and invariant mass resolutions are measured. The signal-to-background ratio and the significance are calculated as additional figures of merit. Based on the obtained results, an estimate of the expected event rate during data taking is provided.

Two independent samples are analyzed in this study: one contains selected $\bar{p}p \to \Xi^- \bar{\Xi}^+ \pi^+ \pi^-$ events (in the following referred as *signal*) and another one contains $\bar{p}p$ collision events, without any preferred channel (*background*). The reconstruction algorithm proceeds backwards, starting from the final state stable particles, combining them into intermediate particles, and combining them further into the initial $\bar{p}p$ system. For this study, pions are considered stable particles, since their decay length is of $\mathcal{O}\,(m)$. The information coming from the Monte Carlo (MC) simulation is exploited to assess and optimize the quality of the analysis procedure. The concept of *Monte Carlo match* is used as well in order to correlate the reconstructed particles with the MC input. Wrongly reconstructed particles do not have a MC partner.

In the following, the analysis strategy is presented, illustrating the results at each step of the reconstruction for both signal and background sample. The two final state pions with opposite charge are emitted from the primary vertex of the interaction and will be therefore referred to as *prompt*. The adopted coordinate system is right handed. It assumes the z-coordinate to be along the beam direction and the y-coordinate to point upwards in the vertical direction.

6.1 Physics Motivation

As discussed in Section 1.2.5, the quark model predicts a substantial number of light baryons which have not been observed so far (missing resonances). Although LQCD has recently made substantial progresses, up to now there is no unique model that can explain the measured baryon spectra. Therefore, experimental inputs are required to find and validate models to describe baryon excitations accurately. Up to now, studies on the baryon spectra have been focused on nucleon and Δ excitation spectra by means of photo-induced reactions. Experimental data on spectroscopy in the sector of baryons with double and triple strangeness content (e.g., Ξ and Ω, respectively) are rather poor. Very little is known about Ξ resonances and the available information comes almost entirely from bubble chamber experiments. This is mostly due to the fact that [106]:

- Ξ resonances can only be produced in often topologically complicated reactions, leading to more complex analysis with respect to the case of direct formation
- the production cross sections are typically small (i.e., few µb)

Since the Particle Data Group (PDG) edition of 1988, nothing significant on the Ξ resonances has been added. According to [106], as of now the experimental status of the Ξ resonances indicates that the existence of only a few states is confirmed and their properties are well established. Among the other states, some are considered very likely to exist, although further investigation is needed in order to determine properties such as quantum numbers and branching fractions, or the evidence of their existence is poor. (Table 6.1)

Table 6.1: Status of the Ξ resonances. Stars indicate the evidence of existence: from certain (****) to poor (*). Table from [106].

Particle	J^P	Overall Status
Ξ (1318)	1/2+	****
Ξ (1530)	3/2+	****
Ξ (1620)		*
Ξ (1690)		***
Ξ (1820)	3/2-	***
Ξ (1950)		***
Ξ (2030)		***
Ξ (2120)		*
Ξ (2250)		**
Ξ (2370)		**
Ξ (2500)		*

Antiproton-proton collisions are an ideal entrance channel to study excited baryons. In fact, a significant fraction of the cross section involves baryons and antibaryons, plus additional mesons, in the final states. The total cross section for the process $\overline{p}p \rightarrow \Xi^- \overline{\Xi}^+$ has been measured to be $(2 \pm 1)\,\mu b$ for $\overline{p}$ with a momentum of $3\,\text{GeV}/c$ [108]. With the HESR operated in high luminosity mode, roughly a million $\Xi^- \overline{\Xi}^+$ pairs will be produced per day, leading to abundant statistics within relatively short measuring times. The PANDA experiment aims to perform, among others, a comprehensive Ξ spectroscopy program in order to:

- confirm established states and search for missing ones
- study decay modes of specific states and determine their branching fractions
- determine the quantum numbers of the observed states.

6.2 Monte Carlo Simulation

6.2.1 PandaRoot Framework for Simulation

The simulation of the events and the analysis are performed within the PandaRoot framework. The first step of the simulation is the generation of the events according to a user defined input. For this step the EvtGen package is used [109]. After the generation follows the propagation of the particles through detector volumes, which are specified in geometry description files. This step keeps into account not only the effects of the material, but also of the magnetic fields and it is handled by GEANT4 [110]. Once the particles have been propagated through the detector volumes, digitization

of the data is performed in order to include all detector effects, such as segmentation, electronic emulation, noise, and timing. After digitization, the data has the same format that would appear in the real experiment. At this stage, the reconstruction of the tracks takes place. The so-called realistic reconstruction algorithm assumes that the tracks originate from the interaction point, but this assumption does not apply to the daughter particles of hyperons involved in this analysis, due to their relatively long lifetime ($c\tau_\Lambda = 7.89$ cm and $c\tau_\Xi = 4.91$ cm [106]). Consequently, ideal algorithms which exploit MC information are employed for tracking in this study. The ideal assumption leads to unrealistic high efficiencies for the reconstruction of tracks which have not left a sufficient number of hits in the detectors and, therefore, would not be reconstructable in the real experiment. Finally, the particle's type is determined by combining information coming from various subdetectors (e.g., energy loss, Cherenkov angles) and comparing this input with expected values generated from γ, e, μ, K, p, and their antiparticles. A probability for each possible identity is assigned to each candidate. In the present case, the particle identification selection is based on a non-realistic approach. The probability for the particle identification is equal to unity for the MC true species and equal to zero for all other species.

6.2.2 Input Parameters

The momentum of the antiproton beam is chosen to be $4.6\,\text{GeV}/c$, corresponding to $\sqrt{s} = 3.25\,\text{GeV}$. This value is roughly $300\,\text{MeV}$ above the threshold for the production of the two Ξ and two π, in order to allow for the population of the resonant states. A decay file, used as an input for the generation of the events, specifies the decay modes that are allowed by the kinematics (Table 6.2). Each mode is assumed to have a uniform phase space distribution, since no information is available in the literature about the angular distributions for the reaction under study. Moreover, this assumption guarantees that both baryons and antibaryons are subjected to the same detector acceptance, thus facilitating the interpretation of any differences in their reconstruction. Each resonant state is also assumed to decay isotropically. The propagation of the two cascades, and therefore their decay, is handled by GEANT4, in order to account for their interaction with the detector volume and the curvature of their trajectories in the solenoidal magnetic field. Ξ^- and $\bar{\Xi}^+$ have a branching ratio of 99.89 % into $\Lambda\pi$ [106]. Λ and $\bar{\Lambda}$ instead, have several decay modes with significant branching ratios. For the present study, it is interesting to observe the process $\Lambda \to \text{p}\pi$, which has a branching ratio of 63.9 %. To avoid the generation of other states, this mode is defined as the only possible for Λ and $\bar{\Lambda}$. The final result is scaled accordingly by the branching ratios. The masses and widths of the resonant states are defined according to [106] as indicated in Table 6.3.

Table 6.2: Decay branches implemented in the simulation of the signal events. *c.c.* stands for charge conjugate.

$\overline{\mathrm{p}}\mathrm{p} \rightarrow$			$\rightarrow \overline{\Xi}^+\Xi^-\pi^+\pi^-$
$\overline{\mathrm{p}}\mathrm{p} \rightarrow$	$\Xi^-(1690)^*\overline{\Xi}^+$	$(+\ \mathrm{c.c.})$	$\rightarrow \overline{\Xi}^+\Xi^-\pi^+\pi^-$
$\overline{\mathrm{p}}\mathrm{p} \rightarrow$	$\Xi^-(1820)^*\overline{\Xi}^+$	$(+\ \mathrm{c.c.})$	$\rightarrow \overline{\Xi}^+\Xi^-\pi^+\pi^-$
$\overline{\mathrm{p}}\mathrm{p} \rightarrow$	$\Xi^0(1530)^*\overline{\Xi}^+\pi^-$	$(+\ \mathrm{c.c.})$	$\rightarrow \overline{\Xi}^+\Xi^-\pi^+\pi^-$
$\overline{\mathrm{p}}\mathrm{p} \rightarrow$	$\Xi^0(1690)^*\overline{\Xi}^+\pi^-$	$(+\ \mathrm{c.c.})$	$\rightarrow \overline{\Xi}^+\Xi^-\pi^+\pi^-$
$\overline{\mathrm{p}}\mathrm{p} \rightarrow$	$\overline{\Xi}^0(1530)^*\Xi^0(1530)^*$		$\rightarrow \overline{\Xi}^+\Xi^-\pi^+\pi^-$
$\overline{\mathrm{p}}\mathrm{p} \rightarrow$	$\overline{\Xi}^0(1530)^*\Xi^0(1690)^*$		$\rightarrow \overline{\Xi}^+\Xi^-\pi^+\pi^-$
$\overline{\mathrm{p}}\mathrm{p} \rightarrow$	$\overline{\Xi}^0(1690)^*\Xi^0(1530)^*$		$\rightarrow \overline{\Xi}^+\Xi^-\pi^+\pi^-$

Table 6.3: Ξ resonances: masses and widths defined for the simulation.

State	Mass [MeV/c^2]	Γ [MeV]
$\Xi(1530)^*$	1532	9.1
$\Xi(1690)^*$	1690	30
$\Xi(1820)^*$	1823	24

6.3 Analysis of the Data Sample

A data sample of 3,816,000 signal events has been generated. The analysis algorithm takes as input the final state particle candidates that have been reconstructed and identified by the detector (i.e., p, $\overline{\mathrm{p}}$, π^+, and π^- after the tracking and PID routines). Starting from these particles, the aim is to reconstruct the signal events according to the decay tree in Fig. 6.1 up to the $\overline{\mathrm{p}}\mathrm{p}$ system.

6.3.1 Track Filtering

The first step in the analysis is the track filtering. As mentioned in Section 6.2.1, the use of an ideal tracking algorithm leads to the reconstruction of particles that would not be possible in the experiment, due to a too low hit multiplicity in the detector. To compensate for this unrealistic efficiency, each track is required to have at least 4 hits in one of the central tracking subdetectors (i.e., MVD, STT, GEM). Otherwise, it would be rejected. This criterion to select reconstructable tracks, which should be considered as a lower limit, is motivated by the trajectories of charged particles in magnetic fields. As a first approximation, neglecting multiple scattering effects and energy loss, one can consider such trajectories as helices in the solenoidal magnetic field. The projection on

the transverse plane to the beam would result in series of circles. In principle, three points are sufficient to define a circle, but considering all the possible combinations of three hits in the detector would lead to a huge number of fake candidates. Therefore, an additional hit is requested in order to suppress ghost tracks.
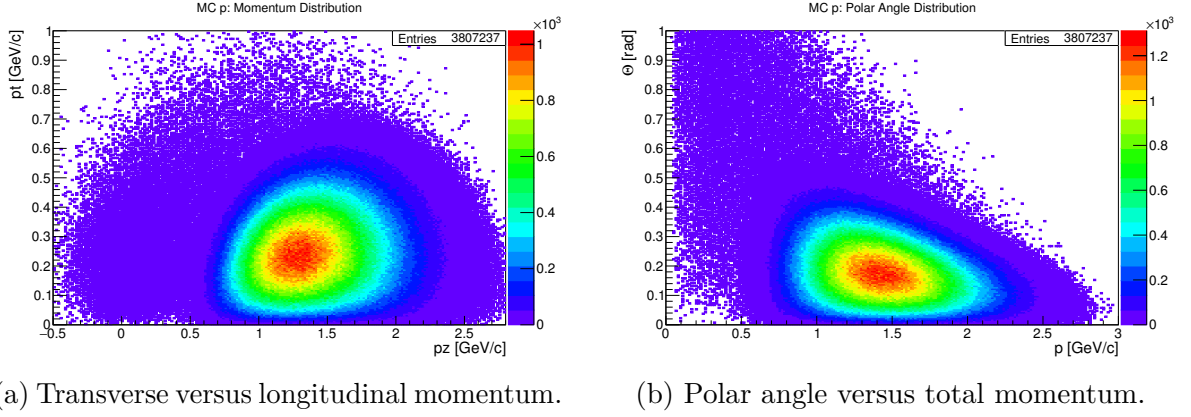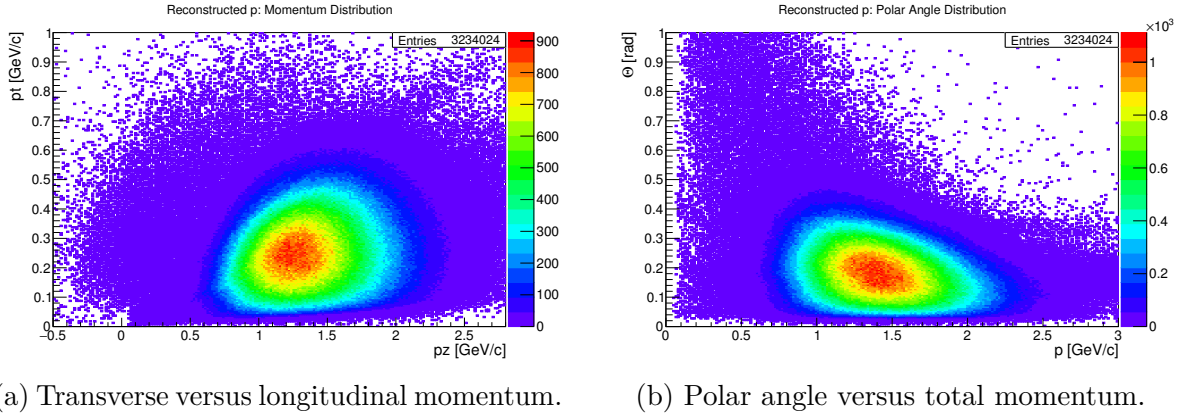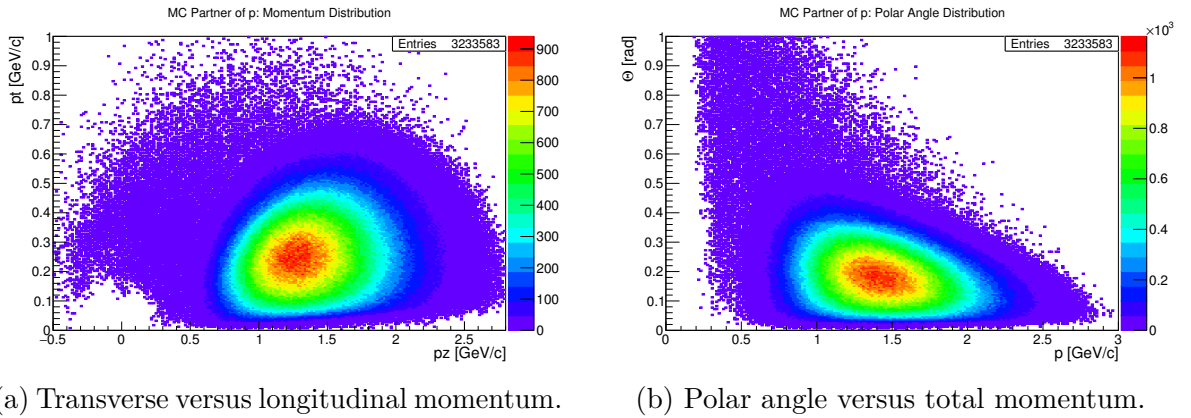
6.3.2   Reconstruction of the Final State Particles

After the track filtering, four lists of particles are generated, one for each final state particle species (i.e., p, $\bar{\mathrm{p}}$, π^+, π^-), according to the particle identification algorithm. To identify among these particles the ones that belong to the signal under study, the genealogy information provided by the MC data is exploited. As an example, signal protons are selected requesting that the mother particle is a Λ and the grandmother particle is a Ξ^- coming from the primary interaction point. By using this selection criteria, it is ensured that the continuum decay branch as well as all the branches involving excited Ξ resonances are kept into account.
Due to the relative large number of final state particles, only a selection of the histograms is presented in this chapter. However, the remaining plots corresponding to the other particles, are collected in Appendix A.1 for completeness.

Angular and Momentum Distributions

Two-dimensional histograms of transverse versus longitudinal momentum and polar angle versus absolute momentum are generated for each of the final state particle species. The MC spectra show the generated kinematics and are used as a comparison to estimate the quality of the reconstruction routines. As an example, the results relative to the protons daughters of Λ are shown. Fig. 6.2 and Fig. 6.3 show the MC generated and reconstructed protons coming from Λ decay, respectively. Moreover, the MC partners of the reconstructed protons are shown (Fig. 6.4). One can observe that the longitudinal component of the proton momentum is mostly concentrated between $0.6\,\mathrm{GeV}/c$ and $2.4\,\mathrm{GeV}/c$, with a peak between $1.1\,\mathrm{GeV}/c$ and $1.6\,\mathrm{GeV}/c$, while the transverse component is concentrated mostly between $0\,\mathrm{GeV}/c$ and $0.6\,\mathrm{GeV}/c$. The pions have an average lower momentum (see for example Fig. A.8a). The peak value in the beam direction is between $0.1\,\mathrm{GeV}/c$ and $0.3\,\mathrm{GeV}/c$. The MC generated distributions are expected to have sharp borders, due to the kinematics of the reaction, and no events are expected outside of this region. Nevertheless, for all the final state particle species, except for the prompt pions, several events appear outside this expected region. A detailed study on these events reveals that, despite the fact that their genealogy matches the signal one, they are not signal events. For example, in several cases, intermediate particles like the Λ, interact with detector or support material causing the emission of neutral particles before their decay. To remove these non-relevant entries from the spectra, a more stringent selection can be performed.

(a) Transverse versus longitudinal momentum.

(b) Polar angle versus total momentum.

Figure 6.2: MC protons coming from Λ decay.

(a) Transverse versus longitudinal momentum.

(b) Polar angle versus total momentum.

Figure 6.3: Reconstructed protons coming from Λ decay.

(a) Transverse versus longitudinal momentum.

(b) Polar angle versus total momentum.

Figure 6.4: MC partners of reconstructed protons coming from Λ decay.

(a) Transverse versus longitudinal momentum.   (b) Polar angle versus total momentum.
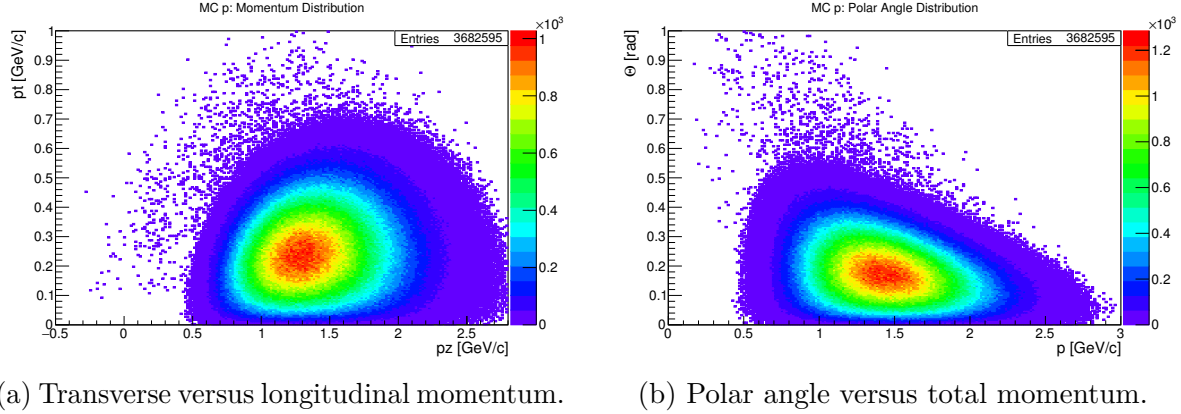
Figure 6.5: MC protons coming from Λ decay with more stringent selection criteria, as explained in the text.

For example, one can include only events that result in the production of two particles, namely the daughter of each composite particle (Λ and Ξ). In this way, the events involving the creation of one or more recoil particles are rejected. This selection is illustrated in Fig. 6.5. One can see that the number of points outside the kinematically allowed region is significantly reduced. The number of entries in these MC histograms differs from the number of originally generated events by 3 %. The loss is due to the track filter, described in Section 6.3.1, applied to discard particles that cause a too low hit multiplicity in the detector. The spectra of the reconstructed events do not differ significantly in shape from the MC ones. Only in case of low momentum particles some discrepancies can be seen, mostly due to worse tracking performances.

Momentum Resolution

The momentum resolution is studied for all species of final state particles. The measured quantity is

$$\frac{\Delta p}{p} = \frac{p - p^{\mathrm{MC}}}{p^{\mathrm{MC}}}$$

where the reconstructed and MC momenta are used. For this observable to be measured, the reconstructed particles are requested to be MC matched. To estimate the resolution, a double Gaussian fit is performed on the distribution and the σ from the inner Gaussian is taken. The error on the measurement is dominated by the systematic contribution, which is estimated, by varying the fit parameters, to be on the second decimal digit. The same procedure for the error estimation is followed throughout this study, when the resolution is determined with a double Gaussian fit. The distribution for the signal protons is shown in Fig. 6.6a. The best momentum resolution is achieved for the π daughter of a Ξ (Fig. 6.6b and Fig. A.30).

(a) Protons.

(b) π^- coming from Ξ^- decay.
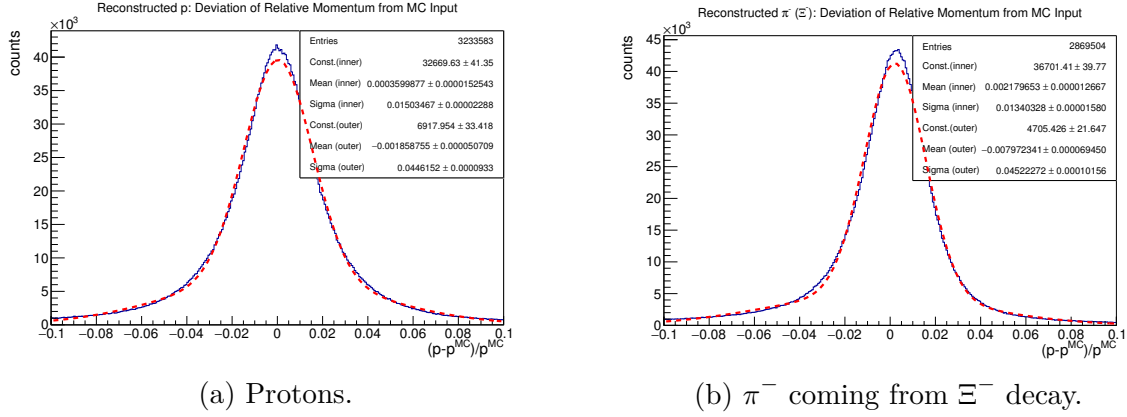
Figure 6.6: Relative deviation of the reconstructed momentum from the MC value of final state stable particles with a double Gaussian fit.

The measured momentum resolution for each of the final state particles are summarized in Table 6.4.

To study systematic effects of the momentum reconstruction depending on the total momentum, the relative momentum difference is also plotted as a function of the absolute momentum, using a profile plot. Each entry in the histogram corresponds to the mean value of the relative momentum together with the RMS for each bin in the total momentum. A pronounced drop towards low momenta can be observed especially for p and $\overline{\text{p}}$ (Fig. 6.7a and Fig. A.6). This indicates that the reconstructed momenta are smaller than the input value. It is likely that this observed behavior is related to how the passage of the particles through matter is handled by the Kalman filter of the GENFIT package in the track reconstruction phase [111]. Since this filter is applied before any particle identification algorithm, it requires an hypothesis on the identity of the particle in order to reconstruct its track. By default, each particle is identified as a pion. In this kinematic region, for a given momentum, the more massive the particle, the higher the deposited energy in the material. Therefore, in case of particles like protons, which are significantly heavier than pions, the Kalman filter estimations are imprecise. The plots of the pions show a better matching, with respect to the protons case, due to their lower mass (Fig. 6.7b). Similar observations have been made also in other studies [52]. The distribution of the proton relative momentum resolution, extracted from the error bars in the profile plot, as a function of the total momentum is illustrated in Fig. 6.8a. One can distinguish three regions in this distribution: the first one extends from the smallest momenta up to roughly $0.6\,\text{GeV}/c$ and it shows the worse measured resolution. This is mostly caused by the higher probability of scattering for low momentum particles. Proceeding towards intermediate values of the total momentum, between $0.6\,\text{GeV}/c$ and $2.2\,\text{GeV}/c$, the distribution presents a flat profile, indicating the range of momenta that can be reconstructed most precisely.

(a) Protons.

(b) π^- coming from Ξ^- decay.
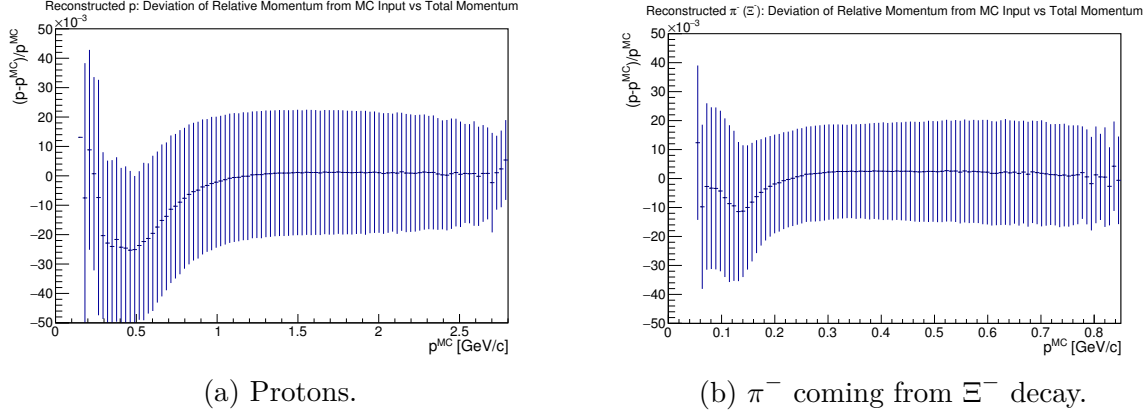
Figure 6.7: Relative deviation of the reconstructed momentum from the MC value as a function of the total momentum.

The corresponding values of the resolution range between 2.0 % and 2.5 %. For momenta above this region, the resolution appears to become better. However, this should not be interpreted as an improved resolution, but rather an effect of the poor statistics for these momenta. In the case of signal pions (e.g., Fig. 6.8b), the rising profile indicating a worse resolution for small momentum particles is present as well. The flat region extends from momenta of 0.2 GeV/c up to 0.7 GeV/c. The corresponding resolution, which varies between 1.5 % and 2.0 %, is better than in the protons case. The comparison between Fig. 6.5a and Fig. A.25a shows that the protons have, on average, higher longitudinal momentum than the pions. Due to the boost in the beam direction, resulting in small polar angles, and to the geometry of the PANDA detector, the resolution in this direction is worse than in the transverse one. Therefore, it is expected that the pions have better resolution than the protons.

The reconstruction efficiency for the final state particles is summarized in Table 6.4 together with the purity of the sample. The efficiency is defined as the fraction of generated particles that is correctly reconstructed, while the purity indicates the number of particles which are correctly reconstructed (i.e., they are MC matched). The highest efficiency is achieved for the prompt pions, mostly due to the fact that they originate from the primary vertex. The smallest efficiency is found for the daughter pions from the Λ. Since the track reconstruction has poorer performance for particles with displaced vertices, like the Λ, this result is not surprising. The protons, also daughters of the Λ, can be reconstructed with slightly higher efficiency. Their average momentum, which is higher than the pions, allows them to travel in the forward direction, enhancing the probability for them to leave hits in the tracking detectors and be reconstructed. This difference between protons and pions coming from the Λ decay can also be understood observing Fig. 6.9, which shows the angular distribution of the MC particles: the protons are emitted on average with a smaller polar angle and therefore are more forward peaked than the pions.

(a) Protons.

(b) π^- coming from Ξ^- decay.
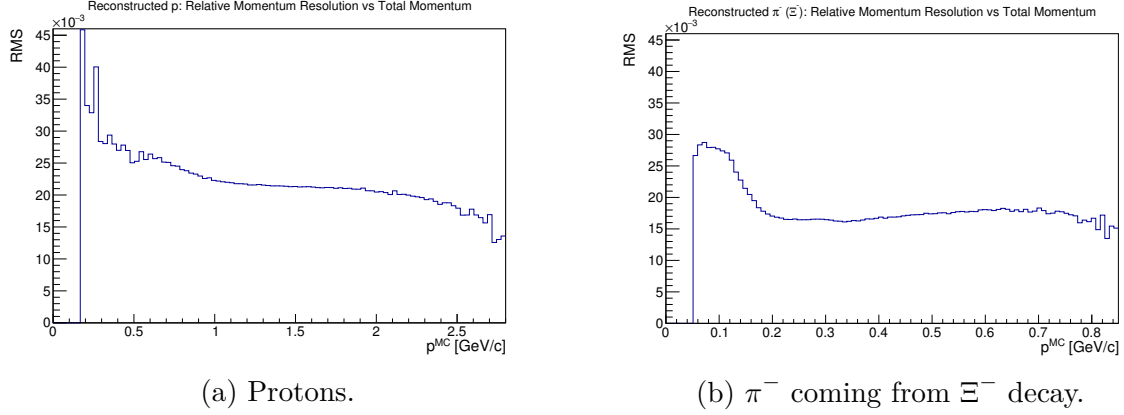
Figure 6.8: Dependence of the relative momentum resolution on the total momentum.

(a) MC p daughters of Λ.

(b) MC π daughters of Λ.
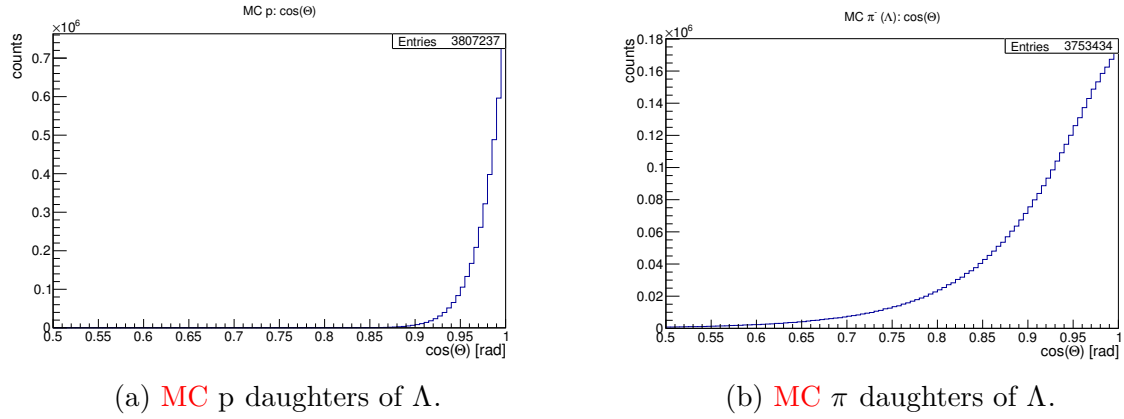
Figure 6.9: Polar angle distribution for MC input.

Table 6.4: Reconstruction efficiency, purity and momentum resolution for the stable final state particles.

	ϵ_{reco} [%]	purity [%]	σ_p/p [%]
p	85	$\simeq 100$	1.50
$\overline{\text{p}}$	82	$\simeq 100$	1.50
π^- (Λ)	70	$\simeq 100$	1.47
π^+ ($\overline{\Lambda}$)	70	$\simeq 100$	1.47
π^- (Ξ^-)	75	$\simeq 100$	1.34
π^+ ($\overline{\Xi}^+$)	75	$\simeq 100$	1.34
π^- prompt	94	$\simeq 100$	1.36
π^+ prompt	94	$\simeq 100$	1.36

For an event to be reconstructable by the analysis algorithm, the minimum requirement is that, after the track filtering, at least one p, one $\bar{\mathrm{p}}$, three π^-, and three π^+ are present in the lists, i.e., in total 8 charged tracks. By looking at the MC events, one finds out that this condition is fulfilled for 14 % of the generated events. This value has therefore to be considered as the upper limit for the reconstruction efficiency of the complete decay channel under study, assuming the ideal case in which every MC event could be correctly reconstructed by the analysis algorithm. Under the assumption that no correlation exists among the reconstruction of the different species, an estimate of the probability to find all the final state particles within one event can also be given multiplying the single final state particle efficiencies. The calculated number is 17 %, thus suggesting the existence of a negative correlation among the reconstruction of the different species.

6.3.3   Reconstruction of the Prompt Dipion System

As already mentioned, the analysis algorithm aims to study the chosen decay channel starting from the final state stable particles. Combining them appropriately, one can reconstruct the intermediate states Λ and $\bar{\Lambda}$. Then combining further, following the decay tree in Fig. 6.1, one reconstructs Ξ^- and $\bar{\Xi}^+$. Finally, including the prompt pions, the original $\bar{\mathrm{p}}$p system is reconstructed. Since there are multiple pions in the final state that can, in principle, be used to form intermediate states, it is useful to reduce the number of possible combinations by identifying which pions are directly coming from the primary vertex and therefore are not related to Λ or Ξ decays. In order to select two pions that originated from a common point, a vertex fit is performed on all the possible $\pi^+\pi^-$ pairs. The fitting class `RhoKinVtxFit` of PandaRoot is used for this purpose. The algorithm applies minimal variations to the tracks of the given particles in order to find a common origin for them. The quality of the fit for each combination is given by the χ^2 and the probability. The distributions of these two quantities for the reconstructed prompt dipion system are shown in Fig. 6.10. The entries with a probability value smaller than 1×10^{-4} are likely to be fake and therefore rejected. This probability threshold has to be considered as a coarse and not optimized cut. In fact, a more stringent selection can be applied in a later stage of the reconstruction of the decay tree, if needed. The candidate pair with the smallest value of χ^2 is labeled as the best, meaning the one that will be used to reconstruct the full event. The reconstructed vertex position distribution is shown in Fig. 6.11 for the three coordinates. By considering only the MC matched candidates, one can estimate the spatial resolution on the vertex position with the Full Width at Half Maximum (FWHM) of the distribution. The error on the measurement is estimated by varying the binning of the histograms. The same approach is used throughout the analysis whenever the FWHM is used. Since the MC prompt pions are produced at the primary vertex, which has coordinates (0, 0, 0), no subtraction of the input value is needed.

(a) χ^2 distribution.

(b) Probability distribution.
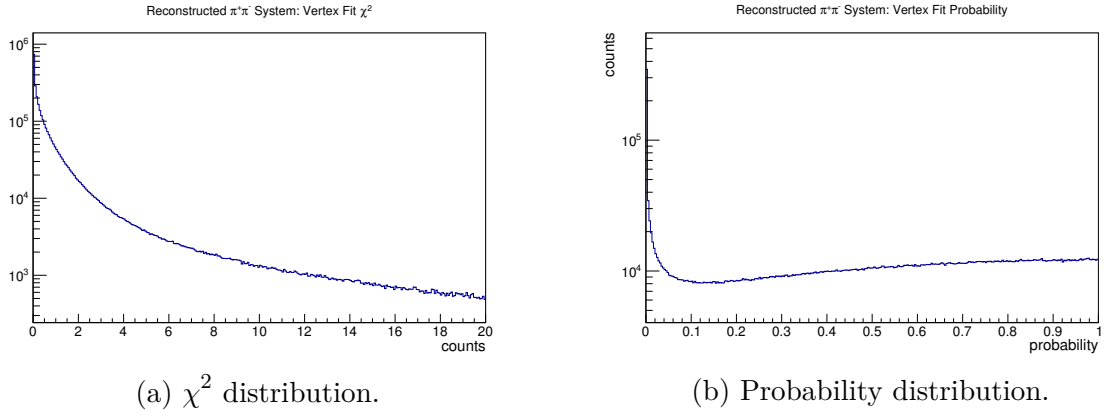
Figure 6.10: Quality of the vertex fit on the prompt $\pi^+\pi^-$ pairs.

(a) x-coordinate

(b) y-coordinate
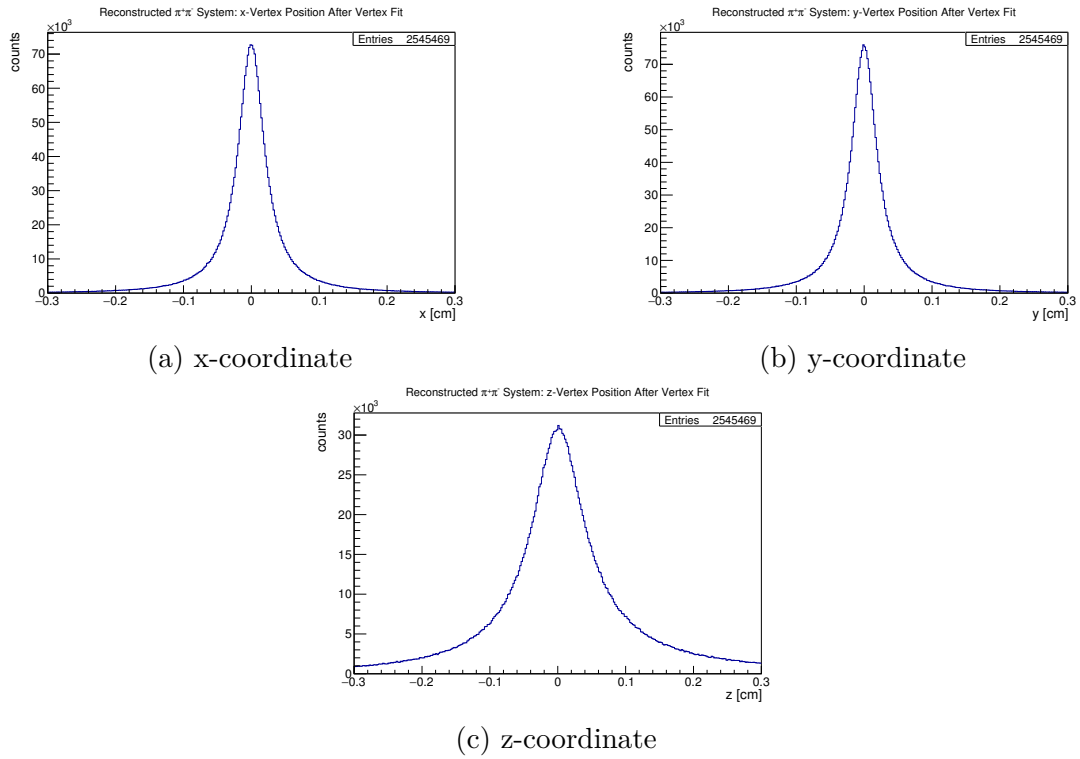
(c) z-coordinate

Figure 6.11: Reconstructed vertex position distribution after the vertex fit on the prompt $\pi^+\pi^-$ pairs.

The values found for the three coordinates, determined with a precision of $\mathcal{O}(10\,\%)$, are: $0.5\,\mathrm{mm}$ for the x and y coordinate and $1\,\mathrm{mm}$ for the z coordinate. The reconstruction efficiency for the prompt pion pair is $65\,\%$ and the purity of the sample after the selection is $96\,\%$. The finally selected pions are removed from the corresponding lists, in order to avoid reusing them for combination in the following steps of the analysis.

6.3.4   Reconstruction of Λ and $\overline{\Lambda}$

In the following paragraph, the study of the reconstructed Λ and $\overline{\Lambda}$ candidates is presented. The plots relative to the Λ candidates are shown here, while the ones relative to the $\overline{\Lambda}$ studies are collected in Appendix A.2.1.

Combinations of Daughter Particles

The reconstruction of a composite particle starts with the combination of the daughter candidates present in the lists by means of the `Combine` method implemented in the `RhoCandidate` class of PandaRoot. This method takes as input up to 10 candidates, sums their four-vectors and assigns the result to a new composite candidate. The procedure followed for the reconstruction of a particle and its antiparticle is identical, except for the input daughter particle candidates. In the case of the Λ, π^- and p are combined, while for $\overline{\Lambda}$, π^+ and $\bar{p}$ are combined. A mass window restricted to the the nominal mass of the $\Lambda \pm 0.15\,\mathrm{GeV}/c^2$ defines which composite candidates are considered valid. The ones with an invariant mass that lies outside this window are rejected. Effectively, the lower limit for the mass is given by the sum of the mass of the two daughter particles. Fig. 6.12 shows an exemplary mass distribution of Λ candidates after the combination of the daughter particles. This distribution refers to a small input sample containing 160,000 $\overline{p}p \to \Xi^-\overline{\Xi}^+\pi^+\pi^-$ events. The long tail that extends towards high invariant mass values is due to combinations involving high momentum particles produced in secondary interactions. By applying the mentioned mass window cut, these entries are discarded. Nevertheless, more than one Λ candidate is expected at this stage, due to the multiplicity of potential daughters in the lists.

Selection of the Best Candidate

To narrow down the selection to a single best candidate per event, two kinematic fits are performed: a vertex and a mass constraint fit. The vertex fit is the same described for the selection of the prompt pion pair. The vertex fitted candidates are subjected to the mass constraint fit implemented in the class `RhoKinFitter` in PandaRoot. The algorithm acts modifying the four-vectors of the daughter candidates in order to match
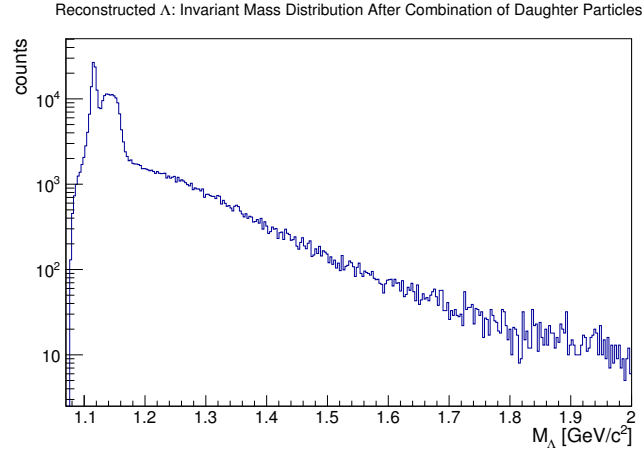
Figure 6.12: Invariant mass distribution of the Λ candidates after combination of their daughters. The y axis is displayed in a logarithmic scale.
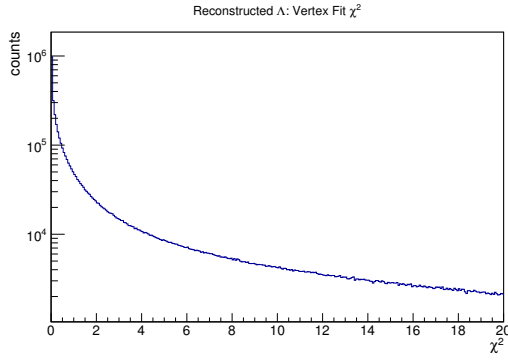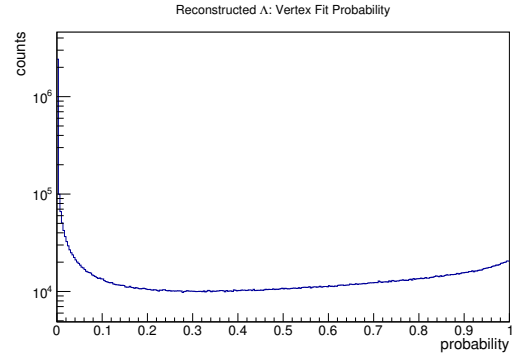
(a) χ^2 distribution.

(b) Probability distribution.

Figure 6.13: Quality of the vertex fit on Λ candidates.
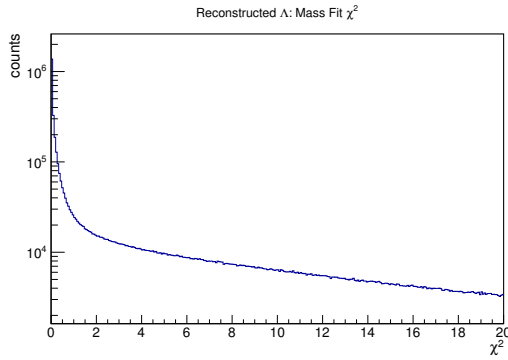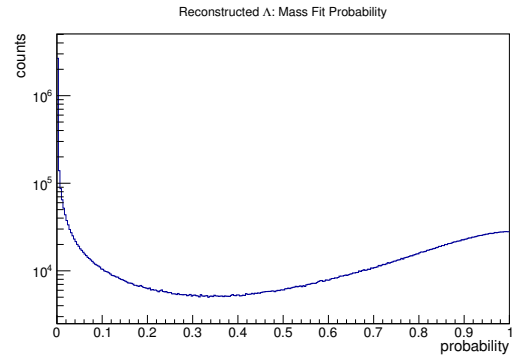
(a) χ^2 distribution.

(b) Probability distribution.

Figure 6.14: Quality of the mass constraint fit on Λ candidates.

the given invariant mass constraint. The quality of the vertex and the mass fit can be seen in Fig. 6.13 and Fig. 6.14, respectively. The probability threshold imposed to the candidates to pass the selection is 1×10^{-4} for each of the two fits. This value can be optimized in a later stage as discussed in Section 6.3.3 for the selection of the prompt pions. Except for the pronounced peak at zero, the probability distributions are expected to be flat. A rise towards probability values close to 1 is observed. At the moment, this behavior is not understood in detail. However, a comparable effect has been observed in similar studies that make use of the same fitting routines [52].

The χ^2 distribution of the candidates that survive both fits is evaluated, while the candidates that do not pass both fits are discarded. The candidate with the smallest χ^2 is considered to be the best one. It can happen, though, that the best candidate for the vertex and the mass fit is not the same. Therefore, the decision between the two best candidates is made by comparing their χ^2: the one that has the smallest χ^2 is finally selected. In most cases the selection is based on the mass constraint fit. The next stage of reconstruction, namely the Ξ^- and $\bar{\Xi}^+$ reconstruction, receives as input the candidate with its properties calculated after the vertex fit. Pions that are daughters of selected best candidate are removed from the list of available pions, in order to avoid erroneous multiple combination of the same particle in the following stages of the analysis.

The reconstruction efficiency for the Λ and $\bar{\Lambda}$ is 54 % and 53 %, respectively. The purity of the Λ and $\bar{\Lambda}$ samples after reconstruction corresponds to 81 % and 82 %, respectively.

Angular and Momentum Distributions

As for the final state particles, for the Λ and $\bar{\Lambda}$ candidates the momentum and angular distributions are studied as well. The generated sample covers a range of longitudinal momentum between $0.7 \, \text{GeV}/c$ and $3 \, \text{GeV}/c$, with a peak around $1.5 \, \text{GeV}/c$ (Fig. 6.15a and Fig. A.48a). In this case as well, as shown for the final state particles, events that lie outside the kinematically allowed region for the decay channel under study are physical events that have the same genealogy as the signal under study, but involve also secondary processes (e.g., nuclear reactions that produce neutrons). Therefore, they should not be considered as interesting events for the present study and can be removed by applying a cut on the number of particles produced in the reaction (Fig. 6.17 and Fig. A.51). Fig. 6.18 shows the MC partners that correspond to the reconstructed Λ. By comparing the number of entries of the MC histograms with the total number of generated events, one notices a loss of 3 %. This is due to the fact that, during their propagation through the detector volume, some particles do not deliver a sufficient number of hit points in the subdetectors for the tracking algorithm to reconstruct their trajectories. The reconstructed spectra, shown in Fig. 6.16, can be compared with the MC generated inputs. One can see that the distributions are consistent with each other.

(a) Transverse versus longitudinal momentum. (b) Polar angle versus total momentum.

Figure 6.15: MC generated Λ.

(a) Transverse versus longitudinal momentum. (b) Polar angle versus total momentum.
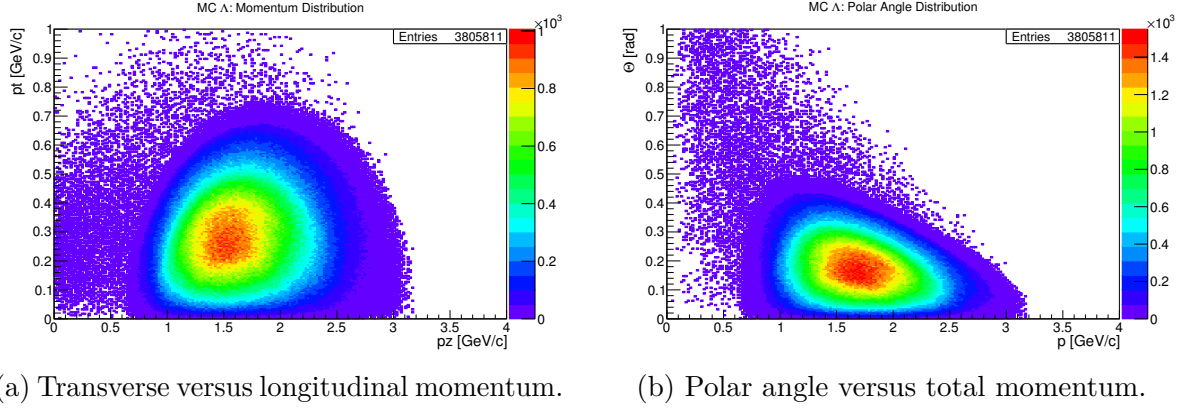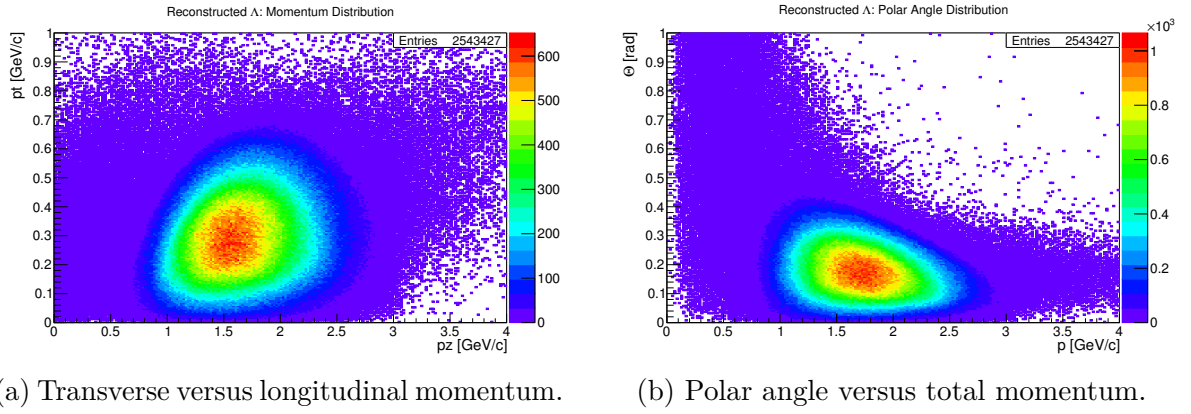
Figure 6.16: Reconstructed Λ.

(a) Transverse versus longitudinal momentum. (b) Polar angle versus total momentum.
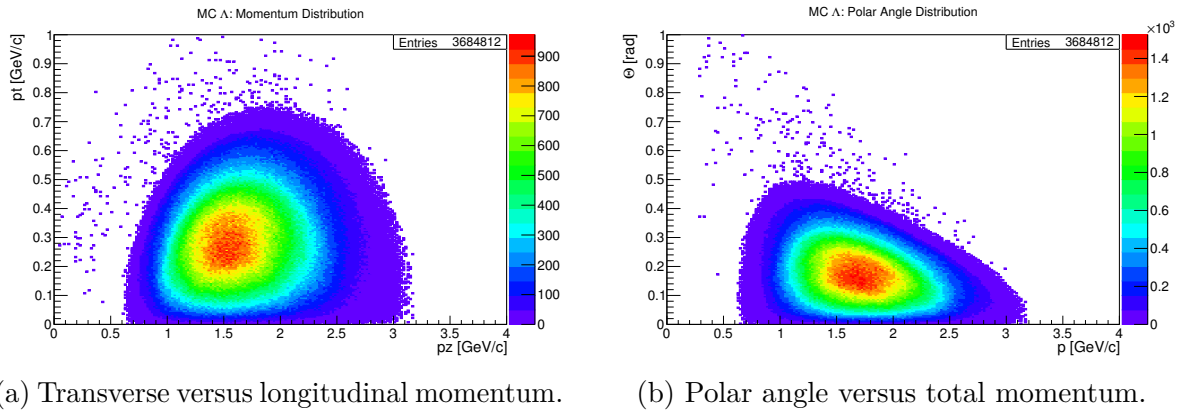
Figure 6.17: MC Λ with more stringent selection criteria, as explained in the text.
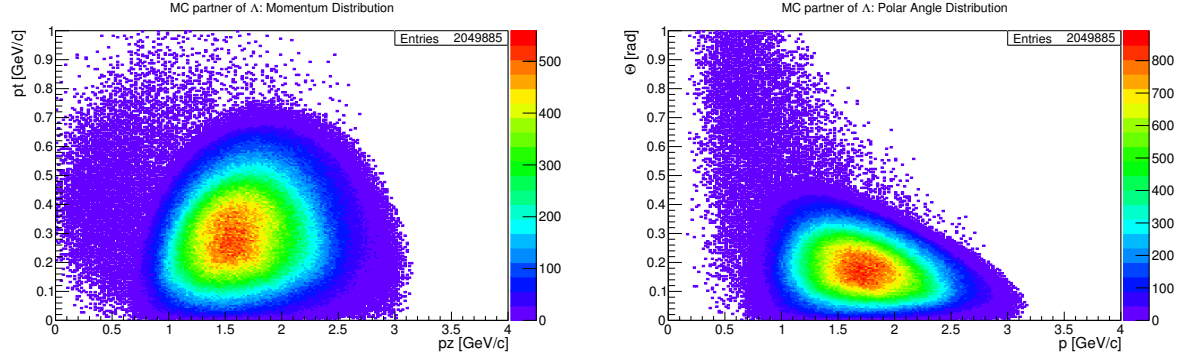
(a) Transverse versus longitudinal momentum.

(b) Polar angle versus total momentum.

Figure 6.18: MC partners of reconstructed Λ.

Decay Vertex Reconstruction

The reconstructed decay vertex distribution for the Λ candidates is shown in Fig. 6.19 for the three coordinates. The discontinuities in the z-coordinate, visible around 15 cm and 20 cm away from the primary interaction point, match the geometry of the MVD disks, indicating regions where the reconstruction efficiency is reduced, possibly due to an insufficient number of hits delivered in the detector. Entries in the negative range along the beam axis are an effect of the limited resolution. The decay vertex resolution can be estimated by looking at the deviation of the reconstructed position of MC matched particle from the generated input shown in Fig. 6.20. The resolution is estimated using the FWHM. The obtained values for both Λ and $\overline{\Lambda}$ candidates are: 0.1 mm for the x and y coordinate and 0.5 mm for the z coordinate. The longitudinal component is reconstructed with lower resolution, consistently with the results discussed for the final state stable particles.

Momentum Resolution

The relative momentum resolution is estimated in the same way as described for the final state particles, by taking the inner sigma of a double Gaussian fit (Fig. 6.21) applied to the distribution of the relative deviation of the reconstructed momentum from the input value. The obtained value is $\sigma_p/p = 1.42\,\%$ for both Λ and $\overline{\Lambda}$. The profile of the relative momentum deviation as a function of the total momentum is shown in Fig. 6.22. The dip corresponding to low momenta is mainly due to the imprecise estimation of the energy loss of the daughter protons by the Kalman filter, as discussed in Section 6.3.2. The distribution of the momentum resolution as a function of the total momentum (Fig. 6.23) exhibits a trend similar to the one observed for the protons.

(a) x-coordinate

(b) y-coordinate

(c) z-coordinate
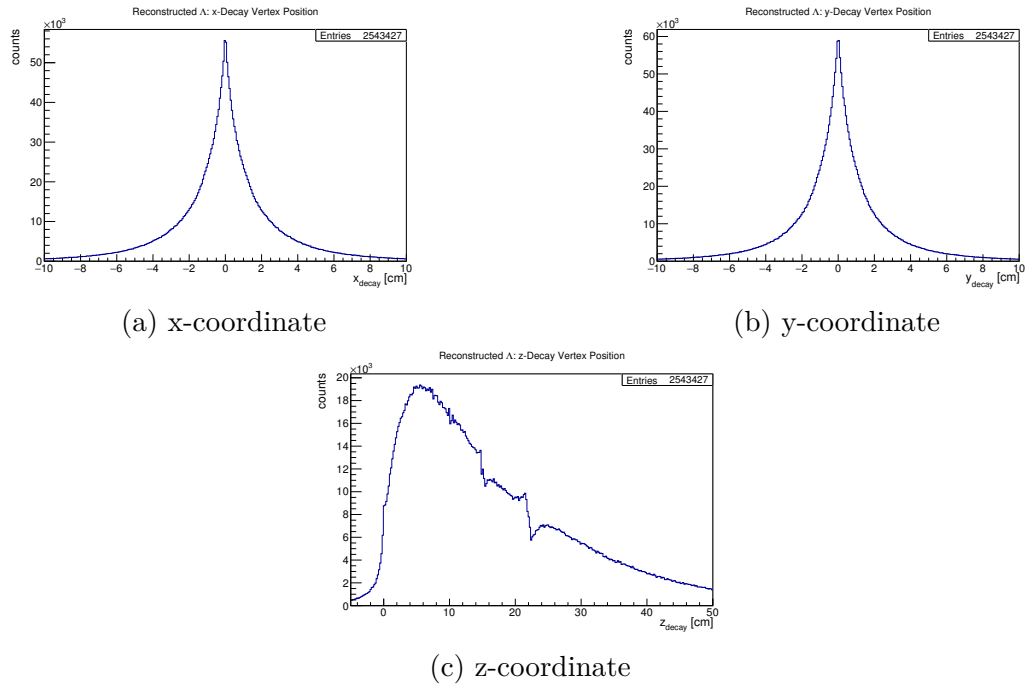
Figure 6.19: Vertex position distribution after the vertex fit on Λ candidates.

(a) x-coordinate

(b) y-coordinate

(c) z-coordinate
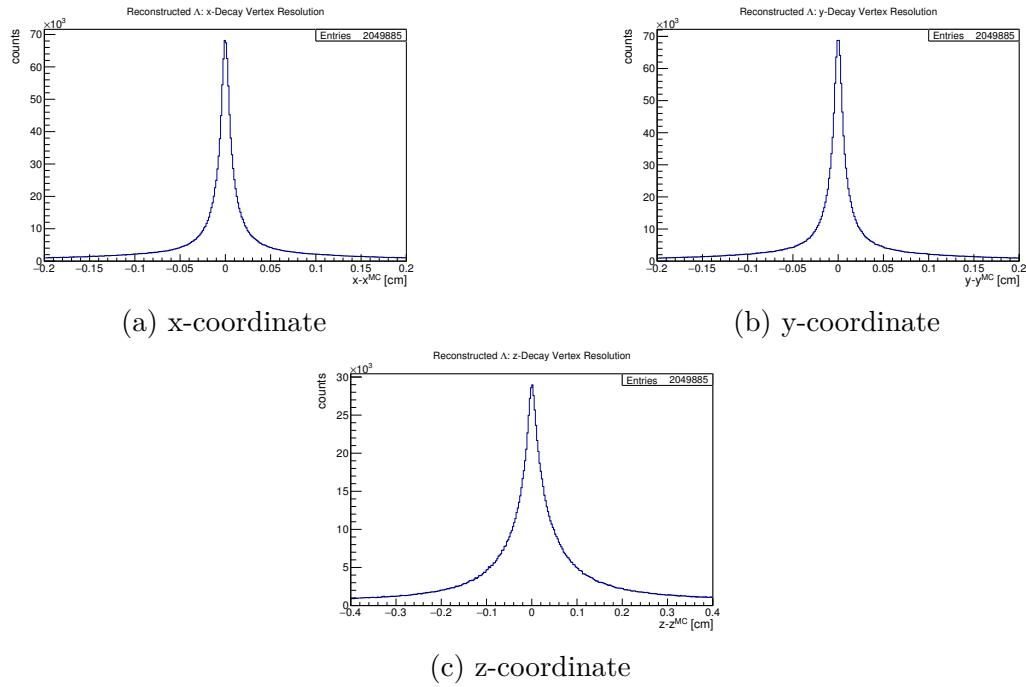
Figure 6.20: Deviation of the reconstructed vertex position from the MC value after the vertex fit on Λ candidates.
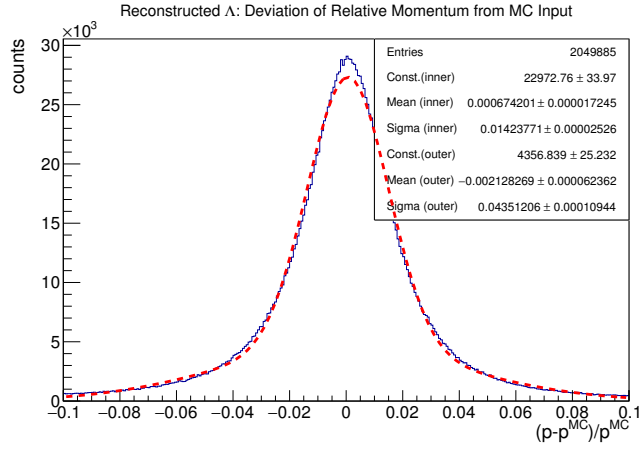
Figure 6.21: Relative deviation of the reconstructed Λ momentum from the MC value with a double Gaussian fit.
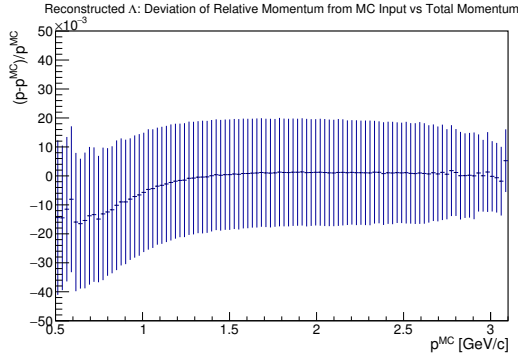
Figure 6.22: Relative deviation of the reconstructed Λ momentum from the MC value as a function of the total momentum.
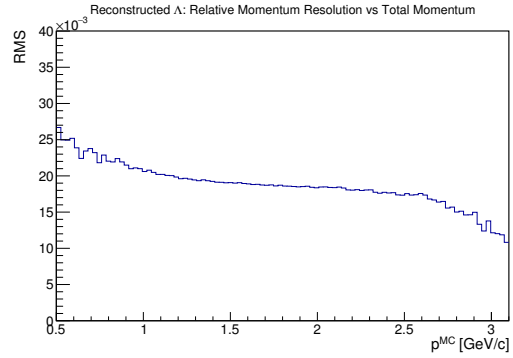
Figure 6.23: Dependence of the relative momentum resolution on the total momentum for reconstructed Λ candidates.

Invariant Mass Distribution

The invariant mass distribution for the Λ candidates at different stages of the selection is compared, in order to illustrate how the cuts influence the distribution. After combining the daughter candidates and applying the mentioned mass window cut, the invariant mass distribution of the Λ candidates has a peak around the nominal mass with a pronounced shoulder extending towards high values (Fig. 6.24a). This shape is due to the wrong combinations of daughter particles, which create Λ candidates that do not correspond to a MC object. Proceeding with the vertex fit, many of these fake candidates can be rejected. After the mass constraint fit, the distribution should appear as a Dirac delta function positioned at the bin corresponding to the nominal mass of the Λ. Fig. 6.24b shows that, although the peak located at the Λ mass is visible as expected, the unphysical low mass region is also populated. The integral of the number of entries within this region corresponds to 0.1 % of the total entries in the histogram. This behavior seems to be an artifact of the mass constraint fit and therefore this tool is currently under investigation. Since the candidates after the mass fit procedure are not propagated to the next stages of the reconstruction, as explained in Section 6.3.4, this aspect does not have an impact on the quality of the analysis algorithm. Performing a double Gaussian fit, after the vertex fit procedure, on the reconstructed candidates that have a MC partner, one finds the mass resolution to be $\sigma_M = 2.0\,\mathrm{MeV/c^2}$ for both Λ and $\overline{\Lambda}$. Similar to the case of the Λ candidates, the invariant mass distribution for the $\overline{\Lambda}$ candidates after the mass fit procedure presents entries in the unphysical low mass region, albeit one order of magnitude less than in the previously discussed case.
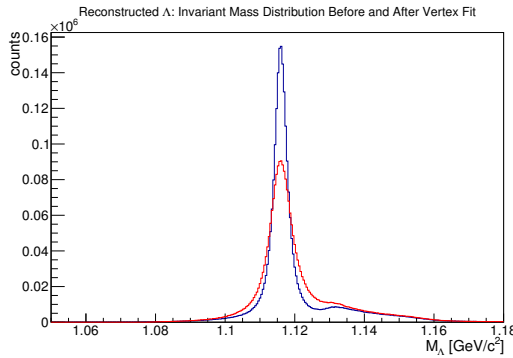
(a) Invariant mass distribution before (red) and after (blue) the vertex fit.
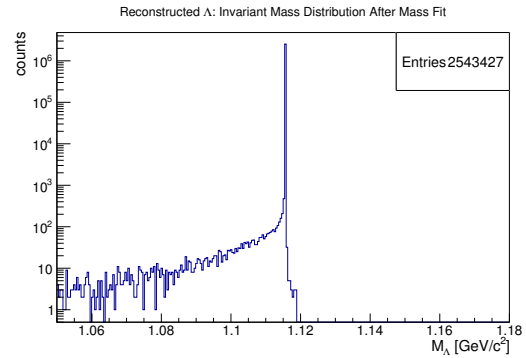
(b) Invariant mass distribution after the mass constraint fit.

Figure 6.24: Invariant mass distribution for the Λ candidates.

Proper Decay Length Distribution

The Λ baryon has a decay length of several cm. This quantity can be measured as

$$\lambda = \frac{|\vec{x}_{decay} - \vec{x}_{prod}|}{|\vec{p}|/m}.$$

The distribution is showed in Fig. 6.25 using a logarithmic scale for the y-axis. The decay time is extracted by fitting the distribution with an exponential function and taking the inverse of the obtained slope. The measured values are (7.752 ± 0.006) cm for Λ and (7.9 ± 0.2) cm for $\bar{\Lambda}$. The given errors are purely statistical. Compared with the value given in [106], i.e., $c\tau = 7.89$ cm, the measurement for Λ is slightly smaller and the one for $\bar{\Lambda}$ is compatible within the error.
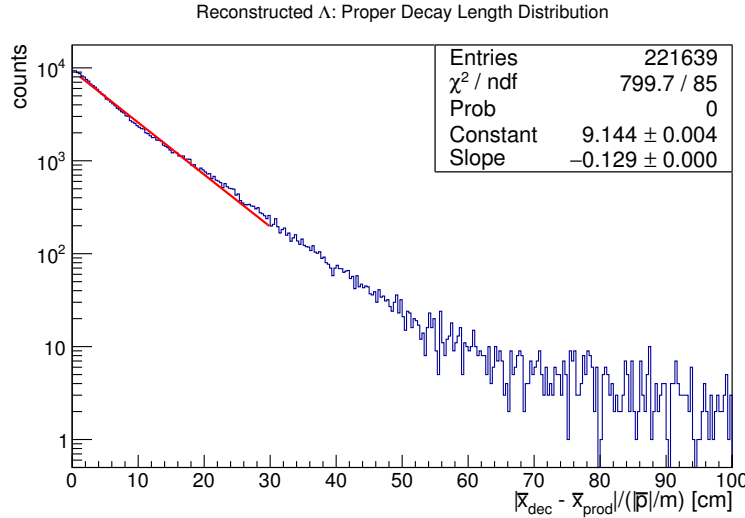
Figure 6.25: Proper decay length distribution with an exponential fit for reconstructed Λ candidates. A logarithmic scale for the y-axis is used.

6.3.5   Reconstruction of Ξ^- and $\bar{\Xi}^+$

The reconstruction of the cascade baryons is carried out using the same strategy as described for the Λ candidates: first the daughter particle candidates are combined, then a selection based on the previously described kinematic fits is applied, in order to find the best Ξ^- and $\bar{\Xi}^+$ for each event. In the following paragraph only the distributions for the Ξ^- are shown. The results are described for the $\bar{\Xi}^+$ candidates as well and the corresponding histograms are collected in Appendix A.2.2.

Combination of Daughter Particles

The selected Λ are combined with the remaining π^- to form a Ξ^- candidate and the selected $\overline{\Lambda}$ with the remaining π^+ to form a $\overline{\Xi}^+$ candidate. A mass cut is applied in this case as well, to reject most unreasonable combinations. The defined window is symmetric around the nominal mass of the Ξ and has a total width of $0.3\,\text{GeV}/c^2$. Fig. 6.26 shows an exemplary invariant mass distribution after the combination of the daughter particles. This distribution refers to a small input sample containing 160,000 $\overline{p}p \rightarrow \Xi^- \overline{\Xi}^+ \pi^+ \pi^-$ events. The mentioned cut around the nominal mass of the Ξ^- eliminates the contribution of the long tail extending towards high values of the invariant mass spectrum. Since for each event only one Λ survives the selection, the multiplicity of cascades candidates is significantly smaller than in the case of Λ reconstruction. Nevertheless, a selection is needed in order to choose a single candidate per event.
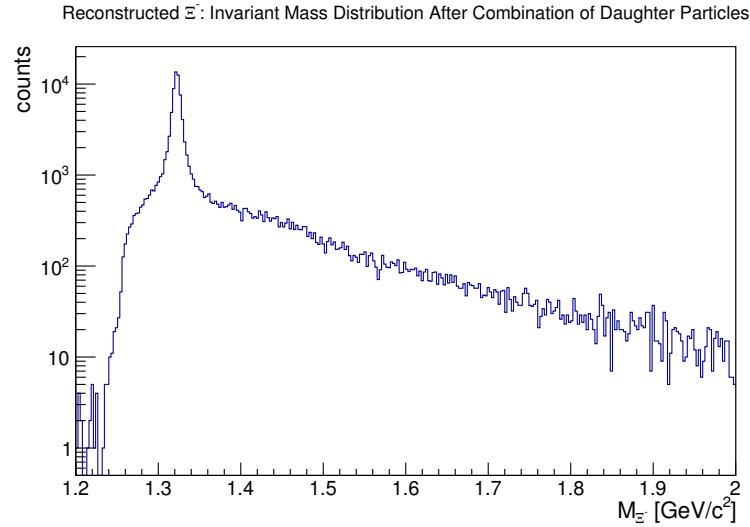
Figure 6.26: Invariant mass distribution of the Ξ^- candidates after combination of their daughters. The y axis is displayed in a logarithmic scale.

Selection of the Best Candidate

A vertex and a mass fit are performed on the available candidates. The best candidates (one Ξ^- and one $\overline{\Xi}^+$ per event) are selected according to the same criteria illustrated for the Λ candidates. The fit quality for the sample is shown in Fig. 6.27 and Fig. 6.28 for vertex and mass fit, respectively. As observed in Fig. 6.13b for the Λ baryons, the probability distribution has an unexpected peak around 1.
The efficiency for the reconstruction of the Ξ^- and $\overline{\Xi}^+$ is 33 %. After the selection of the best candidate for each event, the Ξ^- and $\overline{\Xi}^+$ samples have a purity of 81 % and 82 %, respectively.
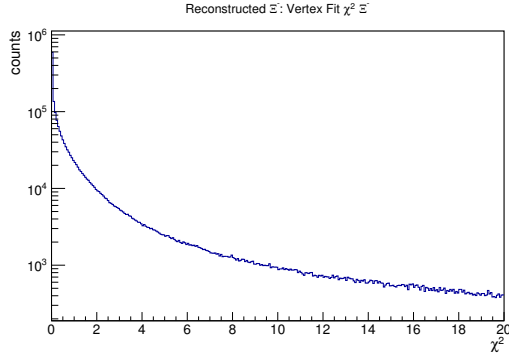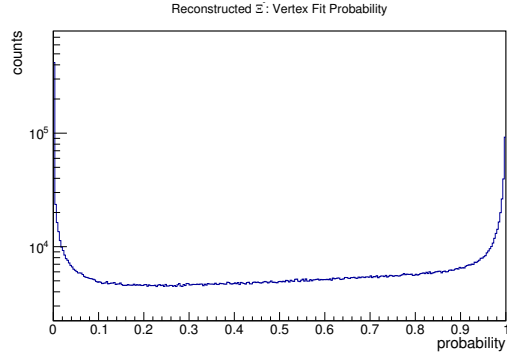
(a) χ^2 distribution.

(b) Probability distribution.

Figure 6.27: Quality of the vertex fit on Ξ^- candidates.
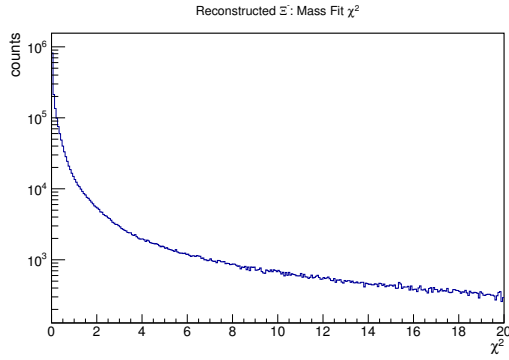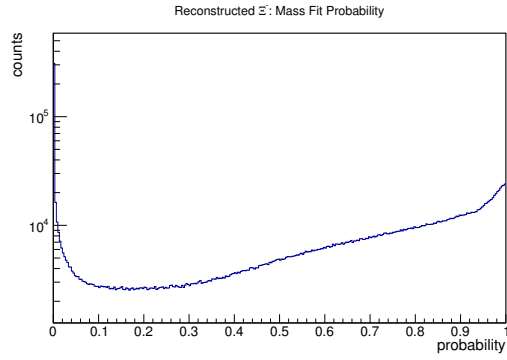
(a) χ^2 distribution.

(b) Probability distribution.

Figure 6.28: Quality of the mass constraint fit on Ξ^- candidates.

Angular and Momentum Distribution

The generated sample covers a longitudinal momentum between $0.9\,\mathrm{GeV}/c$ and $3.3\,\mathrm{GeV}/c$, with a peak around $2\,\mathrm{GeV}/c$ (Fig. 6.29). The studies of the two dimensional spectra of the polar angle versus the total momentum and the transverse versus longitudinal momentum for the Ξ^- lead to similar conclusions to the case of the Λ studies. Comparing the input spectra (Fig. 6.29) with the reconstructed ones (Fig. 6.30) one can observe consistent shapes, despite the difference in the number of entries, due to the reconstruction efficiency. The MC partners of the reconstructed Ξ^-, given in Fig. 6.31, have entries outside the kinematically allowed region, which are not present in the complete MC sample (Fig. 6.29). The cause for this behavior is not understood at the moment and requires further investigation. These entries are removed by the selection applied in the next stages of the analysis and therefore do not impact on the final results (see Section 6.3.7).

Decay Vertex Reconstruction

The three coordinates of the reconstructed decay vertex position for the Ξ^- are shown in Fig. 6.32. As previously observed for the Λ baryons, for the Ξ^- as well, there are decay vertices positioned upstream of the interaction point. This phenomenon is clearly unphysical and it is related to the limited spatial resolution. The peak visible at $z = 0$ (Fig. 6.32c) is populated with non-MC matched candidates and it is therefore caused by wrong combinations of the daughter particles, e.g., combinations involving a prompt pion. The resolution is estimated as the FWHM of the distribution given by the difference between reconstructed and MC generated values (Fig. 6.33). For the three coordinates the found values are in agreement for both Ξ^- and $\overline{\Xi}^+$: $0.3\,\mathrm{mm}$ in x and y and $1.3\,\mathrm{mm}$ in z. These results confirm the worse transverse component resolution, mostly due to the small polar angles of the daughter particles. After having reconstructed the decay vertices of both Λ and Ξ^-, one can measure the quantity

$$\vec{l} = \frac{\vec{p}_\Lambda}{|\vec{p}_\Lambda|} \times \frac{\vec{v}_\Lambda - \vec{v}_{\Xi^-}}{|\vec{v}_\Lambda - \vec{v}_{\Xi^-}|}.$$

This observable is used to estimate the alignment between the Λ momentum vector and the position difference between the Λ decay vertex and the Ξ^- decay vertex. Fig. 6.34 shows the distribution of the norm of the defined quantity, relative to the Λ candidates, which peaks at zero as expected and decreases rapidly. A cut on this quantity can be used for signal filtering in the presence of background.
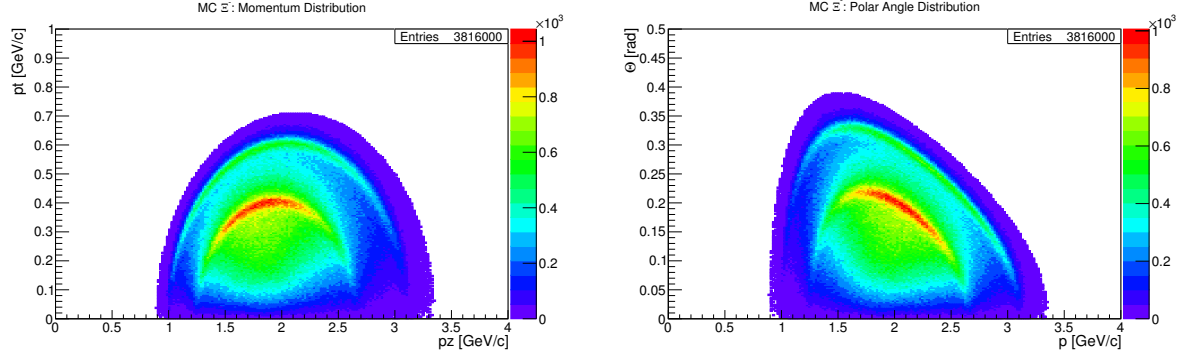
(a) Transverse versus longitudinal momentum.

(b) Polar angle versus total momentum.

Figure 6.29: MC generated Ξ^-.
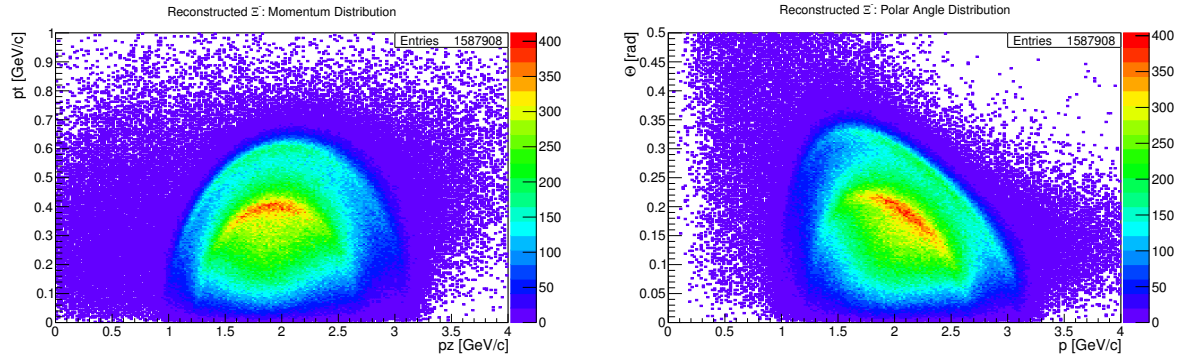
(a) Transverse versus longitudinal momentum.

(b) Polar angle versus total momentum.

Figure 6.30: Reconstructed Ξ^-.
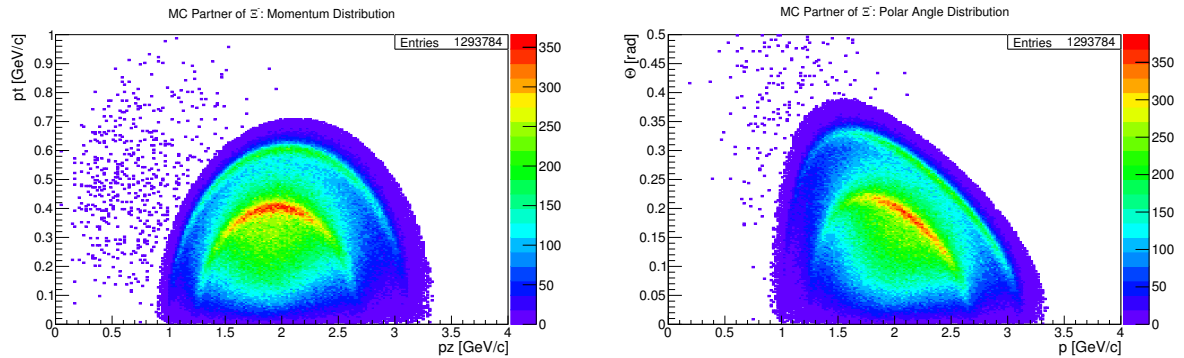
(a) Transverse versus longitudinal momentum.

(b) Polar angle versus total momentum.

Figure 6.31: MC partners of reconstructed Ξ^-.

(a) x-coordinate

(b) y-coordinate

(c) z-coordinate
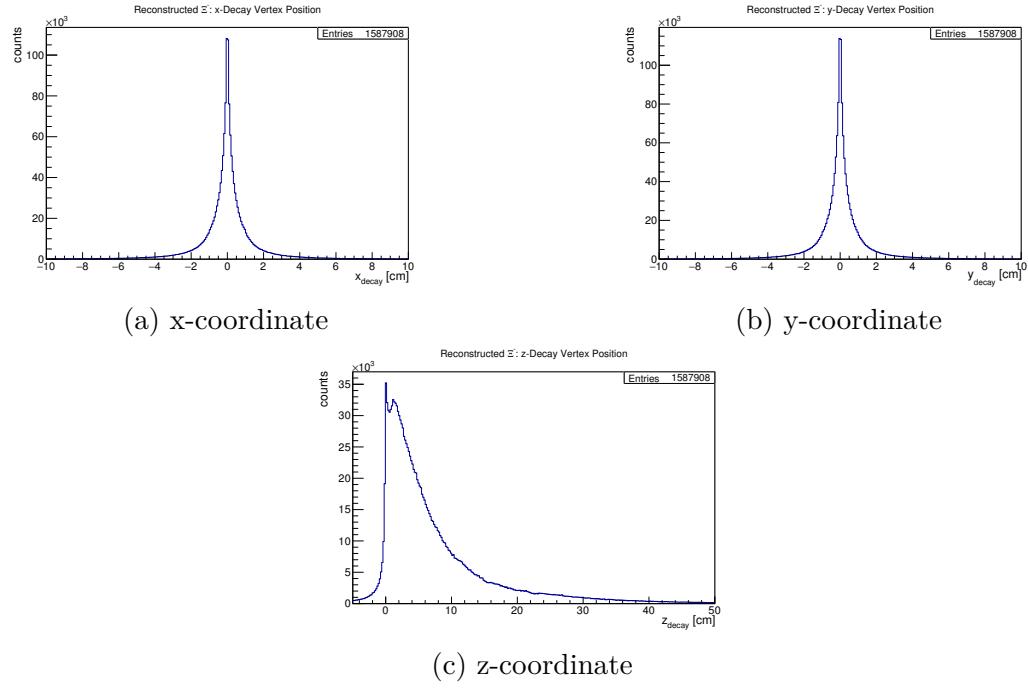
Figure 6.32: Vertex position distribution after the vertex fit on Ξ^- candidates.

(a) x-coordinate

(b) y-coordinate

(c) z-coordinate
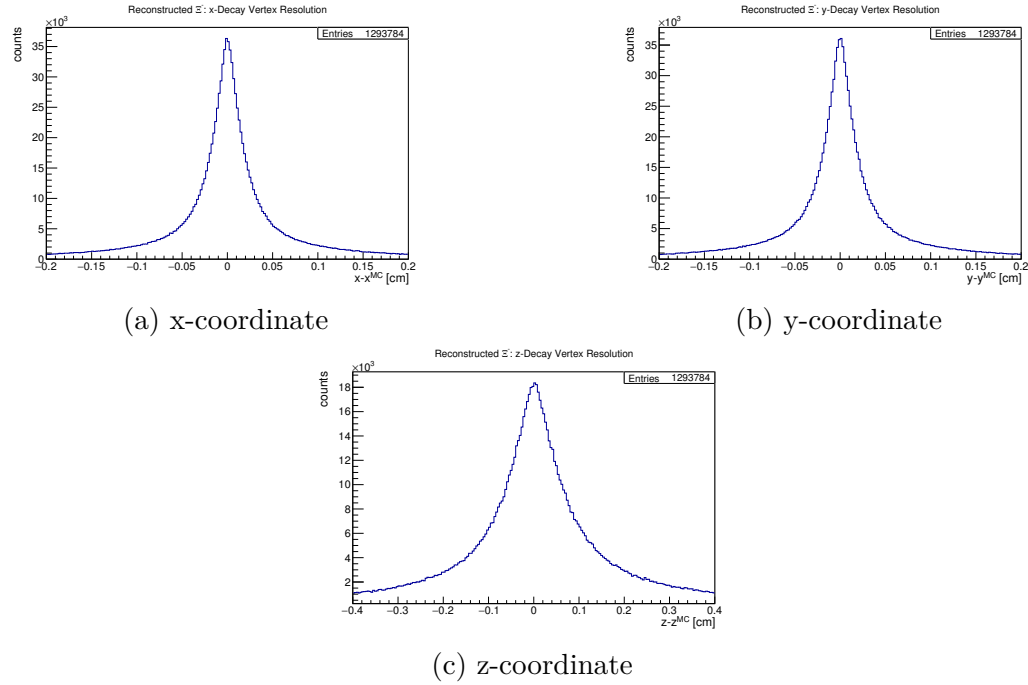
Figure 6.33: Deviation of the reconstructed vertex position from the MC value after the vertex fit on Ξ^- candidates.
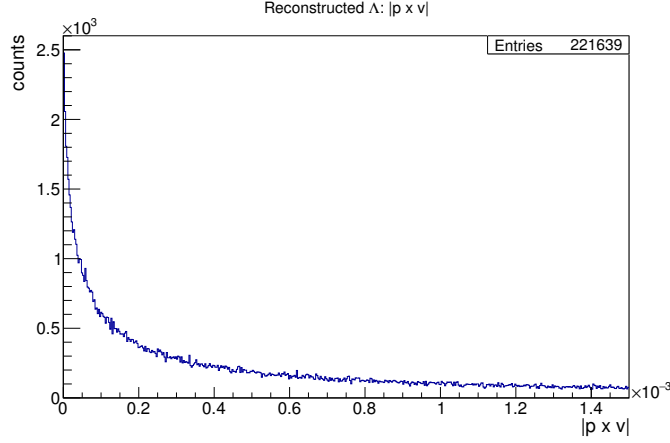
Figure 6.34: Distribution of the norm of the cross product between the Λ momentum vector and the position difference between the Λ decay vertex and the Ξ^- decay vertex.

Momentum Resolution

The relative deviation of the reconstructed momentum from the input value for the Ξ^- is displayed in Fig. 6.35. The inner σ of a double Gaussian fit performed on this distribution gives a resolution of $\sigma_p/p = 1.30\,\%$ for the Ξ^- and $\sigma_p/p = 1.31\,\%$ for the $\bar{\Xi}^+$. The profile histogram of the relative momentum deviation as a function of the momentum is given in Fig. 6.36. The mean value is systematically shifted from zero, for Ξ^- with momentum lower than $1.5\,\mathrm{GeV}/c$, mostly due to the contribution of the reconstructed momentum of the Λ, as discussed in Section 6.3.2. The relative momentum resolution as a function of the total momentum (Fig. 6.37) has a flat profile between $1.2\,\mathrm{GeV}/c$ and $2.2\,\mathrm{GeV}/c$ which corresponds to $4\,\%$.
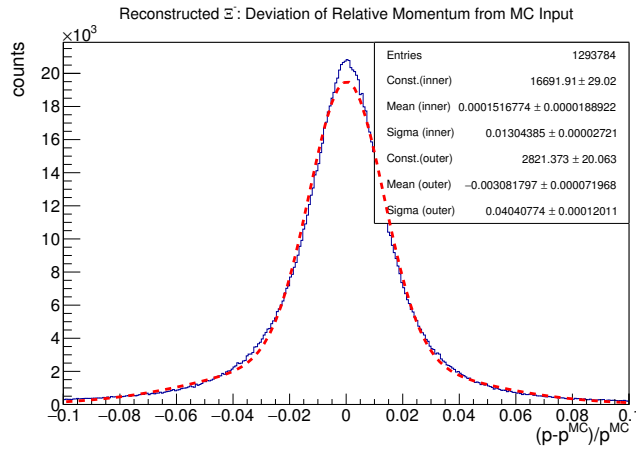
Figure 6.35: Relative deviation of the reconstructed Ξ^- momentum from the MC value with a double Gaussian fit.
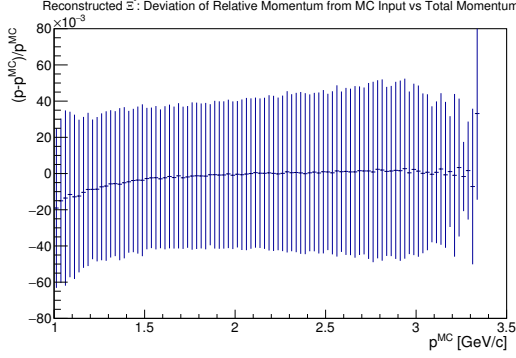
Figure 6.36: Relative deviation of the reconstructed Ξ^- momentum from the MC value as a function of the total momentum for reconstructed Ξ^- candidates.
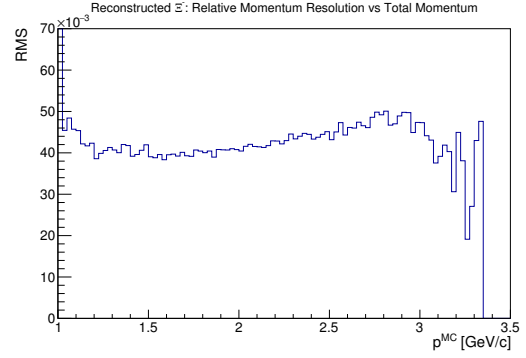
Figure 6.37: Dependence of the relative momentum resolution on the total momentum.

Invariant Mass Distribution

The invariant mass distribution for the reconstructed Ξ^- before and after the vertex fit is shown in Fig. 6.38. The fitting procedure does not modify the shape of the distribution significantly. The invariant mass resolution, obtained with the double Gaussian fit method applied to the distribution of the MC matched candidates, is $\sigma_M = 3.8\,\mathrm{MeV/c^2}$ for both Ξ^- and $\overline{\Xi}^+$. The invariant mass distribution after the mass constraint fit shows entries in the non-physical region, which are $2\,\%$ of the total number of entries. To this regard, the considerations made for the Λ baryon apply as well.
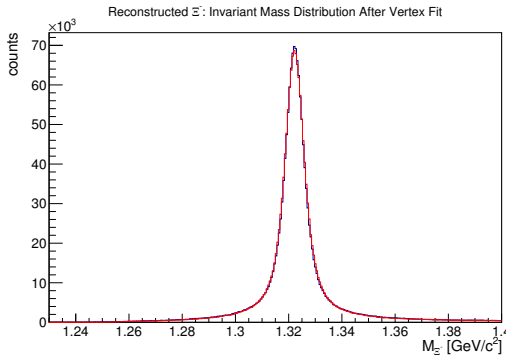
(a) Invariant mass distribution before (red) and after (blue) the vertex fit.
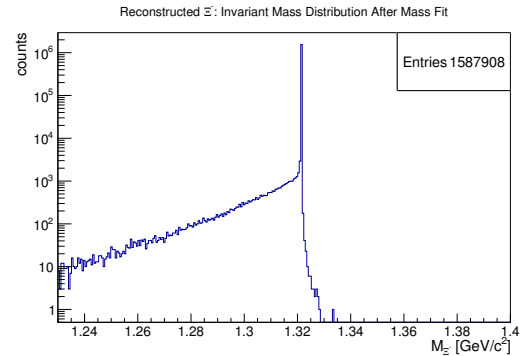
(b) Invariant mass distribution after the mass constraint fit.

Figure 6.38: Invariant mass distribution for the Ξ^- candidates.

Proper Decay Length Distribution

Similar to the Λ baryon, Ξ^{-} has a significant lifetime. The reconstructed proper decay length distribution is shown in Fig. 6.39 together with an exponential fit. The inverse of the slope gives a proper decay length of $(4.89 \pm 0.01)\,\mathrm{cm}$ and $(4.90 \pm 0.02)\,\mathrm{cm}$ for the Ξ^{-} and $\bar{\Xi}^{+}$, respectively. A comparison with the measurement given in [106], i.e., $c\tau = 4.91\,\mathrm{cm}$, shows that the value found for the Ξ^{-} is slightly smaller, while the one for $\bar{\Xi}^{+}$ is compatible within the error.
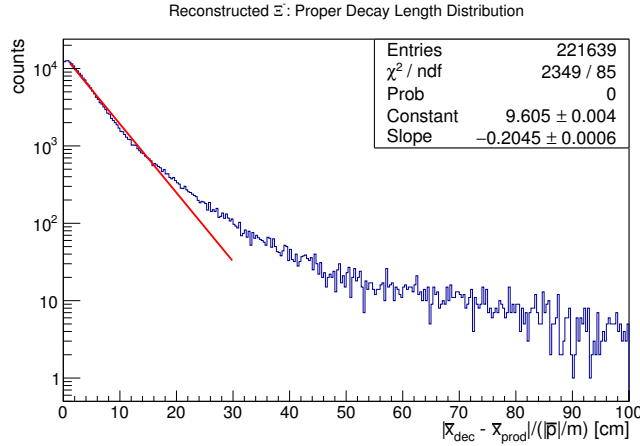
Figure 6.39: Proper decay length distribution with an exponential fit for reconstructed Ξ^{-} candidates. A logarithmic scale for the y-axis is used.

6.3.6　Reconstruction of the $\Xi^{-}\bar{\Xi}^{+}\pi^{+}\pi^{-}$ System

Once the Ξ^{-} and $\bar{\Xi}^{+}$ are identified, the next step in the reconstruction chain is to combine them with the previously selected prompt pion pairs. The multiplicity at this stage is much lower than in the previous stages, for only one candidate of each species survived the selection so far. However, not all the events that have a complete set of particles generate a good candidate for the decay under study. To discriminate the signal events, one more time a vertex fit is performed, forcing the four charged tracks to originate from a common vertex: the primary interaction vertex of the reaction. The quality of the fit, in terms of the probability and χ^2 distributions, is shown in Fig. 6.40. Events whose fit converges, but with a probability value smaller than 1×10^{-4} are rejected, reducing the number of entries in the lowest bin of the histogram in Fig. 6.40b. The previously discussed rising profile towards unitary probability is visible here as well. In the $\bar{p}p$ interaction the momentum of the $\bar{p}$ beam is set to $4.6\,\mathrm{GeV}/c$ and the protons of the target are at rest. This condition allows to calculate the total energy of the beam and target system in the laboratory frame:

$$E_{\bar{p}p} = \sqrt{M_{p}^{2} + p_{p}^{2}} + M_{p} = 5.63\,\mathrm{GeV}/c^{2}.$$

(a) χ^2 distribution.

(b) Probability distribution.
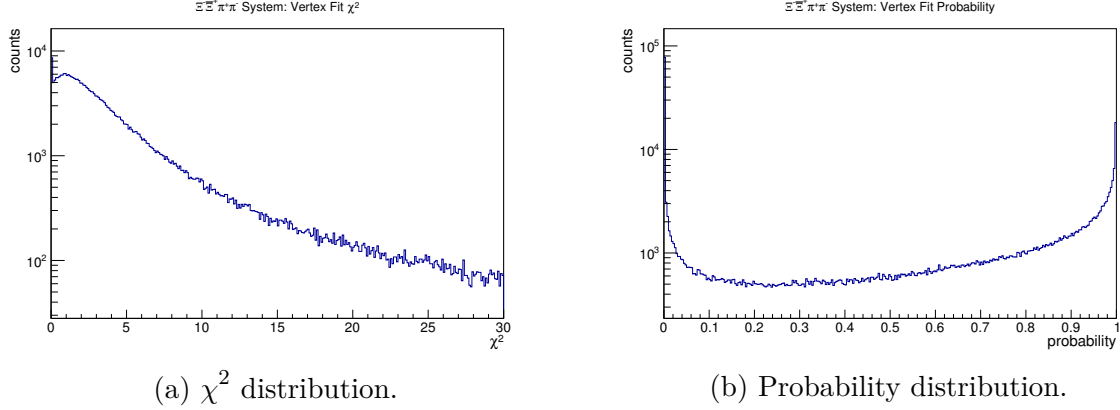
Figure 6.40: Quality of the vertex fit on the $\Xi^-\overline{\Xi}^+\pi^+\pi^-$ system.

(a) χ^2 distribution.

(b) Probability distribution.
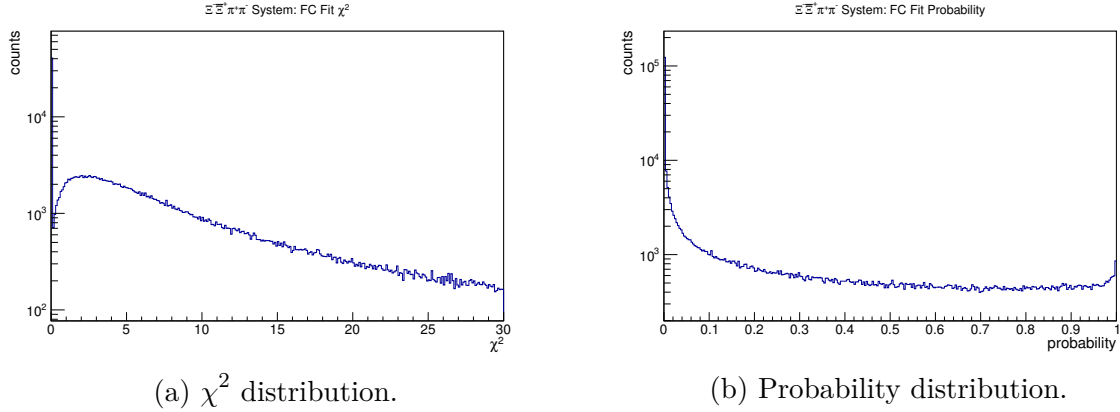
Figure 6.41: Quality of the four-constraint fit on the $\Xi^-\overline{\Xi}^+\pi^+\pi^-$ system.

Since the initial four-vector of the reaction is known, it is possible to exploit this information as a criterion for the selection. A so-called four-constraint fit, implemented in the class `RhoKinFitter` of PandaRoot, acts on the four-momentum vectors of the particles involved in the reaction in order to match it to the initial one. The probability and χ^2 distributions for this fit are given in Fig. 6.41. In this case, as opposed to the fits performed so far, the probability distribution is rather flat and no rising profile towards high values is observed. Unreasonable combinations are rejected by means of a probability cut for entries below 1×10^{-4}.

Decay Vertex Reconstruction

The primary vertex of the interaction is reconstructed. The resolution is estimated with the FWHM of the distribution of the MC matched candidates after the four-constraint fit procedure (Fig. 6.42). The measured values are $0.3\,\mathrm{mm}$ for the x and y coordinates and $1.2\,\mathrm{mm}$ for the z coordinate.

(a) x-coordinate

(b) y-coordinate

(c) z-coordinate
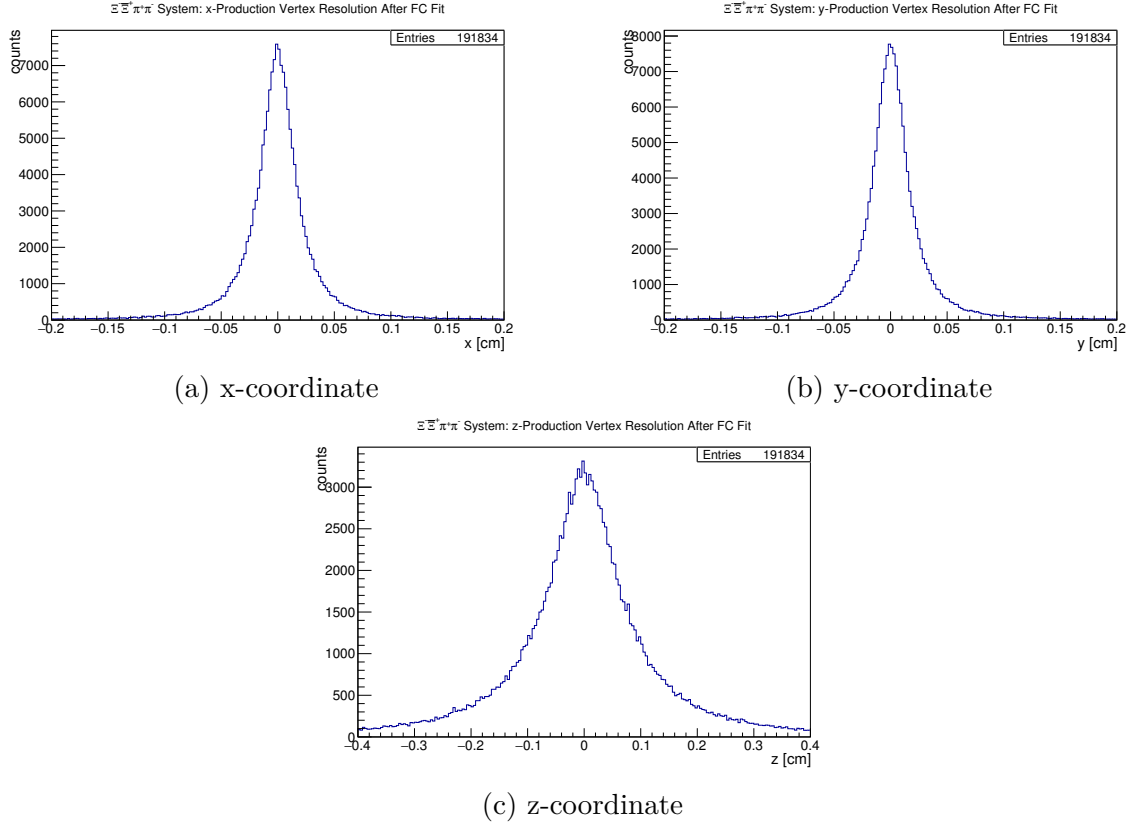
Figure 6.42: Reconstructed primary vertex position resolution.

Invariant Mass Distribution and Goldhaber Plots

The invariant mass distribution of the $\Xi^-\,\bar{\Xi}^+\pi^+\pi^-$ system is not substantially influenced by the vertex fit (see Fig. 6.43a). After the four-constraint fit, it is expected to see a Dirac delta function at $\sqrt{s} = 3.25\,\mathrm{GeV}/c^2$. However, Fig. 6.43b shows not only the delta function, but also entries in the bins corresponding to higher mass values, namely $0.7\,\%$ of the total number of entries. This unphysical result provided by the four-constraint fit is currently not understood and needs further investigation. The candidates corresponding to unphysical invariant mass values are discarded.
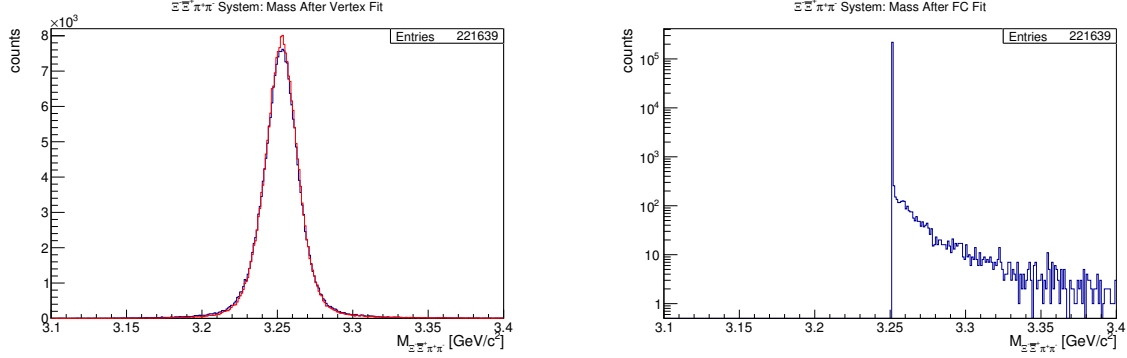
(a) Invariant mass distribution before (red) and after (blue) the vertex fit.

(b) Invariant mass distribution after the four-constraint fit.

Figure 6.43: Invariant mass distribution for the $\Xi^-\overline{\Xi}^+\pi^+\pi^-$ system.

The kinematics of the reaction $\overline{\mathrm{p}}\mathrm{p} \to \Xi^-\overline{\Xi}^+\pi^+\pi^-$ can be studied through the so-called Goldhaber plots. Processes involving two interacting particles a and b that lead to four particles in the final state, having masses m_1, m_2, m_3, and m_4, exhibit a well defined kinematic boundary. The kinematic limit is represented by a right-angled isosceles triangle, also known as Goldhaber triangle (Fig. 6.44). The length of each of the two equal sides of the triangle corresponds to the total kinetic energy available in the reaction

$$Q = W - \sum_{i=1}^{4} m_i$$

where W is the total energy in the center of mass of the initial system. Intermediate states produced in the reaction at specific values of the invariant masses (i.e., resonances) appear in the Goldhaber triangle as horizontal or vertical bands. For examples of the use of Goldhaber plots to study four-body final states reactions see [112, 113]. Applying this theory to the present case, one can look at a two dimensional histogram of the invariant mass of the system, in order to identify neutral cascade resonances decaying either into $\Xi^-\pi^+$ or $\overline{\Xi}^+\pi^-$. It is expected to find events that lie inside a Goldhaber triangle with sides of length $Q = 326\,\mathrm{MeV}/c^2$. The lower limit of each side is given by the sum of the invariant mass of each $\Xi\pi$: $M_\Xi + M_\pi = 1462\,\mathrm{MeV}/c^2$ and the upper limit is $M_\Xi + M_\pi + Q = 1788\,\mathrm{MeV}/c^2$. The expected shape of the Goldhaber plot can be seen in Fig. 6.45a. This histogram is based on 2×10^6 events generated with EvtGen, without involving propagation through the detector. Fig. 6.45b shows the Goldhaber plot for the reconstructed events. Most of the events lie inside the kinematically allowed region. Only $0.2\,\%$ of the total number of entries populates kinematically forbidden regions corresponding to a low invariant mass of one of the two two-body subsystem. The two horizontal and two vertical bands indicate the presence of the expected resonant states: $\Xi(1530)$ and $\Xi(1690)$. Fig. 6.46 shows the projection of the invariant mass on each of the two axis, with peaks at values corresponding to the resonant observed states.
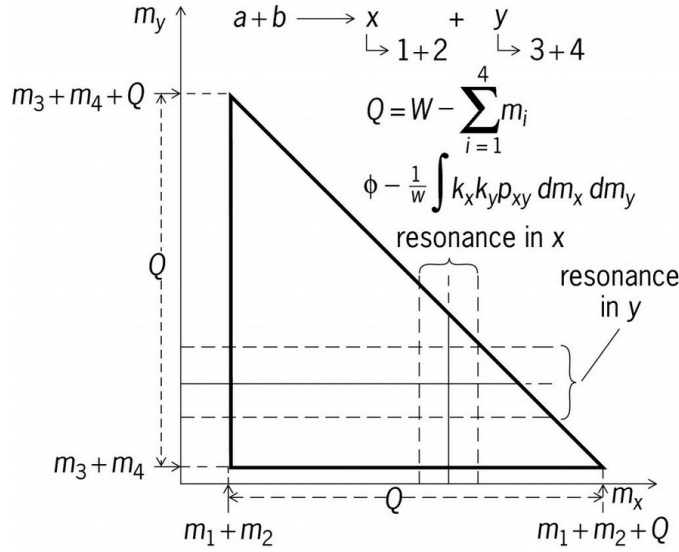
Figure 6.44: Definition of the kinematical boundary of the Goldhaber triangle for four particles. Image from [114].

The Goldhaber plot is not suitable to identify the charged resonances, which decay in three particles. Having a four-body final state, the two three-body subsystems relevant for these resonances, namely $\Xi^- \pi^+ \pi^-$ and $\bar{\Xi}^+ \pi^+ \pi^-$, can be seen as two-body systems, considering the dipion system as a pseudo-particle with variable invariant mass ranging from $2 \cdot M_\pi = 280\,\mathrm{MeV}/c^2$ to $2 \cdot M_\pi + Q = 606\,\mathrm{MeV}/c^2$. Therefore, plotting the squared invariant masses of one of the two three-body subsystem against the other does not lead to a Dalitz plot, but rather to a superposition of Dalitz plots, one for each realized $\pi^+ \pi^-$ mass. As a consequence, the main feature of the Dalitz plot to reveal non-uniformities in the phase-space is no longer present. For this reason, there is no benefit in using the invariant masses squared. Fig. 6.47a shows the invariant mass of the $\bar{\Xi}^+ \pi^+ \pi^-$ systems against the one of the $\Xi^- \pi^+ \pi^-$ system, in linear scale, for the same EvtGen output sample mentioned before. As expected, the resonant states are visible as bands in both systems. The distribution shows an ellipse-like shape with sharp edges towards high values of the masses. The entry corresponding to the highest mass value in both system corresponds to the case in which the invariant mass of the dipion system has its maximum value and the two Ξ are at rest. The sharp edges appearing in both system are those events in which only one of the Ξ is at rest. The same plot for the reconstructed systems exhibit the structures clearly, despite the limited statistics (Fig. 6.47b). The projection on each of the axis for the two systems are particularly useful to observe the peaks corresponding to the resonances located where expected (Fig. 6.48).
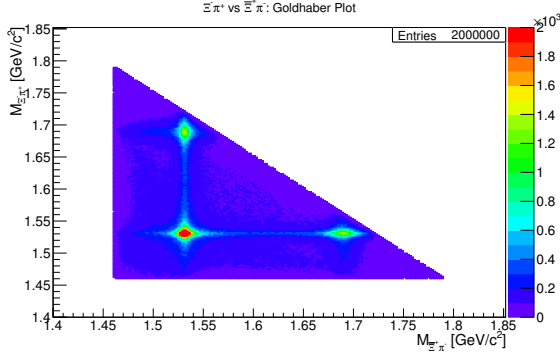
(a) EvtGen sample of the $\Xi\pi$ systems.
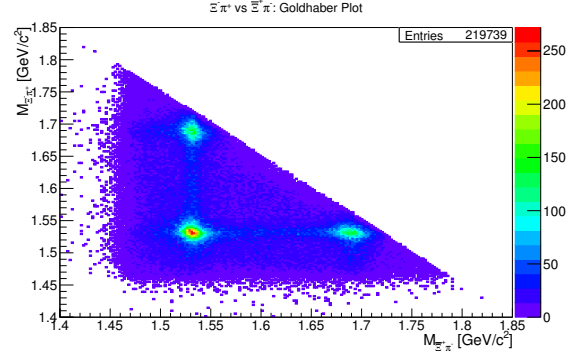
(b) Reconstructed $\Xi\pi$ systems.

Figure 6.45: Goldhaber plot for the neutral $\Xi\pi$ systems. The vertical bands indicate the presence of neutral resonant states.
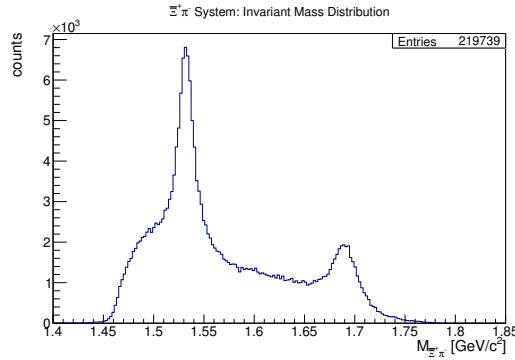
(a) Reconstructed $\overline{\Xi}^+\pi^-$ system.
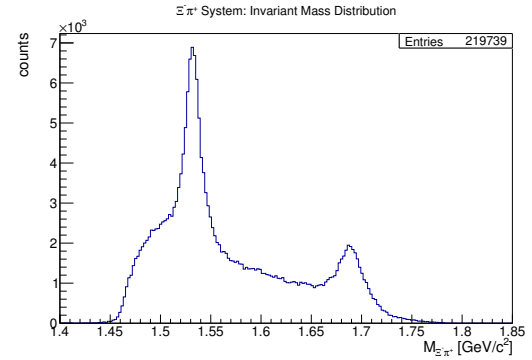
(b) Reconstructed $\Xi^-\pi^+$ system.

Figure 6.46: Invariant mass distribution of the reconstructed $\overline{\Xi}^+$ π^- and $\Xi^-\pi^+$ systems.
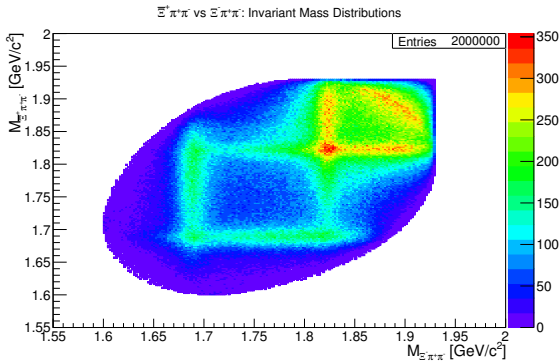
(a) EvtGen sample of the $\Xi\pi\pi$ systems.
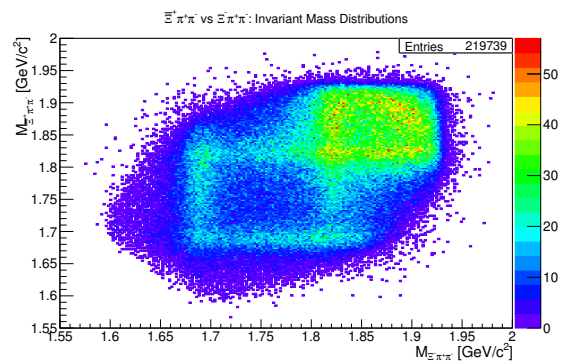
(b) Reconstructed $\Xi\pi\pi$ systems.

Figure 6.47: Two dimensional invariant mass plot for the $\Xi\pi\pi$ systems.

(a) Reconstructed $\Xi^- \pi^+ \pi^-$ system.

(b) Reconstructed $\overline{\Xi}^+ \pi^+ \pi^-$ system.
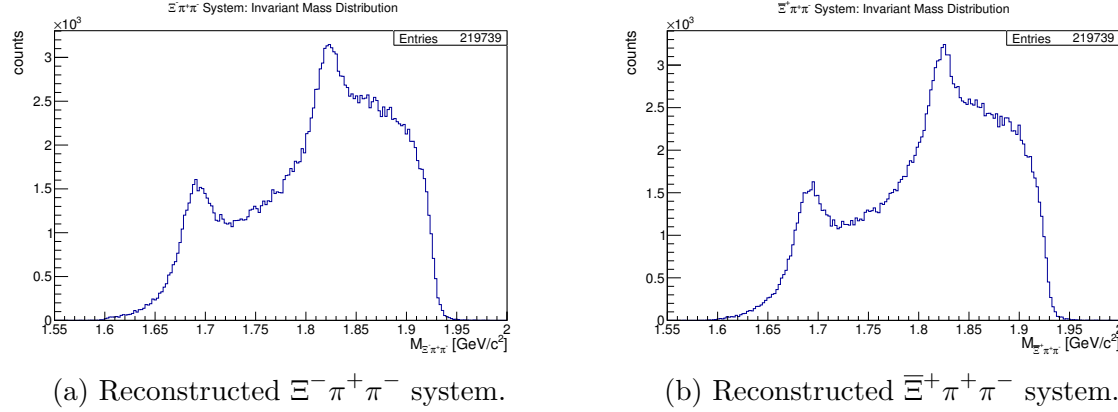
Figure 6.48: Invariant mass distribution of the $\Xi \pi^+ \pi^-$ systems.

6.3.7 Summary of the Reconstruction

Out of 3,816,000 $\Xi^- \overline{\Xi}^+ \pi^+ \pi^-$ generated events, 219,739 are reconstructed by combining the daughter particles into their mothers, starting from the final state stable particles up to the $\bar{p}p$ system. The selection of the candidates at every stage of the reconstruction is based on a threshold applied on the probability distributions of the performed kinematic fits. The chosen value is 1×10^{-4} As previously stated, this cut is unoptimized and it is meant to result in a coarse selection that can then be improved, if required by the experimental conditions (e.g., necessity to improve background suppression). Moreover, candidates that after the four-constraint fit have an unphysical invariant mass are excluded from the sample. Among the reconstructed events, 190,966 match with the MC input. That translates into a total efficiency for the reconstruction of the channel under study of 5 % and a purity of the selected sample of 87 %. The number of correctly reconstructed events corresponds to 36 % of the reconstructable events (i.e., having all the 8 final state stable particles in the MC input). A summary of the reconstruction efficiency and purity of the sample at every stage of the reconstruction is given in Table 6.5. A higher level of purity can be achieved, if needed, by tightening the selection of the $\Xi^- \overline{\Xi}^+ \pi^+ \pi^-$ system candidates, after having performed the four-constraint fit. For example, the choice of a probability threshold of 5×10^{-1} allows to select a sample with 90 % purity, at the expense of the reconstruction efficiency, which drops to 1 %.

Having performed the reconstruction of the complete decay tree, one can study the samples of the composite particles that survive the described selection and observe how they differ from the ones obtained after the intermediate reconstruction stage. Table 6.6 collects the measured values for the mass and momentum resolution of the candidates after their reconstruction and after the reconstruction of the complete decay tree. The purity for the Λ and $\overline{\Lambda}$ sample after their reconstruction is 81 % and 82 %, respectively. After the final selection the measured value is 96 % for both particle and antiparticle. The two dimensional distributions of transverse versus longitudinal momentum and
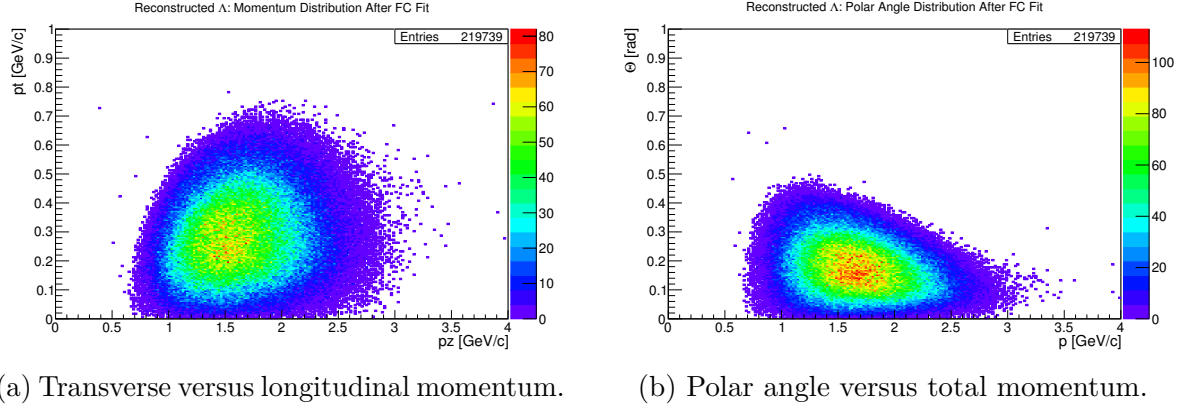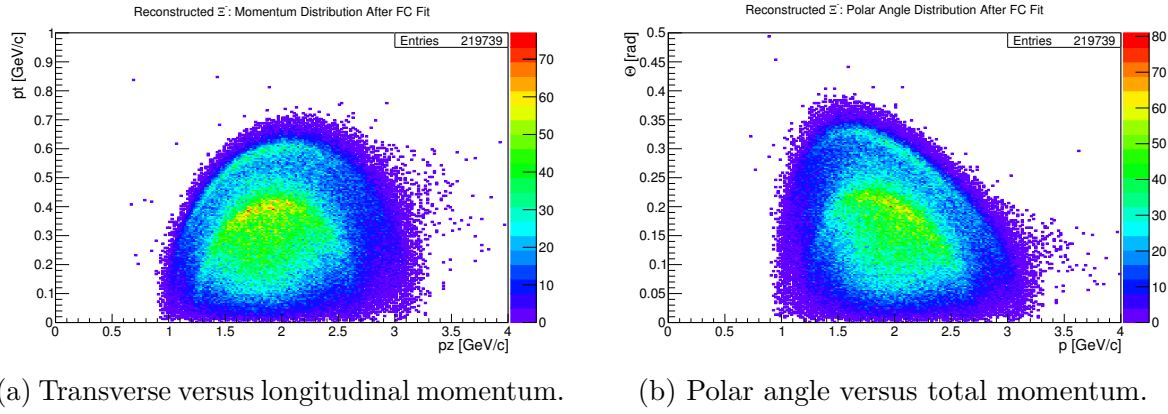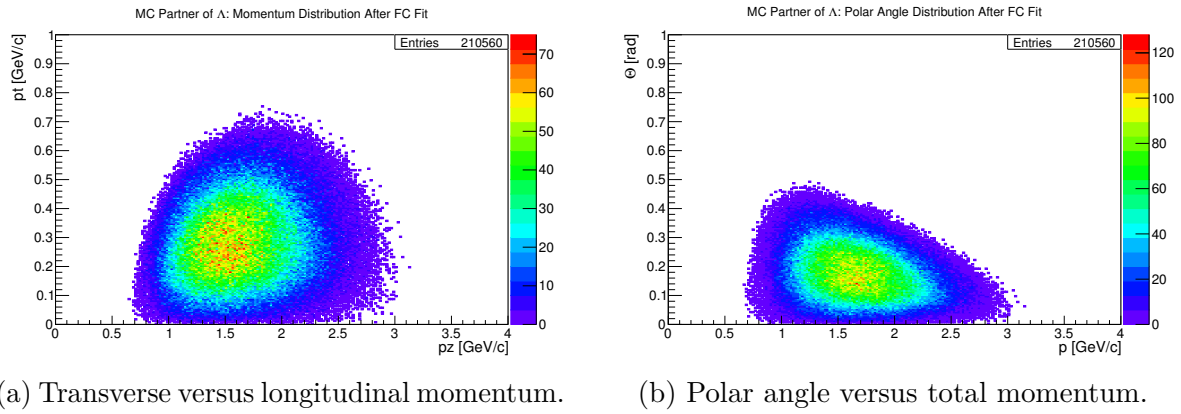
polar angle versus total momentum present a much smaller number of entries outside the main kinematic region, indicating that the final selection removes the majority of spurious reconstructed particles. Fig. 6.49 shows the distribution for the Λ case, which can be compared with Fig. 6.16. The spectra relative to $\overline{\Lambda}$ are shown in Fig. A.59. The momentum resolution is improved to $\sigma_p/p = 1.33\,\%$ for both Λ and $\overline{\Lambda}$. The mass resolution for Λ and $\overline{\Lambda}$ becomes worse after the final selection. The reason why the final selection worsens the mass resolution it is not understood at the moment. Similar to what observed in the case of the Λ baryons, the purity of the two cascades samples increases after the final selection as well: after the reconstruction of the Ξ^- and $\overline{\Xi}^+$ about 81 % of the particles had a MC partner, while after the final selection the MC match level rises to 93 % and 94 %, respectively. The two dimensional distributions of transverse versus longitudinal momentum and polar angle versus total momentum are modified in the same way as described for the Λ case (Fig. 6.50, Fig. A.74 for Ξ^- and $\overline{\Xi}^+$, respectively). The momentum resolution is significantly better: $\sigma_p/p = 0.83\,\%$ for both Ξ^- and $\overline{\Xi}^+$, as well as the mass resolution, which improves to $3.6\,\mathrm{MeV}/c^2$ and $3.7\,\mathrm{MeV}/c^2$, respectively. The MC partner distributions for finally selected Λ and Ξ^- do not show any entry outside the kinematically allowed region (Fig. 6.51, Fig. 6.52 for Λ and Ξ^-, respectively, and Fig. A.60, Fig. A.75 for their antiparticles).

Table 6.5: Reconstruction efficiencies and purity at various stages of the analysis.

Particle reconstruction stage	ϵ_{reco} [%]	purity [%]
$\pi^+\pi^-$ prompt system	65	96
Λ	54	81
$\overline{\Lambda}$	53	82
Ξ^-	34	81
$\overline{\Xi}^+$	33	82
$\Xi^-\overline{\Xi}^+\pi^+\pi^-$	5	87

Table 6.6: Momentum and mass resolution and purity for reconstructed composite particles after their reconstruction and after the full event reconstruction.

	Reconstructed			Finally selected		
	σ_p/p [%]	σ_M [MeV/c^2]	purity [%]	σ_p/p [%]	σ_M [MeV/c^2]	purity [%]
Λ	1.42	2.0	81	1.33	2.4	96
$\overline{\Lambda}$	1.42	2.0	82	1.33	2.4	96
Ξ^-	1.30	3.8	81	0.83	3.6	93
$\overline{\Xi}^+$	1.31	3.8	82	0.83	3.7	93

(a) Transverse versus longitudinal momentum.   (b) Polar angle versus total momentum.

Figure 6.49: Reconstructed Λ after final selection.

(a) Transverse versus longitudinal momentum.   (b) Polar angle versus total momentum.

Figure 6.50: Reconstructed Ξ^- after final selection.

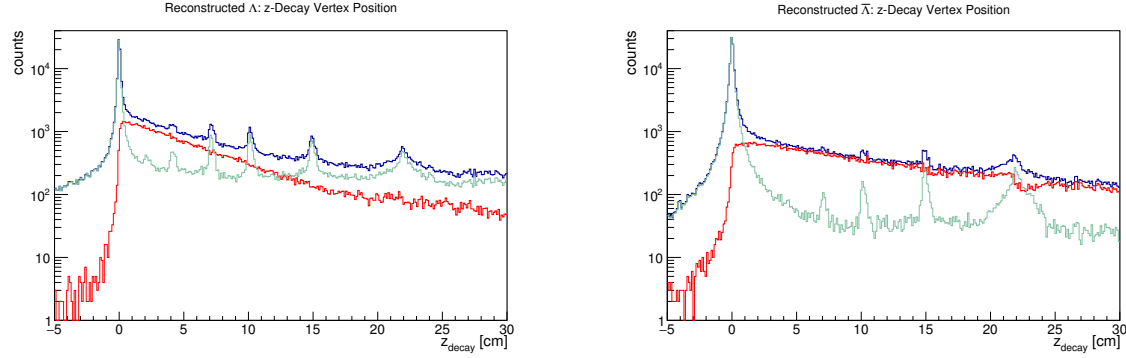(a) Transverse versus longitudinal momentum.   (b) Polar angle versus total momentum.

Figure 6.51: MC partner of reconstructed Λ after final selection.
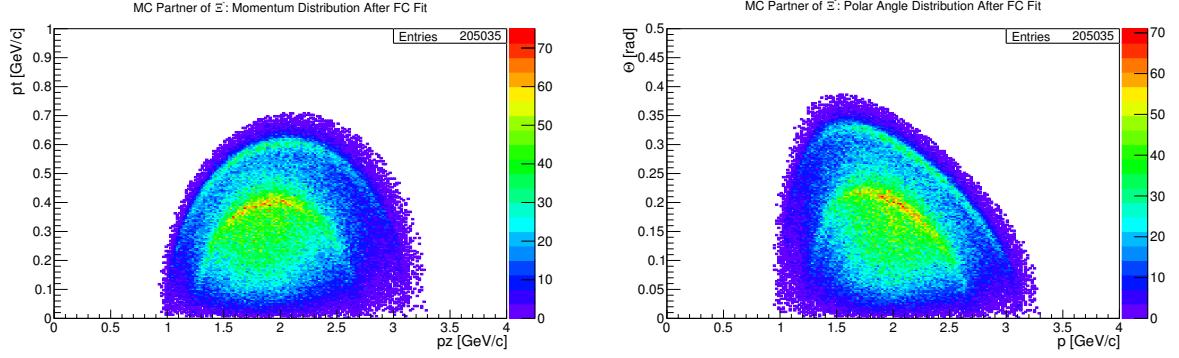
(a) Transverse versus longitudinal momentum.   (b) Polar angle versus total momentum.

Figure 6.52: MC partner of reconstructed Ξ^- after final selection.

6.3.8 Background Studies

The decay channel presented in this study is only one among many reactions that can take place in the $\overline{p}p$ collisions. In the sample studied so far, only signal reactions are present. The only background is therefore the combinatorial one. There is a certain probability that non-signal events create a topology that is similar to the channel of interest. Such cases might not be distinguishable and could be therefore wrongly reconstructed as signal events. To study the impact of the presence of the background on the reconstruction of the signal of interest 22×10^6 events have been generated using the MC generator Dual Parton Model (DPM) implemented in PandaRoot [115, 116]. The simulation of the background includes the total inelastic cross section, which is assumed to be 50 mb at 4.6 GeV/c $\overline{p}$ momentum [117–119]. The background data set is analyzed with exactly the same algorithms as described for the signal data set, including the mentioned cuts. The analysis shows that not even a single event in the sample is misidentified as a signal event. Some Ξ and prompt π are reconstructed by the algorithm, but their combination and the following application of a vertex fit, excludes that they belong to the reaction $\overline{p}p \to \Xi^-\overline{\Xi}^+\pi^+\pi^-$ (Table 6.7).

Table 6.7: Number of reconstructed candidates for the background sample.

	Reconstructed candidates
$\pi^+\pi^-$ prompt	8,925,487
Λ	320,462
$\overline{\Lambda}$	250,450
Ξ^-	28,500
$\overline{\Xi}^+$	9285
$\Xi^-\overline{\Xi}^+\pi^+\pi^-$	0

(a) Reconstructed Λ: total (blue), fake (green), and real (red).

(b) Reconstructed $\overline{\Lambda}$: total (blue), fake (green), and real (red).

Figure 6.53: Decay vertex position in the longitudinal direction for the Λ and $\overline{\Lambda}$ reconstructed candidates in the background sample. The y axis is displayed in a logarithmic scale.

Although zero $\Xi^-\overline{\Xi}{}^+\pi^+\pi^-$ candidates are found in the background sample, it is interesting to observe the distributions relative to the reconstructed composite particles, in order to find observables that might be suitable for signal filtering. The longitudinal component of the vertex position for the reconstructed Λ is shown in Fig. 6.53a. Out of the total number of reconstructed Λ, only 29 % is MC matched and the remaining 71 % corresponds to accidental combinations of a pπ pairs. The background presents a peak around the zero bin and local maxima corresponding to the position of the MVD disks. The background has a similar shape in the case of the reconstructed $\overline{\Lambda}$ (Fig. 6.53b). However, the slope of the distribution relative to the real $\overline{\Lambda}$ is less steep than in the case of the Λ, reflecting the effect of the boost, which is stronger for the $\overline{\Lambda}$. Moreover, a discontinuity around 22 cm is visible in the real $\overline{\Lambda}$ spectrum, which matches with the position of one of the MVD disks. The number of real and fake reconstructed candidates is 41 % and 59 %, respectively.

The majority of the reconstructed Ξ^- and $\overline{\Xi}{}^+$ (Fig. 6.54) are fake candidates: only 9 and 7 of them, respectively, are matched candidates.

These observations suggest that the contribution of prompt background could be removed by applying a cut around the primary vertex position.

The absence of surviving background excludes 2.30 events at the 90 % confidence level. Only a lower limit can be calculated for the signal-to-background ratio, which is given by:

$$\eta = \frac{\sigma_{sig} \cdot \epsilon_{sig} \cdot BR}{\sigma_{bkg} \cdot \epsilon_{bkg}} = 3.9.$$

In the formula the values of the total branching ratio for the signal (BR), the efficiency (ϵ), and cross-section (σ) for both signal (sig) and background (bkg) appear. The signal branching ratio BR has to be included in the formula to correct for the unphysical decay

(a) Total reconstructed Ξ^-.

(b) Total reconstructed $\overline{\Xi}^+$.
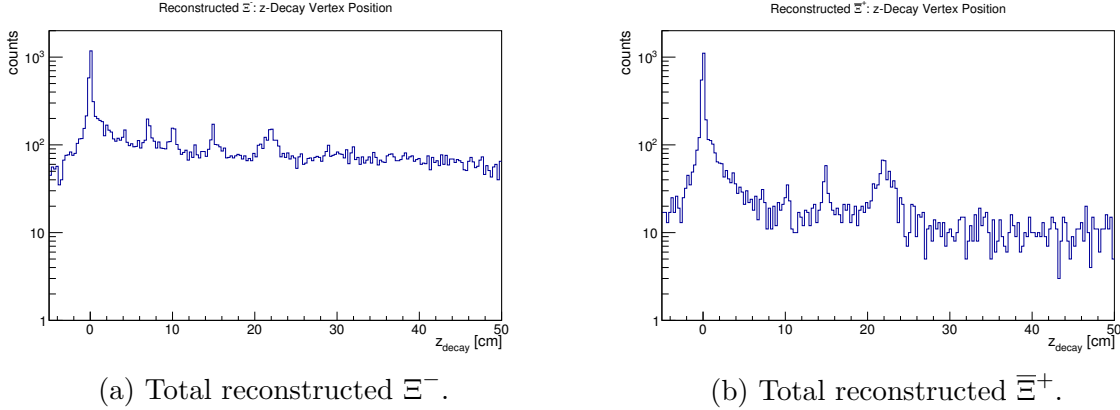
Figure 6.54: Decay vertex position in the longitudinal direction for the Ξ^- and $\overline{\Xi}^+$ reconstructed candidates in the background sample. Out of these reconstructed candidates, only 9 Ξ^- and 7 $\overline{\Xi}^+$ are MC matched and are therefore not shown. The y axis is displayed in a logarithmic scale.

ratio of 100 % used for the Λ baryons producing a pπ pair. The real value is 63.9 % and the squared value of it is used, since both Λ and $\overline{\Lambda}$ decay are present in the channel. As already specified, Ξ^- and $\overline{\Xi}^+$ decay in almost 100 % of the cases in a Λ π pair, therefore no correction is needed for these branches. It has already been mentioned that for the process $\overline{p}p \rightarrow \Xi^-\overline{\Xi}^+$ the cross section has been measured to be (2 ± 1) µb. No data are available though for the reaction including a pion pair in the final state. One can, nevertheless, give an estimate on the cross section by extrapolating from single strange hyperon-antihyperon channels. Studies on the reaction $\overline{p}p \rightarrow \Lambda\overline{\Lambda}$ at $\overline{p}$ momentum $2.434\,\text{GeV}/c$ report (127.0 ± 9.0) µb cross section [120]. For the process $\overline{p}p \rightarrow \Lambda\overline{\Lambda}\pi^+\pi^-$, including an additional pion pair in the final state, the experiments indicate a reduction of the cross section by a factor 6, on average [121, 122]. The cross sections for the channels involving $\Sigma^-\overline{\Sigma}^+$ instead of $\Lambda\overline{\Lambda}$ are measured to be (30.7 ± 9.4) µb at $2.70\,\text{GeV}/c$ and (36 ± 6) µb at $3\,\text{GeV}/c$ [108, 123]. The production of an additional pion pair in the final state reduces the cross section by a factor 2, on average. Based on these observations, one can extrapolate a lower and an upper limit for the case of $\Xi^-\overline{\Xi}^+\pi^+\pi^-$ final state from the $\Lambda\overline{\Lambda}$ and $\Sigma^-\overline{\Sigma}^+$ studies, respectively. The cross section is, therefore, assumed to lie in the range between 0.3 µb and 1 µb. A significant contribution to the pion production may be due to the final state interactions (e.g., $\Xi^-\overline{\Xi}^+ \rightarrow \Xi^-\overline{\Xi}^+\pi^+\pi^-$), which is not possible in the channels involving $\Lambda\overline{\Lambda}$. Consequently, the cross section for the reaction under study has been estimated to be 1 µb.
The signal significance is calculated as follows:

$$S = \frac{N_{sig}^{reco}}{\sqrt{N_{sig}^{reco} + N_{bkg}^{reco} \cdot F}} > 390.$$

N^{reco} is the number of reconstructed events in the case of the signal and background data

set, while F is a scaling factor for the reconstructed background events, that accounts for the difference in cross section between the generated (*gen*) signal and background events. Its value is given by:

$$F = \frac{N_{sig}^{gen}/(\sigma_{sig} \times BR)}{N_{bkg}^{gen}/\sigma_{bkg}}.$$

Having these results, it is possible to calculate the expected rate of signal events during the experiment's data taking. Assuming for the luminosity the value that will be achieved in the first phase of PANDA, the expected number of reconstructed events per day is:

$$N = \mathcal{L} \cdot \sigma_{sig} \cdot \epsilon_{sig} \cdot BR = 17{,}639.$$

According to this calculation, a sample comparable to the one reconstructed in the course of this analysis could be obtained with approximately 10 days of data taking. Table 6.8 summarizes the parameters used for the calculations.

Table 6.8: Parameters used for the background studies.

σ_{sig}	σ_{bkg}	ϵ_{sig}	ϵ_{bkg}	BR
$1\,\mu b$	$50\,mb$	$5\,\%$	$1.05 \times 10^{-5}\,\%$	0.408

N_{sig}^{reco}	N_{bkg}^{reco}	N_{sgn}^{gen}	N_{bkg}^{gen}	$\mathcal{L}$
$190{,}966$	2.3	3.816×10^6	22×10^6	$1 \times 10^{31}\,\mathrm{cm}^{-2}\,\mathrm{s}^{-1}$

6.3.9 Summary and Outlook

Summary

This chapter describes the first steps towards the feasibility study of the reaction $\bar{p}p \to \Xi^-\bar{\Xi}^+\pi^+\pi^-$ with PANDA, using a $\bar{p}$ beam with $4.6\,\mathrm{GeV}/c$ momentum. The continuum case is studied together with the other decay branches which involve the production of resonant Ξ states. Two different data set have been generated and analyzed: 3.816×10^6 signal events and 22×10^6 background events, representing the total inelastic $\bar{p}p$ cross section.

The $\Xi^-\bar{\Xi}^+\pi^+\pi^-$ system is reconstructed starting from the final state stable particles and moving backwards, according to the decay branches $\Xi^- \to \Lambda\pi^- \to p\pi^-\pi^-$ and $\bar{\Xi}^+ \to \bar{\Lambda}\pi^+ \to \bar{p}\pi^+\pi^+$. Since a realistic tracking algorithm for particles with displaced vertices is currently not available in the PandaRoot software, an ideal one is adopted.

To compensate for the consequent unrealistic efficiency, a filter is applied to discard final state stable particles which cause a low hit multiplicity in the innermost subdetectors, namely less than 4 hits in either the MVD, STT, or GEM. Having applied this filter, the probability to find all the 8 final state particles per event (i.e., $3\,\pi^+$, $3\,\pi^-$, 1 p, and 1 $\bar{\text{p}}$) is 14 %. The measured values for the reconstruction efficiencies are lowest for the π^- daughters of Λ (70 %) and highest for the pions coming directly from the primary interaction point (96 %). For all the species, the reconstructed candidates match to the MC input in almost 100 % of the cases. The best momentum resolution, relative to the generated input, is found for the π^- daughters of Ξ^-, while the worse is found for the π daughters of Λ, due to their average lower momenta and smaller polar angles. To reduce the combinatorial background caused by a high multiplicity of π in the final state, kinematic constraints are applied to identify the prompt pion pairs.

Moving on to the composite particles, i.e., Λ and Ξ, the selection of the best reconstructed candidate for each event is carried out by applying kinematic fits to constraint the origin of the daughter particles and the mass of the composite system they form. A coarse probability threshold of 10^{-4} is applied to the candidates after the fits. The spatial, momentum, and mass resolutions are measured for each composite species, leading to consistent results for baryon-antibaryon conjugates. The reconstruction efficiencies are around 50 % for the Λ baryons and around 30 % for the Ξ baryons.

Once the Ξ^- and $\overline{\Xi}^+$ are selected, they are further combined with the prompt pion pair to reconstruct the initial system. Two kinematic fits, on the primary vertex position and on the four-momentum vectors are applied. Among the candidates that survive a probability cut of 10^{-4}, 0.7 % have an unphysical mass and are, therefore, rejected. The overall efficiency for the reconstruction of the full decay tree is found to be 5 %, which corresponds to 36 % of the reconstructable events (i.e., with a complete set of final state stable particles in the MC).

As expected, the Goldhaber plot of the neutral $\Xi\pi$ subsystems and the two dimensional invariant mass distributions of the $\Xi\pi^+\pi^-$ give a clear indication of the presence of the reconstructed neutral resonant states and the charged resonant states, respectively.

The non-resonant background is analyzed using the same algorithm as for the signal sample, including the mentioned cuts. Out of 22×10^6 events, not even a single $\Xi^-\overline{\Xi}^+\pi^+\pi^-$ candidate is found. Since some intermediate particles are reconstructed, possible observables, which can be used to filter the signal in presence of background, are identified. For example, a cut around the primary interaction vertex is a good candidate to reduce the contribution of the prompt background.

Based on the assumption that the signal and background cross section are 1 µb and 50 mb, respectively, the signal to background ratio and a lower limit for the significance are estimated. Their values are $\eta = 3.9$ and $S > 390$, respectively. It is calculated that a sample comparable in size to the reconstructed sample in this analysis can be collected in about 10 days of data taking during the initial phase of PANDA.

Discussion and Outlook

The tools developed for this analysis prove to be suitable to study the process $\bar{p}p \to \Xi^- \bar{\Xi}^+ \pi^+ \pi^-$, including the decays of the baryons and antibaryons and the produced Ξ resonant states. The limiting factor for the reconstruction efficiency is the combined acceptance of all the 8 final state particles. On the other hand, the topology of the decay provides a good intrinsic suppression of the background. The adopted cuts can be further optimized to maximize the significance and enhance the signal-to-background ratio. In order to do that, more input from background data simulation is necessary. One order of magnitude more statistics would already allow to make more realistic estimations. Moreover, the use of a second background generator could be considered, with the aim to reduce the model dependency of the results.

The present study assumes a uniform phase space distribution for the generation of the signal events, since no data, nor theoretical predictions are available at present for this channel. A future follow up study could include the impact on the reconstruction of a non-uniform angular distribution (e.g. the one measured in $\bar{p}p \to \Lambda\bar{\Lambda}$). An essential next study is the effect of realistic tracking, when it will be suitable in the case of particles with displaced vertices as well, and realistic particle identification algorithms.

The use of the kinematic fits available in PandaRoot shows some critical issues whose origins need to be understood and possibly removed. The evaluation of useful observables, such as the Distance of Closest Approach (DOCA) of the daughters of the composite particles (i.e., Λ, Ξ), could not be carried out within this study, due to some problems in the software implementation. A valid option for the future would be to repeat the study by exploiting a different fitter, called decay tree fitter, available in the PandaRoot software. Its evaluation is ongoing and it is showing promising results.

The calculated value for the expected event rate indicates that good statistics can be collected in a few weeks, during the first phase of data taking with PANDA. This will contribute to the formulation and verification of theoretical models in the double strange baryon sector and improve the knowledge and understanding of the strong interaction in hyperons.

Chapter 7

Conclusions

During this work of thesis three main topics have been covered: the contribution to the development of a data acquisition system for the front-end ASIC prototypes of the PANDA MVD, the evaluation of the performance of the first version of the strip ASIC PASTA, and the study of the reaction $\overline{\mathrm{p}}\mathrm{p} \to \Xi^-\overline{\Xi}^+\pi^+\pi^-$ within the PandaRoot framework.

7.1   Developments for the JDRS

The JDRS is a readout system intended to be used to test the prototypes of the front-end ASICs of the PANDA MVD. It features a combination of off-the-shelf components (i.e., the ML605 evaluation kit) and custom elements (i.e., the board that hosts the ASIC under evaluation). The deployment of a fully functional front-end requires several development and production iterations. This demands that the data acquisition system is highly flexible, in order to adapt to the different versions of the chips. Therefore, a clear distinction between resources that can be shared or reused and ASIC specific (or version specific) resources is desired. The developments concerning the JDRS described in this thesis address exactly this aspect.

The existing project has been restructured in order to achieve the mentioned modularity and enhance the reusability of the resources. Additionally, the integration of the first version of the strip front-end ASIC (PASTA) in the JDRS lead to several additional implementations, in the FPGA logic as well as in the software part. First of all, several modules to communicate with the ASIC and control it (i.e., handle its configuration) have been implemented. Subsequently, several routines to automatize measurements and visualize the results in real time have been added, to facilitate the calibration procedures and the assessment of the performance of the chip. With the newly implemented features, the JDRS allows to operate PASTA in various conditions, e.g., in a laboratory

environments where the event rate is low, as well as during irradiation with an ionizing particle beam, where the event rate increases significantly.

The operation of the data acquisition proved to be reliable and stable throughout long lasting calibration runs, as well as during data taking in presence of a particle beam. The modularity of the system and consequently the ease to apply modifications played a key role when the implementation of new features was necessary. Additionally, the user-friendly interface allowed even inexperienced users to operate the system without effort. Furthermore, the synchronization of the JDRS with an external system during beam test operation has been successfully performed.

7.2   Verification of PASTA

The first prototype of PASTA has been evaluated by using its internal charge injection mechanism, as well as under a proton beam. Preliminary tests to establish a stable communication with the device confirmed that all the foreseen configuration operations can be carried out reliably. The ASIC responded to stimuli and produced data that could be received on the PC.

Some critical issues have been found during the calibration procedures. The significant number of configuration parameters and their wide variations resulted in the impossibility to find an operational point suitable for proper operation of all the 64 channels (e.g., threshold calibration parameters). The measurements showed that with this prototype it is not possible to reliably detect deposited charges in the low end of the working range of PASTA. Moreover, it has been observed that the internal circuit for charge generation has a too low sensitivity in this region. Studies on the dependency of the response of PASTA on the readout frequency revealed that it cannot be operated at the nominal frequency of 160 MHz. Moreover, a significant data loss is noticeable for frequencies above 100 MHz. As a consequence, the requirements of the experiment, which demand a time resolution better than 10 ns, are not met.

The response of the front-end as a function of the deposited charge confirmed the expected linear behavior for approximately half of the total number of channels. The power consumption of the full ASIC has been measured to be below the requirements, at an operation frequency corresponding to half of the nominal one.

7.3   Reconstruction and Analysis of $\overline{\mathrm{p}}\mathrm{p} \rightarrow \Xi^-\overline{\Xi}^+\pi^+\pi^-$

The reaction $\overline{\mathrm{p}}\mathrm{p} \rightarrow \Xi^-\overline{\Xi}^+\pi^+\pi^-$ has been studied using the PandaRoot framework, on a sample of 3.816×10^6 events. The signal sample included the non-resonant decay

branch as well as all the kinematically allowed decay branches involving Ξ resonances. A background sample of 22×10^6 events has been analyzed as well. The analysis strategy, applied to both generated samples, foresees the reconstruction of the decay channel starting from the final state stable particles and moving backwards up to the p$\bar{\text{p}}$ system. The quality of the signal reconstruction has been evaluated in terms of reconstruction efficiency, spacial, momentum, and mass resolution at various stages of the analysis. Moreover, the signal-to-background ratio and the significance have been calculated.

The selection of particle candidates for the reconstruction of the channel under study was based on a probability cut applied on the result of kinematic fits implemented in PandaRoot. Constraints were applied on the point of origin of daughter particles, on the mass of the composite candidates (i.e., Λ, Ξ and antiparticles), and on the four-momentum of the initial state. The use of these kinematic fits showed some critical issues, which will require further investigation.

The total efficiency for the reconstruction has been measured to be $5\,\%$. A significant limiting factor was the combined acceptance of the 8 tracks in the final state. Despite the relatively low efficiency, both the neutral and charged resonant states could be clearly reconstructed.

The analyzed decay channel presented a good intrinsic background suppression. In fact, not even a single event was reconstructed after the analysis of the background sample. Since the number of generated background events was rather small, more statistics is needed to have a more realistic picture. A few observables that can be useful for signal filtering in presence of background have been identified. The absence of surviving background events excludes 2.30 events at the $90\,\%$ confidence level. Under this assumption, the signal-to-background ratio and the significance are $\eta > 3.9$ and $S > 390$, respectively.

Appendix A

Additional Plots

A.1 Final State Particles
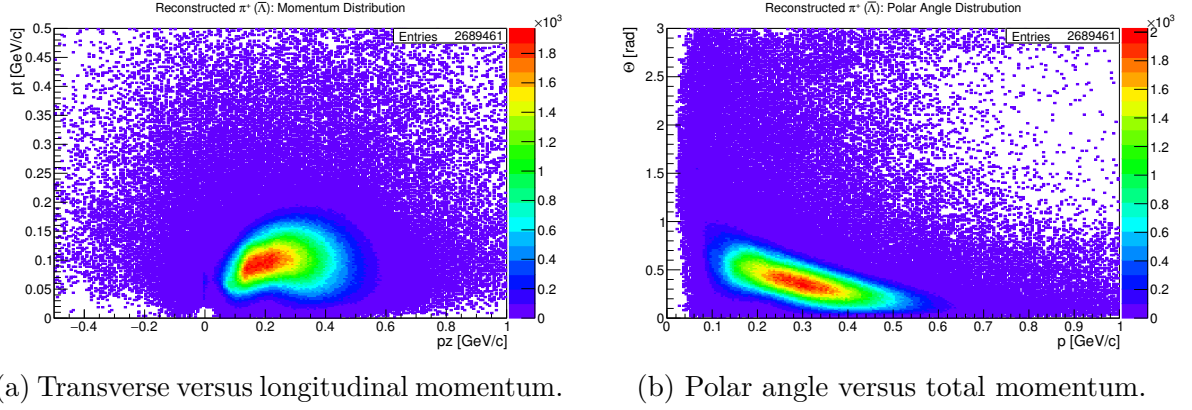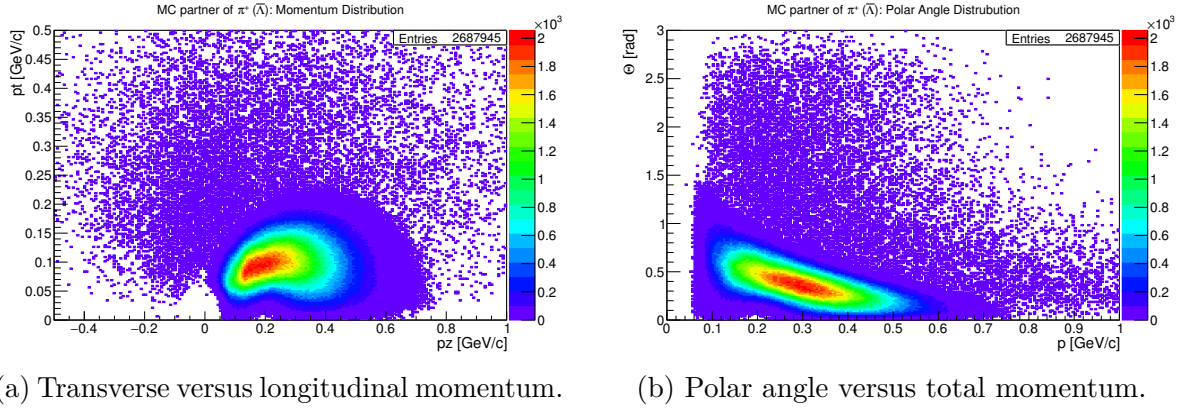
A.1.1 $\bar{\mathrm{p}}$
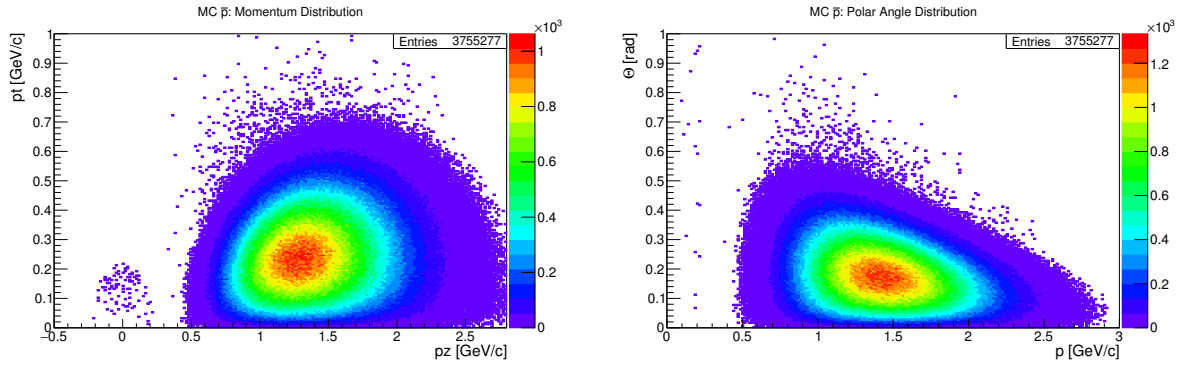
(a) Transverse versus longitudinal momentum.

(b) Polar angle versus total momentum.

Figure A.1: MC generated $\bar{\mathrm{p}}$ coming from $\bar{\Lambda}$ decay.

(a) Transverse versus longitudinal momentum.   (b) Polar angle versus total momentum.
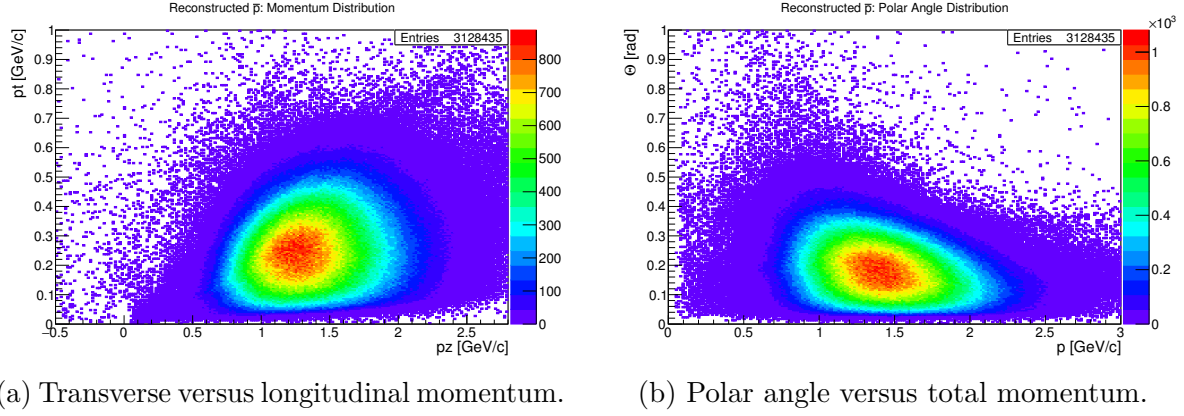
Figure A.2: Reconstructed $\overline{p}$ coming from $\overline{\Lambda}$ decay.

(a) Transverse versus longitudinal momentum.   (b) Polar angle versus total momentum.
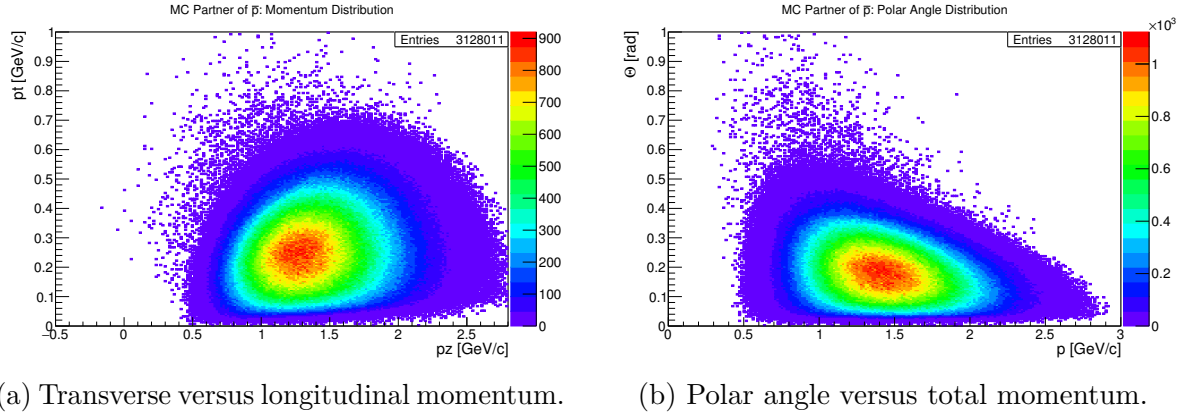
Figure A.3: MC partners of reconstructed $\overline{p}$ coming from $\overline{\Lambda}$ decay.

(a) Transverse versus longitudinal momentum.   (b) Polar angle versus total momentum.
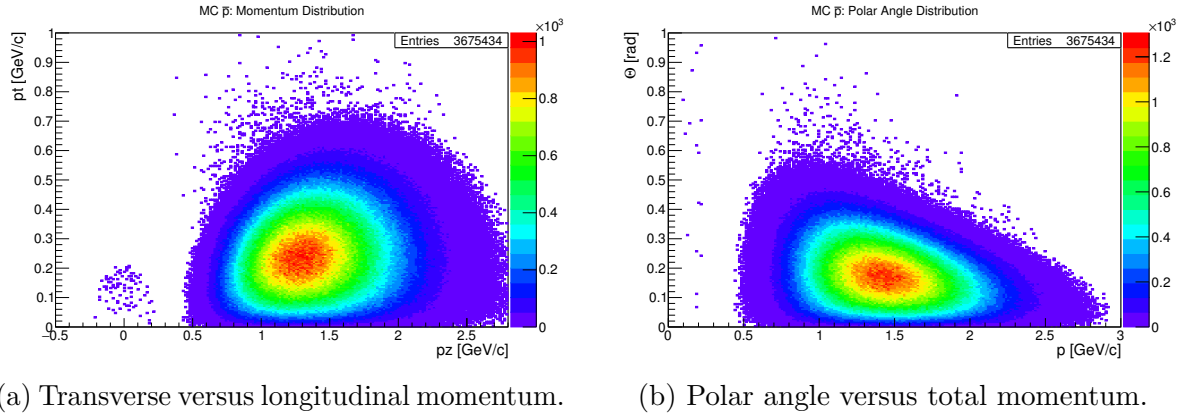
Figure A.4: MC generated $\overline{p}$ coming from $\overline{\Lambda}$ decay with more stringent selection criteria, as explained in the text.
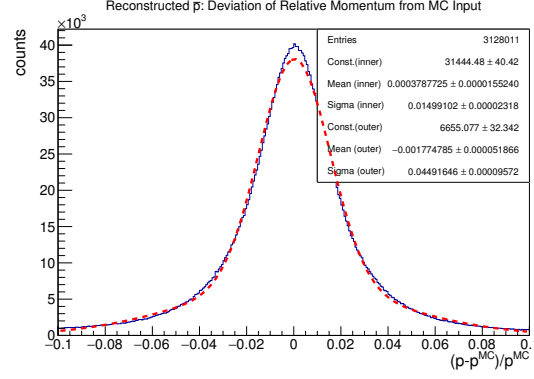
Figure A.5: Relative deviation of the reconstructed $\bar{\text{p}}$ momentum from the MC value distribution with a double gaussian fit.
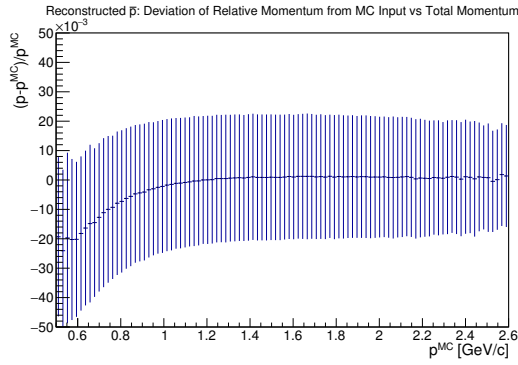
Figure A.6: Relative deviation of the reconstructed $\bar{\text{p}}$ momentum from the MC value as a function of the total momentum for the $\bar{\text{p}}$.
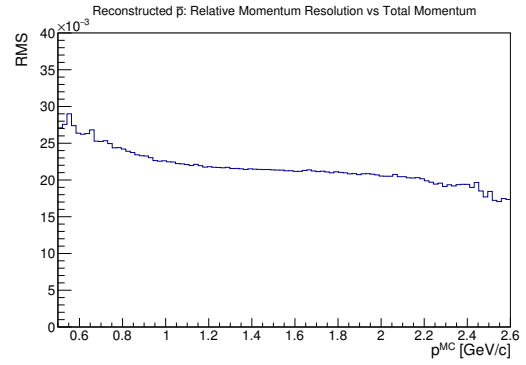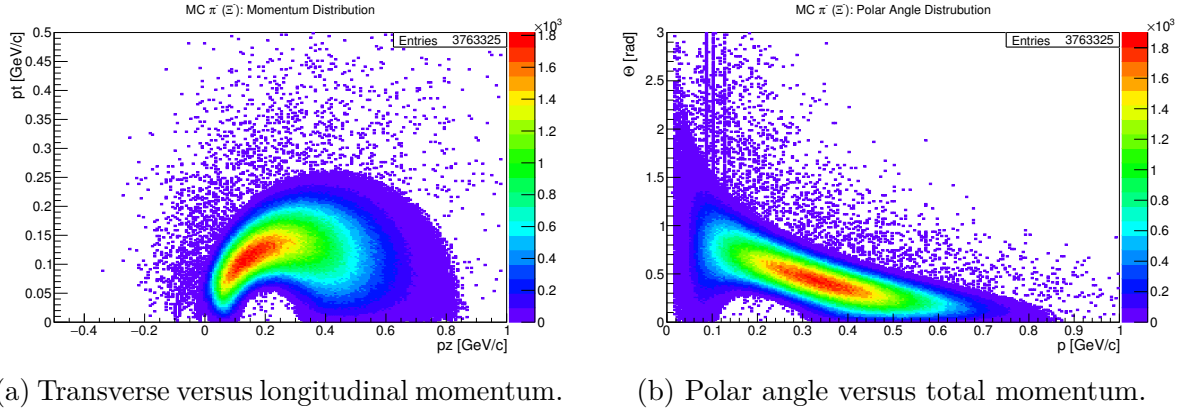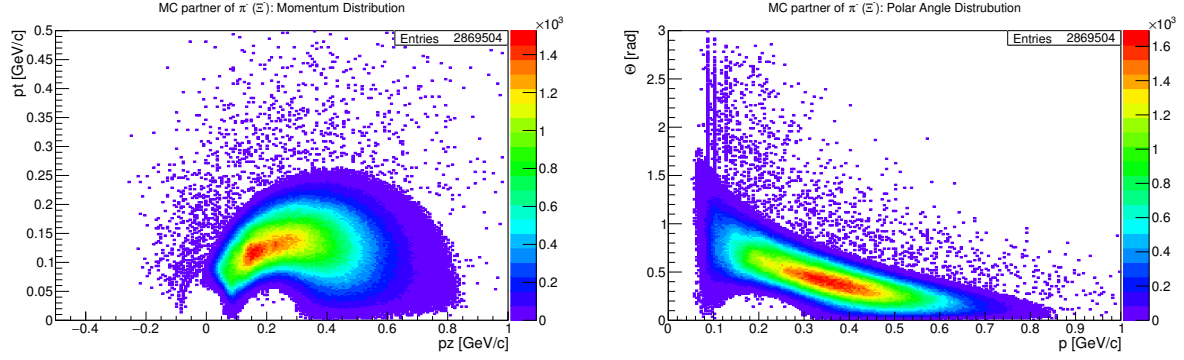

Figure A.7: Dependence of the relative momentum resolution on the total momentum.

A.1.2 π^- from Λ Decay
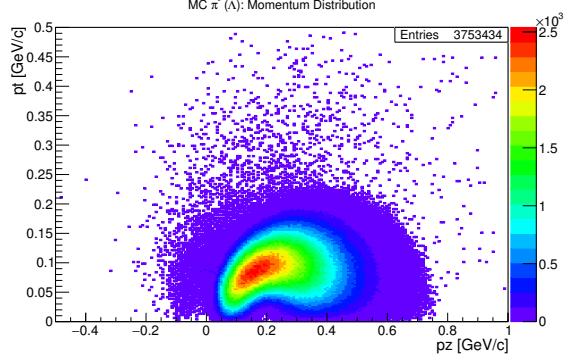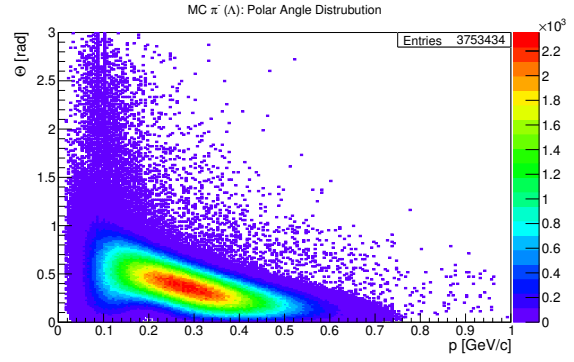
(a) Transverse versus longitudinal momentum.   (b) Polar angle versus total momentum.

Figure A.8: MC generated π^- coming from Λ decay.
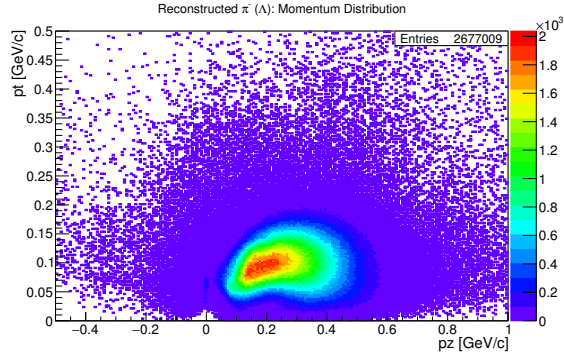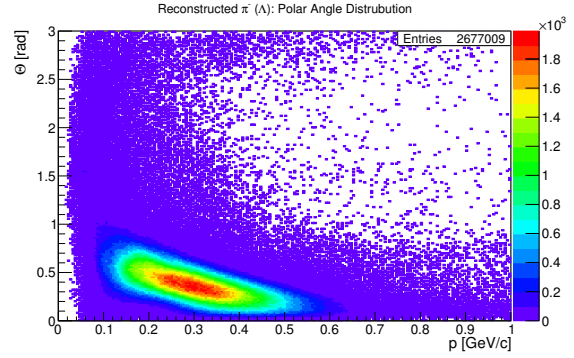
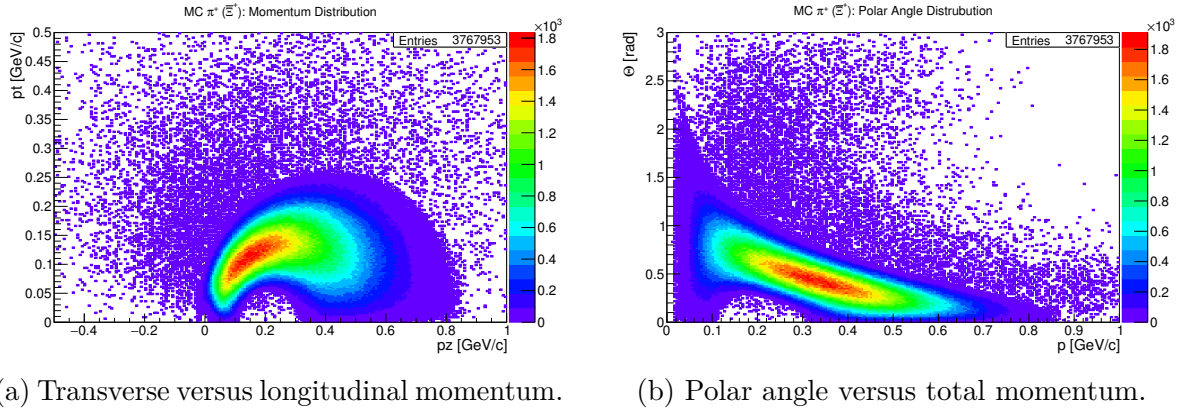(a) Transverse versus longitudinal momentum.   (b) Polar angle versus total momentum.

Figure A.9: Reconstructed π^- coming from Λ decay.
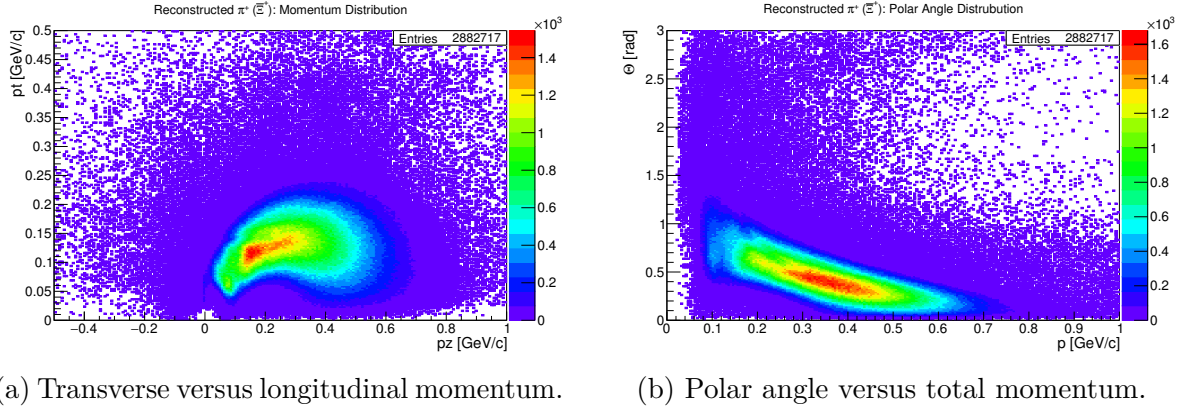
(a) Transverse versus longitudinal momentum.
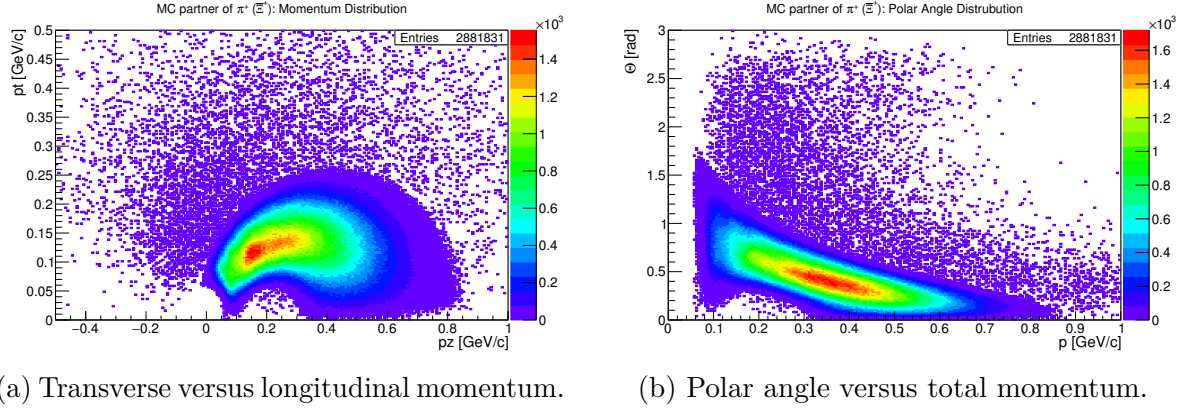
(b) Polar angle versus total momentum.
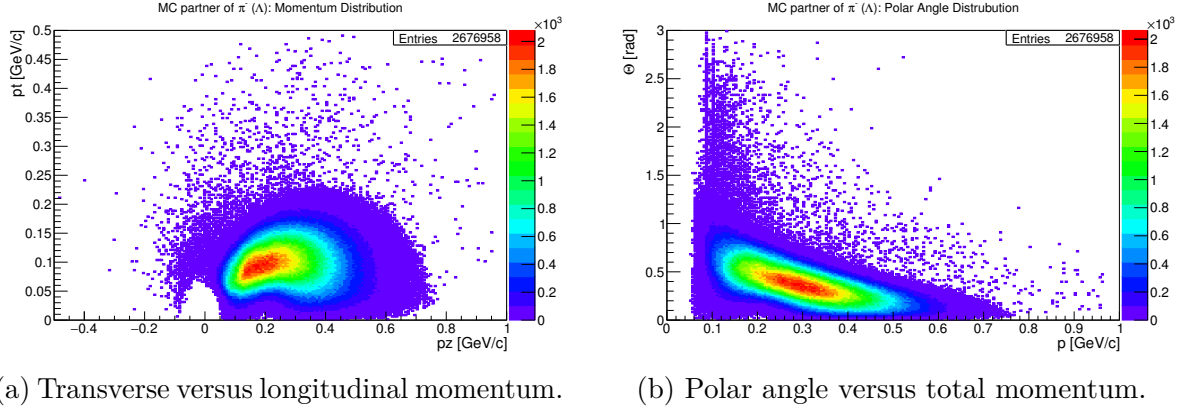
Figure A.10: MC partners of reconstructed π^- coming from Λ decay.

(a) Transverse versus longitudinal momentum.

(b) Polar angle versus total momentum.
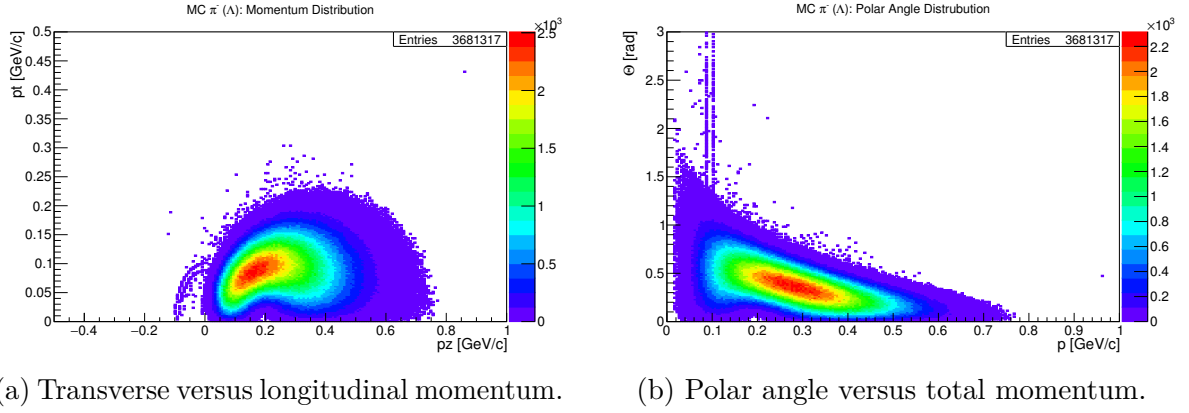
Figure A.11: MC generated π^- coming from Λ decay with more stringent selection criteria, as explained in the text.
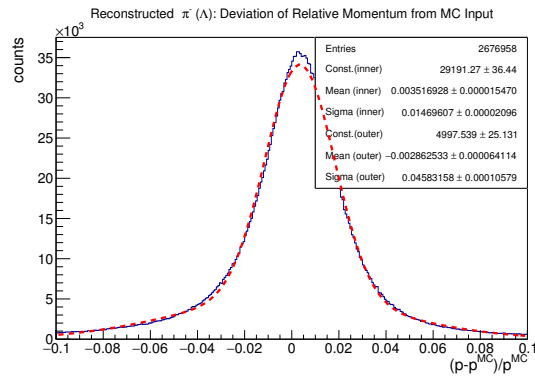
Figure A.12: Relative deviation of the reconstructed momentum from the MC value distribution with a double gaussian fit for the π^- coming from Λ decay.
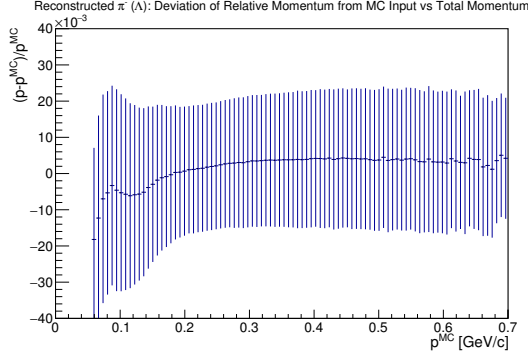
Figure A.13: Relative deviation of the reconstructed momentum from the MC value as a function of the total momentum for the π^- daughters of Λ.
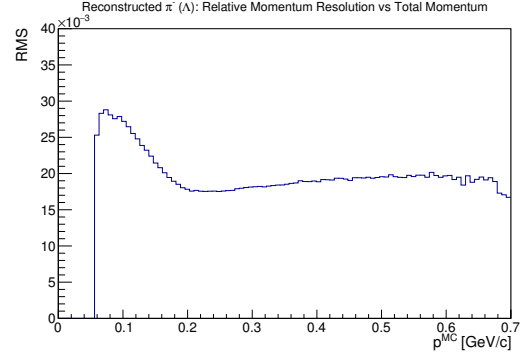
Figure A.14: Dependence of the relative momentum resolution on the total momentum for the π^- daughters of Λ.
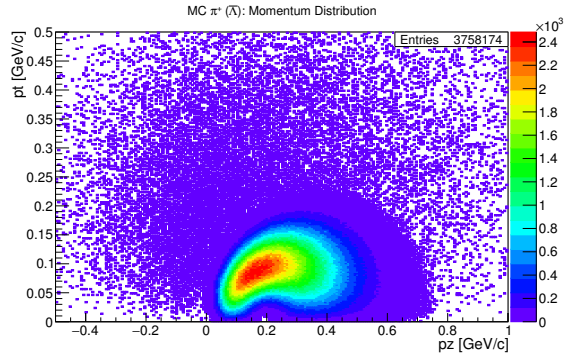
A.1.3 π^+ from $\overline{\Lambda}$ Decay

(a) Transverse versus longitudinal momentum.
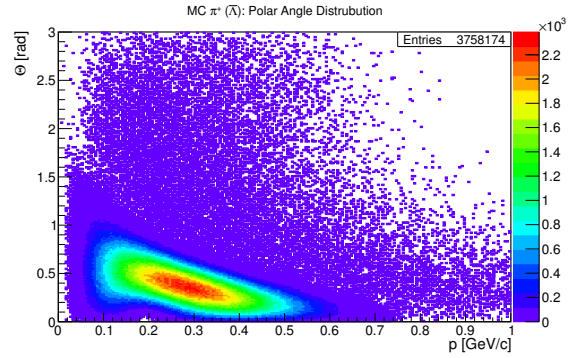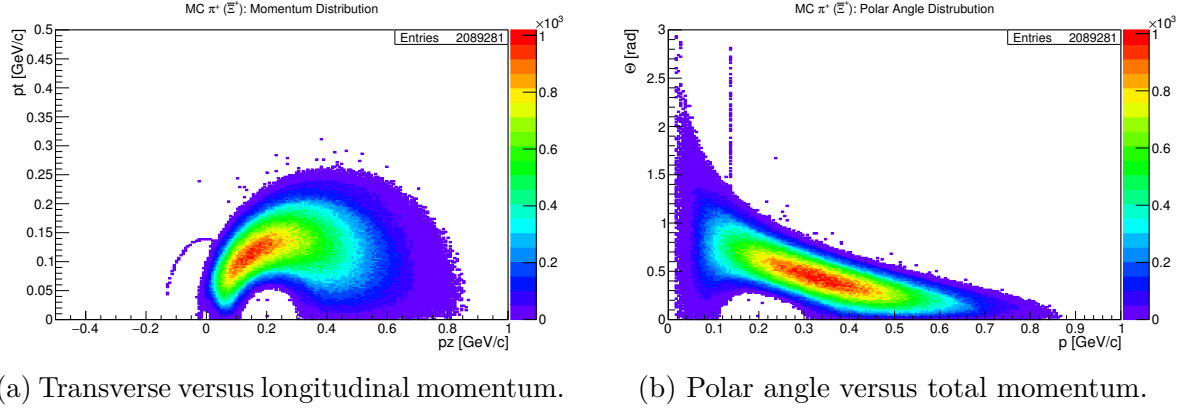

(b) Polar angle versus total momentum.

Figure A.15: MC generated π^+ coming from $\overline{\Lambda}$ decay.

(a) Transverse versus longitudinal momentum.

(b) Polar angle versus total momentum.

Figure A.16: Reconstructed π^+ coming from $\overline{\Lambda}$ decay.

(a) Transverse versus longitudinal momentum.

(b) Polar angle versus total momentum.

Figure A.17: MC partners of reconstructed π^+ coming from $\overline{\Lambda}$ decay.

(a) Transverse versus longitudinal momentum.

(b) Polar angle versus total momentum.
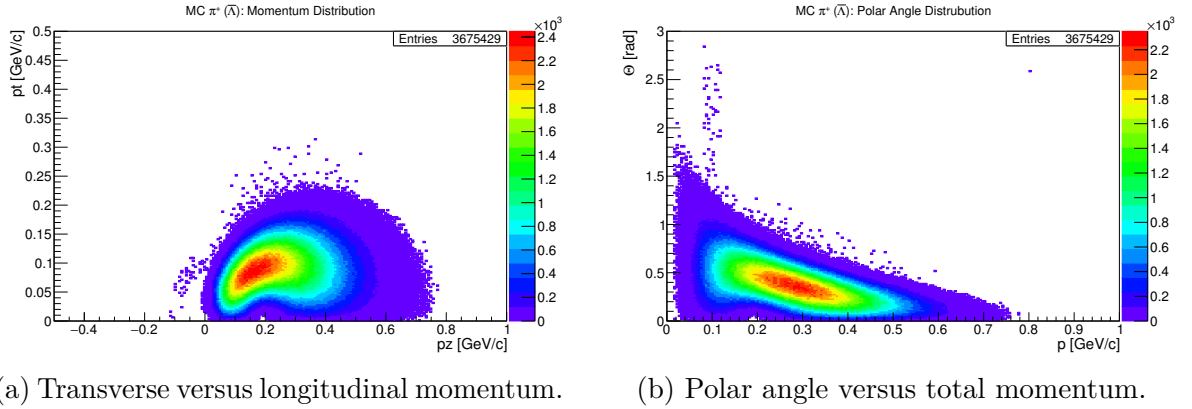
Figure A.18: MC generated π^+ coming from $\overline{\Lambda}$ decay with more stringent selection criteria, as explained in the text.
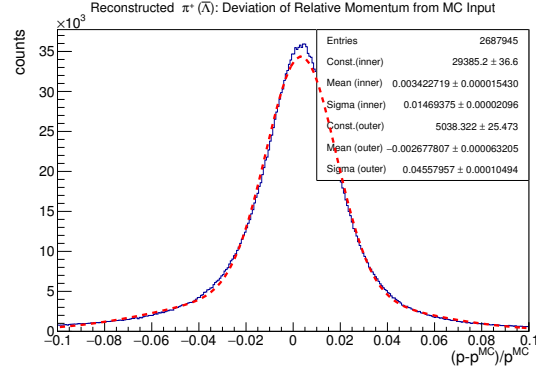
Figure A.19: Relative deviation of the reconstructed momentum from the MC value distribution with a double gaussian fit for the π^+ coming from $\overline{\Lambda}$ decay.
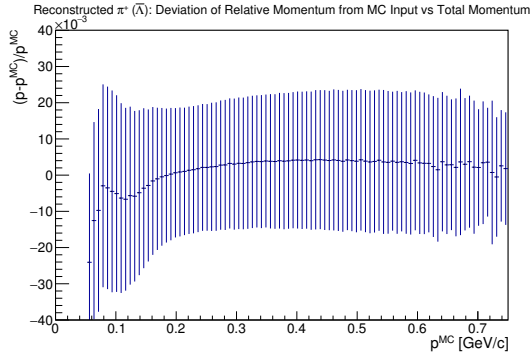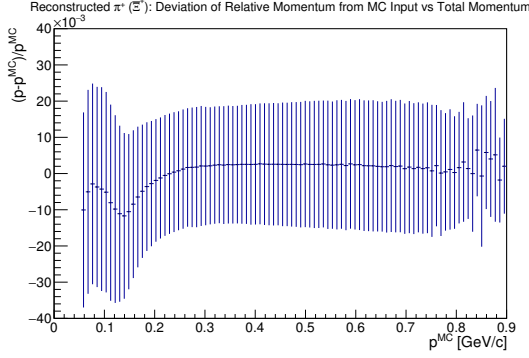

Figure A.20: Relative deviation of the reconstructed momentum from the MC value as a function of the total momentum for the π^+ daughters of $\overline{\Lambda}$.
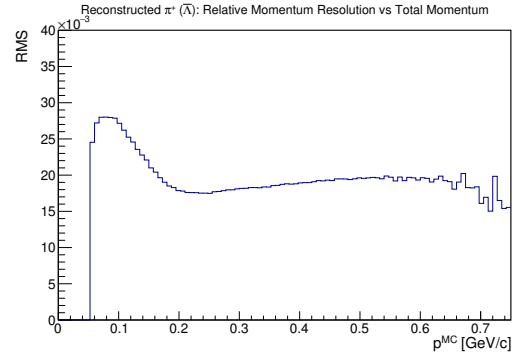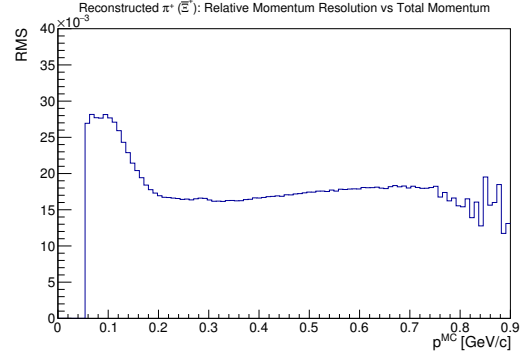

Figure A.21: Dependence of the relative momentum resolution on the total momentum for the π^+ daughters of $\overline{\Lambda}$.

A.1.4 π^- from Ξ^- Decay

(a) Transverse versus longitudinal momentum.

(b) Polar angle versus total momentum.

Figure A.22: MC generated π^- coming from Ξ^- decay.

(a) Transverse versus longitudinal momentum.

(b) Polar angle versus total momentum.
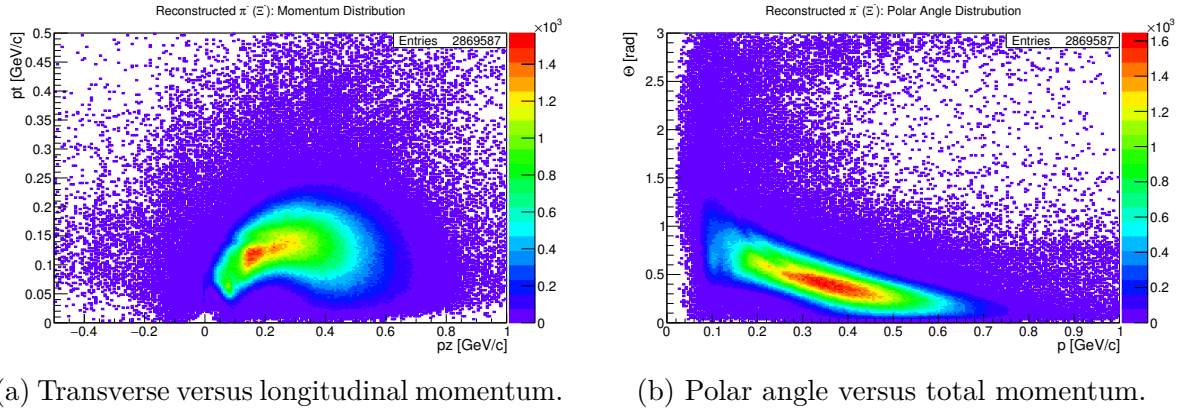
Figure A.23: Reconstructed π^- coming from Ξ^- decay.

(a) Transverse versus longitudinal momentum.   (b) Polar angle versus total momentum.

Figure A.24: MC partners of reconstructed π^- coming from Ξ^- decay.
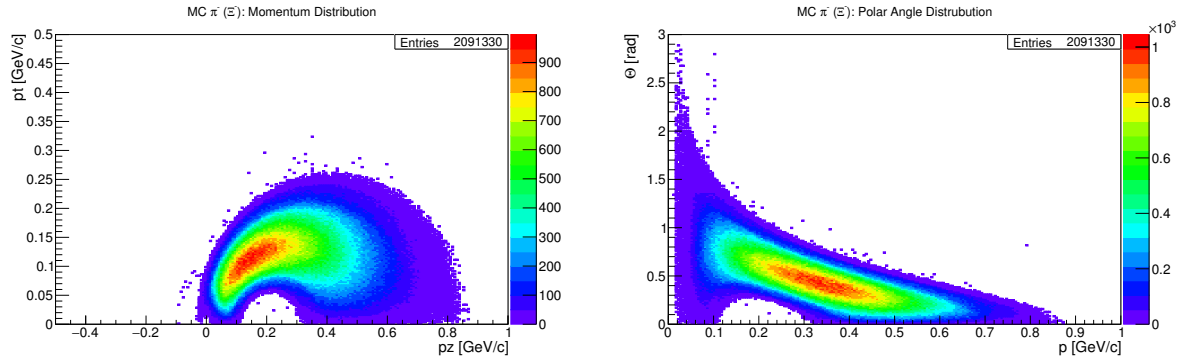
(a) Transverse versus longitudinal momentum.   (b) Polar angle versus total momentum.

Figure A.25: MC generated π^- coming from Ξ^- decay with more stringent selection criteria, as explained in the text.

A.1.5 π^+ from $\overline{\Xi}^+$ Decay

(a) Transverse versus longitudinal momentum.

(b) Polar angle versus total momentum.

Figure A.26: MC generated π^+ coming from $\overline{\Xi}^+$ decay.

(a) Transverse versus longitudinal momentum.

(b) Polar angle versus total momentum.

Figure A.27: Reconstructed π^+ coming from $\overline{\Xi}^+$ decay.

(a) Transverse versus longitudinal momentum.   (b) Polar angle versus total momentum.

Figure A.28: MC partners of reconstructed π^+ coming from $\overline{\Xi}^+$ decay.

(a) Transverse versus longitudinal momentum.   (b) Polar angle versus total momentum.

Figure A.29: MC generated π^+ coming from $\overline{\Xi}^+$ decay with more stringent selection criteria, as explained in the text.
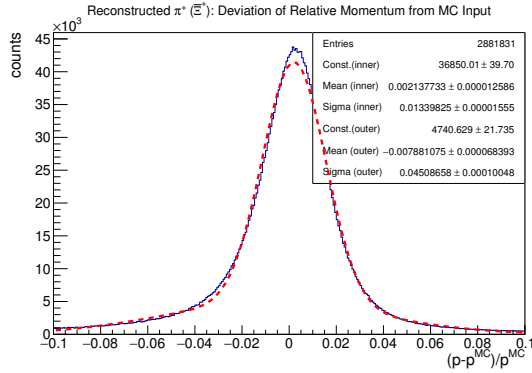
Figure A.30: Relative deviation of the reconstructed momentum from the MC value distribution with a double gaussian fit for the π^+ coming from $\overline{\Xi}^+$ decay.
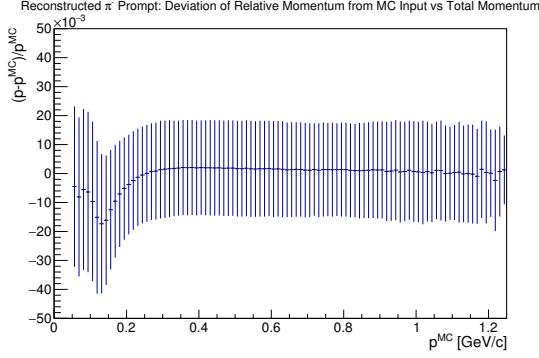
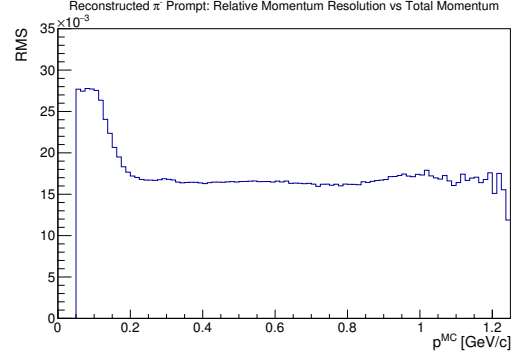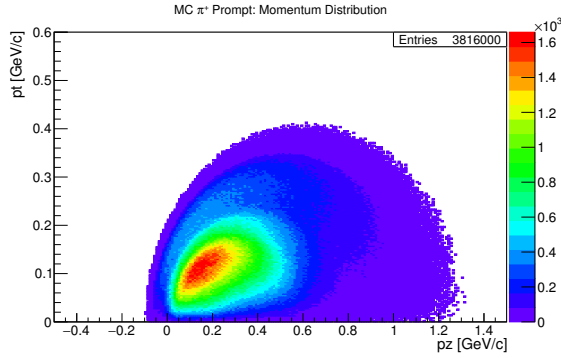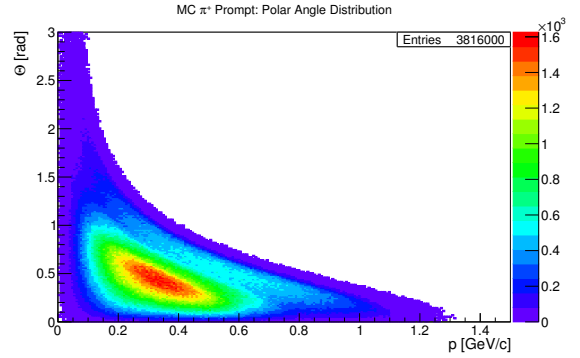Figure A.31: Relative deviation of the reconstructed momentum from the MC value as a function of the total momentum for the π^+ daughters of $\overline{\Xi}^+$.

Figure A.32: Dependence of the relative momentum resolution on the total momentum for the π^+ daughters of $\overline{\Xi}^+$.
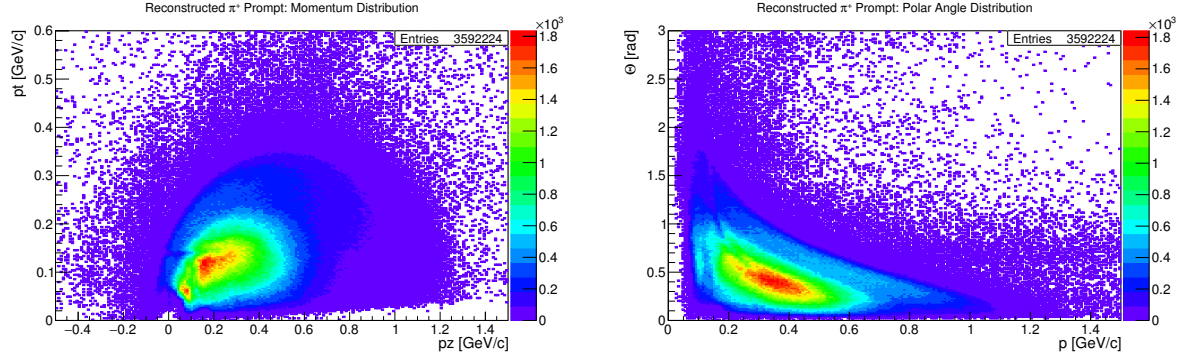
A.1.6 π^- Prompt
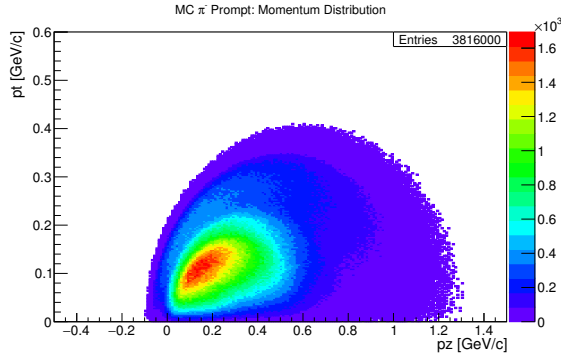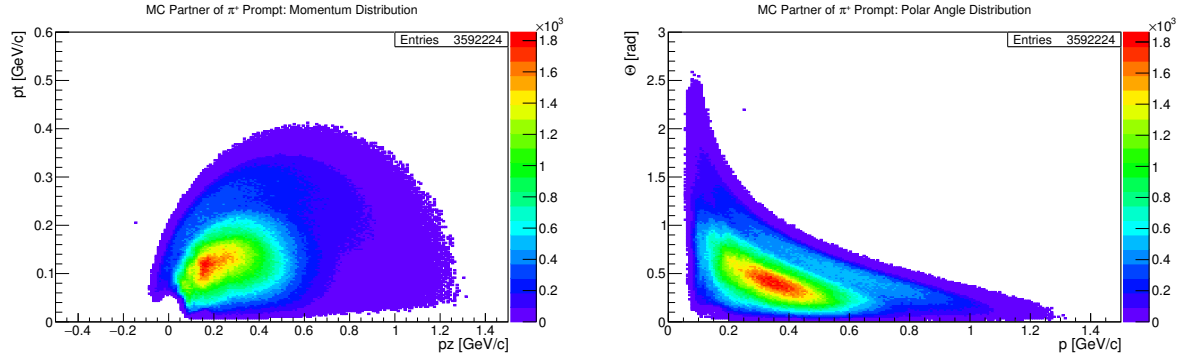

(a) Transverse versus longitudinal momentum.
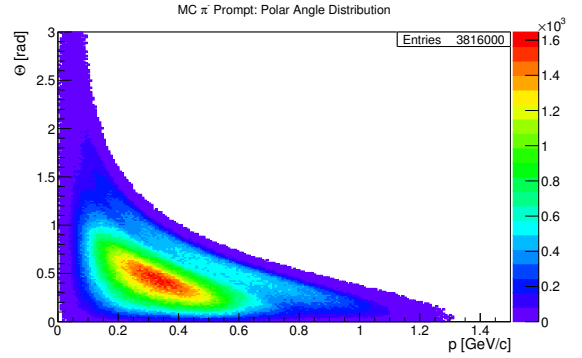
(b) Polar angle versus total momentum.

Figure A.33: MC generated π^- prompt.
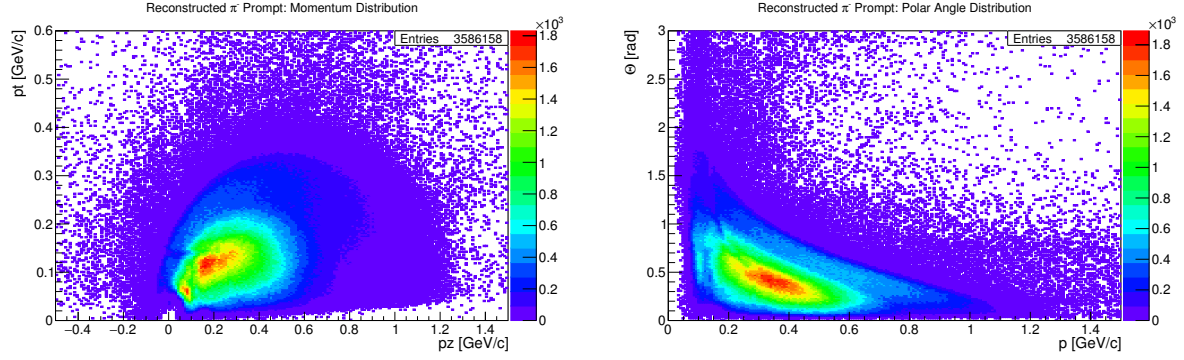
(a) Transverse versus longitudinal momentum.

(b) Polar angle versus total momentum.

Figure A.34: Reconstructed π^- prompt.
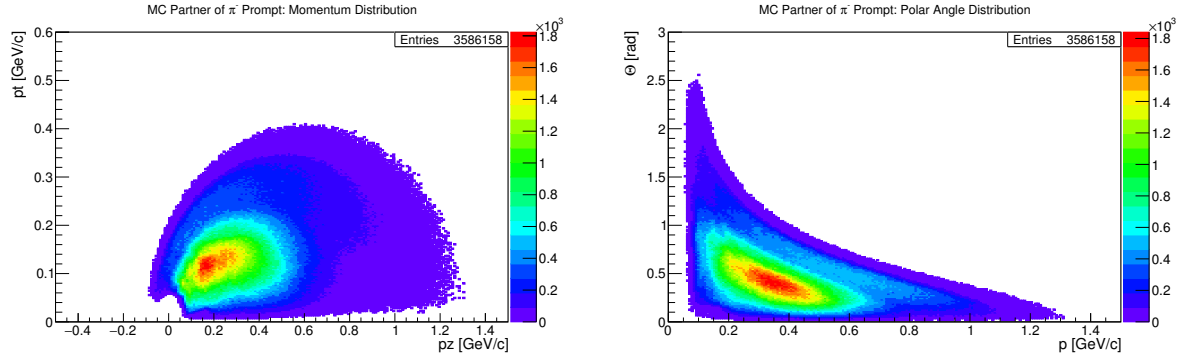
(a) Transverse versus longitudinal momentum.

(b) Polar angle versus total momentum.

Figure A.35: MC partners of reconstructed π^- prompt.
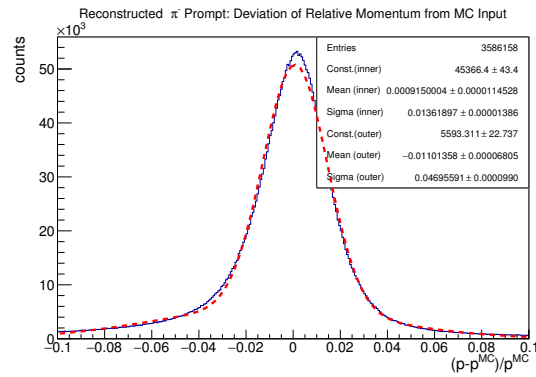
Figure A.36: Relative deviation of the reconstructed momentum from the MC value distribution with a double gaussian fit for the π^- prompt.

Figure A.37: Relative deviation of the reconstructed momentum from the MC value as a function of the total momentum for the π^- prompt.

Figure A.38: Dependence of the relative momentum resolution on the total momentum for the π^- prompt.

A.1.7 π^+ Prompt

(a) Transverse versus longitudinal momentum.

(b) Polar angle versus total momentum.

Figure A.39: MC generated π^+ prompt.

(a) Transverse versus longitudinal momentum.   (b) Polar angle versus total momentum.

Figure A.40: Reconstructed π^+ prompt.

(a) Transverse versus longitudinal momentum.   (b) Polar angle versus total momentum.

Figure A.41: MC partners of reconstructed π^+ prompt.
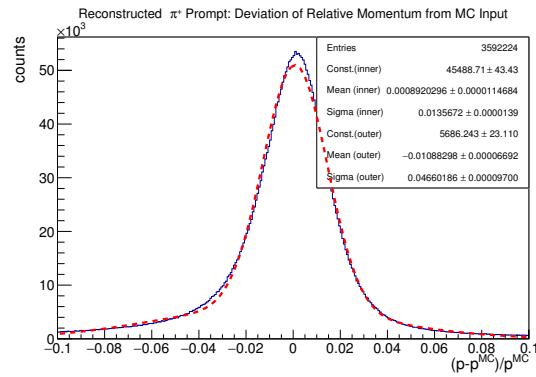
Figure A.42: Relative deviation of the reconstructed momentum from the MC value distribution with a double gaussian fit for the π^+ prompt.
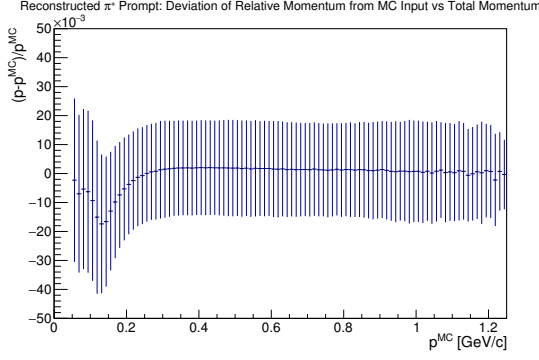
Figure A.43: Relative deviation of the reconstructed momentum from the MC value as a function of the total momentum for the π^+ prompt.
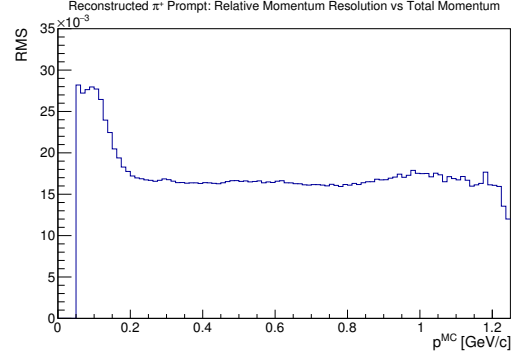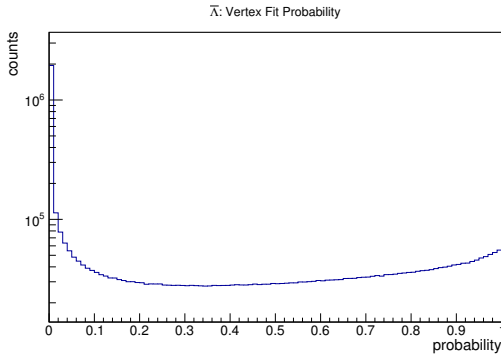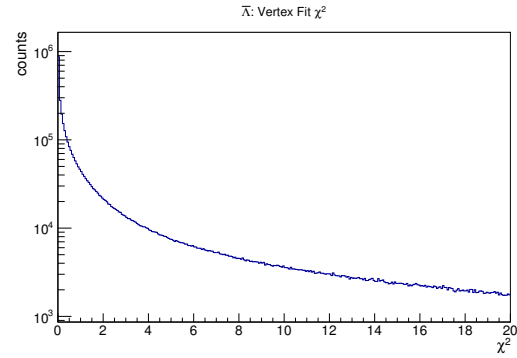

Figure A.44: Dependence of the relative momentum resolution on the total momentum for the π^+ prompt.
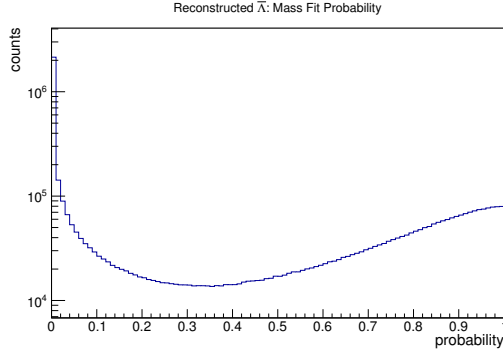
A.2 Composite Particles

A.2.1 $\overline{\Lambda}$

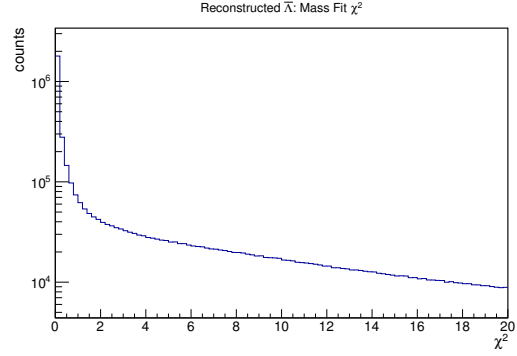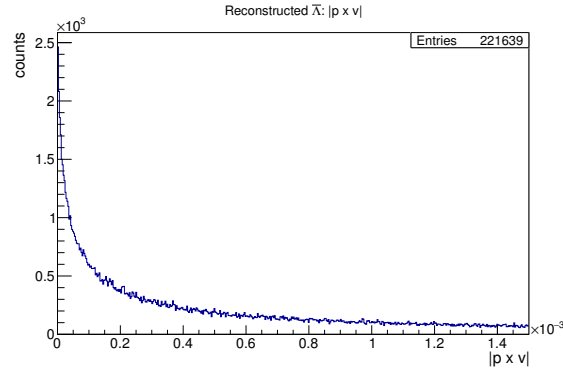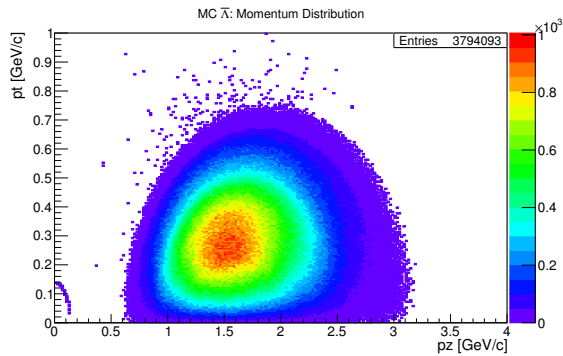(a) Probability distribution.

(b) χ^2 distribution.

Figure A.45: Quality of the vertex fit on $\overline{\Lambda}$ candidates.

(a) Probability distribution.

(b) χ^2 distribution.

Figure A.46: Quality of the mass constraint fit on $\overline{\Lambda}$ candidates.

Figure A.47: Distribution of the norm of the cross product between the $\overline{\Lambda}$ momentum vector and the position difference between the $\overline{\Lambda}$ vertex and the $\overline{\Xi}^+$ vertex.

(a) Transverse versus longitudinal momentum.
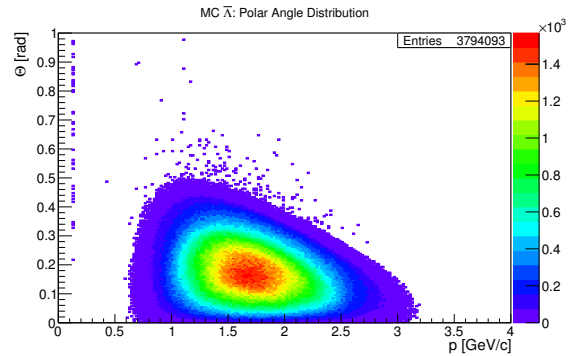
(b) Polar angle versus total momentum.

Figure A.48: MC generated $\overline{\Lambda}$.

(a) Transverse versus longitudinal momentum.

(b) Polar angle versus total momentum.
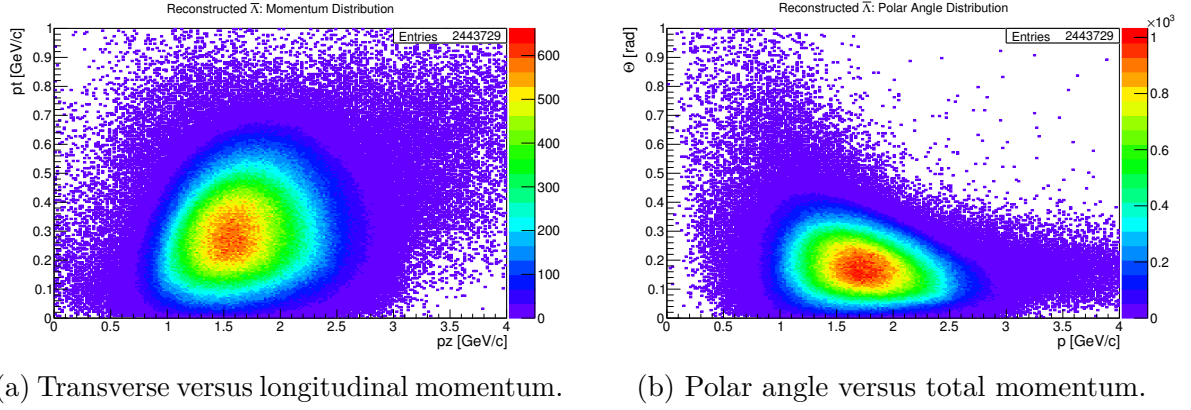
Figure A.49: Reconstructed $\overline{\Lambda}$.

(a) Transverse versus longitudinal momentum.

(b) Polar angle versus total momentum.
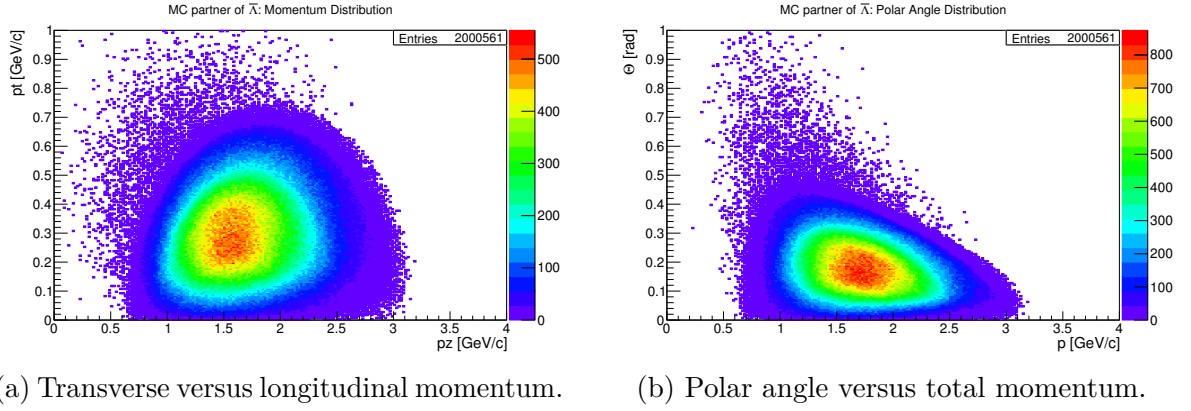
Figure A.50: MC partners of reconstructed $\overline{\Lambda}$.

(a) Transverse versus longitudinal momentum.

(b) Polar angle versus total momentum.
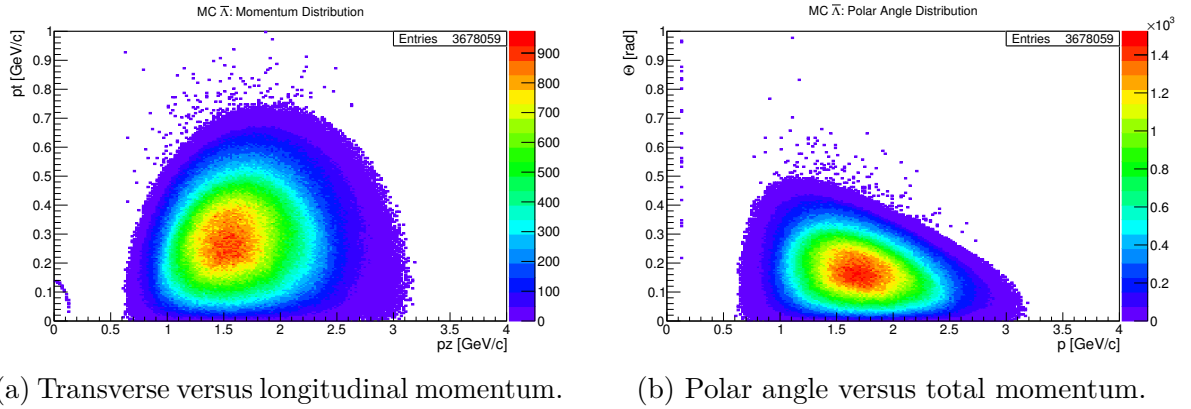
Figure A.51: MC generated $\overline{\Lambda}$ with more stringent selection criteria, as explained in the text.

(a) x-coordinate

(b) y-coordinate

(c) z-coordinate
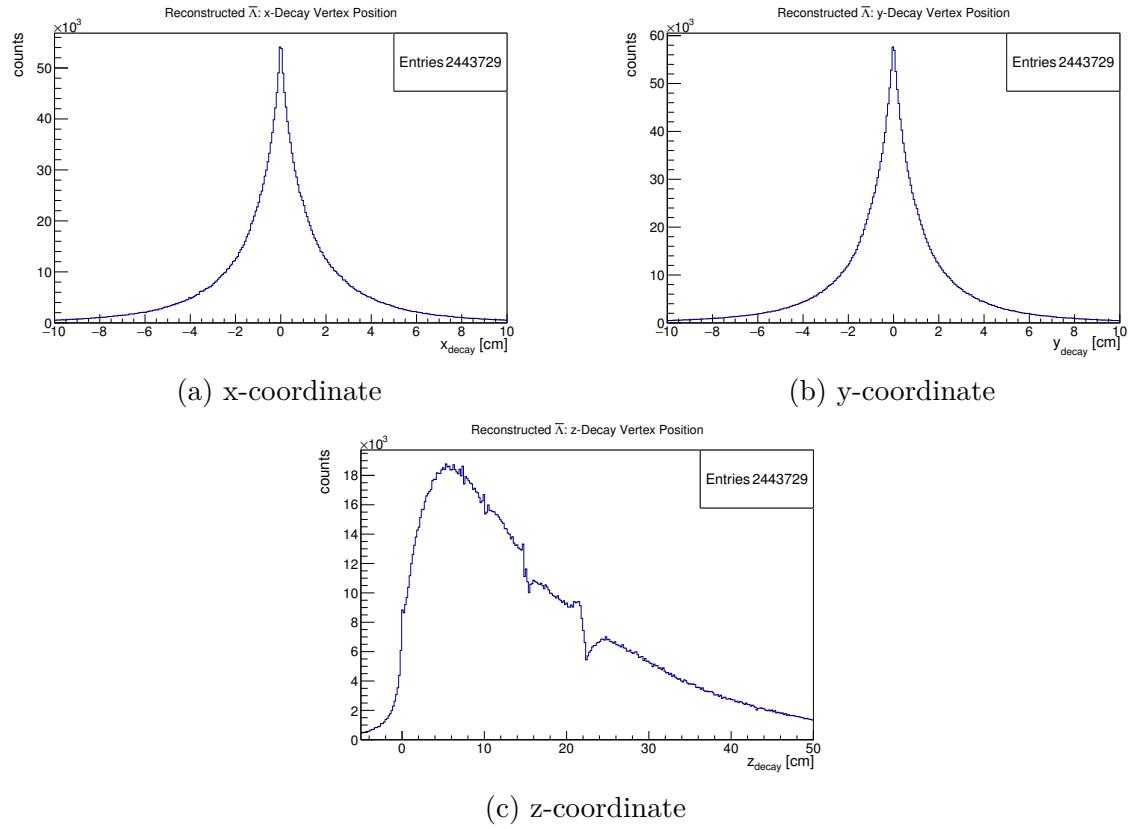
Figure A.52: Vertex position distribution after the vertex fit on $\overline{\Lambda}$ candidates.

(a) x-coordinate

(b) y-coordinate

(c) z-coordinate

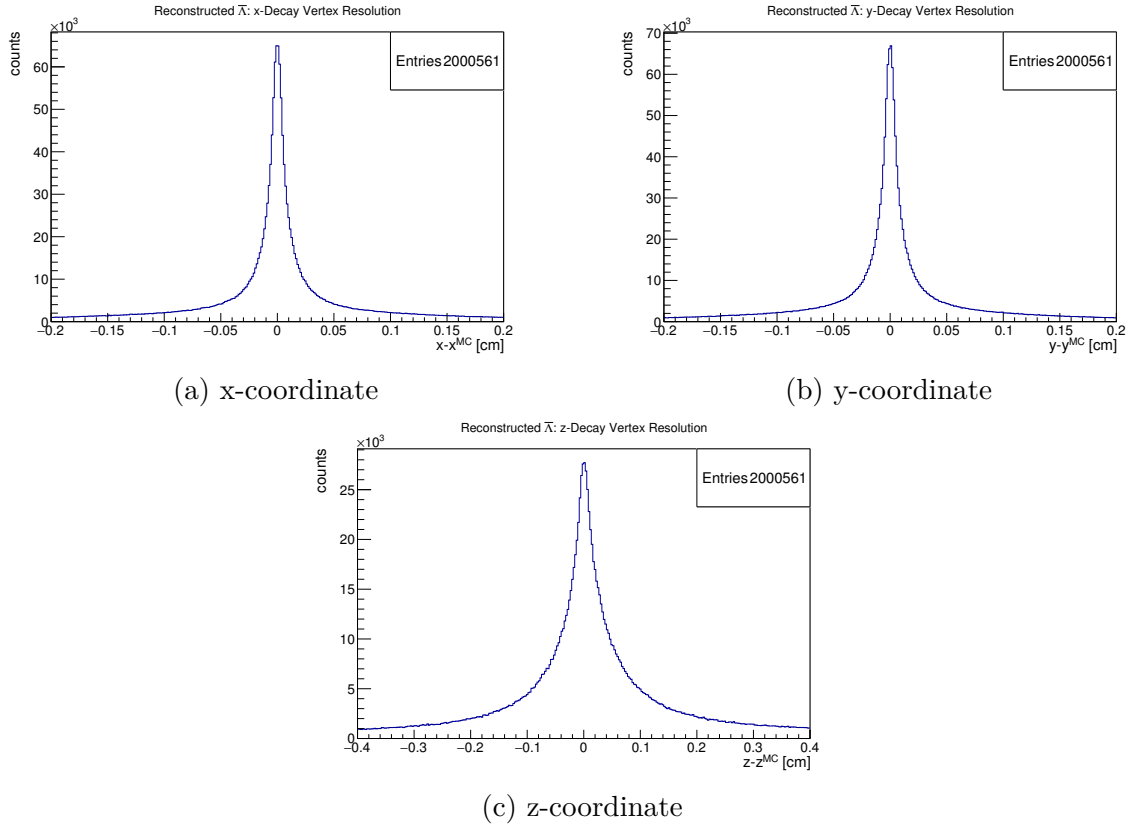Figure A.53: Deviation of the reconstructed vertex position from the MC value after the vertex fit on $\overline{\Lambda}$ candidates.
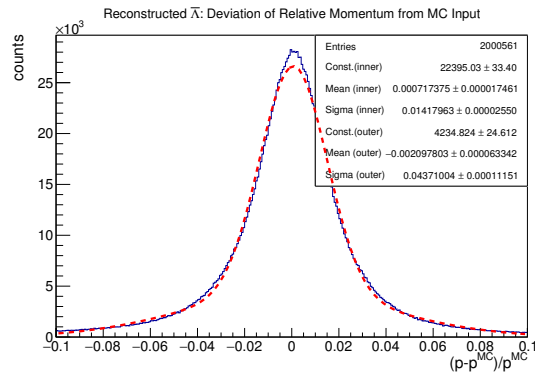
Figure A.54: Relative deviation of the reconstructed $\overline{\Lambda}$ momentum from the MC value distribution with a double gaussian fit.
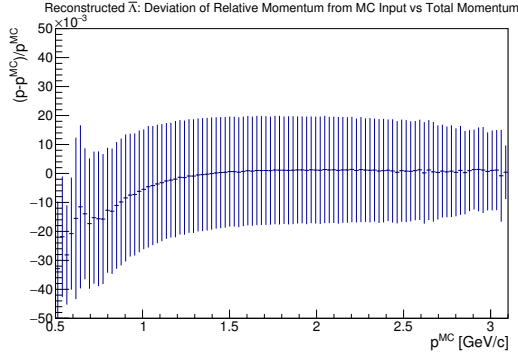
Figure A.55: Relative deviation of the reconstructed $\overline{\Lambda}$ momentum from the MC value as a function of the total momentum.
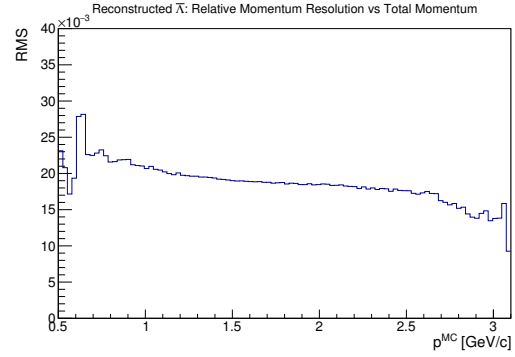
Figure A.56: Dependence of the relative momentum resolution on the total momentum for reconstructed $\overline{\Lambda}$ candidates.
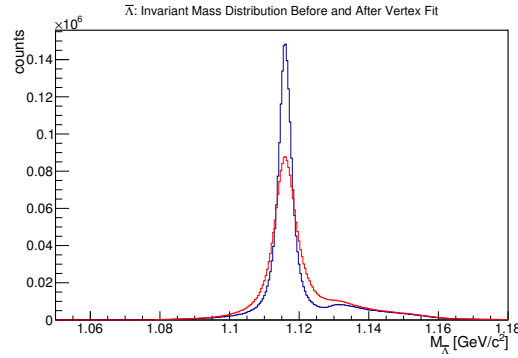
(a) Invariant mass distribution before (red) and after (blue) the vertex fit.
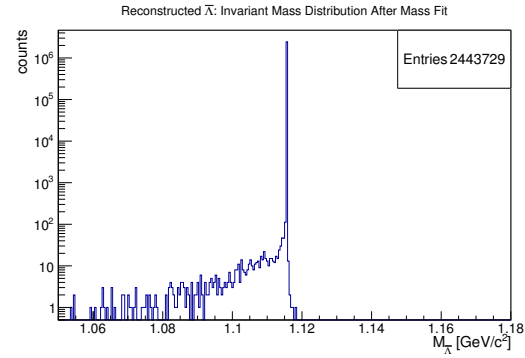
(b) Invariant mass distribution after the mass constraint fit.

Figure A.57: Invariant mass distribution for the $\overline{\Lambda}$ candidates.
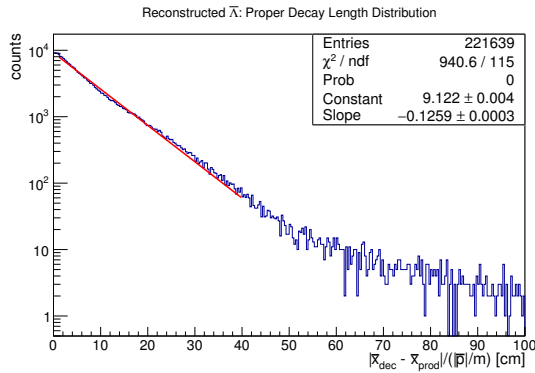
Figure A.58: Proper decay length distribution with an exponential fit for reconstructed $\overline{\Lambda}$ candidates. A logarithmic scale for the y-axis is used.

(a) Transverse versus longitudinal momentum.

(b) Polar angle versus total momentum.
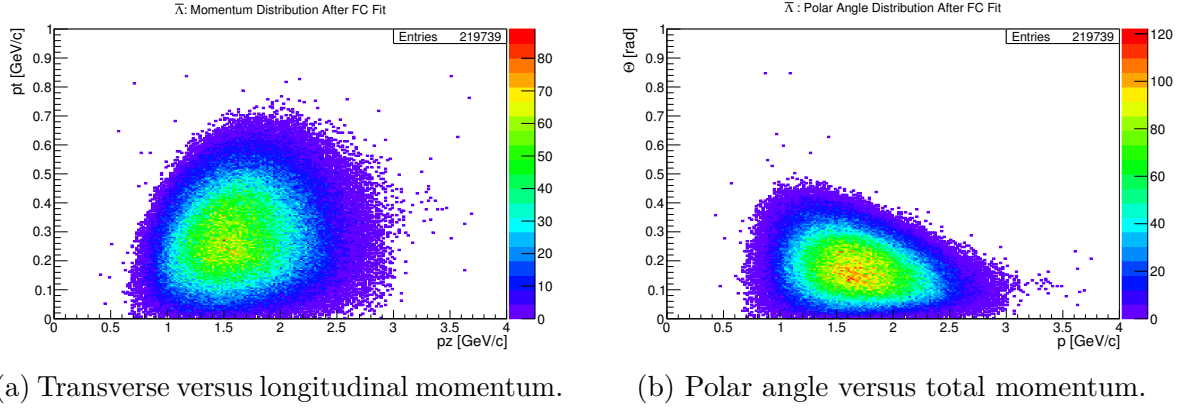
Figure A.59: Reconstructed $\overline{\Lambda}$ after final selection.

(a) Transverse versus longitudinal momentum.

(b) Polar angle versus total momentum.

Figure A.60: MC partner of reconstructed $\overline{\Lambda}$ after final selection.

A.2.2 $\overline{\Xi}^+$
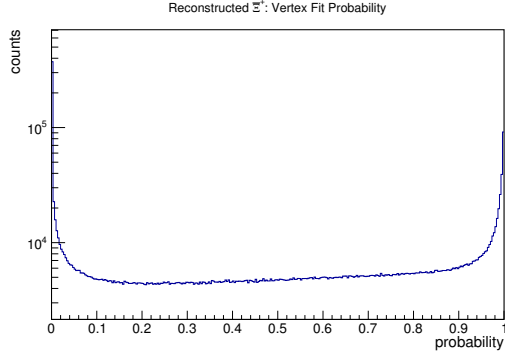
(a) Probability distribution.
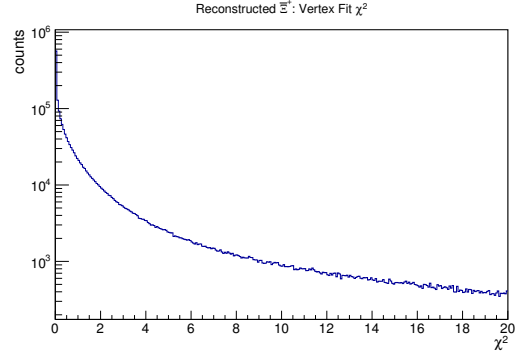
(b) χ^2 distribution.

Figure A.61: Quality of the vertex fit on $\overline{\Xi}^+$ candidates.
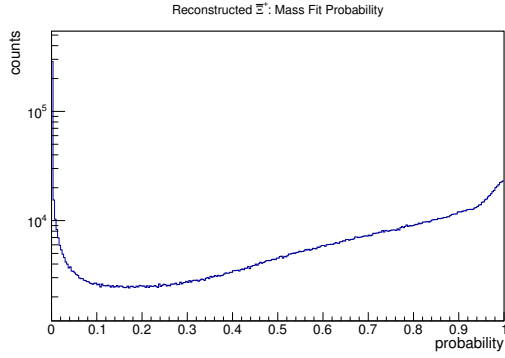
(a) Probability distribution.
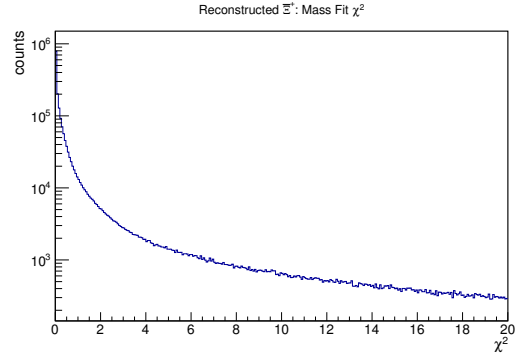
(b) χ^2 distribution.

Figure A.62: Quality of the mass constraint fit on $\overline{\Xi}^+$ candidates.
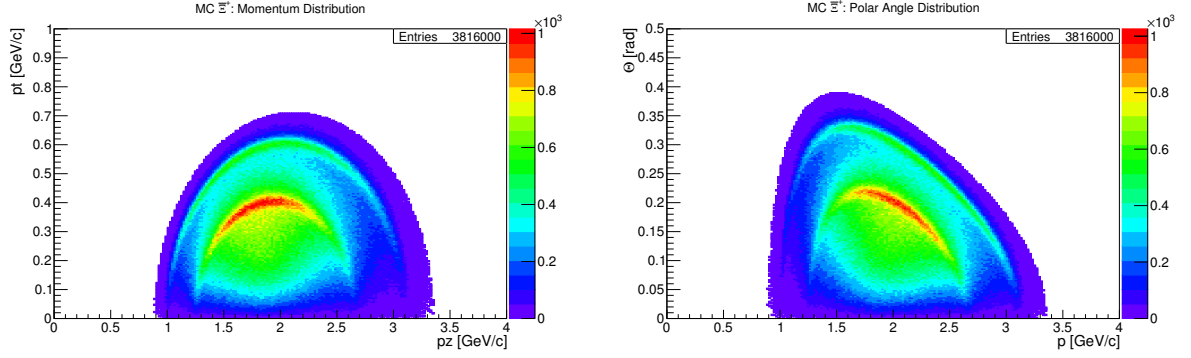
(a) Transverse versus longitudinal momentum.   (b) Polar angle versus total momentum.

Figure A.63: MC generated $\overline{\Xi}^+$.
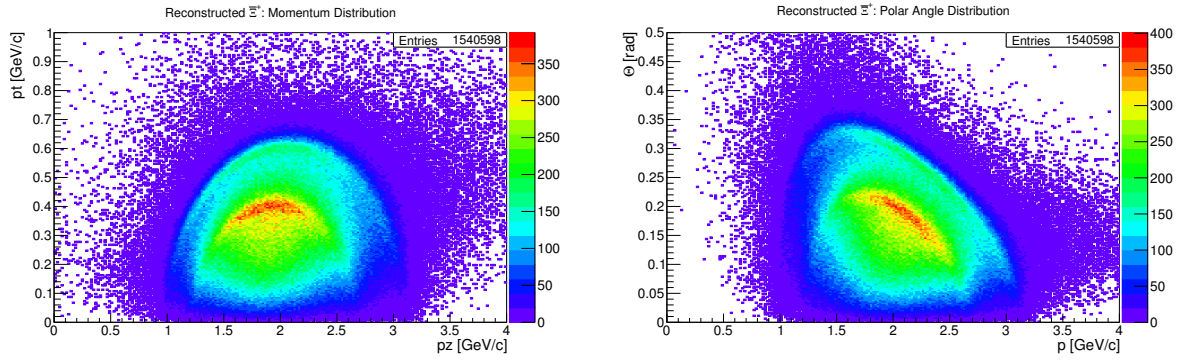
(a) Transverse versus longitudinal momentum.   (b) Polar angle versus total momentum.

Figure A.64: Reconstructed $\overline{\Xi}^+$.
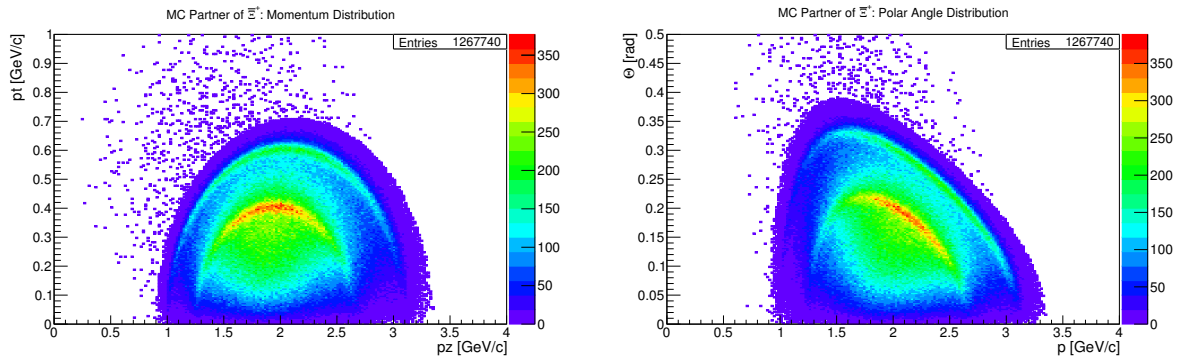
(a) Transverse versus longitudinal momentum.   (b) Polar angle versus total momentum.

Figure A.65: MC partners of reconstructed $\overline{\Xi}^+$.
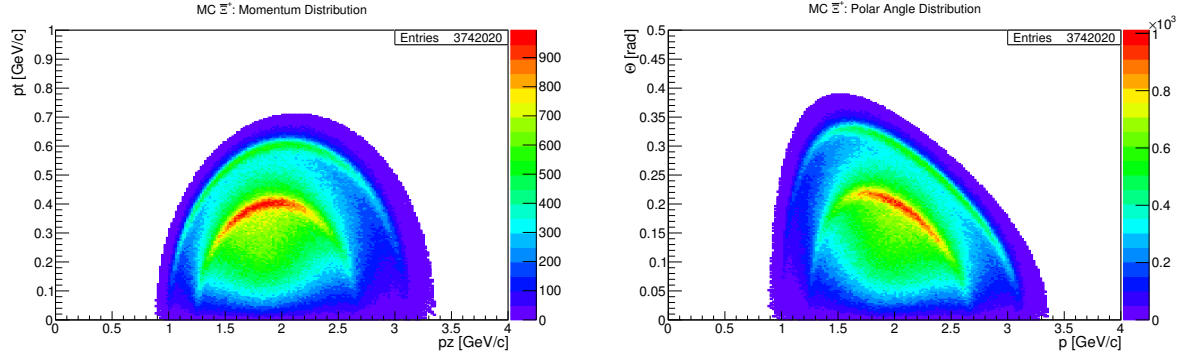
(a) Transverse versus longitudinal momentum.   (b) Polar angle versus total momentum.

Figure A.66: MC generated $\overline{\Xi}^+$ with more stringent selection criteria, as explained in the text.
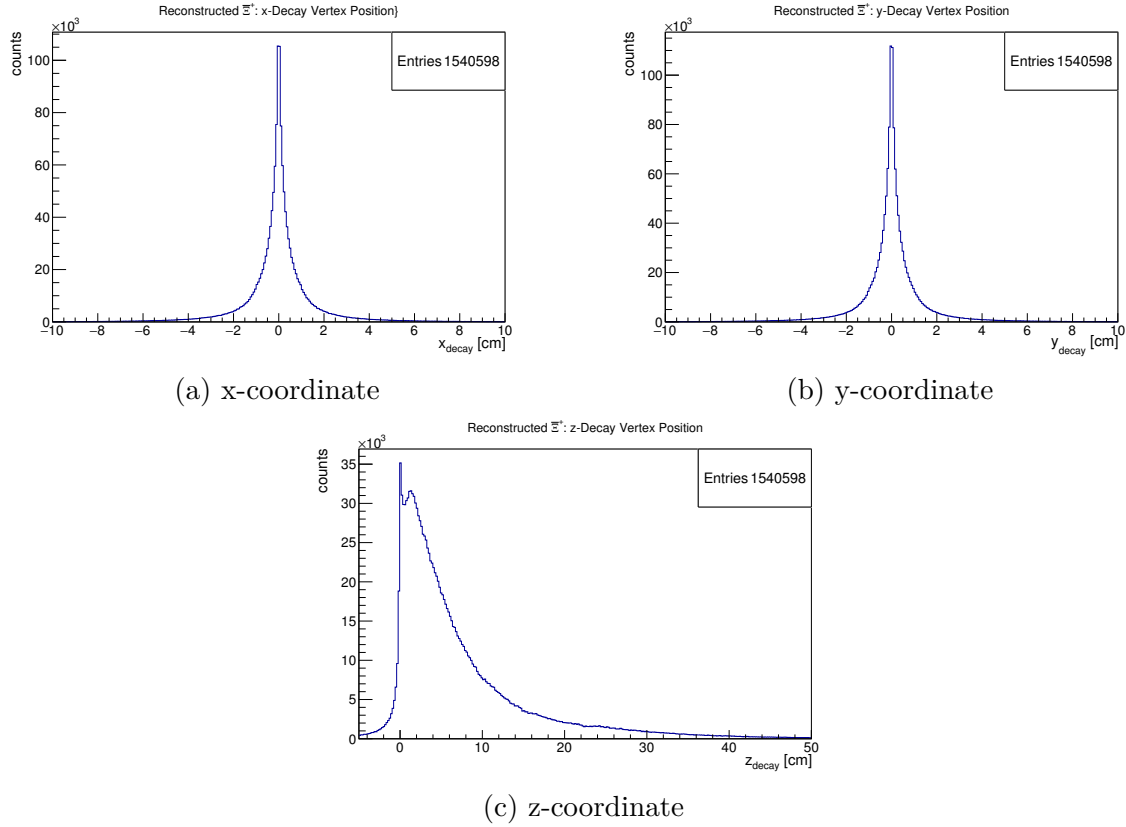
(a) x-coordinate   (b) y-coordinate

(c) z-coordinate

Figure A.67: Vertex position distribution after the vertex fit on $\overline{\Xi}^+$ candidates.

(a) x-coordinate

(b) y-coordinate

(c) z-coordinate
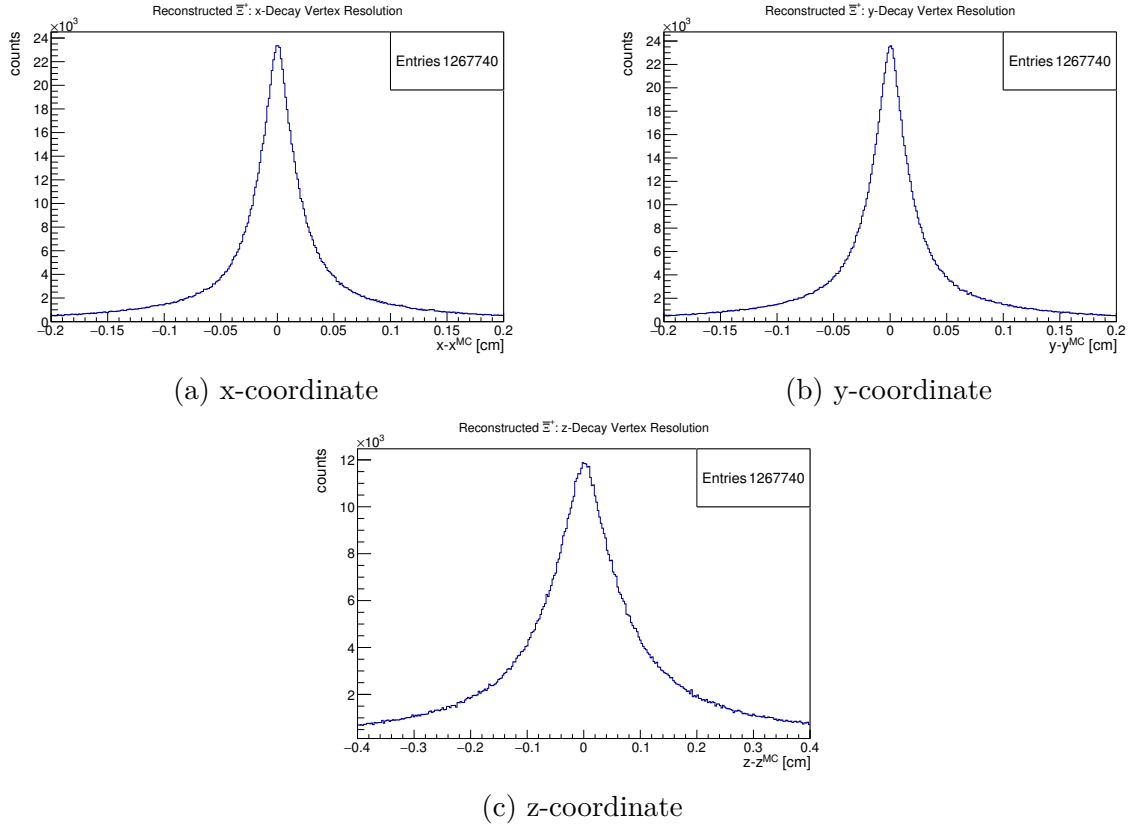
Figure A.68: Deviation of the reconstructed vertex position from the MC value after the vertex fit on $\overline{\Xi}^+$ candidates.
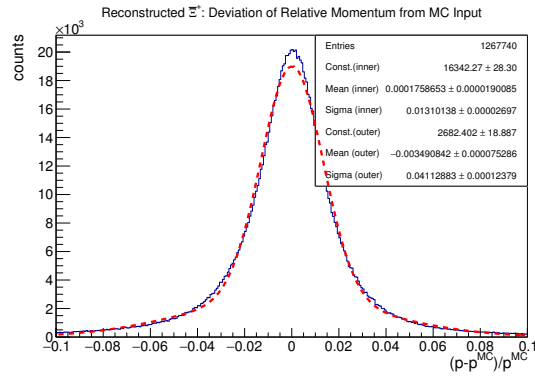
Figure A.69: Relative deviation of the reconstructed $\overline{\Xi}^+$ momentum from the MC value distribution with a double gaussian fit.
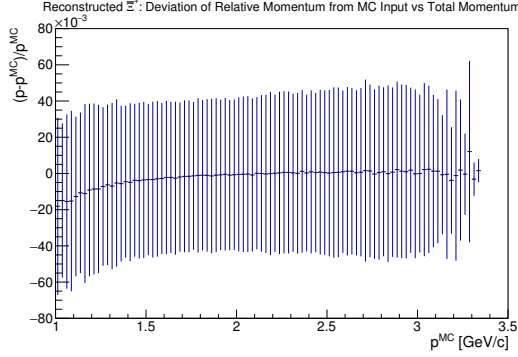
Figure A.70: Relative deviation of the reconstructed $\overline{\Xi}^+$ momentum from the MC value as a function of the total momentum.
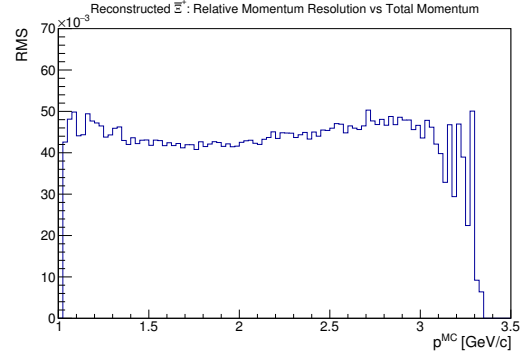
Figure A.71: Dependence of the relative momentum resolution on the total momentum for reconstructed $\overline{\Xi}^+$ candidates.
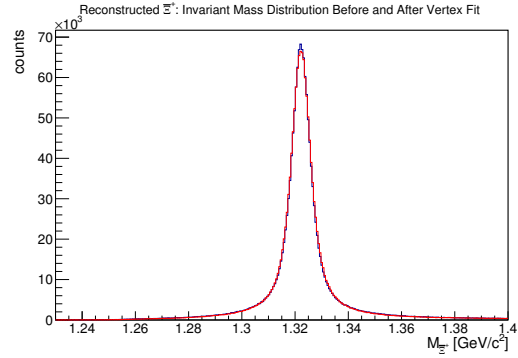
(a) Invariant mass distribution before (red) and after (blue) the vertex fit.
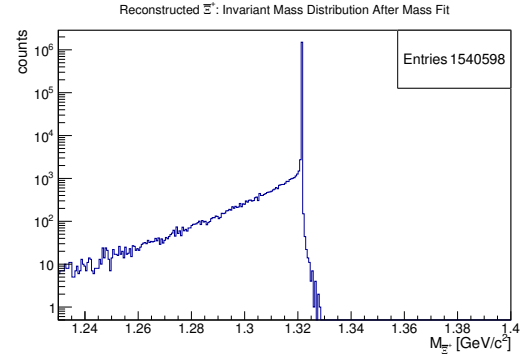
(b) Invariant mass distribution after the mass constraint fit.
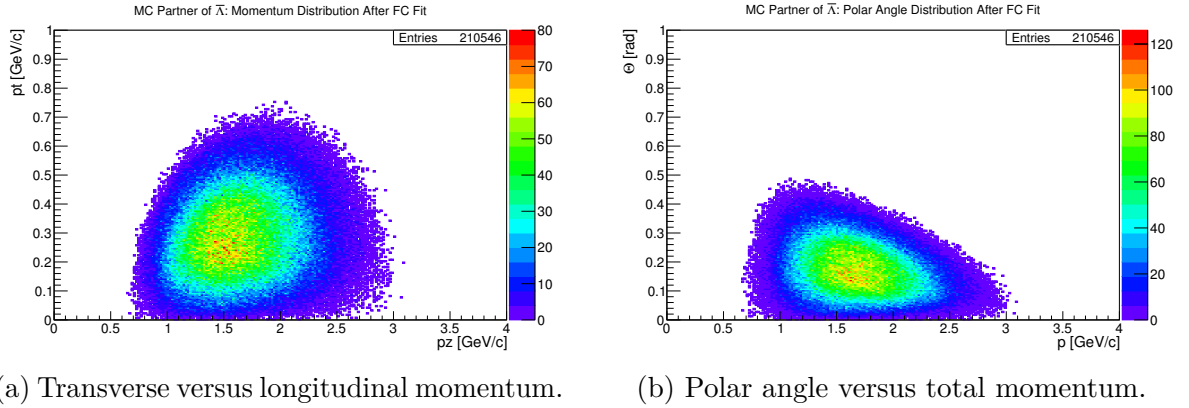
Figure A.72: Invariant mass distribution for the $\overline{\Xi}^+$ candidates.
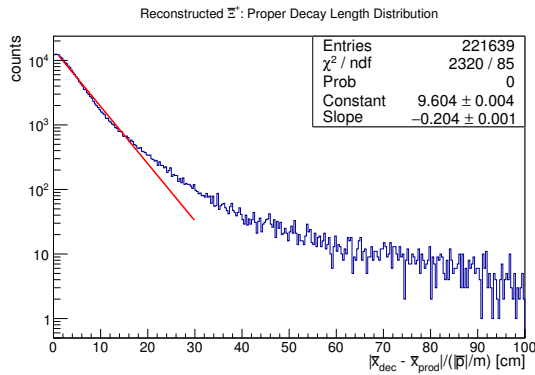
Figure A.73: Proper decay length distribution with an exponential fit for reconstructed $\overline{\Xi}^+$ candidates. A logarithmic scale for the y-axis is used.

(a) Transverse versus longitudinal momentum.

(b) Polar angle versus total momentum.
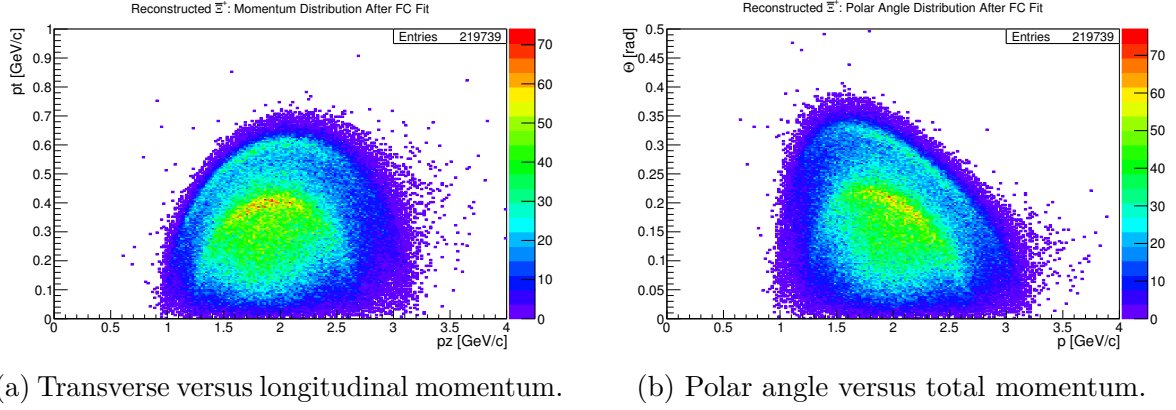
Figure A.74: Reconstructed $\overline{\Xi}^+$ after final selection.

(a) Transverse versus longitudinal momentum.

(b) Polar angle versus total momentum.
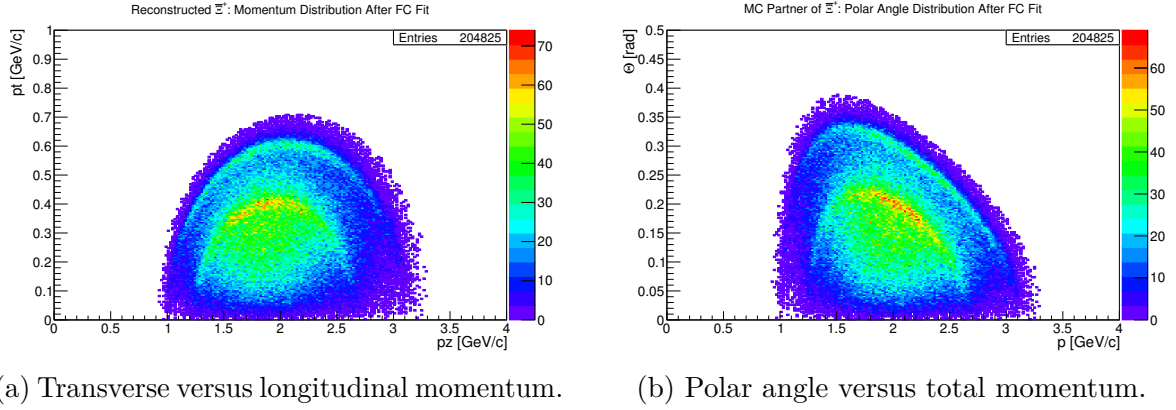
Figure A.75: MC partner of reconstructed $\overline{\Xi}^+$ after final selection.

Acronyms

APD	Avalanche Photo Diode	**DSP**	Digital Signal Processor
ASIC	Application Specific Integrated Circuit	**DSSD**	Double-Sided Silicon Micro-Strip Detector
CAD	Computer Aided Design	**DUT**	Device Under Test
CERN	European Organization for Nuclear Research	**EMC**	Electromagnetic Calorimeter
CMOS	Complementary Metal Oxide Semiconductor	**ESR**	Experimental Storage Ring
COSY	Cooler Synchrotron	**FAIR**	Facility for Antiproton and Ion Research
CRC-8	Cyclic Redundancy Check	**FIFO**	First In First Out
CR	Collector Ring	**FPGA**	Field Programmable Gate Array
CSA	Charge Sensitive Amplifier		
`CS`	Chip Select	**FRS**	Fragment Separator
CVD	Chemical Vapour Deposition	**FSM**	Finite State Machine
		FT	Forward Tracker
DAQ	Data Acquisition	**FTOF**	Forward Time of Flight
DDR3	Double Data Rate Type 3	**FWHM**	Full Width at Half Maximum
DIRC	Detection of Internally Reflected Cherenkov Light	**GBTX**	Gigabit Transceiver
DLL	Delay-Locked Loop	**GCC**	GNU Compiler Collection
DOCA	Distance of Closest Approach	**GEM**	Gas Electron Multiplier
DPM	Dual Parton Model	**GPD**	Generalized Parton Distribution

GPIO	General Purpose Input/Output	**LQCD**	Lattice Quantum Chromodynamics
GSI	GSI Helmholtzzentrum für Schwerionenforschung GmbH	**LVDS**	Low-Voltage Differential Signaling
		MAC	Media Access Control
GUI	Graphical User Interface	**MC**	Monte Carlo
HCGDAC+	Hysteresis Comparator Global Digital to Analog Converter (Positive Input)	**MCP**	Micro-Channel Plate
		MCP-PMT	Micro-Channel Plate Photo Multiplier Tube
HCGDAC−	Hysteresis Comparator Global Digital to Analog Converter (Negative Input)	**MDC**	Module Data Concentrator
		MDS	Muon Detector System
HDL	Hardware Description Language	**MDT**	Mini Drift Tubes
HESR	High Energy Storage Ring	**MicroTCA**	Micro Telecommunication Computing Architechture
HTTP	Hypertext Transfer Protocol	**MMB**	MVD Multiplexer Board
HVMAPS	High Voltage Monolithic Active Pixel Sensor	**MOC**	Meta Object Compiler
		MP	Micropulses
INP	Institute of Nuclear Physics	**MRF**	MVD Readout Framework
I/O	Input/Output	**MSV**	Modularized Start Version
IP	Intellectual Property	**MVD**	Micro Vertex Detector
IP	Internet Protocol	**NESR**	New Experimental Storage Ring
ISO	International Organization for Standardization		
		OSI	Open System Interconnection
JDRS	Jülich Digital Readout System	**PANDA**	Antiproton Annihilation at Darmstadt
JSON	JavaScript Object Notation		
JTAG	Joint Test Action Group	**PASTA**	PANDA Strip ASIC
LCD	Liquid Crystal Display	**PC**	Personal Computer
LED	Light Emitting Diode	**PCB**	Printed Circuit Board
LMD	Luminosity Detector	**PCIe**	Peripheral Component Interconnect Express

PDG	Particle Data Group	**SMA**	SubMiniature version A
PID	Particle Identification	**SODANET**	Synchronization Of Data Acquisition
p-LINAC	Proton Linear Accelerator		
PLL	Phase-Locked Loop	**STT**	Straw Tube Tracker
PMT	Photo Multiplier Tube	**TAC**	Time to Analog Converter
QCD	Quantum Chromodynamics	**TCP**	Transmission Control Protocol
RAM	Random Access Memory		
RESR	Recuperated Experimental Storage Ring	**TDC**	Time to Digital Converter
		TMR	Triple Modular Redundancy
RICH	Ring Image Cherenkov	**TOF**	Time of Flight
RMS	Root Mean Square	**TOFPET**	Time of Flight for Positron Electron Tomography
SciTil	Scintillator Tile Hodoscope		
SCLK	Slow Clock	**ToPix**	Torino Pixel
SDI	Slow Data In	**ToT**	Time over Threshold
SDO	Slow Data Out	**UDP**	User Datagram Protocol
SD	Secure Digital	**UIC**	User Interface Compiler
SERDES	Serializer-Deserializer	**UNILAC**	Universal Linear Accelerator
SEU	Single Event Upset		
SiPM	Silicon Photo Multiplier	**VHDL**	Very High Speed Integrated Circuit Hardware Description Language
SIS	Schwerionen Synchrotron		
SLVS	Scalable Low Voltage Signaling		
		XML	Extensible Markup Language

Bibliography

[1] FAIR. FAIR Baseline Technical Report. Technical report, March 2006. URL http://www.fair-center.eu/for-users/publications/fair-publications.html.

[2] GSI Helmholtzzentrum fur Schwerionenforschung GmbH webpage. https://www.gsi.de/forschungbeschleuniger/fair.htm.

[3] FAIR GmbH and GSI. *MSV Green Paper, The Modularized Start Version: FAIR - Facility for Antiproton and Ion Research*. FAIR, Damstadt, 2009. URL http://repository.gsi.de/record/54094.

[4] Andreas Herten. *GPU-based Online Track Reconstruction for PANDA and Application to the Analysis of $D \to K\pi\pi$*. PhD thesis, Ruhr-Universität Bochum, Apr 2015. URL https://hss-opus.ub.ruhr-uni-bochum.de/opus4/frontdoor/deliver/index/docId/4384/file/diss.pdf.

[5] G. I. Budker. An effective method of damping particle oscillations in proton and antiproton storage rings. *Soviet Atomic Energy*, 22(5):438–440, May 1967. ISSN 1573-8205. doi: 10.1007/BF01175204. URL https://doi.org/10.1007/BF01175204.

[6] Simon van der Meer. Stochastic damping of betatron oscillations in the ISR. *CERN-ISR-PO-72-31*, pages 261–269, 1972.

[7] A. Lehrach, O. Boine-Frankenheim, F. Hinterberger, et al. Beam performance and luminosity limitations in the high-energy storage ring (HESR). *Nuclear Instruments and Methods in Physics Research Section A: Accelerators, Spectrometers, Detectors and Associated Equipment*, 561(2):289 – 296, 2006. ISSN 0168-9002. doi: https://doi.org/10.1016/j.nima.2006.01.017. URL http://www.sciencedirect.com/science/article/pii/S0168900206000477. Proceedings of the Workshop on High Intensity Beam Dynamics.

[8] The PANDA Collaboration, W. Erni, I. Keshelashvili, B. Krusche, H. Steinacher, et al. Physics Performance Report for PANDA: Strong Interaction Studies with Antiprotons. March 2009. URL http://arxiv.org/abs/0903.3905.

[9] The PANDA Collaboration. Technical Progress Report for: PANDA (AntiProton Annihilation at Darmstadt) Strong Interaction Studies with Antiprotons. Technical report, Feb 2005. URL http://www-panda.gsi.de/archive/public/panda_tpr.pdf.

[10] S.-K. Choi, S. L. Olsen, K. Abe, et al. Observation of a Narrow Charmoniumlike State in Exclusive $B^{\pm} \to K^{\pm}\pi^{+}\pi^{-}J/\psi$ Decays. *Phys. Rev. Lett.*, 91:262001, Dec 2003. doi: 10.1103/PhysRevLett.91.262001. URL https://link.aps.org/doi/10.1103/PhysRevLett.91.262001.

[11] B. Aubert, R. Barate, D. Boutigny, et al. Study of the $B^{-} \to J/\psi K^{-}\pi^{+}\pi^{-}$ decay and measurement of the $B^{-} \to X(3872)K^{-}$ branching fraction. *Phys. Rev. D*, 71:071103, Apr 2005. doi: 10.1103/PhysRevD.71.071103. URL https://link.aps.org/doi/10.1103/PhysRevD.71.071103.

[12] D. Acosta, T. Affolder, M. H. Ahn, et al. Observation of the Narrow State $X(3872) \to J/\psi\pi^{+}\pi^{-}$ in $\bar{p}p$ Collisions at $\sqrt{s} = 1.96$ TeV. *Phys. Rev. Lett.*, 93: 072001, Aug 2004. doi: 10.1103/PhysRevLett.93.072001. URL https://link.aps.org/doi/10.1103/PhysRevLett.93.072001.

[13] V. M. Abazov, B. Abbott, M. Abolins, et al. Observation and Properties of the $X(3872)$ Decaying to $J/\psi\pi^{+}\pi^{-}$ in $p\bar{p}$ Collisions at $\sqrt{s} = 1.96$ TeV. *Phys. Rev. Lett.*, 93:162002, Oct 2004. doi: 10.1103/PhysRevLett.93.162002. URL https://link.aps.org/doi/10.1103/PhysRevLett.93.162002.

[14] Stephen Godfrey and Stephen L. Olsen. The Exotic XYZ Charmonium-Like Mesons. *Annual Review of Nuclear and Particle Science*, 58(1):51–73, 2008. doi: 10.1146/annurev.nucl.58.110707.171145. URL https://doi.org/10.1146/annurev.nucl.58.110707.171145.

[15] Paola Gianotti. Results and perspectives in hadron spectroscopy. *Physica Scripta*, 2012(T150):014014, 2012. URL http://stacks.iop.org/1402-4896/2012/i=T150/a=014014.

[16] P. Chen, X. Liao, and T. Manke. Relativistic quarkonia from anisotropic lattices. *Nuclear Physics B - Proceedings Supplements*, 94(1):342 – 345, 2001. ISSN 0920-5632. doi: https://doi.org/10.1016/S0920-5632(01)00921-5. URL http://www.sciencedirect.com/science/article/pii/S0920563201009215. Proceedings of the XVIIIth International Symposium on Lattice Field Theory.

[17] Chris Michael. Quarkonia and Hybrids from the Lattice. *Proceedings of Heavy Flavours 8, Southampton*, 1999.

[18] Eberhard Klempt and Alexander Zaitsev. Glueballs, hybrids, multiquarks: Experimental facts versus QCD inspired concepts. *Physics Reports*, 454(1):1 – 202, 2007. ISSN 0370-1573. doi: https://doi.org/10.1016/j.physrep.2007.07.006. URL http://www.sciencedirect.com/science/article/pii/S0370157307003560.

[19] Colin J. Morningstar and Mike Peardon. Glueball spectrum from an anisotropic lattice study. *Phys. Rev. D*, 60:034509, Jul 1999. doi: 10.1103/PhysRevD.60. 034509. URL https://link.aps.org/doi/10.1103/PhysRevD.60.034509.

[20] Philip R. Page. Multi-GeV gluonic mesons. In *Low-energy anti-p storage ring. Proceedings, Workshop, anti-p 2000, Chicago, USA, August 3-5, 2000*, pages 55–63, 2001.

[21] Richard Jones. Partial wave analysis results from jetset. Talk at Gluonic Excitations Workshop, JLAB, Newport News, VA, May 2003.

[22] A. Bertin, M. Bruschi, M. Capponi, et al. A search for axial vectors in $pp \rightarrow K^{\pm}K^0\pi^{\mp}\pi^+\pi^-$ annihilations at rest in gaseous hydrogen at NTP. *Physics Letters B*, 400(1):226 – 238, 1997. ISSN 0370-2693. doi: https://doi.org/10.1016/ S0370-2693(97)00300-6. URL http://www.sciencedirect.com/science/article/pii/ S0370269397003006.

[23] Stephen Godfrey and Nathan Isgur. Mesons in a relativized quark model with chromodynamics. *Phys. Rev. D*, 32:189–231, Jul 1985. doi: 10.1103/PhysRevD.32. 189. URL https://link.aps.org/doi/10.1103/PhysRevD.32.189.

[24] M. Di Pierro and E. Eichten. Excited heavy-light systems and hadronic transitions. *Phys. Rev. D*, 64:114004, Oct 2001. doi: 10.1103/PhysRevD.64.114004. URL https://link.aps.org/doi/10.1103/PhysRevD.64.114004.

[25] B. Aubert, R. Barate, D. Boutigny, et al. Observation of a narrow meson state decaying to $D_s^+\pi^0$ at a mass of 2.32 GeV/c^2. *Phys. Rev. Lett.*, 90:242001, Jun 2003. doi: 10.1103/PhysRevLett.90.242001. URL https://link.aps.org/doi/10. 1103/PhysRevLett.90.242001.

[26] D. Besson, S. Anderson, V. V. Frolov, et al. Observation of a narrow resonance of mass 2.46 GeV/c^2 decaying to $D_s^{*+}\pi^0$ and confirmation of the $D_{sJ}^*(2317)$ state. *Phys. Rev. D*, 68:032002, Aug 2003. doi: 10.1103/PhysRevD.68.032002. URL https://link.aps.org/doi/10.1103/PhysRevD.68.032002.

[27] P. Krokovny, K. Abe, K. Abe, et al. Observation of the $D_{sJ}(2317)$ and $D_{sJ}(2457)$ in B Decays. *Phys. Rev. Lett.*, 91:262002, Dec 2003. doi: 10.1103/PhysRevLett. 91.262002. URL https://link.aps.org/doi/10.1103/PhysRevLett.91.262002.

[28] S.-K. Choi, S. L. Olsen, A. Abdesselam, et al. Measurements of $B \rightarrow \overline{D}D_{s0}^{*+}(2317)$ decay rates and a search for isospin partners of the $D_{s0}^{*+}(2317)$. *Phys. Rev. D*, 91: 092011, May 2015. doi: 10.1103/PhysRevD.91.092011. URL https://link.aps.org/ doi/10.1103/PhysRevD.91.092011.

[29] Marius Christian Mertens and the PANDA Collaboration. Determination of the $D_{s0}^*(2317)$ width with the PANDA detector. *Hyperfine Interactions*, 209 (1-3):111–115, 2012. ISSN 0304-3843. doi: 10.1007/s10751-012-0565-z. URL http://dx.doi.org/10.1007/s10751-012-0565-z.

[30] Eberhard Klempt. Mass formula for baryon resonances. *Phys. Rev. C*, 66:058201, Nov 2002. doi: 10.1103/PhysRevC.66.058201. URL https://link.aps.org/doi/10.1103/PhysRevC.66.058201.

[31] I. Zychor, V. Koptev, M. Büscher, et al. Evidence for an Excited Hyperon State in $pp \to pK^+Y^{0*}$. *Phys. Rev. Lett.*, 96:012002, Jan 2006. doi: 10.1103/PhysRevLett.96.012002. URL https://link.aps.org/doi/10.1103/PhysRevLett.96.012002.

[32] M. I. Adamovich et al. Observation of a resonance in the K(s)p decay channel at a mass of $1765\,\mathrm{MeV}/c^2$. *Eur. Phys. J.*, C50:535–538, 2007. doi: 10.1140/epjc/s10052-007-0284-9.

[33] A. B. Kaidalov and P. E. Volkovitsky. Binary reactions in $\overline{p}p$ collisions at intermediate energies. *Zeitschrift fur Physik C Particles and Fields*, 63:517–524, September 1994. doi: 10.1007/BF01580332.

[34] Tord Johansson. Antihyperon-Hyperon Production in Antiproton-Proton Collisions. *AIP Conference Proceedings*, 796(1):95–101, 2005. doi: 10.1063/1.2130143. URL https://aip.scitation.org/doi/abs/10.1063/1.2130143.

[35] M. Danysz, K. Garbowska, J. Pniewski, et al. Observation of a Double Hyperfragment. *Phys. Rev. Lett.*, 11:29–32, Jul 1963. doi: 10.1103/PhysRevLett.11.29. URL https://link.aps.org/doi/10.1103/PhysRevLett.11.29.

[36] N. Kaiser and W. Weise. Chiral SU(3) dynamics and Λ hyperons in the nuclear medium. *Phys. Rev. C*, 71:015203, Jan 2005. doi: 10.1103/PhysRevC.71.015203. URL https://link.aps.org/doi/10.1103/PhysRevC.71.015203.

[37] G. Bardin, G. Burgun, R. Calabrese, et al. Determination of the electric and magnetic form factors of the proton in the time-like region. *Nuclear Physics B*, 411(1): 3 – 32, 1994. ISSN 0550-3213. doi: https://doi.org/10.1016/0550-3213(94)90052-3. URL http://www.sciencedirect.com/science/article/pii/0550321394900523.

[38] J. P. Lees, V. Poireau, V. Tisserand, et al. Measurement of the $e^+e^- \to p\bar{p}$ cross section in the energy range from 3.0 to 6.5 GeV. *Phys. Rev. D*, 88:072009, Oct 2013. doi: 10.1103/PhysRevD.88.072009. URL https://link.aps.org/doi/10.1103/PhysRevD.88.072009.

[39] M. Ablikim, M. N. Achasov, X. C. Ai, et al. Measurement of the proton form factor by studying $e^+e^- \to p\bar{p}$. *Phys. Rev. D*, 91:112004, Jun 2015. doi: 10.1103/PhysRevD.91.112004. URL https://link.aps.org/doi/10.1103/PhysRevD.91.112004.

[40] The PANDA Collaboration. Feasibility studies of time-like proton electromagnetic form factors at $\overline{\text{P}}$ANDA at FAIR. *Eur. Phys. J.*, A52(10):325, 2016. doi: 10.1140/epja/i2016-16325-5.

[41] M. Diehl. Generalized parton distributions. *Phys. Rept.*, 388:41–277, 2003. doi: 10.1016/j.physrep.2003.08.002,10.3204/DESY-THESIS-2003-018.

[42] D. Bonaventura. CAD-Renderings of the PANDA Detector, Jan 2015. URL https://panda-wiki.gsi.de/foswiki/bin/view/Detector/Pictures.

[43] The PANDA Collaboration. Technical Design Report for the PANDA Internal Targets: The Cluster-Jet Target and Developments for the Pellet Target. Technical report, Mar 2012. URL https://fair-center.eu/fileadmin/fair/publications_exp/PANDA_Targets_TDR.pdf.

[44] Örjan Nordhage. *On a Hydrogen Pellet Target for Antiproton Physics with PANDA*. PhD thesis, Uppsala University, Department of Nuclear and Particle Physics, 2006. URL http://www.diva-portal.org/smash/get/diva2:168848/FULLTEXT01.pdf.

[45] The PANDA Collaboration. Technical Design Report for the PANDA Solenoid and Dipole Spectrometer Magnets. Technical report, 2009. URL http://arxiv.org/abs/0907.0169.

[46] The PANDA Collaboration. Technical design report for the PANDA (AntiProton Annihilations at Darmstadt) Straw Tube Tracker. *The European Physical Journal A*, 49(2):1–104, 2013. ISSN 1434-6001. doi: 10.1140/epja/i2013-13025-8. URL http://dx.doi.org/10.1140/epja/i2013-13025-8.

[47] Peter Wintz. STT Status Report. Talk at Panda Collaboration Meeting, Novosibirsk, Sep. 2017.

[48] Fabio Sauli. The gas electron multiplier (GEM): Operating principles and applications. *Nuclear Instruments and Methods in Physics Research Section A: Accelerators, Spectrometers, Detectors and Associated Equipment*, 805:2 – 24, 2016. ISSN 0168-9002. doi: https://doi.org/10.1016/j.nima.2015.07.060. URL http://www.sciencedirect.com/science/article/pii/S0168900215008980. Special Issue in memory of Glenn F. Knoll.

[49] FLC - Forschung mit Lepton Collider. URL https://flc.desy.de/tpc/basics/gem/index_eng.html.

[50] CERN Gas Detector Development Group. URL http://gdd.web.cern.ch/GDD/.

[51] The PANDA Collaboration. Technical Design Report for the PANDA Barrel DIRC Detector. 2017. URL https://arxiv.org/abs/1710.00684.

[52] Andre Zambanini. *Development of a Free-Running Readout ASIC for the PANDA Micro Vertex Detector and Investigation of the Performance to Reconstruct* $\bar{p}p \rightarrow \bar{\Xi}^+ \Xi^-(1690)$. PhD thesis, Ruhr-Universität Bochum, Aug 2015. URL https://hss-opus.ub.ruhr-uni-bochum.de/opus4/frontdoor/deliver/index/docId/4123/file/diss.pdf.

[53] Jochen Schwiening. Status of the PANDA Barrel DIRC. Talk at Panda Collaboration Meeting, GSI, Darmstadt, Mar 2014.

[54] O. Merle, R. Dzhygadlo, A. Gerhardt, et al. Development of an Endcap DIRC for PANDA. *Nuclear Instruments and Methods in Physics Research Section A: Accelerators, Spectrometers, Detectors and Associated Equipment*, 766:96 – 100, 2014. ISSN 0168-9002. doi: https://doi.org/10.1016/j.nima.2014.04.016. URL http://www.sciencedirect.com/science/article/pii/S0168900214003957. RICH2013 Proceedings of the Eighth International Workshop on Ring Imaging Cherenkov Detectors Shonan, Kanagawa, Japan, December 2-6, 2013.

[55] The PANDA Collaboration. Technical Design Report for the Panda Forward Spectrometer Calorimeter. Technical report, 2017. URL https://arxiv.org/abs/1704.02713.

[56] G. Schepers K. Goetzen, H. Orth et al. Proposal for a Scintillator Tile Hodoscope for PANDA. Mar 2011. URL https://panda.gsi.de/system/files/user_uploads/ken.suzuki/RE-TDR-2016-003_0.pdf.

[57] The PANDA Collaboration. Technical Design Report for: PANDA Forward Time of Flight Detector (FToF wall). Technical report, In preparation, 2018.

[58] The PANDA Collaboration. Technical Design Report for the: PANDA Muon System. Technical report, 2012. URL http://www-panda.gsi.de/archive/MuonTDR/Muon_TDR.pdf.

[59] The PANDA Collaboration. Technical Design Report for: PANDA Electromagnetic Calorimeter (EMC). Technical report, Oct 2008. URL http://arxiv.org/abs/0810.1216.

[60] The PANDA Collaboration. Technical Design Report for the PANDA Luminosity Detector. Technical report, In preparation, 2015.

[61] The PANDA Collaboration. Technical Design Report for the: PANDA Micro Vertex Detector. Technical report, Aug 2012. URL https://arxiv.org/abs/1207.6581.

[62] S. Bianco, T. Wurschig, T. Stockmanns, and K.-Th. Brinkmann. The CAD model of the PANDA Micro-Vertex-Detector in physics simulations. *Nucl. Instrum. Meth.*, A654:630–633, 2011. doi: 10.1016/j.nima.2011.05.021.

[63] D. Grunwald, Private Communications.

[64] Tommaso Quagli. *Hardware Developments for the Strip Detector of the PANDA MVD.* PhD thesis, Justus-Liebig-Universität Giessen, December 2015. URL http://geb.uni-giessen.de/geb/volltexte/2015/11820/pdf/QuagliTommaso-2015-12-07.pdf.

[65] N. Wermes. Pixel for Vertex Detectors. URL https://arxiv.org/pdf/physics/0611075.pdf.

[66] G. Mazza, D. Calvo, P. De Remigis, et al. The ToPiX v4 prototype for the triggerless readout of the PANDA silicon pixel detector. *Journal of Instrumentation*, 10(01):C01042, 2015. URL http://stacks.iop.org/1748-0221/10/i=01/a=C01042.

[67] S. Bonacini P. Moreira, S. Baron et al. The GBT-SerDes ASIC prototype. *Journal of Instrumentation*, 5(11):C11022, 2010. URL http://stacks.iop.org/1748-0221/5/i=11/a=C11022.

[68] Claude Leroy and Pier-Giorgio Rancoita. *Silicon Solid State Devices and Radiation Detection.* World Scientific Publishing Co. Pte. Ltd., 2012. ISBN 978-981-4290-04-0.

[69] R. Turchetta. Spatial resolution of silicon microstrip detectors. *Nuclear Instruments and Methods in Physics Research Section A: Accelerators, Spectrometers, Detectors and Associated Equipment*, 335(1):44 – 58, 1993. ISSN 0168-9002. doi: https://doi.org/10.1016/0168-9002(93)90255-G. URL http://www.sciencedirect.com/science/article/pii/016890029390255G.

[70] Hans-Georg Zaunick. *Developments toward a Silicon Strip Tracker for the PANDA Experiment.* PhD thesis, Universität Bonn, 2012. URL http://hss.ulb.uni-bonn.de/2013/3185/3185.htm.

[71] V. Di Pietro, K.-Th. Brinkmann, A. Riccardi, J. Ritman, et al. A time-based front-end ASIC for the silicon micro strip sensors of the PANDA Micro Vertex Detector. *Journal of Instrumentation*, 11(03):C03017, 2016. URL http://stacks.iop.org/1748-0221/11/i=03/a=C03017.

[72] V. Di Pietro R. Schnell, K.-Th. Brinkmann et al. The Readout Chain for the PANDA MVD Strip Detector. *Journal of Instrumentation*, 10(02):C02003, 2015. URL http://stacks.iop.org/1748-0221/10/i=02/a=C02003.

[73] H. Kleines, P. Wüstner, M. Ramm, et al. Developments for the readout of the PANDA Micro Vertex Detector. In *2010 17th IEEE-NPSS Real Time Conference*, pages 1–3, May 2010. doi: 10.1109/RTC.2010.5750459.

[74] I. Konorov, H. Angerer, A. Mann, and S. Paul. SODA: Time distribution system for the PANDA experiment. In *Nuclear Science Symposium Conference Record (NSS/MIC), 2009 IEEE*, pages 1863–1865, Oct 2009. doi: 10.1109/NSSMIC.2009. 5402172. URL http://dx.doi.org/10.1109/NSSMIC.2009.5402172.

[75] A. Lai. The PANDA Strip ASIC: PASTA. *Journal of Instrumentation*, 13(01): C01043, 2017. URL http://stacks.iop.org/1748-0221/13/i=01/a=C01043.

[76] F. B. Mimoun N. Aubry, E. Auffray et al. EndoTOFPET-US: a novel multimodal tool for endoscopy and positron emission tomography. *Journal of Instrumentation*, 8(04):C04002, 2013. URL http://stacks.iop.org/1748-0221/8/i=04/a=C04002.

[77] F. Gonçalves M. D. Rolo, R. Bugalho et al. TOFPET ASIC for PET applications. *Journal of Instrumentation*, 8(02):C02050, 2013. URL http://stacks.iop.org/1748-0221/8/i=02/a=C02050.

[78] C. S. Guenzer, E. A. Wolicki, and R. G. Allas. Single Event Upset of Dynamic Rams by Neutrons and Protons. *IEEE Transactions on Nuclear Science*, 26(6): 5048–5052, Dec 1979. ISSN 0018-9499. doi: 10.1109/TNS.1979.4330270.

[79] R. E. Lyons and W. Vanderkulk. The use of triple-modular redundancy to improve computer reliability. *IBM Journal of Research and Development*, 6(2):200–209, April 1962. ISSN 0018-8646. doi: 10.1147/rd.62.0200.

[80] R. W. Hamming. Error detecting and error correcting codes. *The Bell System Technical Journal*, 29(2):147–160, April 1950. ISSN 0005-8580. doi: 10.1002/j.1538-7305.1950.tb00463.x.

[81] Frank Gray. Pulse Code Communication. *U.S. Patent 2,632,058*, Nov 1947. URL http://www.google.com/patents/US2632058.

[82] Alberto Riccardi. *Low power integrated system for a simultaneous time and energy measurement in the PANDA micro-strip detector*. PhD thesis, Justus-Liebig-Universität Giessen, May 2017. URL http://geb.uni-giessen.de/geb/volltexte/2017/12828/pdf/RiccardiAlberto-2017-05-02.pdf.

[83] Valentino Di Pietro. *A Time-Based Front-End ASIC for the Silicon Micro Strip Sensors of the PANDA Micro Vertex Detector*. PhD thesis, Justus-Liebig-Universität Giessen, May 2017. URL http://geb.uni-giessen.de/geb/volltexte/2017/12827/pdf/DiPietroValentino-2017-05-04.pdf.

[84] The PANDA MVD Group. *PASTA User Guide*, Jan 2016.

[85] Marius C. Mertens. *Der PANDA Mikro Vertex Detektor: Entwicklung eines Labormesssystems, Simulation der MVD-Betriebsparameter sowie Untersuchungen zur Auflösung der Breite des $D_{s0}^*(2317)$*. PhD thesis, Ruhr-Universität Bochum, 2010. URL http://www-brs.ub.ruhr-uni-bochum.de/netahtml/HSS/Diss/MertensMariusC/diss.pdf.

[86] Simone Esch. *Evaluation of the PANDA Silicon Pixel Front-End Electronics and Investigation of the $\bar{\Lambda}\Lambda$ Final State*. PhD thesis, Ruhr-Universität Bochum, 2014. URL http://hss-opus.ub.ruhr-uni-bochum.de/opus4/frontdoor/deliver/index/docId/4123/file/diss.pdf.

[87] S. Esch, W. Erven, M. C. Mertens, et al. Development of a readout system for the PANDA Micro Vertex Detector. *Journal of Instrumentation*, 8(01):C01043, 2013. URL http://stacks.iop.org/1748-0221/8/i=01/a=C01043.

[88] A. Lai, K.-Th. Brinkman, D. Calvo et al. Design, Implementation and Verification of a Data Acquisition System for the Prototypes of the Front-End Electronics of the PANDA Micro Vertex Detector. In *Nuclear Science Symposium Conference Record (NSS/MIC), 2017 IEEE*, Publication Pending.

[89] Xilinx. Virtex-6 FPGA ML605 Evaluation Kit. https://www.xilinx.com/products/boards-and-kits/ek-v6-ml605-g.html.

[90] U. Farooq, Z. Marrakchi, and H. Mehrez. *Tree-based Heterogeneous FPGA Architectures*. Springer, 2012.

[91] ISO/IEC International Organization for Standardization. *Open Systems Interconnection - Basic Reference Model: The Basic Model*, Nov 1994. Standard 7498-1:1994(E).

[92] Qt Documentation. http://doc.qt.io/, 2018.

[93] A. X. Widmer and P. A. Franaszek. A DC-Balanced, Partitioned-Block, 8B/10B Transmission Code. *IBM Journal of Research and Development*, 27(5):440–451, Sept 1983. ISSN 0018-8646. doi: 10.1147/rd.275.0440.

[94] The PANDA MVD Group. *DISH User Guide*, Apr 2016.

[95] Qt documentation archives: Creating project files. http://doc.qt.io/archives/qt-5.7/qmake-project-files.html, 2018.

[96] Qt Documentation Archives: Variables. http://doc.qt.io/archives/qt-5.7/qmake-variable-reference.html, 2018.

[97] Qt Documentation Archives: Signals and Slots. http://doc.qt.io/qt-5/signalsandslots.html, 2018.

[98] JSON. https://www.json.org/.

[99] Qt Documentation Archives: QJson Document Class. http://doc.qt.io/qt-5/qjsondocument.html, 2018.

[100] BOOST Serialization. https://www.boost.org/doc/libs/1_67_0/libs/serialization/doc/.

[101] J. Adamczewski-Musch and S. Linev. THttpServer class in ROOT. *Journal of Physics: Conference Series*, 664(6):062032, 2015. URL http://stacks.iop.org/1742-6596/664/i=6/a=062032.

[102] Xilinx. ChipScope Pro Software and Cores User Guide, October 2012. URL https://www.xilinx.com/support/documentation/sw_manuals/xilinx14_3/chipscope_pro_sw_cores_ug029.pdf.

[103] H Stockhorst, U Bechstedt, J Dietrich, et al. Progress and developments at the Cooler Synchrotron COSY. 09 2018. URL http://citeseerx.ist.psu.edu/viewdoc/download?doi=10.1.1.526.9026&rep=rep1&type=pdf.

[104] Simone Bianco. *Tracking and vertex reconstruction with the PANDA Micro-Vertex-Detector.* PhD thesis, Universität Bonn, 2013. URL http://hss.ulb.uni-bonn.de/2013/3296/3296.pdf.

[105] M Raymond, G Cervelli, Marcus French, et al. The CMS tracker APV25 0.25 µm CMOS readout chip. Sep. 2018. URL https://cds.cern.ch/record/478270/files/raymond.pdf.

[106] M. Tanabashi, K. Hagiwara, K. Hikasai, et al. Review of particle physics. *Phys. Rev. D*, 98:030001, Aug 2018. doi: 10.1103/PhysRevD.98.030001. URL https://link.aps.org/doi/10.1103/PhysRevD.98.030001.

[107] Stefano Spataro and the PANDA Collaboration. The PandaRoot framework for simulation, reconstruction and analysis. *Journal of Physics: Conference Series*, 331(3):032031, 2011. URL http://stacks.iop.org/1742-6596/331/i=3/a=032031.

[108] B. Musgrave and G. Petmezas. Study of YY Production in Two, Three, and Four Body Final States by 3.0, 3.6 and 4.0 GeV/c Antiprotons in Hydrogen. *Nuovo Cim.*, 35:735, 1965. doi: 10.1007/BF02739338.

[109] David J. Lange. The EvtGen particle decay simulation package. *Nuclear Instruments and Methods in Physics Research Section A: Accelerators, Spectrometers, Detectors and Associated Equipment*, 462(1):152–155, 2001. doi: 10.1016/S0168-9002(01)00089-4.

[110] S. Agostinelli, J. Allison, K. Amako, et al. Geant4 – a simulation toolkit. *Nuclear Instruments and Methods in Physics Research Section A: Accelerators, Spectrometers, Detectors and Associated Equipment*, 506(3):250 – 303, 2003. ISSN 0168-9002. doi: 10.1016/S0168-9002(03)01368-8. URL http://www.sciencedirect.com/science/article/pii/S0168900203013688.

[111] Johannes Rauch and Tobias Schlüter. Genfit — a generic track-fitting toolkit. *Journal of Physics: Conference Series*, 608(1):012042, 2015. URL http://stacks.iop.org/1742-6596/608/i=1/a=012042.

[112] William Chinowsky, Gerson Goldhaber, Sulamith Goldhaber, et al. On the Spin of the K* Resonance. *Phys. Rev. Lett.*, 9:330–332, Oct 1962. doi: 10.1103/PhysRevLett.9.330. URL https://link.aps.org/doi/10.1103/PhysRevLett.9.330.

[113] M. Silarski and P. Moskal. Chodrow plot and the interaction of K$^+$K$^-$. *AIP Conference Proceedings*, 950(1):77–82, 2007. doi: 10.1063/1.2819056. URL https://aip.scitation.org/doi/abs/10.1063/1.2819056.

[114] McGraw-Hill Concise Encyclopedia of Physics. Goldhaber Triangle, 2002.

[115] A. Galoyan and V. V. Uzhinsky. New Monte Carlo Implementation of Quark-Gluon-String Model of $\overline{\text{p}}$p-Interactions. *AIP Conference Proceedings*, 796(1):79–82, 2005. doi: 10.1063/1.2130140. URL https://aip.scitation.org/doi/abs/10.1063/1.2130140.

[116] A. Capella, U. Sukhatme, C.-I. Tan, and J. Tran Thanh Van. Dual parton model. *Physics Reports*, 236(4):225 – 329, 1994. ISSN 0370-1573. doi: https://doi.org/10.1016/0370-1573(94)90064-7. URL http://www.sciencedirect.com/science/article/pii/0370157394900647.

[117] Vincenzo Flaminio, W. G. Moorhead, Douglas Robert Ogston Morrison, and Nicole Rivoire. *Compilation of cross-sections*. CERN, Geneva, 1984. URL https://cds.cern.ch/record/101631. Updated version of CERN HERA 79-03; contains all data published up to the beginning of 1982.

[118] W.W.M. Allison, A.Q. Jones, T. Fields, W.A. Cooper, and D.S. Rhines. Proton-antiproton elastic scattering at 2.32 GeV/c. *Nuclear Physics B*, 56(1):1 – 14, 1973. ISSN 0550-3213. doi: https://doi.org/10.1016/0550-3213(73)90216-2. URL http://www.sciencedirect.com/science/article/pii/0550321373902162.

[119] K. Böckmann, B. Nellen, E. Paul, et al. Elastic scattering, pion production, and annihilation into pions in antiproton-proton interactions at 5.7 GeV/c. *Nuovo Cimento A Serie*, 44:316–317, July 1966. doi: 10.1007/BF02720204.

[120] J. Badier, A. Bonnet, Ph. Briandet, and B. Sadoulet. Reactions $\overline{p}p \rightarrow \Lambda\overline{\Lambda}$ at 2.5 GeV/c. *Physics Letters B*, 25(2):152 – 155, 1967. ISSN 0370-2693. doi: https://doi.org/10.1016/0370-2693(67)90212-2. URL http://www.sciencedirect. com/science/article/pii/0370269367902122.

[121] B.Y. Oh, P.S. Eastman, Z. Ming Ma, et al. A Formation Study of NN Interactions Between 1.09 and 3.45 GeV/c (II). Strange particles. *Nuclear Physics B*, 51:57 – 76, 1973. ISSN 0550-3213. doi: https://doi.org/10.1016/0550-3213(73)90500-2. URL http://www.sciencedirect.com/science/article/pii/0550321373905002.

[122] C. Baltay, J. Sandweiss, H. D. Taft, et al. Antihyperon Production in Antiproton-Proton Reactions at 3.7 BeV/c. *Phys. Rev.*, 140:B1027–B1038, Nov 1965. doi: 10.1103/PhysRev.140.B1027. URL https://link.aps.org/doi/10.1103/PhysRev.140. B1027.

[123] G. P. Fisher, V. Domingo, Å. J. Eide, et al. Hyperon Production in Interactions of 2.7 GeV/c Antiprotons on Protons. *Phys. Rev.*, 161:1335–1343, Sep. 1967. doi: 10.1103/PhysRev.161.1335. URL https://link.aps.org/doi/10.1103/PhysRev.161. 1335.

Lebenslauf

Persönliche Daten

Name:	Alessandra Lai
Geburtsdatum:	12.12.1988
Geburtsort:	Oristano, Sardinien, Italien

Schulbildung

1994 - 1999	Grundschule S. Cuore Oristano
1999 - 2002	Mittelschule G. Deledda Oristano
2002 - 2007	Neusprachliches Gymnasium B. Croce Oristano

Studium

2007 - 2011	Studium Physik, Università degli Studi di Cagliari. B.Sc.-arbeit: *Use of APDs at Low Temperature as Detectors for High Energy Physics*
2012 - 2014	Studium Physik, Università degli Studi di Torino. M.Sc.-arbeit: *Design of an FPGA-Based Calibration and Monitoring System for the HADES Electromagnetic CALorimeter*

Promotion

2015 - 2018	Promotion im Fach Physik and der Ruhr-Universität Bochum in Kooperation mit dem Institut für Kernphysik am Forschungszentrum Jülich. Doktorarbeit: *Development of a Data Acquisition System for the Custom Front-End Prototypes of the PANDA Micro Vertex Detector and Study of the Reaction* $\bar{p}p \rightarrow \Xi^{-}\bar{\Xi}^{+}\pi^{+}\pi^{-}$